UNIVERSITÀ
DEGLI STUDI
DI PADOVA

Sede Amministrativa: Università degli Studi di Padova

Dipartimento di

Biologia

CORSO DI DOTTORATO DI RICERCA IN: Bioscienze e Biotecnologie

CURRICOLO: Biologia Cellulare

CICLO XXIX

STEM CELL EXTRACELLULAR VESICLES FOR NEURAL REGENERATION

Coordinatore: Ch.mo Prof. Paolo Bernardi

Supervisore: Ch.mo Prof. Paolo Bernardi

Co-Supervisore: Ch.mo Prof. Nicola Elvassore

Dottorando: Mario Barilani

Foreword

The results herein presented are original and they were produced during the completion of the Cell Biology program of the Biosciences and Biotechnology PhD School, XXIX cycle. References to studies carried out by others are explicitly indicated.

Concerning the scientific dissemination of the obtained data, the following articles were published:

- **Barilani M**, Lavazza C, Viganò M, et al. Dissection of the Cord Blood Stromal Component Reveals Predictive Parameters for Culture Outcome. *Stem Cells and Development*. 2015;24(1):104-114. doi:10.1089/scd.2014.0160.
- **Barilani M**, Lavazza C, Boldrin V, Ragni E, Parazzi V, Crosti M, Montelatici E, Giordano R, Lazzari L. A Chemically Defined Medium-Based Strategy to Efficiently Generate Clinically Relevant Cord Blood Mesenchymal Stromal Colonies. *Cell Transplant*. 2016;25(8):1501-14. doi: 10.3727/096368916X690827.
- Caron I, Rossi F, Papa S, Aloe R, Sculco M, Mauri E, Sacchetti A, Erba E, Panini N, Parazzi V, **Barilani M**, Forloni G, Perale G, Lazzari L, Veglianese P. A new three dimensional biomimetic hydrogel to deliver factors secreted by human mesenchymal stem cells in spinal cord injury. *Biomaterials*. 2016;75:135-47. doi: 10.1016/j.biomaterials.2015.10.024.
- Montemurro T, Viganò M, Ragni E, **Barilani M**, Parazzi V, Boldrin V, Lavazza C, Montelatici E, Banfi F, Lauri E, Giovanelli S, Baccarin M, Guerneri S, Giordano R, Lazzari L. Angiogenic and anti-inflammatory properties of mesenchymal stem cells from cord blood: soluble factors and extracellular vesicles for cell regeneration. *Eur J Cell Biol*. 2016 Jun-Jul;95(6-7):228-38. doi: 10.1016/j.ejcb.2016.04.003.

The following articles are submitted or under submission:

- Ragni E, Banfi F, **Barilani M**, Cherubini A, Parazzi V, Larghi P, Dolo V, Bollati V, Lazzari L. Extracellular vesicle-shuttled mRNA in mesenchymal stem cell communication.
- **Barilani M**, Ragni E, Banfi F, Sironi S, Cherubini A, Lazzari L. IGF1, NG2 and CD56 as mesenchymal stromal cell markers reminiscent of perinatal or adult tissue harvest.

Some of the results were presented at the following international conferences:

- **Barilani M**, Lavazza C, Viganò M, Ragni E, Boldrin V, Montemurro T, Parazzi V, Montelatici E, Budelli S, Baluce B, Marino L, Crosti M, Moro M, Giordano R, Lazzari L. Dissection of the cord blood stromal component reveals predictive parameters for the isolation of mesenchymal stem cells with superior osteogenic properties. 2014. *TERMIS EU Meeting*, Genova, Italy.
- **Barilani M**, Parazzi V, Ragni E, Lavazza C, Viganò M, Montemurro T, Giordano R, Motta V, Dioni L, Bollati V, Lazzari L. Long- and short-living cord blood multipotent stromal cells at the cross road between epigenetics and bioenergetics. 2015. *ISSCR Annual Meeting*, Stockholm, Sweden.
- Ragni E, Banfi F, Parazzi V, Lavazza C, **Barilani M**, Dolo V, Bollati V, Lazzari L. Mesenchymal stromal cell-derived extracellular vesicles as vehicle of therapeutic mRNA: evidences for Walker-Warburg muscular dystrophy treatment. 2016. *ISEV Annual Meeting*, Rotterdam, Netherlands.
- **Barilani M**, Montemurro T, Vigano M, Ragni E, Lavazza C, Montelatici E, Banfi F, Giordano R, Lazzari L. Angiogenic and anti-inflammatory properties of mesenchymal stem cells from cord blood: soluble factors and extracellular vesicles for cell regeneration. 2016. *Extracellular vesicles: friends and foes*, Rehovot, Israel.

Summary

In the last decade, multipotent mesenchymal stromal cells (MSCs) demonstrated a significant therapeutic efficacy, particularly in cell therapy approaches aiming at tissue regeneration. MSCs exert their action via trophic support, induction of angiogenesis, immunomodulation and reduction of necrosis at affected tissues. Importantly, these regenerative and protective properties are largely associated to MSC secretome. Unfortunately, cell-based approaches not always meet the criteria for a smooth translation to the clinic. For instance, the use of stem cells in pathologies with a very short therapeutic window, such as few hours, is not compatible with the requested minimal criteria for MSC release, before administration to the patient.

Notwithstanding, in the regenerative medicine field, the MSC mechanism of action paradigm was recently extended to include the action of extracellular vesicles (EVs), which are cytoplasm-containing cellular bodies secreted by a wide range of cell types. Intriguingly, many studies reported that EVs generated by MSCs are able to recapitulate the majority of the regenerative properties of parental MSCs.

Starting from these premises, the objectives of the present doctoral research project were: to address EV-mediated cell-to-cell communication as novel MSC mechanism of action; to address reprogrammed MSC-EV generation; to define, for the first time in the literature, stem cell EV molecular content (*e.g.*: miRNome), comparing reprogrammed to non-reprogrammed MSC-EVs; to challenge stem cell-EV therapeutic potential in a model of acute tissue damage, as a proof-of-concept for feasibility and effectiveness of a stem cell-based albeit cell-free regenerative strategy. Intriguingly, EVs may be produced in a ready-to-use formulation, so that clinicians could use them as soon as a therapeutic need arises, also in the case of an urgent one. In this way, EV-shuttled MSC regenerative properties could exert beneficial effects also on pathologies currently lacking any cell therapy option.

To develop this innovative therapeutic strategy, MSCs were isolated from different tissues and their biological properties were evaluated in order to choose the MSC source most suitable for the implementation of the project. Thus, both MSC transcriptome and immunophenotype were addressed. MSCs from adult sources (*e.g.*: bone marrow) showed senescence-related features *in vitro*, correlated to donor's age *in vivo*. On the other hand, MSCs from perinatal tissues (*e.g.*: cord blood) showed a phenotype more similar to that of pericytes, which are the *in vivo* progenitors of MSCs. Therefore, cord blood was chosen as MSC source, also in the prospective of clinical translation, since public banking of cord blood units for clinical use already exists worldwide.

Next, thanks to an extended analysis of the stromal populations present in cord blood, a MSC subpopulation showing higher proliferation properties and significantly longer telomeres was isolated. In addition, the standard cord blood MSC isolation protocol was improved, leading to an efficiency of 80%. Eventually, MSC secretome-associated anti-inflammatory and anti-apoptotic properties were observed *in vitro* and *in vivo*. In order to investigate if EVs contributed to MSC paracrine properties, MSC-EV secretion and regenerative properties were assessed. The MSC-EV therapeutic effectiveness was challenged in an *in vitro* model of acute tissue damage. Intriguingly, MSC-EVs could rescue damage-induced cell mortality, showing the same protective effect of parental MSCs.

In spite of the use of a high proliferative cord blood MSC subpopulation, primary cultures still show a limited lifespan. In order to increase their replicative potential and to better exploit their EV production, induced cellular reprogramming was tested on MSCs as an alternative to traditional immortalization techniques. In this way, MSC-derived cell lines endowed with unlimited lifespan were generated, and permanent modification of their genome was avoided. The next step was to confirm the generation of EVs from reprogrammed MSCs, since reprogramming drastically changes cell identity. Furthermore, the EV miRNome load of reprogrammed and non-reprogrammed MSCs was addressed. Importantly, the majority of miRNAs were common between the two samples, indicating that reprogramming did not change the EV miRNA content. This result could have relevant consequences on the functional features of reprogrammed MSC-EVs, since EV-mediated miRNA transfer from donor to target cells was proposed as one of MSC mechanisms of action.

In the last part of this doctoral research, stem cell (non-reprogrammed and reprogrammed MSCs)-EV therapeutic effectiveness was addressed and compared to that of parental MSCs. In order to do that, an organotypic *ex vivo* mouse model of brain ischemia was used. This model recapitulated the modulation of some ischemic damage-related parameters, including increased secretion of inflammatory cytokines, high tissue necrosis and the impairment of neuronal and astrocytic cell populations. Therefore, this model mimicked early phase events of brain ischemia, whose thrombolytic clinical treatment must be administered within 3-6 hours of first signs of ischemia. Notably, stem cell-EVs were tested for the first time in this pathological context to verify their potential role in tissue regeneration. Strikingly, stem cell-EV administration to affected tissues showed significant neuroprotective properties, which were comparable to those of parental MSCs. Importantly, the ischemic damage-related parameters previously described were rescued. In particular, inflammatory-associated parameters underwent the most statistically significant decrease, showing levels similar to or better than those of the uninjured brain tissue. This is of uttermost importance, considering that chronic inflammation is detrimental to tissue regeneration.

To conclude, the results of the present PhD thesis confirmed the feasibility of stem cell EV-based therapies in regenerative medicine approaches. In the future, this innovative EV therapy may be applied to pathological contexts currently without a cell therapy option. In the framework of advanced therapy medicinal products, the new drug would be the EVs, rather than the parental stem cells. Finally, EVs could play the role of ready-to-use anti-inflammatory molecule carriers, in order to guarantee a rapid therapeutic action for the regeneration of injured tissues.

Sommario

Negli ultimi anni, le cellule stromali mesenchimali multipotenti umane (CSM) hanno mostrato una grande efficacia terapeutica, soprattutto in approcci di terapia cellulare aventi come obiettivo la rigenerazione tissutale. L'azione delle CSM avviene attraverso supporto trofico, induzione di angiogenesi, modulazione della risposta immunitaria e diminuzione della necrosi a livello dei tessuti colpiti. Inoltre, recente letteratura ha dimostrato che queste capacità rigenerative e protettive sono in larga parte associate al secretoma delle CSM. Purtroppo, gli approcci di terapia cellulare non sono sempre traslabili alla clinica. Ad esempio, l'utilizzo di cellule staminali in patologie caratterizzate da una finestra terapeutica molto stretta, dell'ordine di poche ore, non è compatibile con la necessità di scongelare e valutare i minimi standard di qualità delle CSM prima della somministrazione al paziente.

Nonostante ciò, il paradigma del meccanismo d'azione delle CSM nel campo della medicina rigenerativa si è ulteriormente arricchito. Infatti, molti recenti studi hanno dimostrato che le vescicole extracellulari, ossia porzioni di citoplasma delimitate da membrana cellulare secrete dalle CSM, sono in grado di riprodurre la maggior parte delle proprietà rigenerative delle CSM stesse.

Date queste premesse, gli obiettivi del progetto di ricerca del presente Dottorato sono stati i seguenti: indagare la comunicazione intercellulare tramite vescicole extracellulari quale innovativo meccanismo d'azione delle CSM; studiare la produzione di vescicole extracellulari da parte di CSM riprogrammate, e, per la prima volta in letteratura, definirne il contenuto molecolare (es.: miRNoma), a confronto con le CSM d'origine; testare il potenziale terapeutico di vescicole extracellulari da cellule staminali in un modello di danno tissutale acuto, come *proof-of-concept* della funzionalità di una strategia terapeutica *cell-free*. Infatti, le vescicole extracellulari potrebbero essere prodotte in formulazioni pronte all'uso, a immediata disposizione per ogni richiesta clinica, anche urgente. In questo modo le proprietà rigenerative delle CSM potrebbero essere veicolate dalle vescicole extracellulari anche in contesti patologici attualmente senza alcuna opzione di terapia cellulare.

Per lo sviluppo di questa innovativa strategia terapeutica, CSM isolate da vari tessuti sono state caratterizzate e confrontate in base al loro trascrittoma e al loro immunofenotipo, allo scopo di valutarne le proprietà biologiche e quindi scegliere le CSM più adatte all'implementazione del progetto di Dottorato. Le CSM da tessuti adulti (*e.g.*: midollo osseo) hanno mostrato *in vitro* caratteristiche di senescenza correlate all'età del donatore *in vivo*. Al contrario, le CSM da tessuti perinatali (*e.g.*: sangue di cordone ombelicale) hanno mostrato un fenotipo più simile a quello dei periciti, ossia i progenitori delle CSM *in vivo*. Quindi, tenuto conto anche della traslabilità clinica, il sangue di cordone ombelicale è stato scelto come fonte di CSM, visto che la raccolta e la crioconservazione di unità di sangue placentare a fini terapeutici è già una realtà clinica. In seguito, un'analisi estesa delle popolazioni stromali presenti nel sangue di cordone ombelicale ha portato alla definizione di una sottopopolazione di CSM dotata di maggiori capacità proliferative e con una lunghezza del telomero significativamente più alta. Inoltre il protocollo standard di isolamento delle CSM da sangue di cordone ombelicale è stato migliorato, arrivando ad un'efficienza di circa 80%. Infine, le proprietà anti-infiammatorie e anti-apoptotiche del secretoma delle CSM sono state studiate sia *in vitro* che *in vivo*. Al fine di verificare se le vescicole extracellulari contribuissero alle proprietà paracrine delle CSM, se ne è caratterizzata la secrezione e se ne sono indagate le proprietà rigenerative. Una chiara efficacia terapeutica da parte delle vescicole extracellulari di CSM è stata dimostrata in un modello *in vitro* di danno tissutale acuto, in cui le vescicole extracellulari hanno eguagliato i risultati ottenuti con le CSM stesse.

Nonostante l'utilizzo di CSM dalle elevate proprietà proliferative, la loro *lifespan* in coltura, in quanto cellule primarie, rimane limitata. Allo scopo di aumentarne il potenziale replicativo e di sfruttarne al meglio così la produzione di vescicole extracellulari, le CSM sono state sottoposte alla riprogrammazione cellulare indotta. In questo modo sono state generate linee cellulari derivate da CSM dal potenziale di crescita illimitato, evitando però di modificarne il genoma come nelle tradizionali tecniche di immortalizzazione. Siccome la riprogrammazione implica una modificazione radicale dell'identità della cellula d'origine, il passo successivo è stato quello di confermare la capacità di questa nuova popolazione di generare vescicole extracellulari, poi opportunamente caratterizzate.

In particolare, il miRNoma delle vescicole extracellulari da cellule riprogrammate è stato oggetto di studio e di confronto con quello delle vescicole extracellulari delle CSM d'origine. Si è così potuto dimostrare che la maggior parte dei miRNA era presente nelle vescicole extracellulari sia prima che dopo la riprogrammazione. Ciò indica che il processo di riprogrammazione non ne ha alterato in modo sostanziale il contenuto. Questo potrebbe avere importanti ricadute sugli aspetti funzionali delle vescicole extracellulari da CSM riprogrammate. Infatti è stato ipotizzato che il trasferimento di miRNA specifici da cellule donatrici a cellule target mediato dalle vescicole extracellulari sia uno dei meccanismi d'azione delle CSM.

Nell'ultima parte di questo progetto di Dottorato, l'utilità terapeutica delle vescicole extracellulari da cellule staminali (CSM e CSM riprogrammate) è stata confrontata con quella delle CSM d'origine. A tale scopo è stato utilizzato un modello *ex vivo* di ischemia cerebrale, in cui è stato osservato il movimento di alcuni parametri di danno ischemico acuto, tra cui un picco di produzione di citochine infiammatorie, una forte necrosi tissutale e una riduzione delle popolazioni cellulari neuronali e astrocitiche. Questo particolare modello mima infatti la fase acuta di questa condizione patologica, il cui trattamento a base di agenti trombolitici deve avvenire entro 3-6 ore dall'insorgenza dei primi sintomi. Quindi le vescicole extracellulari prodotte dalle CSM riprogrammate sono state testate per la prima volta in questo contesto patologico per verificare se potessero esercitare una funzione rigenerativa. La loro somministrazione al tessuto colpito dal danno ischemico ha generato uno spiccato effetto neuroprotettivo, pari a quello delle CSM d'origine, che ha riportato a valori simili a quelli del tessuto cerebrale non danneggiato i parametri di danno sopra descritti. Il risultato più interessante e statisticamente significativo è stato soprattutto a carico di quei parametri legati ai processi infiammatori, i quali sfavoriscono il recupero del danno tissutale.

In conclusione, i risultati presentati in questa tesi di Dottorato confermano la possibilità di utilizzo di vescicole extracellulari secrete da cellule staminali in strategie di medicina rigenerativa. Questa innovativa *extracellular vesicle therapy* potrebbe in futuro essere applicata in contesti patologici per i quali ad oggi non è praticabile una terapia cellulare.

A questo punto, nel quadro dei prodotti medicinali per le terapie avanzate, il “farmaco” non sarebbe più la cellula staminale, ma le rispettive vescicole extracellulari. Queste acquisirebbero così il ruolo di *carrier* di molecole antinfiammatorie, pronte all’uso e capaci di garantire un’azione terapeutica tempestiva per la rigenerazione di tessuti danneggiati.

Contents

Chapter 1

Development of a stem cell-based albeit cell-free regenerative approach

Nowadays, human stem cells are being widely tested, or already effectively used, in clinical protocols referring to the general area of regenerative medicine. Whether the therapeutic rationale roots on differentiation or “drugstore”-like properties, stem cell clinical trial numbers steadily increase (Fig. 1.1).

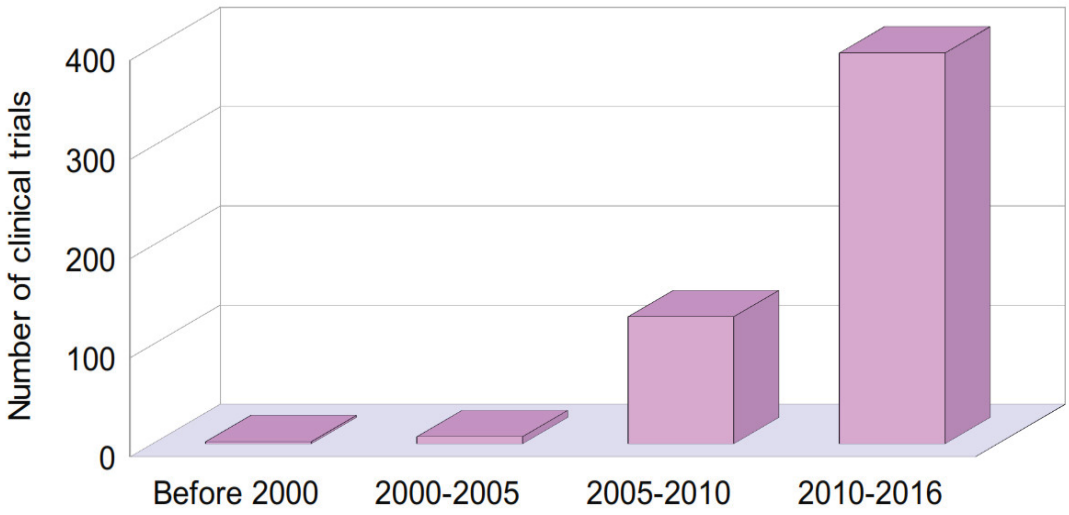

Figure 1.1. Stem cells in translational research. Source: ClinicalTrial.gov; search terms: (“cell therapy” OR “regenerative medicine” OR “advanced medicinal product” OR “Tissue Engineering”) AND “stem cell”; 09/11/2016.

Despite the high expectations regarding stem cell-based therapies, many hurdles have frequently impeded their complete fulfillment so far (*e.g.*: [1, 2]), as shown by the number of phase 3 and 4 clinical trials, compared to total approved studies (Fig. 1.2).

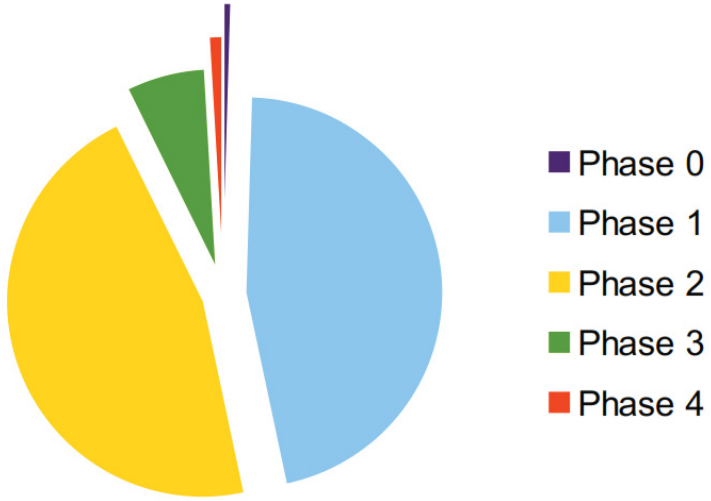

Figure 1.2. Stem cell clinical trial phases. Source: ClinicalTrial.gov; search terms: ("cell therapy" OR "regenerative medicine" OR "advanced medicinal product" OR "Tissue Engineering") AND "stem cell", filtered for phase 0, 1, 2, 3 or 4; 09/11/2016.

Various reasons behind this have been proposed, ranging from inadequacy of *pre*-clinical models to heterogeneity of cell preparations, i.e. *inter*- and *intra*-stem cell donor variability [3-7]. Yet, one major issue in this field is that the precise stem cell mechanisms of action (MoA) are often not fully understood and characterized, in spite of a demonstrated functionality [8-10]. This happens also for multipotent mesenchymal stromal cells (MSCs), which are frequently used in reason of a plethora of secretome-associated properties (*e.g.*: [11-13]).

Recently, extracellular vesicles (EVs) budding from stem cells were shown to recapitulate many therapeutic properties ascribed to their cellular counterpart [12, 14-16]. Thus, it is of utmost importance to assess if EVs play a role in MSC secretome-associated MoA. If this is the case, EVs may be used to develop more affordable cell-free regenerative approaches, keeping in mind that the more thoroughly the MoA is defined, the more consistent the clinical outcome will be.

1.1 Introduction

As a branch of translational research, regenerative medicine ultimate goal is “to regenerate, replace or repair cells, tissues or even organs” (cited from [17]). Such a concept was first theorized in 1992 by L. Kaiser as “A new branch of medicine [...] that attempts to change the course of chronic disease and [...] (to) regenerate tired and failing organ systems” (cited from [18]). The starting point of this field is that many regenerative processes may be indeed observed in nature, for invertebrates and vertebrates alike, involving complete or partial limb regeneration (*e.g.*: Axolotl limbs, human pediatric fingertips) [19, 20], or internal organ reconstitution (*e.g.*: adult human liver) [21]. Thus, the underlying ratio is to mimic, substitute, trigger or aid endogenous processes to restore impaired physiological functions.

Different approaches, aiming at the development of the so-called advanced therapy medicinal products (ATMPs), have been used so far to achieve such a goal, ranging from cell therapy, modulation of stem cell biology, tissue replacement, gene therapy, bioengineering or a combination of them [22]. In particular, cell therapy approaches rely on the assumption that a dynamic system such as a living cell would modulate its behavior responding to the extracellular environment of the target tissue. Thus, a more refined therapeutic action and a better clinical outcome would be guaranteed, compared to traditional pharmacological treatments. Yet, the path a cell therapy protocol must follow implies very high costs and many technical and regulatory hurdles to cope with. In this scenario, it is not trivial to underline that the simpler is the better: the simpler the ATMP formulation and the production workflow, the easier to standardize the process and to obtain consistent ATMP batches and clinical results.

Concerning stem cell types currently used in cell therapy, multipotent mesenchymal stromal cells (MSCs) gained a prominent role, representing a third of total stem cell clinical trials[1]. MSC widespread use is due to their multipotent differentiation capabilities (*i.e.*: bone and cartilage reconstruction), but also in reason of MSC secretome-associated properties.

1 Source: ClinicalTrial.gov; search terms: (“cell therapy” OR “regenerative medicine” OR “advanced medicinal product” OR “Tissue Engineering”) AND “stem cell”, for total stem cell trials; (“cell therapy” OR “regenerative medicine” OR “advanced medicinal product” OR “Tissue Engineering”) AND “mesenchymal”, for MSC trials.

As an instance, MSCs are successfully employed in clinical protocols requiring immunomodulation (*e.g.*: graft-*versus*-host disease) [23]; nonetheless, angiogenic, anti-inflammatory and anti-apoptotic effects can be attained, too [24-26]. Unfortunately, the precise molecular and biological processes (mechanisms of action, MoA), which allow MSCs to exert such regenerative functions, have often been so far quite elusive. Revising the literature, MSC MoA paradigm changed swiftly in the last decade, switching from transdifferentiation to tissue modulation [27], not without causing sometime fierce scientific debates [28-30]. Admittedly, this issue could be in part responsible of inconsistencies observed in the effectiveness of some MSC-based clinical trials [31, 32]. Hence, in spite of the clinical interest aroused by MSCs, it is of paramount importance to achieve first a more accurate definition of what MSC MoAs are, in order to better control MSC therapeutic action and to achieve more satisfying and consistent clinical outcomes.

In this context, recent findings demonstrated that some MSC secretome-associated properties might be partially ascribed not only to secreted soluble factors, but also to the so-called extracellular vesicles (EVs) [33]. These are membrane-enclosed particles, which contain biologic material from the cell of origin cytoplasm [34]. In the frame of cell-to-cell communication mechanisms, EVs represent a peculiar solution to the problem of horizontal transfer of bioactive molecules across the extracellular space, toward distant organism compartments. The extent EVs participate in the already known MSC secretome-associated properties is presently under debate and it will complete the current MSC MoA paradigm.

In the following sections, the scientific background that accounts for the development of a stem cell-based albeit cell-free regenerative approach is introduced, focusing on the advantages of MSCs as stem cell source and on the aforementioned novel cell-to-cell communication mechanism as candidate carrier of stem cell-derived regenerative information.

1.2 Motivation for a cell-free stem cell-based strategy

Multipotent mesenchymal stromal cells (MSCs) are extensively used in clinical applications in reason of their regenerative properties. This implies that they are already available at the clinical-grade level. Therefore, their use for the development of a cell-free therapeutic approach is feasible and promising. Innovative therapeutic agents could be detected from the dissection of MSC secretome, since many MSC applications rely on their capacity to release bioactive molecules, rather than on their differentiation properties. The next paragraphs illustrate why, in our working hypothesis, extracellular vesicles (EVs) could play that role.

1.2.1 "Curative" versus "replacement-focused" stem cell paradigm

In the field of regenerative medicine, two main stem cell paradigms might be distinguished. In the first case, stem cells are used for their differentiation properties and translational research is focused on cell, tissue or organ replacement strategies. In the second, the stem cell secretome is seen as a therapeutic tool *per se*. Thus, cells are introduced into patients, so that they can unleash their secretome at the target tissue to exert a regenerative effect. This last approach, that can be referred to as "curative", has been heavily relying on the use of MSCs. Thanks to their anti-apoptotic and anti-inflammatory secretome properties, MSCs were proven effective in a variety of pathological conditions, where control of the immune system response or treatment of acute tissue damage is needed. On the other hand, a "replacement-focused" approach is based on the stem cell potency degree, in order to generate a specific set of differentiated cell types starting from the same undifferentiated cell. From this point of view, multipotent MSCs have *in vitro* differentiation abilities limited to the mesodermal lineage (*i.e.*: bone, cartilage, adipose tissue) [35], if compared to pluripotent stem cells, which can give rise to derivatives of all the three germ layers [36]. Furthermore, it is worth noting that while pluripotent stem cells present serious safety issues related to their high tumorigenic risk, MSCs are completely safe [37].

This seemingly dual and contrasting nature of MSCs may be attributed to their *in vivo* function, postulated as tissue niche regulation [38]. As a matter of facts, MSCs reside virtually in any vascularized tissue of the body, as their *in vivo* precursors are pericytes [39], which are cells wrapped around capillaries and venules. Depending on the tissue of origin or pathological condition, pericytes can exert trophic functions (*e.g.*: angiogenesis and endothelial cell survival) [40] or physical support (*e.g.*: maintenance of the blood-brain barrier) [41], or they can even differentiate into tissue-specific cells and replace the damaged ones (*e.g.*: skeletal muscle regeneration) [42]. As a consequence, MSCs can be isolated from many vascularized adult tissues, such as the bone marrow [35] and the adipose tissue [43], but also from perinatal tissues, such as the cord blood [44] or the Wharton's jelly [45]. As already mentioned, the tissue of origin influences MSC behavior and properties *in vitro*. In particular, a piece of literature is starting to point out how donor age is important to determine stem cell potential and biological features [46]; this aspect will be discussed more in detail in Chapter 2.
In conclusion, MSCs represent a valid option as a stem cell type whose secretome could be employed to vehicle cell-free regenerative messages, already observed in traditional cell-based approaches, to affected tissues.

1.2.2 A novel cell-to-cell communication mechanism

The term "extracellular vesicle" (EV) was recently coined to describe a heterogeneous set of membrane-encircled cytoplasm-containing bodies of cell origin, whose cargo comprises a wide range of nucleic acids (*e.g.*: DNA, mRNA, miRNA) and proteins. A growing body of literature is showing how some, if not all, MSC properties may be ascribed to the action of EVs. Examples range from modulation of differentiation properties (*e.g.*: stimulation of osteogenic program in recipient cells) [47] to immunomodulatory effects (*e.g.*: promotion of anti-inflammatory M2 macrophage phenotype acquisition) [48]. It is worth noting that the same properties were demonstrated in the past for non-fractionated MSC-conditioned media, in which the role of soluble factors was studied [49-51].

It is likely that such contribute was predominant over the one exerted by EVs present in the same MSC-conditioned medium, unnoticed by the researchers. Notwithstanding, it can be envisioned that EVs could act as a delayed courier of the same messages conveyed by more rapid intracellular signaling pathway-activating soluble factors. While the latter are free to interact swiftly with cell receptors in the extracellular environment, the former, in addition, may need either to be internalized by the cell or to fuse with the cell membrane to deliver their bioactive content and to influence cell physiology.

From these premises, EVs were considered optimal candidates as cell-free carriers of stem cell-generated regenerative clues.

1.3 State of the art

1.3.1 Exosomes and microvesicles

Extracellular vesicles (EVs) represent an elegant and evolutionally conserved cell-to-cell communication strategy, exploited by both prokaryotic and eukaryotic cells. The involvement of EVs in pathological conditions is under intense study, as their role could be that of disease biomarkers or also of disease-propagating agents. EVs were shown to have a role also in the maintenance of homeostasis and of cell physiological functions, even though this aspect have been less investigated. Since their discovery in 1946 by Chargaff and West [52], as procoagulant platelet-derived particles in normal plasma, under the name of "platelet dust" [53], EVs were then observed during bone calcification [54], in cell cultures [55], in seminal plasma [56] and as tumor-originating cell fragments [57]. In all these cases, the researchers were observing microvesicles (MVs), cellular microparticles generated by outward budding and fission of cellular plasma membranes. It was only in 1983 when ultrastructural studies demonstrated that vesicles are also produced as intraluminal vesicles contained in multivesicular bodies, which, upon fusion with the plasma membrane, are released in the extracellular space [58]. These particles were later characterized in transformed B lymphocytes and called exosomes [59]. Yet, in spite of distinct biogenesis pathways, unambiguous markers distinguishing these two populations still lack [60]. This is due in part to inefficiency of current isolation methodologies in the purification of homogeneous classes of vesicles, whereas they actually yield composite vesicle mixtures [61]. Waiting for more accurate isolation methodologies and definitive vesicle subpopulation markers, the general term "extracellular vesicle" was adopted by the field. It is important to underline that this could be further complicated by the presence of apoptotic bodies, so that thoroughly characterization of the EV source is pivotal for consistent results. Nonetheless, a classification of EVs by physical parameters has become a common practice [62]: exosomes are usually described as particles 30-100 nm in size; MVs range from 50 to 1,000 nm; apoptotic bodies show greater variability and higher sizes (500-5,000 nm) (Fig. 1.3).

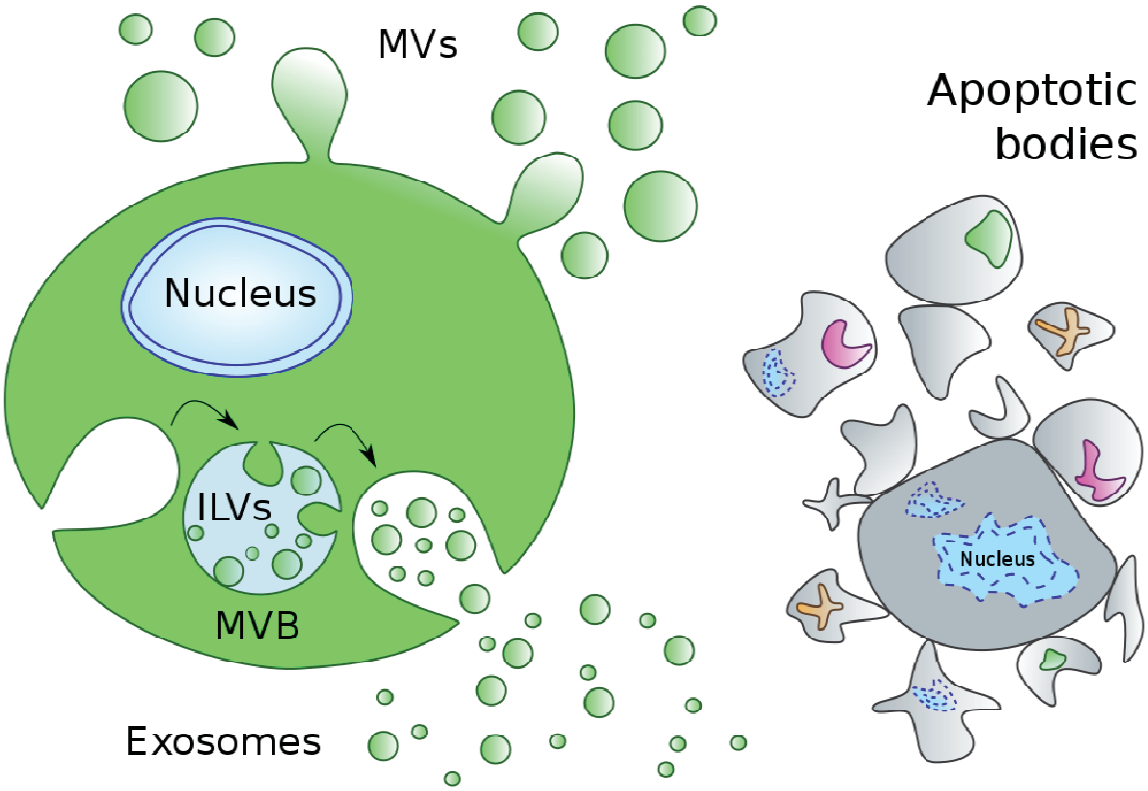

Figure 1.3. Biogenesis and release of extracellular vesicles. Extracellular vesicles (EVs) can be divided into 3 classes, depending on their biogenesis: i) microvesicles/microparticles/ectosomes, generated by outward budding and fission of the plasma membrane; ii) exosomes, produced by the endosomal network and secreted into the extracellular space; iii) apoptotic bodies, following programmed cell death. MVs, microvesicles; ILVs, intraluminal vesicles; MVB, multivesicular body.

The most appealing feature of EVs is their capability to carry different classes of bioactive molecules, such as mRNA, miRNA, DNA, lipids and proteins [63]. Concerning proteins, extensive catalogs are already available online for different kind of samples (*i.e.*: biological fluids, cell or tissue cultures), even if proteomic profiles were found to be dependent on the isolation methodology or on the experimental condition applied [64-67]. Nevertheless, EVs were generally shown to be enriched in proteins involved in vesicle trafficking or coming from cytosol and plasma membrane. On the other hand, presence of intracellular organelle proteins was shown to be significantly reduced. Among the proposed protein markers, which still lack general consensus and validation, are: some tetraspanins (i.e.: CD9, CD63, CD81, CD82), 14-3-3 proteins, MHC molecules, heat shock proteins, and Endosomal Sorting Complex Required for Transport (ESCRT) pathway proteins Tsg101 and Alix [68].

Even though CD9, CD63 and CD81 were initially considered exosome-specific markers, they were subsequently observed also in MVs and apoptotic bodies [69-72]. Thus, many efforts will be necessary to define reliable EV markers.

With regard to RNA, it was observed that EVs incorporate preferentially <700 nt RNA molecules, hinting at a predominance of small RNA species, as miRNAs [73, 74]. Yet, the presence of intact mRNAs was also demonstrated [75]. For proteins and RNAs alike, the mechanisms that control sorting to EVs remain elusive. Whereas protein incorporation seems dependent on aspecific mechanisms related to EVs biogenesis, such as tetraspanin-enriched plasma membrane microdomain formation or the membrane curvature machinery [76-78], RNAs were demonstrated to undergo more regulated processes [79]. The enrichment of certain RNAs, compared to parental cells, was ascribed to active sorting mechanisms relying on the coordinated action of nucleotide motifs and RNA-binding proteins [80].

Being carriers of biological information, EV uptake and biodistribution mechanisms are crucial aspects, too, currently under research. The importance of surface-exposed receptors and ligands was already demonstrated, in particular for glycan-binding proteins [81-83]. Specifically, surface glycosylation patterns could play an essential role in EV uptake [67, 84-87], in a heparin sulphate proteoglycan-dependent manner [88, 89]. After the interaction with the target cell is established, EVs may trigger intracellular signaling pathways, undergo internalization, or transfer lipids and functional receptors [34]. Internalization was observed to occur mostly by phagocytosis, but also macropinocytosis and direct fusion may be involved [89-93]. The choice among these mechanisms would be influenced by recipient cell capabilities, or also by extracellular environment pH conditions. For instance, similar membrane fluidity is needed for direct fusion, something that occurs only at acidic pH in the case of plasma membranes and EVs [90, 94-97]. Biodistribution was shown to be dependent on cell source, injection site, availability of target sites and physiological conditions. In some cases, it was regulated by specific adhesion molecules (e.g.: CD169, ICAM1) [98-101].

A study with rat red blood cell-EVs found out that EVs were retained mostly in the liver (44.9%) and bone (22.5%), but also in skin (9.7%), muscle (5.8%), spleen (3.4%), kidney (2.7%), and lung (1.8%) [102]; almost complete clearance of EVs from blood circulation was observed after 5 minutes. Yet, another study using melanoma-derived EVs showed preferential uptake in lungs and spleen after intravenous injection [103], but with a similar half-life. This very short half-life was confirmed by other studies, and in all cases complete clearance was assessed within 30 minutes [102, 103]. Human platelet concentrate-derived EVs represented an exception, with a half-life of 5.5 hours, probably depending on lower organ uptake, as complement-induced lysis would be escaped by EV surface CD55 and CD59-mediated protection [104]. A recent report investigated biodistribution of mouse EVs from different cell sources and different routes of administration. Strikingly, EVs were retained in different tissue compartments for 48 hours. More importantly, both EV cell source and administration route significantly influenced biodistribution. For instance, dendritic cell EVs localized preferentially in the spleen, whereas myoblast cell line EVs were found at higher amounts in the liver; intra-venous delivery enhanced spleen EV uptake, while intra-peritoneal and sub-cutaneous deliveries increased gastro-intestinal tract EV uptake.

1.3.1.1 Methodological considerations on extracellular vesicle isolation

Various approaches can be employed to isolate and purify EV preparations. Even though no definitive methodology is currently available, the most used in research laboratories is ultracentrifugation [105]. This technique allows separation for both density and size at 100,000 g, and it assures higher purity if coupled with the use of gradients. The disadvantages are possible EV aggregation and laborious or multi-step protocols to remove dead cells and debris from the sample before EV harvest. Precipitation with volume-excluding polymers is a faster and simpler alternative, but it lacks size specificity and it needs a final polymer purification step for very small amounts of sample. Another option is size-exclusion chromatography, which guarantees high purity in a single-step process, although it currently works only on a small scale. Tangential-flow filtration represents the most promising method in terms of scalability. It is fast and it efficiently enriches the sample; nonetheless, additional steps are needed to obtain higher purity.

For this doctoral project, ultracentrifugation was chosen over the other methodologies, because it already allows the processing of high amounts of different biological fluids at the same time (8 different samples, 100 mL each). Furthermore, high enrichment and purity can be obtained if additional differential centrifugations are performed; EV aggregation is partially avoided with shorter centrifugation protocols, even if a lower isolation efficiency might be taken into account (Fig. 1.4).

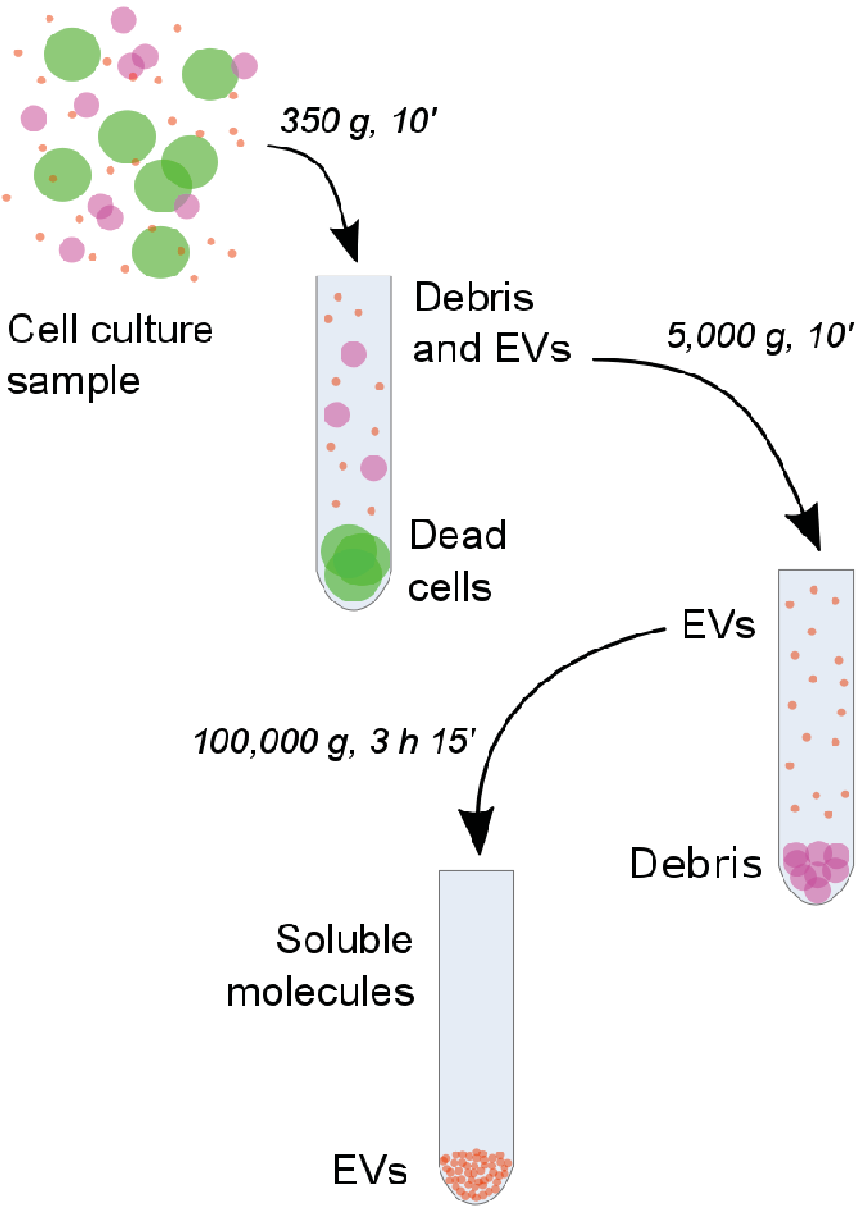

Figure 1.4. Extracellular vesicle isolation workflow. In order to isolate extracellular vesicles (EVs) secreted in cell culture media, dead cells (i) and cell debris (ii) must be first removed. After these purification steps, EVs are collected by ultracentrifugation (iii); soluble molecules, as secreted proteins, remain in the discarded supernatant. EVs can now be resuspended in the appropriate solution for functional assays, or they can be immediately lysed for molecular analysis.

1.3.2 Stem cell extracellular vesicles

So far, little is known about the role of EVs in stem cell physiology. Most of the information concerns MSC-derived EVs, considered the new players in MSC paracrine/endocrine therapeutic mechanism of action (MoA), and mainly in immunological contexts (Fig. 1.5).

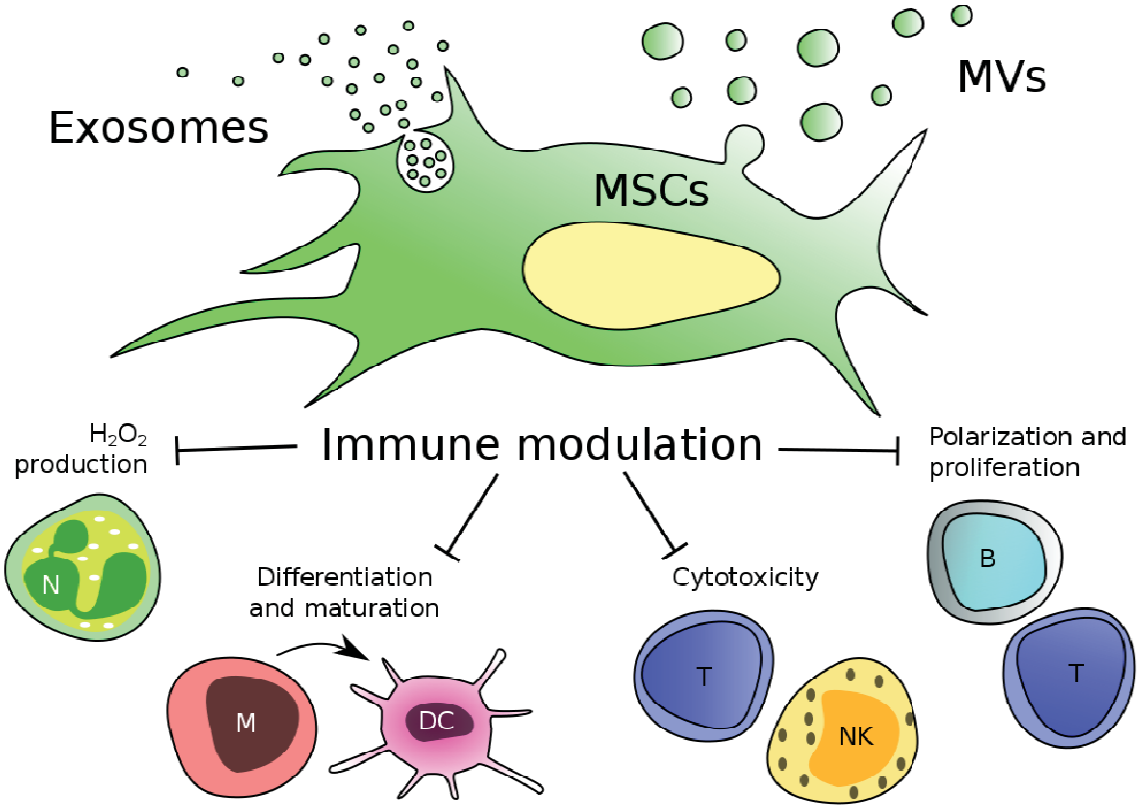

Figure 1.5. MSC paracrine properties. MSC extracellular vesicles (EVs) exert various effects on immune system cells, as illustrated here. MVs, microvesicles; MSCs, multipotent mesenchymal stromal cells; N, neutrophil; M, monocyte; DC, dendritic cell; T, T lymphocyte; NK, natural killer cell; B, B lymphocyte.

For instance, they were shown to drive M2 macrophage polarization and Treg cell induction [48], to reduce T-cell proliferation and promote Treg cell proliferation [23, 106], and to modulate also innate immune responses [107-109], such as the induction of immature anti-inflammatory IL10-secreting dendritic cells [110]. Concerning MSC-EV molecular cargo, they were shown to contain 239 mRNAs involved in immune regulation, but also cell differentiation, proliferation and gene transcription [14, 111]. These mRNAs could be translated into full-length proteins in the recipient cells, where they exerted a protective action.

Furthermore, EVs were proved to maintain hematopoietic stem cells undifferentiated [111] and to support their expansion [112], to promote angiogenesis [113], but also to be able to act as carriers of exogenous molecules, such as anti-cancer pharmaceuticals [114]. In addition, an effective role of MSC-EVs as tissue repair agents is under investigation, with an increasing amount of more and more robust data.

Summarizing some reports, EVs were found to protect bone marrow hematopoietic cells after irradiation injury [115], adult or fetal brain tissues after stroke [116-118], renal tubular cells after ATP depletion-driven or chronic/acute kidney injury [119-122], mesangial cells from hyperglycemia [123], pancreas and lung from acute inflammation [124, 125], retinal cells by laser injury [126], liver from hepatic ischemia [127], and heart from acute myocardial infarction [128]. Intriguingly, even though the exact MoA of EVs is not frequently investigated, some of the aforementioned reports point at miRNAs as the key molecules horizontally transferred by EVs to alter the phenotype of target cells.

In conclusion, EV-triggered cellular plasticity and phenotype modulation could contribute to tissue regeneration by the delivery of bioactive molecules to affected organs, in alternative to stem cell transdifferentiation.

1.4 Rationale for cell-free regenerative approaches

A “cellular”-to-“vesicular” therapeutic paradigm switch would allow the preparation of “off-the-shelf” Advanced Therapy Medicinal Products (ATMPs) with equivalent functionality, but different application areas. Homogeneous batches of extracellular vesicles (EV)-based ATMPs could be produced, tested for efficacy, and stored for later ready-to-use application. Many patients suffering from pathological conditions for which a therapeutic time window lasts few hours (*e.g.*: thrombolytic therapy within 3-6 hours for stroke), could benefit from a prompt EV-based treatment. Admittedly, the same rapidity is utterly unfeasible with cell-based treatments, as longer preparation and unavoidable *post*-thawing analyses, addressing at least viability, must be completed by highly qualified operators, before release to patient bedside. Indeed, the very identity of EVs as non-living entities would allow dealing with them more like as pharmaceuticals, something still hard and tricky to do with cells. In particular, EVs showed less vulnerability to freezing procedures [129], and EV lyophilization was proposed as a feasible storage option to consider [130], which would allow easier usage and availability in the clinical practice. Additionally, EVs possess the intriguing biological feature of privileged access to the blood-brain barrier (BBB), which was reported in both directions through a still to define route [131-133]. This property is of high value since cells can cross the BBB only if such structure is disrupted [134].

From an industrial perspective, EVs could be generated as byproducts of other ATMP productions, resulting in a higher return for nearly the same economic investment. In the current situation, many biotechnology companies already produce EVs in the context of cell manufacturing for other purposes, but they discard them as waste. Thus, minimal revisions of cell culture processes would lead to an easy harvest of both cells and EVs at the same time.

Taken together, these considerations justify the development of a cell-free therapeutic approach based on the use of EVs.

1.5 Aim of the thesis

The aim of this doctoral project is to explore the feasibility of stem cell-derived extracellular vesicle (EV) use as an effective therapeutic strategy, testing their regenerative functionality in a proof-of-concept model of tissue damage. In order to do that, some issues will be addressed: the selection of the more appropriate multipotent mesenchymal stromal cell (MSC) source; the evaluation of MSC vesicular secretion properties; the use of induced reprogramming to obtain immortalized cell lines preserving the secretion properties of the starting stem cells; the therapeutic potentiality of EVs to protect an injured tissue.

The presentation of the results is organized as follows:

- In Chapter 2, the advantages and disadvantages of different MSC sources are discussed, and a protocol for the efficient isolation of MSCs from cord blood (CBMSCs) is implemented;
- Chapter 3 deals with CBMSC secretion properties, with a focus on EV production and function;
- In Chapter 4, the reprogramming of CBMSCs into a pluripotent state is presented as an option to obtain long-lived cell lines; in addition, EVs are proposed as a new feature of pluripotent cell biology;
- In Chapter 5, stem cell EV efficacy as a regenerative tool is challenged in an *ex vivo* organotypic mouse model of brain ischemia, compared to traditional treatment by parental stem cells;
- Chapter 6 discusses implications and future challenges of this research and of EV-based therapy.

Chapter 2

Isolation of multipotent mesenchymal stromal cells from cord blood

2.1 Motivations for cord blood as stem cell source

As commented earlier (paragraph 1.3.1), multipotent mesenchymal stromal cells (MSCs) can be isolated from both adult and perinatal tissues. Even though bone marrow-derived MSCs have been considered so far the gold standard in the field, it is now becoming more and more evident how donor age affects MSC properties *in vitro* and *in vivo*. The main *in vitro* effect is earlier senescence entry and decreased growth properties [46, 135-137], which affect cell expansion feasibility and *vivo* functionality [138-140]. At the molecular level, adult MSCs present shorter telomeres and decreased, if not absent, telomerase activity, compared to perinatal MSCs [141-144]. Importantly, impaired telomere structure is linked to replicative senescence and genomic instability [145, 146], a phenomenon that would be delayed in perinatal MSCs, if subjected to the same telomere erosion rate.

Among birth-associated tissues, cord blood offers specific advantages over adult or other perinatal stem cell sources in terms of easy and safe tissue collection. Both adipose tissue and bone marrow need surgical procedures to be harvested, and so it is quite rare to have access to healthy donors. Also amniotic fluid, a very promising source of different kind of stem and progenitor cells, rely on amniocentesis, an invasive technique which present some minor risks for both the mother and the baby, and therefore it is performed as a prenatal test only in presence of significant genetic risks. Moreover, it has been demonstrated how MSCs from cord blood possess superior stemness properties in terms of differentiation potential and wound healing, compared to MSCs isolated from the umbilical cord Wharton's jelly [147]. It is worth noting that a plethora of other gestational tissues are currently under investigation as MSC sources [148]. Yet, notwithstanding noticeable efforts addressing MSC properties from different sources, comparative studies still produce often contrasting results [149].

In order to unveil molecular aspects distinguishing adult from perinatal MSCs, biological triplicates of MSCs from various sources (*i.e.:* bone marrow, adipose tissue, cord blood, Wharton's jelly, perivascular cells, amniotic fluid), and skin fibroblasts as stromal non-stem control, were characterized for their immunophenotype, by extensive flow cytometry, and for their transcriptome, by PCR-array (see Appendix II.a for detailed protocols).

Statistically significant increased levels of pericytic surface marker Neural/Glial 2 (NG2) and CD56 were found for all perinatal MSCs, compared to adult MSCs (Fig. 2.1, a and b, respectively). Since pericytes are considered the *in vivo* progenitors of *in vitro* MSCs, higher NG2 expression could hint at a more "naive" or less committed state of perinatal MSCs; furthermore, CD56 is known to play a crucial role in cell-cell adhesion during embryonic development [150]. Therefore, these results would be in line with the aforementioned notions regarding senescence-related feature of adult *versus* perinatal MSCs. In contrast, adult MSCs were enriched, even though with high variability, in CD271-positive cells (Fig. 2.1, c), a neural crest cell marker that was proposed to discriminate a bone marrow MSC subpopulation with superior stemness and differentiation properties [151, 152].

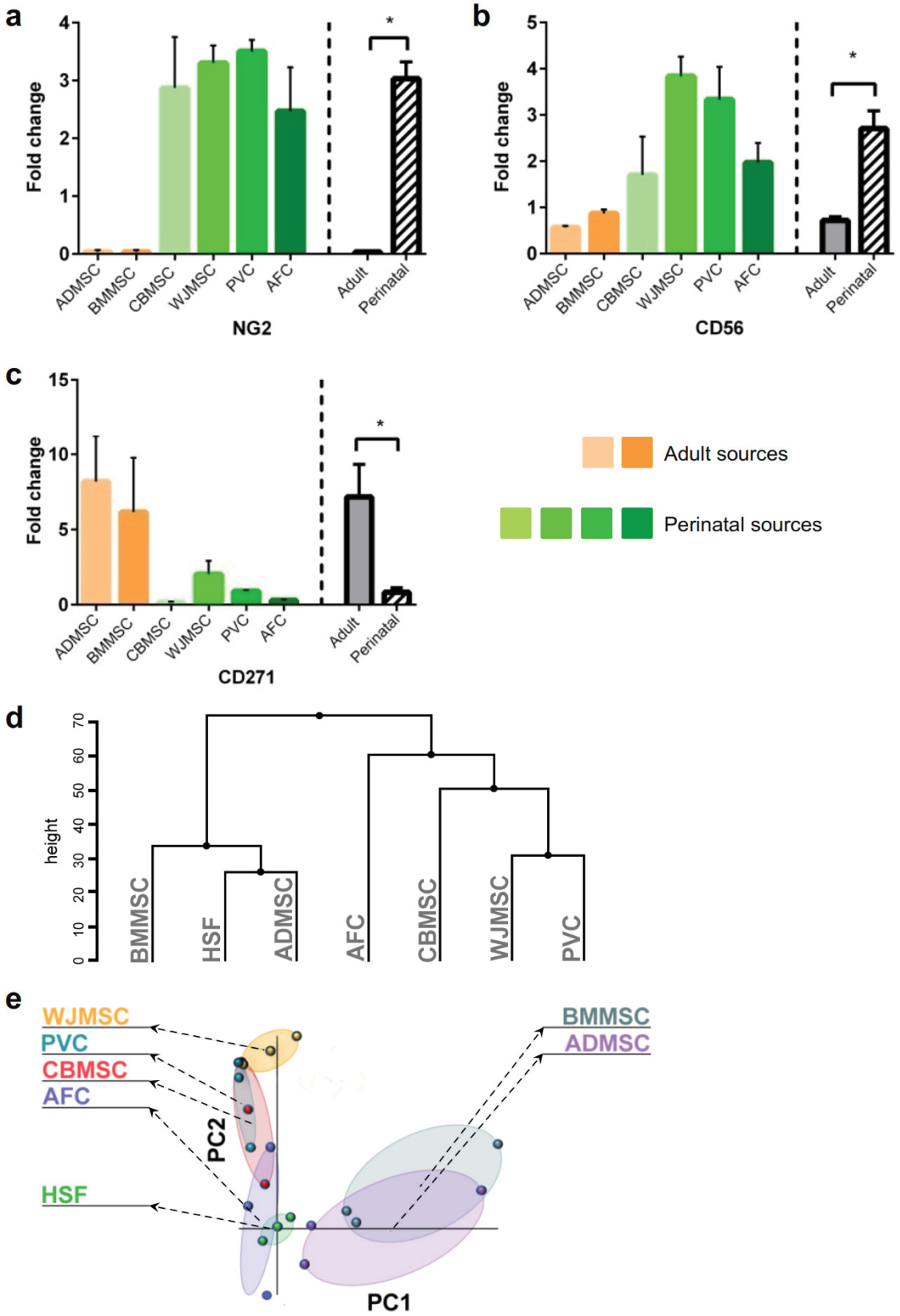

Figure 2.1. Adult and perinatal multipotent mesenchymal stromal cell (MSC) specific surface markers. In a), b) and c) surface marker expression is shown for Neural/Glial antigen 2 (NG2), CD56 and CD271, respectively, normalized to stromal non-stem control (human foreskin fibroblast, HSF); mean and standard error of the mean for single MSC types (n=3) or for adult (n=6) *versus* perinatal (n=12) MSC groups (separated by dotted line) is presented. Statistical analysis: Kolmogorov-Smirnov normality test, followed by

t-test; * p<0.05. The dendrogram in d) was generated by single linkage clustering; height parameter represents relative distance between clusters. Principal component analysis in e) shows grouping of MSCs by source, centered on HSF, relative to principal component (PC)1 and PC2 variables. ADMSC, adipose tissue MSC; BMMSC, bone marrow MSC; CBMSC, cord blood MSC; WJMSC, Wharton's jelly MSC; PVC, perivascular cells; AFC, amniotic fluid cells; adult, MSCs from adult sources (grey bar); perinatal, MSCs from perinatal sources (black and white stripes).

Intriguingly, cluster analysis revealed that the complete immunophenotype panel was sufficient to group and discriminate adult and perinatal MSCs (Fig. 2.1, d). In addition, Principal Component Analysis (PCA) was applied to the flow cytometry data, plotted against fibroblasts as control (Fig. 2.1, e). PCA showed a clear separation of adult from perinatal MSCs, which again underlined how MSCs from the two sources possessed distinct phenotypes.

From the transcriptome analysis, Insulin-like Growth Factor 1 (IGF1) was found to be almost undetectable in perinatal MSCs, whereas it was expressed in adult MSCs (Fig. 2.2, a), as confirmed by Real Time qRT-PCR (Fig. 2.2, b).

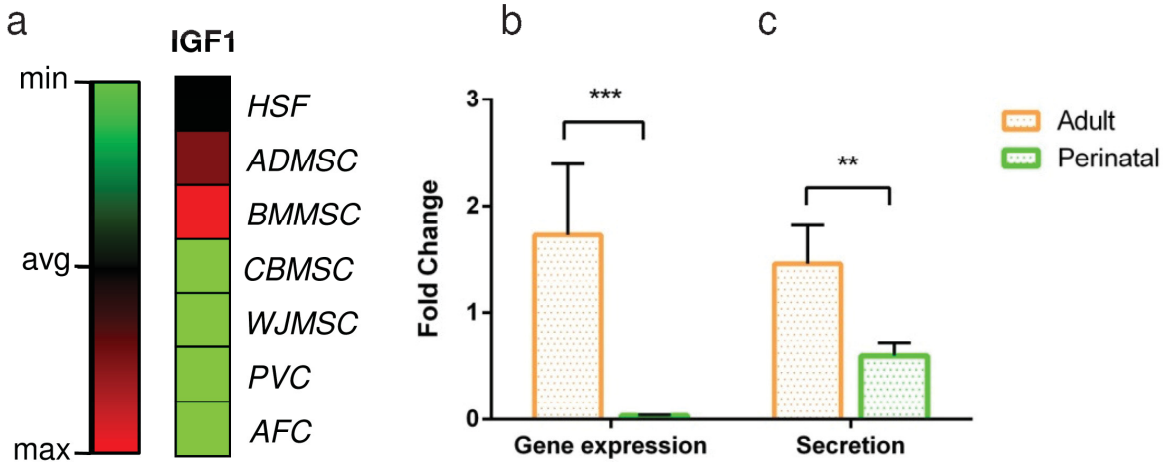

Figure 2.2. Insulin-like Growth Factor 1 (IGF1) discriminates adult and perinatal multipotent mesenchymal stromal cells (MSCs). An elaboration of IGF1 PCR-array data is pictured in a); color intensity represents gene expression magnitude for each MSC type (n=3), as shown in the legend (min, minimum value; avg, average value; max, maximum value); see Appendix II.a for complete PCR-array heatmap. In b), IGF1 Real Time qRT-PCR data (gene expression) normalized to stromal non-stem control (human skin fibroblast, HSF) are presented. In c), the amount of IGF1 secreted into the culture medium (secretion), measured by ELISA assay, is shown. In b) and c), mean with standard error of the mean of adult MSCs (n=6) *versus* perinatal MSCs (n=12) is presented. Statistical analysis: Kolmogorov-Smirnov normality test, followed by t-test; ** p<0.01; *** p<0.001. ADMSC, adipose tissue MSC; BMMSC, bone marrow MSC; CBMSC, cord blood MSC; WJMSC, Wharton's jelly MSC; PVC, perivascular cells; AFC, amniotic fluid cells; adult, adult MSCs (orange bar); perinatal, perinatal MSCs (green bar).

This result is of uttermost importance, as it confirms that the donor age of source tissues can affect molecular properties of MSCs. Notably, higher signaling triggered by IGF1 pathway activation leads to earlier senescence and decreased lifespan [153, 154], a biological feature shown by adult MSCs, as previously commented. To confirm these data, IGF1 secretion was also assessed. In accordance, adult MSCs produced higher amounts of IGF1 (Fig. 2.2, c), compared to perinatal MSCs, even though the difference was less marked, compared to the transcriptional level.

All these data point at perinatal MSCs as a better option to develop cell therapy protocols, mainly because they are described as less senescent cells, endowed with superior stemness and differentiation properties.

Switching point of view with a clinical translation perspective, a crucial feature possessed by cord blood MSCs is the lower risk regarding transmission of pathogens. This is due to the protection exerted by the placental interface between fetus and mother [155]. A peculiar aspect of cord blood is that no full Human Leukocyte Antigen (HLA) compatibility with the recipient is needed for successful transplantation, as other tissues require, in reason of lower immunogenicity and lower risk of chronic graft-*versus*-host disease [156], a biological feature possessed also by cord blood MSCs [157]. Another aspect that support the use of cord blood as MSC source is that international networks of cord blood banks already exist, which store clinical-grade cord blood units available mainly for hematopoietic stem cell transplantation into onco-hematological pediatric patients. Thus, the collection of cord blood is a common practice in hospitals worldwide, and so it is the donation of cord blood units, in the case they do not satisfy banking quality criteria, for research purposes. As a matter of facts, a collaboration with the Milano Cord Blood Bank (MICB) was established to allow the implementation of this doctoral project.

2.2 Isolation of MSCs from cord blood

The main drawback of cord blood (CB) as multipotent mesenchymal stromal cell (MSC) source is that MSCs are found at a lower frequency in this tissue, compared to other sources, as described by [136]. Thus, this and other issues, concerning efficient isolation of MSCs from cord blood, will be addressed in the following paragraphs.

2.2.1 Dissection of the cord blood stromal component

Despite the intriguing features of CB as MSC source, translation to the clinic has to face one major obstacle, which is inconsistency of isolation protocols, due to the low frequency of MSCs in CB, compared to other sources. A small number of reports proposed experimental conditions for high efficiency isolation of CBMSCs, but the success rate is still controversial and they often require very fresh and abundant CB units [158, 159]. Furthermore, CB was reported to give rise to distinct stromal populations in terms of morphology, isolation frequency, proliferation rate, differentiation potential and surface markers [160-163]. In order to address these issues, 243 CB units were processed (see Appendix I.a and I.d for detailed protocols). Importantly, to evaluate whether a CB unit was successfully processed, only colonies composed by at least 10 fibroblastic-like cells were considered, in accordance to previous studies [159]. This standard was adopted to facilitate the assessment of colony formation within the context of CB primary stromal cell culture, characterized by a mixed cell environment. The methodological approach was based on the immunodepletion of non-mesenchymal cell populations (negative selection of T lymphocytes by CD3, monocytes by CD14, B lymphocytes by CD19, red blood cells by glycophorin A and granulocytes by CD66b) from CB mononuclear cells before seeding. The ratio behind this choice was indeed to remove adherent and non-adherent ‘‘contaminant’’ cell types, often observed in CB cultures, which could hamper the attachment of CBMSCs to the culture surface and the subsequent generation of a colony [158, 164]. Among the adherent non-clonogenic ‘‘contaminant’’ cells, there were osteoclast-like poli-nucleated cells with very large cytoplasm, and spindle-shaped cells with short and stretched cytoplasmic extensions (Fig. 2.3, a).

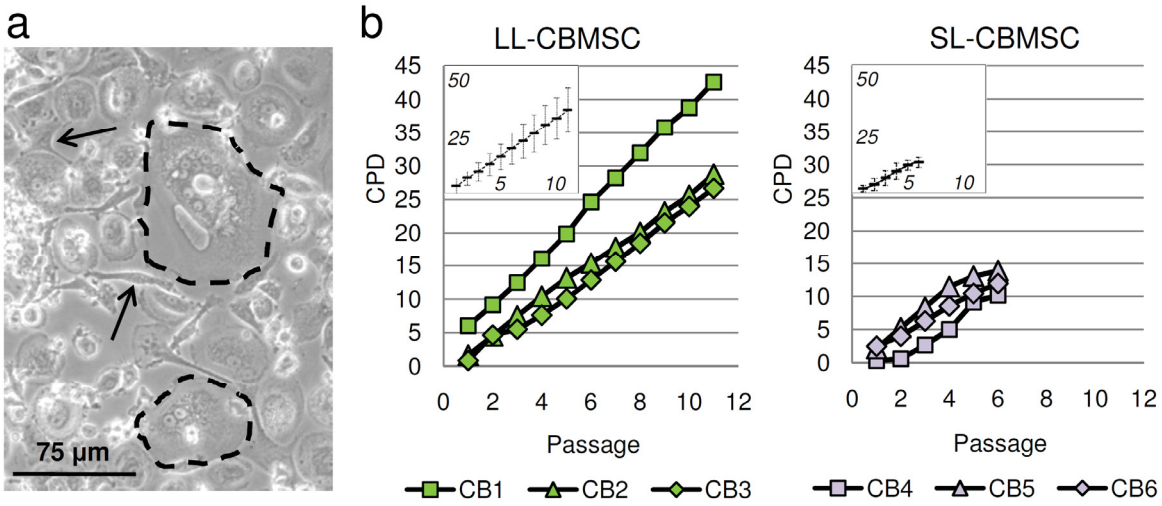

c

	Number of colonies (mean)	*Clonogenic potential (%)*
LL-CB 1	40.5	20.3
LL-CB 2	38.5	19.3
SL-CB 4	3.5	1.8
SL-CB 5	4.5	2.3

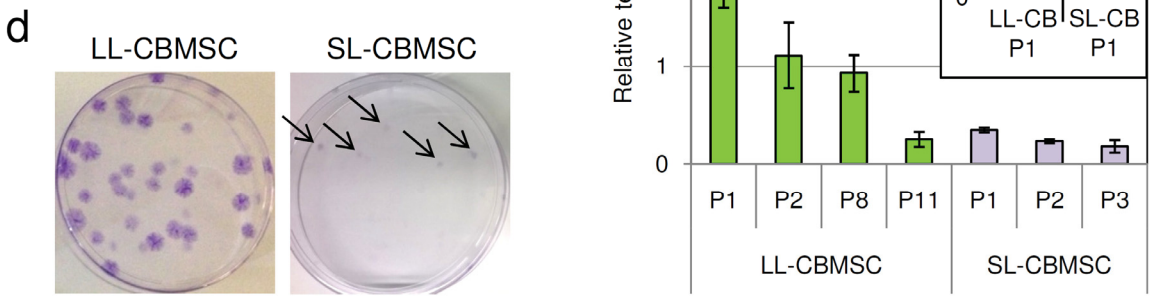

Figure 2.3. Dissection of cord blood stromal cells. Non-mesenchymal stromal cells are frequent in cord blood primary cultures (a, representative image). Among them non-proliferating fibroblast-like cells (indicated by arrows) and poli-nucleated (2-7 distinguishable nuclei) cells with a very large cytoplasm (dashed circles). In b), representative growth curves of CBMSCs grouped by similar cumulative population doubling (CPD) values (vertical axis) and longevity (horizontal axis) are shown. In the boxes the means (n=3, black rectangle) and deviation standards (vertical bars) of CPDs for each passage are shown. Table c) summarizes mean number (n=2) of colony forming unit-fibroblasts (CFU-Fs) and related clonogenic potential (percentage of clonogenic cells out of the total amount of seeded cells) for two long-living (LL)- and two short living (SL)-CBMSC populations at passage (P) 4. Representative images of CFU-F assay are shown in d): LL-CBMSC colonies are bigger and more easily detectable, compared to SL-CBMSCs, whose colonies are very small and difficult to detect (indicated by arrows). Mean telomere length (n=3) with standard error of the mean (black bars) for LL- and SL-CBMSCs at different passages are shown in e); in the box, representative P1 LL- and SL-CBMSCs show dramatic differences in telomere length, presented as mean (n=3) and standard deviation (black bars). Statistical analysis: Z-score formula-based normality test, followed by t-test; **p<0.01. CB, CBMSC; LL-CB, LL-CBMSC; SL-CB, SL-CBMSC.

Whereas the former are the result of fusion of monocytes [165], which probably escaped the immunodepletion treatment, the immunophenotyping of the latter revealed high expression of CD105 (>95%) and CD45 (>95%) and no presence of CD90-positive cells (<5%), both indicating presence of mature endothelial cells.

Stromal colonies composed of fibroblast-like cells were obtained from 40% of total processed CB units, and the majority of them (90%) were detected within 4 weeks (a median of 16 days) after seeding. Following long-term culture of the isolated colonies, a dissection of the CB stromal component was obtained: while half of them failed to establish a CBMSC population, the remaining ones generated CBMSCs showing two distinct *in vitro* behaviors in terms of growth and clonogenic properties. One population demonstrated higher proliferation kinetics and delayed senescence, whereas the other showed impaired growth and shorter lifespan. In reason of their growth properties, the former were named long-living (LL)-CBMSCs and the latter short-living (SL)-CBMSCs. Cumulative Population Doubling (CPD) was used as an indicator of replicative potential, and a threshold of CPD=15 was defined to distinguish LL- from SL-CBMSCs (Fig. 2.3, b). At passage 5, SL-CBMSCs tended to reach plateau and arrest growth, while LL-CBMSCs continued to grow until higher CPD peaks (CPD>30). Interestingly, LL-CBMSCs were capable to generate many secondary colonies under low density-seeding conditions (colony forming unit-fibroblasts assay), whereas SL-CBMSCs failed (Fig. 2.3, c and d).

Since lifespan is a major difference between LL-CBMSCs and SL-CBMSCs, the role of replicative senescence as stem cell regulator [166] was investigated. Thus, telomere length, as direct contributor of cellular senescence, was assessed. The results showed that LL-CBMSCs possessed statistically significant longer telomeres, compared to SL-CBMSCs (Fig. 2.3, e), and that this feature was maintained until late passages.

Both LL- and SL-CBMSCs grew in adherence to plastic surfaces, with a fibroblast-like morphology (Fig 2.4, a), and they showed a typical MSC immunophenotype (Fig 2.4, b); their differentiation potential into mesodermal derivatives was also investigated (Fig 2.4, c), as requested by the ISCT MSC definition criteria presented in paragraph 1.3.1.

a

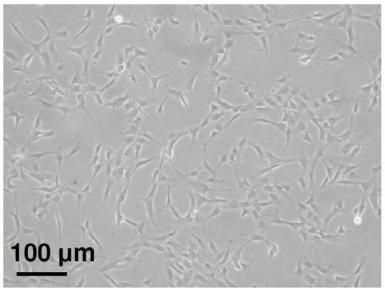

b

Surface marker	% of expression
CD90	99.8
CD105	99.8
CD73	99.9
CD45	0.0
CD34	0.5
CD14	0.1

c

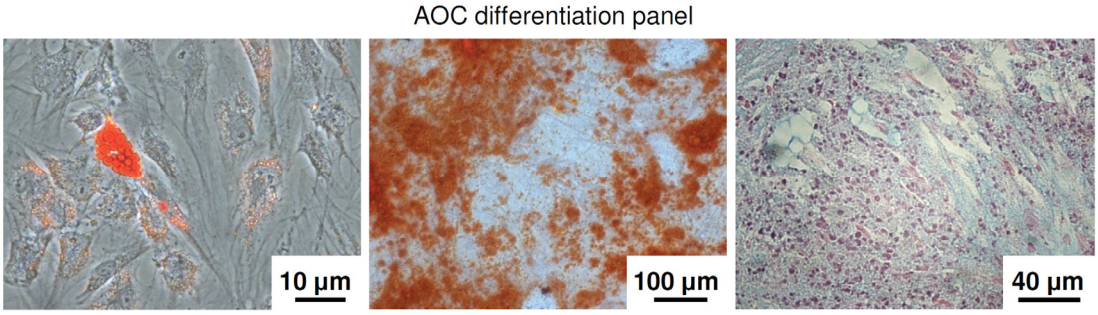

Figure 2.4. Long-living cord blood-multipotent mesenchymal stromal cells (LL-CBMSCs) fulfill all MSC definition criteria. LL-CBMSCs showed typical MSC morphology (a, representative image), expression of MSC canonical markers (b, representative immunophenotype), and capability to differentiate into mesodermal derivatives (c, representative images): Oil Red O-positive adipocytes (A, left panel); Alizarin Red S-positive osteoblasts (O, central panel); alcian blue-positive chondroblasts (C, right panel) constitute the AOC MSC differentiation panel.

Concerning the differentiation potential, some differences were found. Adipogenesis was slower and the intracellular fat droplets generated were smaller and fewer compared to MSCs from adult sources, as already reported in the literature [167]. This is thought to be due to the perinatal origin of these cells, for which molecular programs related to adult organism physiology are still inactive or silenced [168]. Osteogenesis was present in both population, even though LL-CBMSCs tended to produce larger calcium deposits, compared to SL-CBMSCs. Chondrogenesis was detected for LL-CBMSCs, but seemed somehow impaired for SL-CBMSCs, indicating a lower differentiation potential.

This paragraph is a modified excerpt of Appendix I.a and I.d.

2.2.2 Increasing the efficiency of cord blood stromal colony generation

In spite of the advances in the knowledge of different stromal populations present in CB, the establishment of CBMSCs remained a low efficiency process, because only a half of processed CB units generated MSC colonies. In order to improve the efficiency of the aforementioned isolation protocol and at the same time to generate CBMSCs showing the same or improved qualities of LL-CBMSCs, alternative cell culture conditions relying on a chemically defined medium were applied to the LL-CBMSC isolation protocol (see Appendix I.b for detailed protocols).

A total number of 100 CB units were processed following different approaches. The idea was to determine which isolation procedure offered the best environment to facilitate MSC progenitor attachment to the growth surface and to better support the proliferation of stromal colonies (see figure 2.5 for the complete schematic).

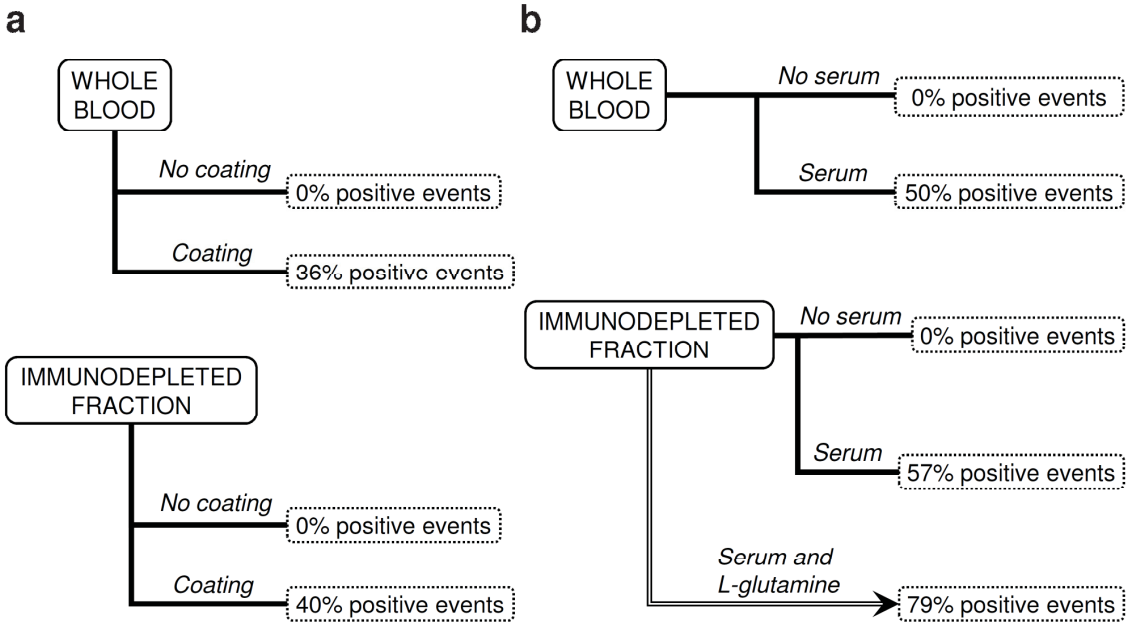

Figure 2.5. Experimental schematic. In the isolation experiments, importance of coating (a) and serum (b) was assessed. Whole blood, non-fractioned cord blood; immunodepleted fraction, cord blood mononuclear cells after immunodepletion treatment; positive event, appearance of *bona fide* MSC colony.

In a first series of isolations, the importance of collagen I-III coating was investigated for the optimal use of a chemically defined medium (for complete formulation see Appendix Ib). Whole blood samples (WB) *versus* immunodepleted fractions (ID) were compared, and again the appearance of the first fibroblastic colony composed of at least 10 cells was considered as a positive event. Positive events on coated surfaces were obtained from five WB (14 total units) and from two ID (5 total units). On the contrary, no positive event was observed without the coating (5 WB and 11 ID) (Fig. 2.5, a). In a second set of experiments, the addition of a standard percentage of serum was investigated as a possible replacement of collagen I-III coating, based on the common practice of coating plastic surfaces with serum. In this way, positive events were obtained from three WB (6 total units) and from 17 ID (30 total units), representing the most efficient isolation strategy for the experimental conditions herein reported (Fig. 2.5, b).

The analysis of CB unit characteristics demonstrated that the observed results were not biased by differences between the experimental groups in terms of time elapsed from CB collection to processing (Fig. 2.6, a) or WBC content (Fig. 2.6, b), two crucial parameters for CBMSC isolation [158, 159]. The evaluation of processed sample volume revealed that no statistically significant differences were present within WB (WB coating and WB serum conditions; Fig. 2.6, c) and ID (ID coating and ID serum conditions; Fig. 2.6, d) experimental groups.

Following this experimental design, the use of serum as a substitute for collagen I-III coating to culture the CB immunodepleted fraction appeared as the most promising approach to ameliorate further the generation of MSC colonies, due to its higher isolation efficiency. Thus, in order to further improve this rate of positive events, l-glutamine supplementation, as a further energy source for cultured cells, was tested in ID isolation experiments (complete medium), along with a preference for significantly richer-in-volume CB units, compared to the other immunodepleted samples (ID serum and l-glutamine condition; Fig. 2.6, d). Under these conditions, positive events were observed in almost 80% of the processed samples (23 out of 29 units) (Fig. 2.5, b). Following this isolation procedure, the previously observed presence of “contaminant” adherent cell types, already described in paragraph 2.2.1, were dramatically decreased.

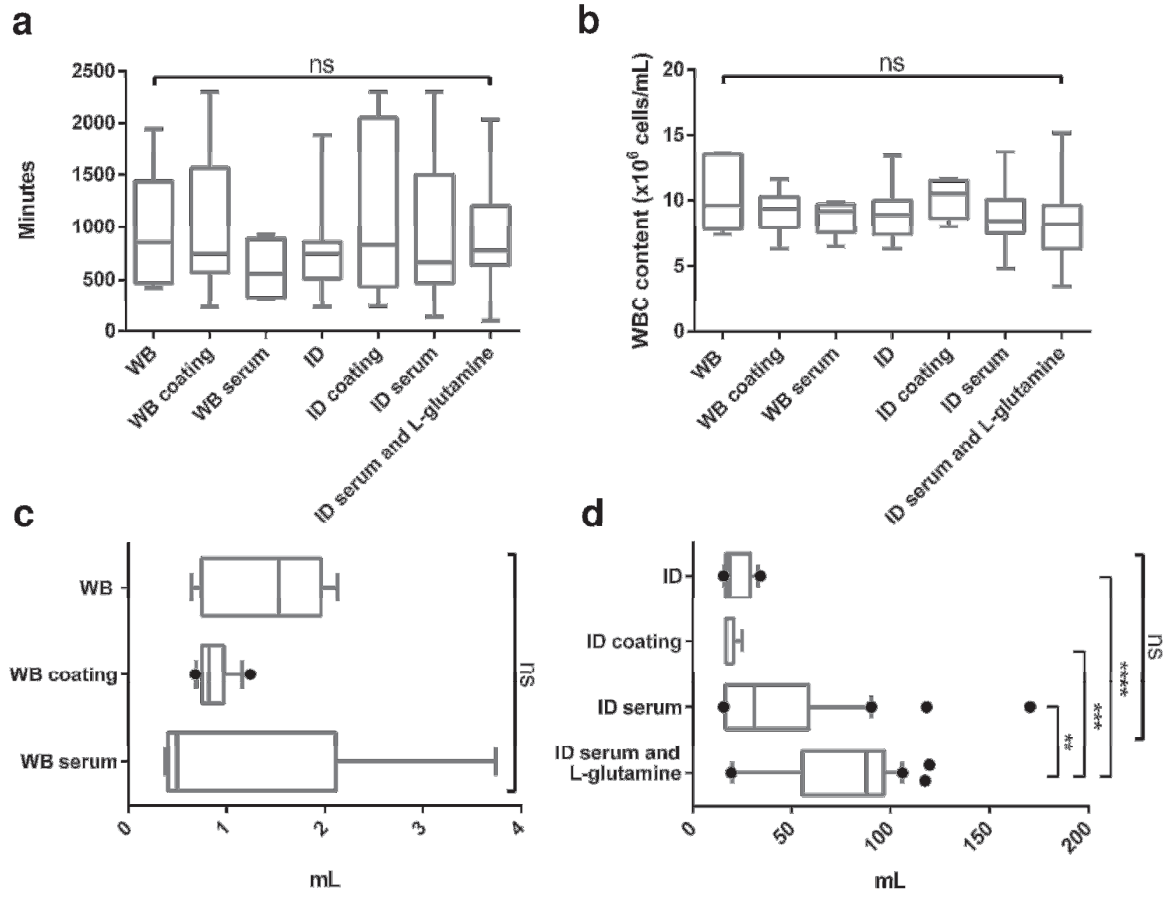

Figure 2.6. Cord blood unit characteristics. The following cord blood unit parameters were evaluated for whole blood (WB) and immunodepleted fraction (ID) isolation experiments: time from collection to processing (a), white blood cell (WBC) content (d) and processed volume (c, d). Box and whiskers graphs show 25th and 75th percentiles (plot hinges), median, minimum and maximum values (a, b) or 10th and 90th percentiles with outside values (c, d). Statistical analysis: non-parametric Kruskal-Wallis test, followed by Dunn's multiple comparisons tests. **p<0.01; ***p<0.005; ****p<0.001; ns=statistically non-significant difference.

The CBMSCs generated by this improved protocol were thoroughly characterized (n=3). First of all, they were positive for canonical MSC markers CD90, CD105 and CD73, while they were negative for CD45 and CD34; a more extensive flow cytometry panel revealed also expression of NG2 and CD56, but almost no expression of CD271, resembling the data presented in paragraph 2.1 (data shown in Appendix I.b). Maintenance of tri-lineage differentiation potential was assessed (data shown in Appendix I.b). In addition, the established CBMSC populations showed enhanced growth properties, with regard to both CPD peak values (Fig. 2.7, a and b) and CFU-F assay (Fig. 2.7, c), compared to LL-CBMSC cultured in standard conditions.

Telomere length was also assessed (Fig. 2.7, d): in spite of a dramatic and significant decrease in mean telomere length comparing passage 0 to passage 1 CBMSCs, this parameter was subsequently maintained at a constant length (statistically non-significant differences between P1 and P9 CBMSCs).

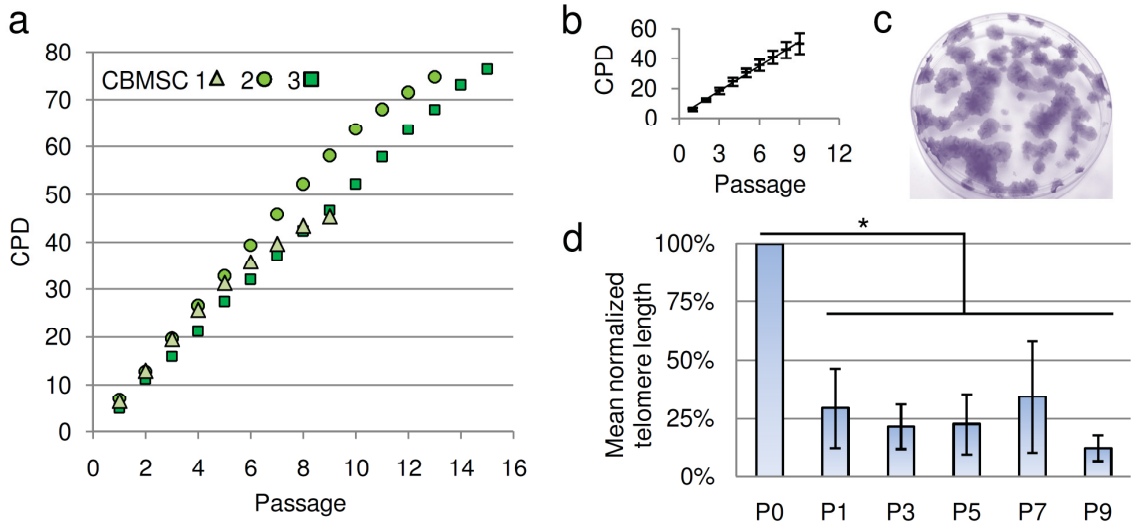

Figure 2.7. Cord blood-multipotent mesenchymal stromal cell (CBMSC) growth properties. CBMSC growth curves (a) and mean proliferation rate (b, n=3) with standard deviation are presented. A representative image of CBMSC Colony forming unit-fibroblast (CFU-F) assay is shown in c). Mean CBMSC telomere length (d, n=3) for each analyzed passage (P), is shown as percentage of P0 with standard deviation. Statistical analysis: D'Agostino & Pearson omnibus normality test, followed by one-way analysis of variance (ANOVA) and Newman-Keuls multiple comparison tests; *p<0.05. CPD, cumulative population doubling.

This paragraph is a modified excerpt of Appendix I.b.

2.3 Conclusions

A previously widespread notion described MSCs deriving from different tissue compartments as a homogeneous group of stem cells, endowed with the same biological features. Yet, it has become clear that the tissue of origin determines MSC stemness properties. A comparative study of MSCs isolated from six different sources revealed substantial differences between them, correlated to their perinatal or adult harvest. Moreover, a senescence-associated feature as Insulin-like Growth Factor 1 (IGF1) expression was found to be increased in adult compared to perinatal MSCs. Based on these data and other clinical-related advantages, cord blood (CB) was chosen as stem cell source. From the dissection of the CB stromal component, long-living (LL)- and short-living (SL)-CBMSCs were characterized. In this context, LL-CBMSCs stood out for their increased lifespan and differentiation properties. Thus, they were considered the best option to develop regenerative medicine approaches. An interesting point to underline is that telomere length showed statistically significant differences between LL- and SL-CBMSCs at very early cell culture stages, so that it could be used as a predictive parameter of culture outcome. In this way, clinically relevant LL-CBMSCs could be selected *a priori*. Eventually, since isolation rate is a major issue for LL-CBMSC clinical translation, an improved procedure leading to nearly 80% MSC colony generation efficiency was described, solving one major issue in CBMSC clinical translation feasibility.

Chapter 3

Re-defining cord blood multipotent mesenchymal stromal cell paracrine properties

Multipotent mesenchymal stromal cell (MSC) paracrine potential is extensively described in the literature, as reviewed in paragraph 1.3. Nonetheless, the role extracellular vesicles (EVs) play in secretome-associated MSC properties still needs to be elucidated. In order to discern EV secretome contribution from that of MSC-secreted soluble factors, different proof-of-concept *in vitro* and *in vivo* injury models addressing secretome *in toto*, or LL-CBMSC EVs compared to LL-CBMSC conditioned medium, were used. In either cases, the focus was maintained on LL-CBMSC anti-apoptotic and anti-inflammatory properties, which are considered essential to set up a pro-regenerative environment, which allows a damaged tissue to ameliorate its condition. Therefore, the generation and characterization of EVs from LL-CBMSCs were addressed, and their feasibility as regenerating agents mimicking parental cell properties was tested.

3.1 Anti-apoptotic and anti-inflammatory properties of cord blood multipotent mesenchymal stromal cells

Initially, an *in vitro* model of renal acute damage, caused by the chemotherapeutic agent cisplatin, was implemented (see Appendix I.d for detailed protocol). First, the secretion of immunomodulatory molecules was assayed. Human renal cells produced significantly higher amounts of cytokines upon damage, compared to the same cells in non-contact co-culture with LL-CBMSCs (Fig. 3.1).

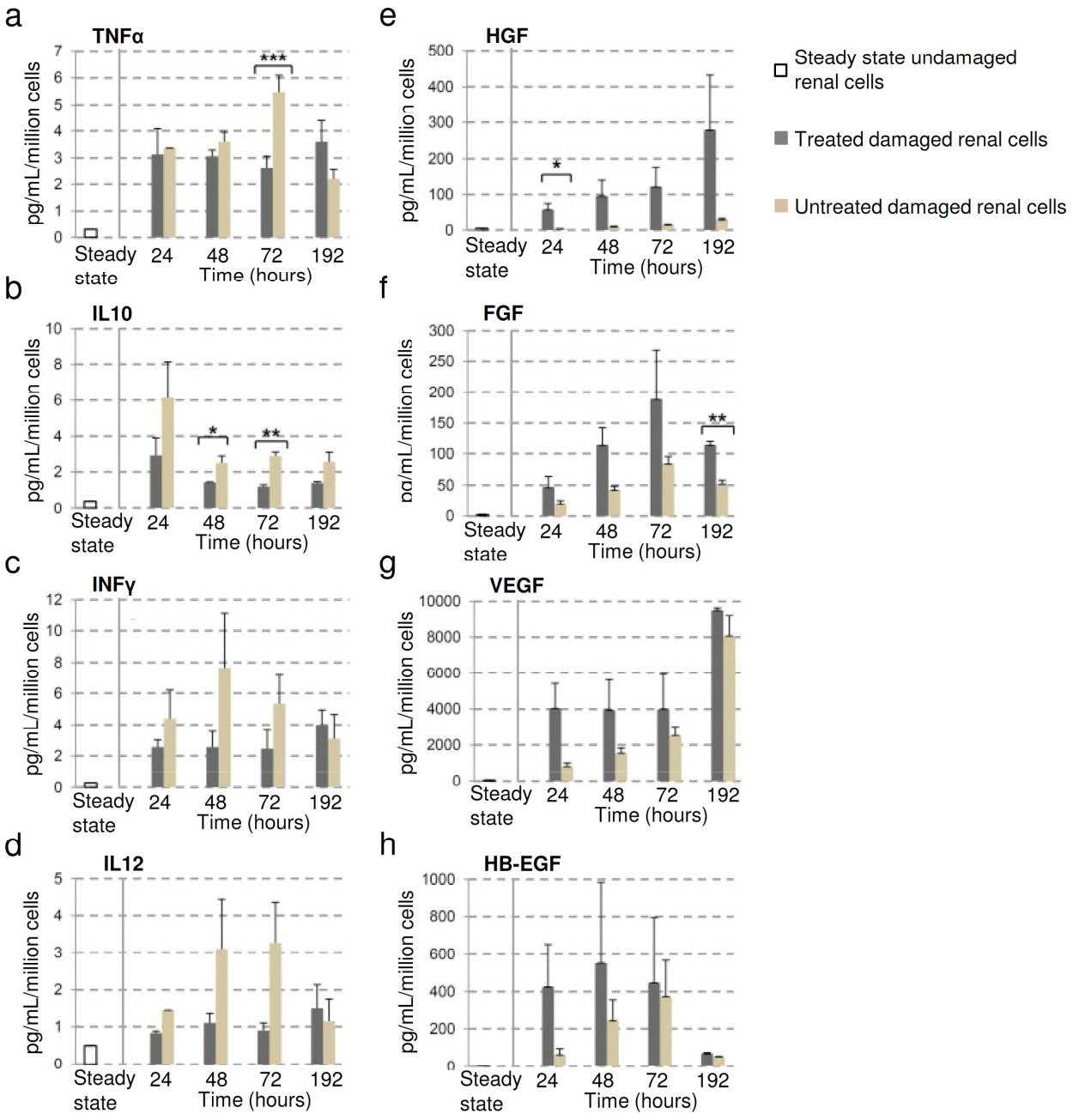

Figure 3.1. Long-living (LL)-cord blood (CB) multipotent mesenchymal stromal cell (MSC) secretory profile. Renal cells were damaged (untreated cells), damaged and co-cultured with LL-CBMSCs (treated cells), or cultured without damage (steady state). Results are reported as mean (n=5) with standard deviation, and they are expressed as pg per mL per 10^6 cells. Statistical analysis: z-score formula-based normality test, followed by t-test; *p-value<0.05; **p-value<0.01; *** p-value<0.001. TNFα, tumor necrosis factor α; IL10, interleukin 10; INFγ, interferon γ; IL12, interleukin 12; HGF, hepatocyte growth factor; FGF, basic fibroblast growth factor; VEGF, vascular endothelial growth factor; HB-EGF, heparin binding-endothelial growth factor.

In particular, Tumor Necrosis Factor (TNFα) and Interleukin (IL)10 underwent a statistically significant reduction (Fig. 3.1, a and b, respectively), but also Interferon (INF)γ and IL12 showed a similar trend (Fig. 3.1, c and d, respectively). Among all the time points analyzed, 72 hours appeared the most effective in the rescue of the damage-induced inflammatory profile.

Second, the production of growth factors known to exert anti-apoptotic effects was investigated [169-172]. Higher amounts of these factors were released into the co-culture medium, compared to untreated damaged renal cells. In particular, Hepatocyte Growth Factor (HGF) and basic Fibroblast Growth Factor (FGF) showed the most relevant and statistically significant differences (Fig. 3.1, a and b, respectively), even though also Vascular Endothelial Growth Factor (VEGF) and Heparin Binding (HB)-Endothelial Growth Factor (EGF) showed increasing trends in secreted protein levels (Fig. 3.1, a and b, respectively).

Concerning *in vivo* experiments, anti-inflammatory properties of LL-CBMSCs were assessed in a spinal cord injury mouse model (see Appendix I.c for detailed protocols). First, the capacity of LL-CBMSCs to modulate resident microglia and recruited macrophages at the injured site was assessed, by flow cytometry. Therefore, $CD11b^{pos}/CD45^{low}$ microglia and $CD11b^{pos}/CD45^{high}$ macrophages were detected in the injured tissue, and their amount evaluated: mice treated with LL-CBMSCs showed a significantly increased amount of recruited macrophages, compared to untreated mice (Fig. 3.2, a). Furthermore, inflammatory (TNFα) and anti-inflammatory Arginase (Arg) I gene expression at the injured tissue was assessed to investigate LL-CBMSC ability to modulate pro-inflammatory (M1) and anti-inflammatory (M2) phenotypes, respectively. TNFα mRNA was significantly increased in LL-CBMSC treated injured mice (1.5-fold change), compared to untreated injured mice (Fig 3.2, b).

Noteworthy, a much more relevant and significant mRNA level increase in anti-inflammatory Arg I was observed (10-fold change), compared to untreated injured mice (Fig 3.2, c). These results suggested a skew toward a M2 pro-regenerative environment for the LL-CBMSC treated injured tissue.

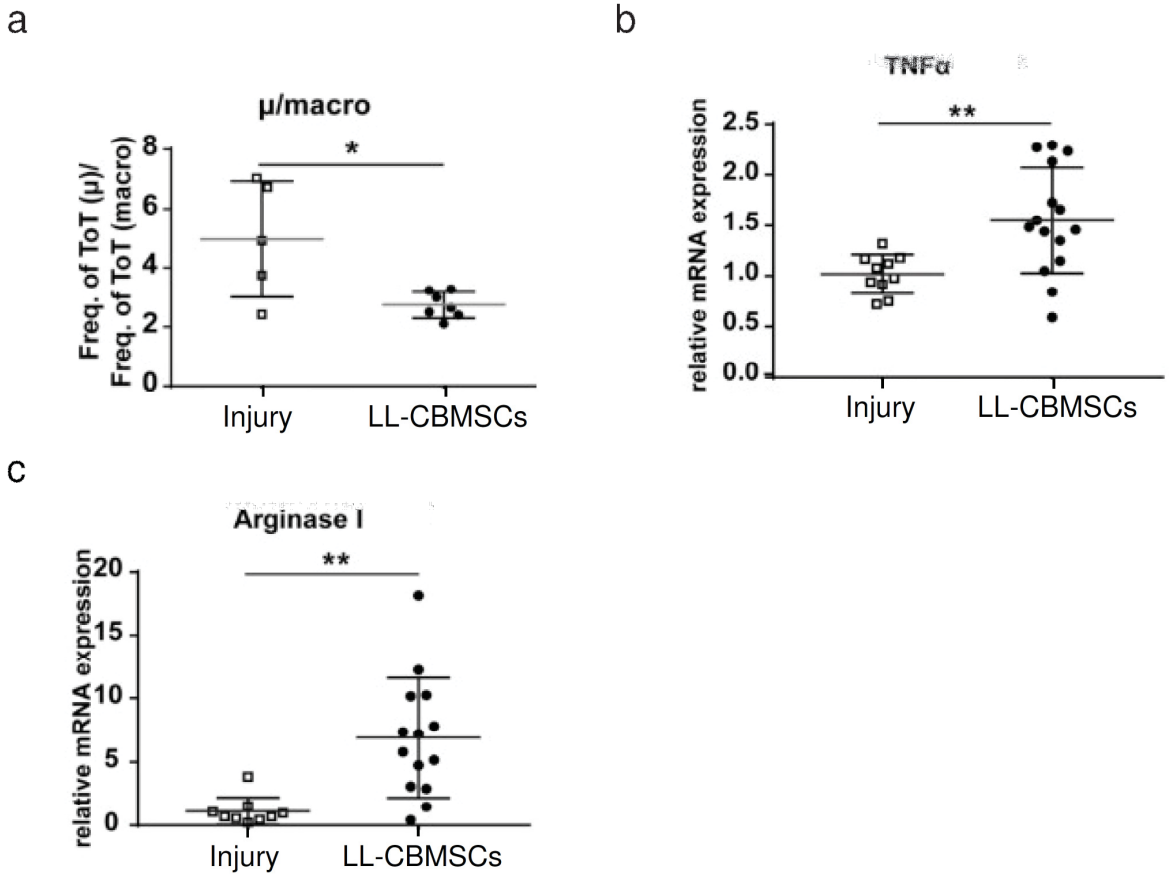

Figure 3.2. Modulation of inflammation. In a), microglia (μ) to macrophages (macro) ratio in the injured tissue of untreated (injury) or LL-CBMSC treated (LL-CBMSCs) mice is shown (n=5–7 per group). In b) and c), gene expression of M1/M2 polarization markers in the injured tissue of untreated or LL-CBMSCs treated mice is shown (n=10–14 per group). Mean with standard error of the mean is reported. Statistical analysis: Mann Whitney test; *p<0.05, **p<0.01. TNFα, tumor necrosis factor α.

Modified excerpts from Appendix I.c and I.d.

3.2 Regenerative extracellular vesicles from cord blood multipotent mesenchymal stromal cells

Following reports defining a prominent role of extracellular vesicles (EVs) in multipotent mesenchymal stromal cell (MSC) secretome-associated properties, the generation of EVs by long-living (LL)-cord blood (CB) MSCs was studied (see Appendix II.b for detailed protocols). Scanning electron microscopy analysis confirmed production of EVs by LL-CBMSCs, as outward structures protruding from the cell surface (Fig. 3.2, a). Interestingly, EV secretion was located in the peripheral protrusions of the cells and it was particularly concentrated at the edges of the plasma membranes.

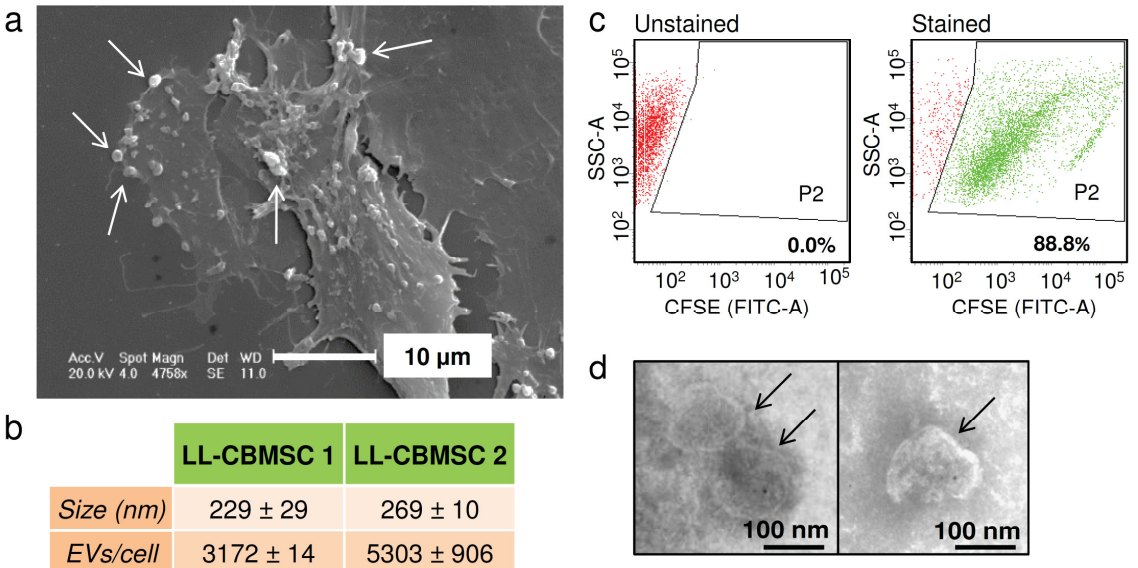

	LL-CBMSC 1	LL-CBMSC 2
Size (nm)	229 ± 29	269 ± 10
EVs/cell	3172 ± 14	5303 ± 906

Figure 3.3. Long-living (LL)-cord blood (CB) multipotent mesenchymal stromal cell (MSC) extracellular vesicle (EV) characterization. EVs were detected by scanning electron microscopy as outward structures protruding from the cell surface (a); representative EVs are indicated by arrows. Table b) summarizes EV size and count per cell for two representative LL-CBMSC populations, assessed by nanoparticle tracking analysis; mean (n=10) with standard deviation is reported. Flow cytometry analysis (c) revealed positivity for carboxyfluorescein ester (CFSE), which produced fluorescence in the fluorescein isothiocyanate channel (FITC-A) (P2), demonstrating that LL-CBMSC EVs are intact cytoplasm containing membrane-enclosed particles; SSC-A, side scatter. Transmission electron microscopy (d) visualized the ultrastructural morphology of isolated EVs; intact membrane is indicated by arrows.

Then, EV size was assessed by nanoparticle tracking analysis (NTA), which revealed a size range of 40–700 nm, although the mean values laid between 230 nm and 270 nm (Fig. 3.2, b). Interestingly, the observed particle size suggested the absence of apoptotic bodies, which usually fall into the size range of 1-5 µm.

NTA was also used for EV quantification: in one day, LL-CBMSCs produced up to 5,000 EVs per cell (Fig. 3.2, b). To assess EV integrity, carboxyfluorescein diacetate succinimidyl ester (CFDA-SE) staining was performed. CFDA-SE can passively diffuse through cellular membranes thanks to its acetate groups, which are subsequently removed by cytoplasmic esterases. This converts CFDA-SE into a fluorescent carboxyfluorescein succinimidyl ester (CFSE). Flow cytometry analysis showed that >85% of the detected events were CFSE positive, which indicated that EVs were intact cytoplasm-containing membrane-enclosed bodies (Fig. 3.2, c); moreover, 50% of total CFSE-positive events expressed CD63 and CD81 EV markers. Finally, transmission electron microscopy images showed a morphology consistent with pure EV preparations (Fig. 3.2, d).

In order to study the role of EVs in LL-CBMSC secretome-associated properties, the renal acute injury *in vitro* model previously used (paragraph 3.1) was repeated with slight modifications (see Appendix II.b for detailed protocols). Human renal cells were damaged with cisplatin and, after drug removal, LL-CBMSC conditioned medium or 20,000 LL-CBMSC EVs per cell were added. Cell viability was monitored at 24, 48 and 72 hours, by the MTT assay. Notably, the 72-hour time point showed the higher and most significant rescue in viability (81% compared to undamaged cells), in line with what presented for modulation of inflammation and growth factor production in the previous paragraph (Fig. 3.4). At 24 hours, the EV-driven effect was still not detectable, while at 48 hours a relevant viability increase was already appreciable (70% compared to undamaged cells). Notably, also conditioned medium showed viability rescue, but with a lower efficiency (67% compared to undamaged cells), while untreated cells continued to die (36% compared to undamaged cells).

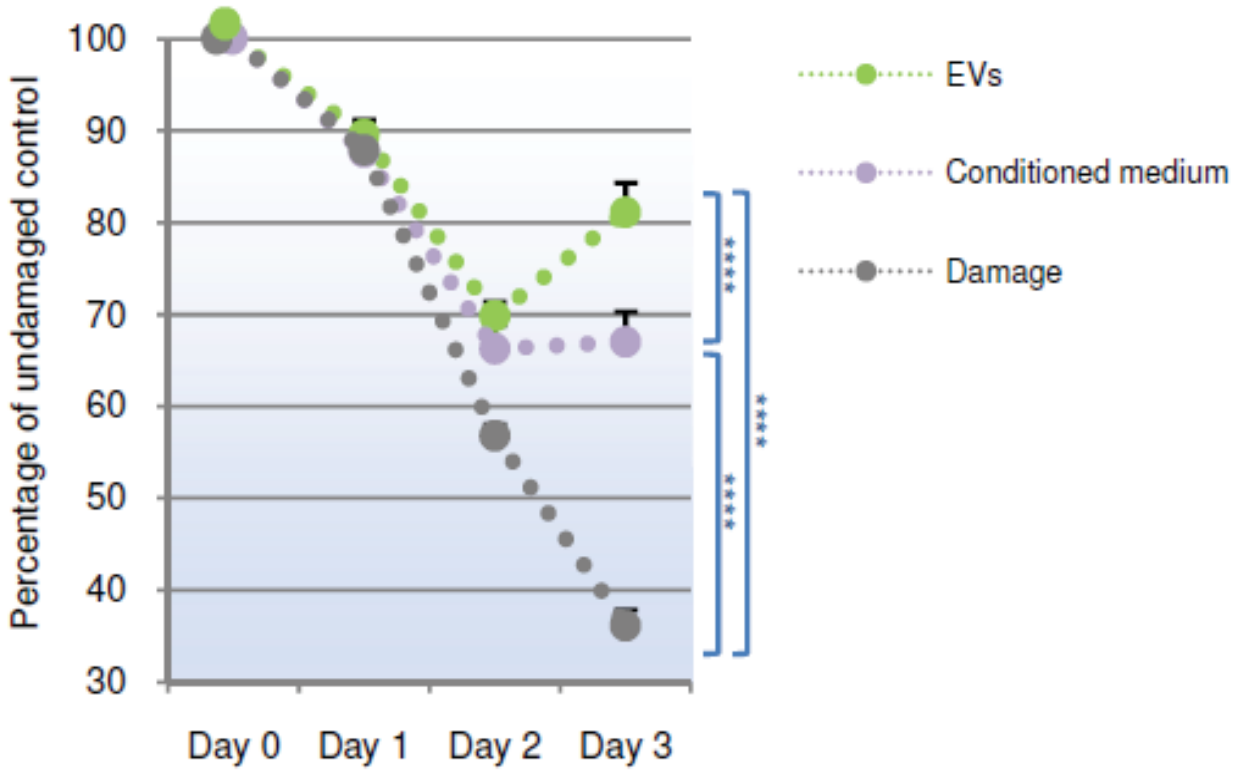

Figure 3.4. Long-living (LL)-cord blood (CB) multipotent mesenchymal stromal cell (MSC) extracellular vesicles (EVs) rescue damaged renal cells mimicking parental cell properties. In the graph, renal cell viability assessed by MTT assay is normalized to undamaged control (100% viability); mean (n=6) with standard deviation is shown. Statistical analysis: Kolmogorov-Smirnov normality test, followed by two-way ANOVA and Tukey's multiple comparison test; ****p<0.0001.

These paragraphs are modified excerpts from Appendix II.b.

3.3 Conclusions

Long-living (LL)-cord blood (CB) multipotent mesenchymal stromal cells (MSCs) were shown to produce extracellular vesicles (EVs), which were able to recapitulate parental MSC secretome-associated properties in a proof-of-concept *in vitro* model of acute damage. Moreover, anti-inflammatory and anti-apoptotic LL-CBMSC paracrine properties were demonstrated in two different *in vitro* and *in vivo* models of tissue injury. This hinted at a broad protective mechanism, which relied on modulation of the inflamed environment. This is a relevant feature of LL-CBMSCs, because inflammation can be detrimental to tissue regeneration [173-175]. In summary, these results support the use of EVs as therapeutic agents, able to convey stem cell regenerating properties.

Chapter 4

Induction of pluripotency in cord blood multipotent mesenchymal stromal cells

4.1 Motivation for a pluripotent stem cell source of extracellular vesicles

One major drawback of LL-CBMSCs as extracellular vesicles (EV) source is that, unlike pluripotent stem cells, they are primary cells with limited lifespan *in vitro*. Even though LL-CBMSCs can be extensively expanded thanks to their growth properties, an immortalized cell line would have the advantage of an unlimited use. In addition, preservation of EV therapeutic features after immortalization would have to be demonstrated. Admittedly, LL-CBMSCs from different donors may present differences in EV therapeutic potential, which should be addressed every time a new LL-CBMSC population is isolated. All considered, an immortalized cell line would represent a more homogeneous EV cell source, compared to primary MSCs. Consequently, also flaws in EV quality and efficacy would be reduced. Unfortunately, the current immortalization protocols rely on the permanent genetic modification of the target cells, through the integration of viral DNA in the genome. Hence, EV safety issues, such as tumorigenic risk and genome instability, would have to be fully addressed, as a prerequisite for any clinical application.

Giving these premises, the feasibility of reprogramming as a tool to extend LL-CBMSC lifespan *in vitro* was explored. Indeed, this technique induces pluripotency in differentiated cells, leading to a much more extensive *in vitro* lifespan. Reprogramming is achieved by transient overexpression of key transcription factors involved in the so-called pluripotency gene network, which governs self-renewal and pluripotency of pluripotent stem cells. Taking advantage of a specific methodology, which does not rely on the genetic modification of the target cell, but still induce a permanent change of its biological identity, major safety issues related to traditional immortalization protocols would be reduced.

4.2 Derivation of induced pluripotent stem cells

LL-CBMSCs reprogramming was achieved using a non-integrating viral-based system, which guarantees the expression of the classic four reprogramming factors (*OCT4*, *SOX2*, *KLF4*, *cMYC*). This methodology is zero-fingerprint, because no exogenous DNA is integrated into the host genome and the vector remains in the cytoplasm, so that the genetic information of the reprogrammed cell is not altered. Moreover, only one infection is needed to obtain successful reprogramming, compared to viral-free reprogramming methods [176] (for detailed protocol see Appendix III.a).

First, the feasibility of LL-CBMSCs infection and forced exogenous protein expression was investigated. For this purpose, an emerald green fluorescent protein (emGFP)-expressing variant of this system was used. LL-CBMSCs were successfully infected and the protein expressed (Fig. 4.1, a and b).

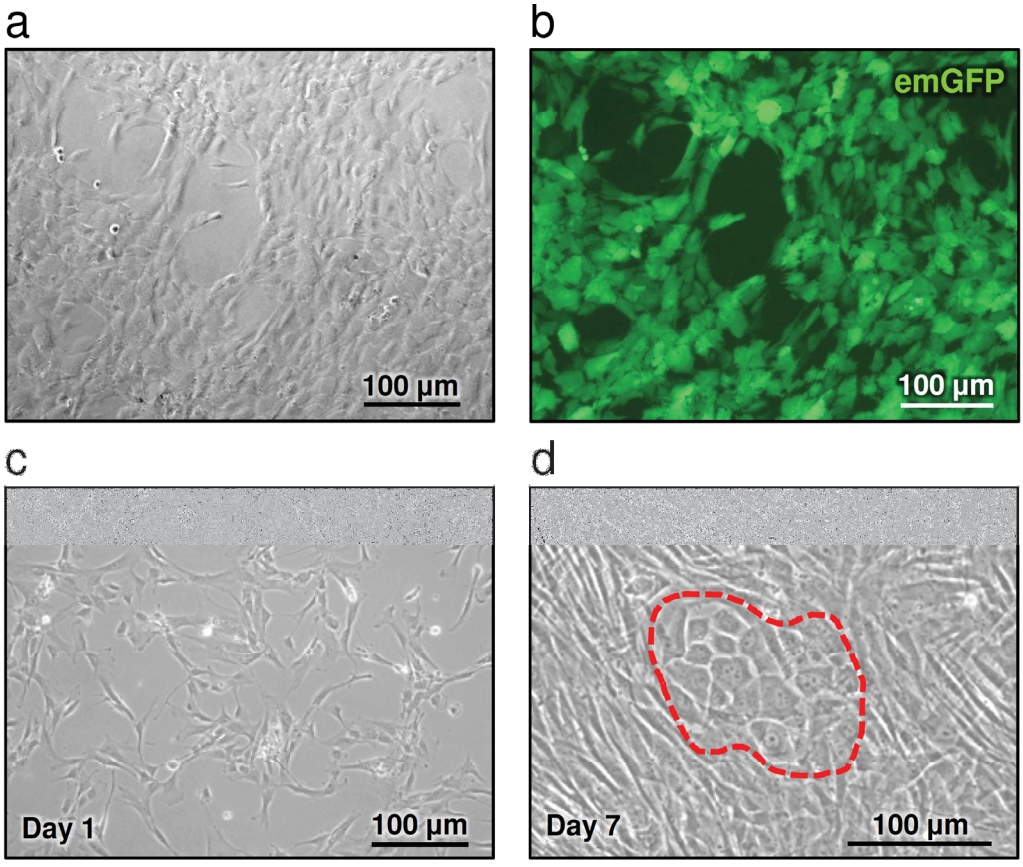

Figure 4.1. Reprogramming long-living (LL)-cord blood (CB) multipotent mesenchymal stromal cells (MSCs). The feasibility of LL-CBMSC infection was tested using an emerald green fluorescent protein (emGFP)-expressing virus (a, bright field; b, fluorescence); multiplicity of infection=5 is shown. In c), infected LL-CBMSCs still show a fibroblast-like morphology at day 1. In d), a *bona fide* reprogrammed colony growing onto a non-reprogrammed LL-CBMSC layer is visible (dashed circle).

Second, the reprogramming protocol was applied to LL-CBMSCs, using MOI=5, and the cells were monitored for the appearance of colonies. Cell morphology changes were not visible the first day (Fig. 4.1, c), whereas small colonies composed of highly packed cells with epithelial-like shape were detected starting one week after (Fig. 4.1, d). Notably, mesenchymal-to-epithelial transition is one major event that has to take place to reprogram cells toward pluripotency [177]. It is also important to underline that the protocol did not rely on the use of a layer of feeder cells, usually mouse embryonic fibroblasts (MEFs) or human foreskin fibroblasts (HFFs), to sustain the reprogramming process. This was possible thanks to the feeder properties of LL-CBMSCs, which were demonstrated to be able to act as a substitute for traditional feeder cells [178].

After LL-CBMSC-derived *bona fide* hiPSC colonies (referred to as hiPSCs from now on) reached confluence at week 3 *post*-infection, hiPSC lines (n=3) were generated by manual mechanical "picking" of single colonies, using a 150 µm diameter needle mounted on a stripper micropipette. Notably, this choice guarantees more *intra*-population homogeneity, compared to bulk or clone-pooled subcloning techniques [179]. The established hiPSC lines grew for more than 40 passages and showed a typical pluripotent stem cell morphology, growing as densely packed epithelial-like cells forming colonies with well-defined edges (Fig. 4.2, a). In order to assess the immunophenotypic status of hiPSCs, the expression of classic MSC markers was addressed, by flow cytometry. Noteworthy, human leukocyte antigens A, B and C (HLA-ABC) expression on hiPSC membrane surface was drastically reduced, compared to parental LL-CBMSCs (Fig. 4.2, b), in line with the pluripotent stem cell phenotype. On the contrary, CD90 and CD44 were retained, even though the signal intensity was strongly reduced; interestingly, the pluripotent control showed almost no positivity for CD44. Analogous to HLA-ABC, CD73 expression was completely lost in hiPSCs (Fig. 4.2, b). Therefore, HLA-ABC and CD73 represent a minimal immunophenotype panel that could be useful to assess the successful reprogramming of MSCs. Finally, to ensure the maintenance of genomic stability, the karyotype of parental and reprogrammed cells was investigated. Importantly, no chromosomal abnormalities were detected (Fig. 4.2 c).

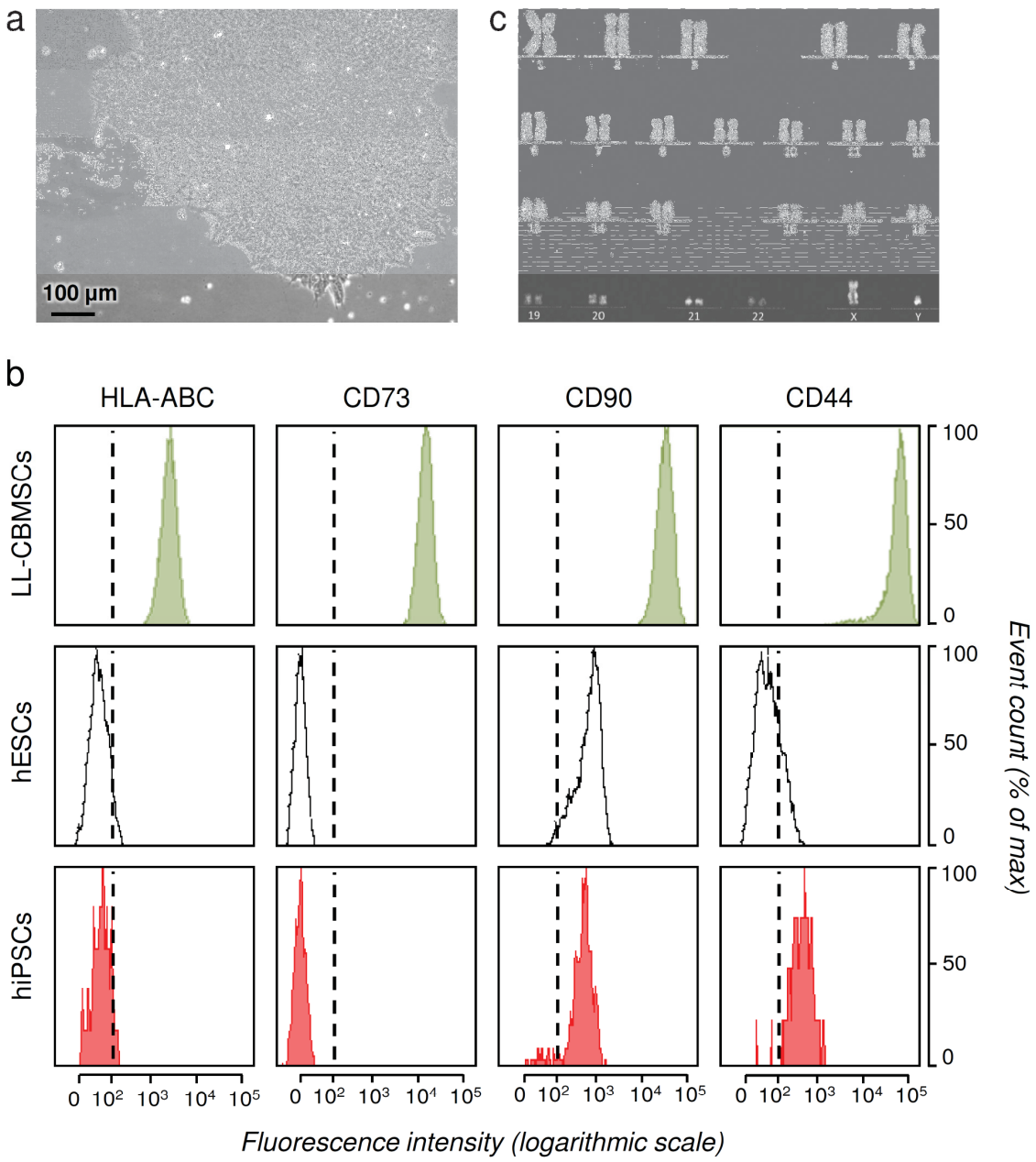

Figure 4.2. Long-living (LL)-cord blood (CB) multipotent mesenchymal stromal cell (MSC)-derived *bona fide* pluripotent stem cells. In a), a representative pluripotent colony with epithelial-like morphology is shown. In b), the immunophenotype of a representative hiPSC line, assessed by flow cytometry, is presented; the horizontal axis reports fluorescence intensity in a logarithmic scale, the vertical axis reports event count as percentage of maximum count for each sample. The karyotype of the generated cell lines was normal, as shown in a representative karyogram in c).

4.2.1 Stemness and pluripotency assessment

The hiPSC lines could grow for many passages (>40), and they were thoroughly characterized to assess their identity (see Appendix III.b for detailed protocols). First, alkaline phosphatase (AP) activity was assessed, as a typical feature of pluripotent stem cells (Fig. 4.3, a).

Notwithstanding, also parental non-reprogrammed LL-CBMSCs showed strong AP activity, in line with the literature [180], suggesting that it is not a useful parameter to consider in the context of MSC reprogramming, unlike the immunophenotype panel previously proposed (paragraph 4.2).

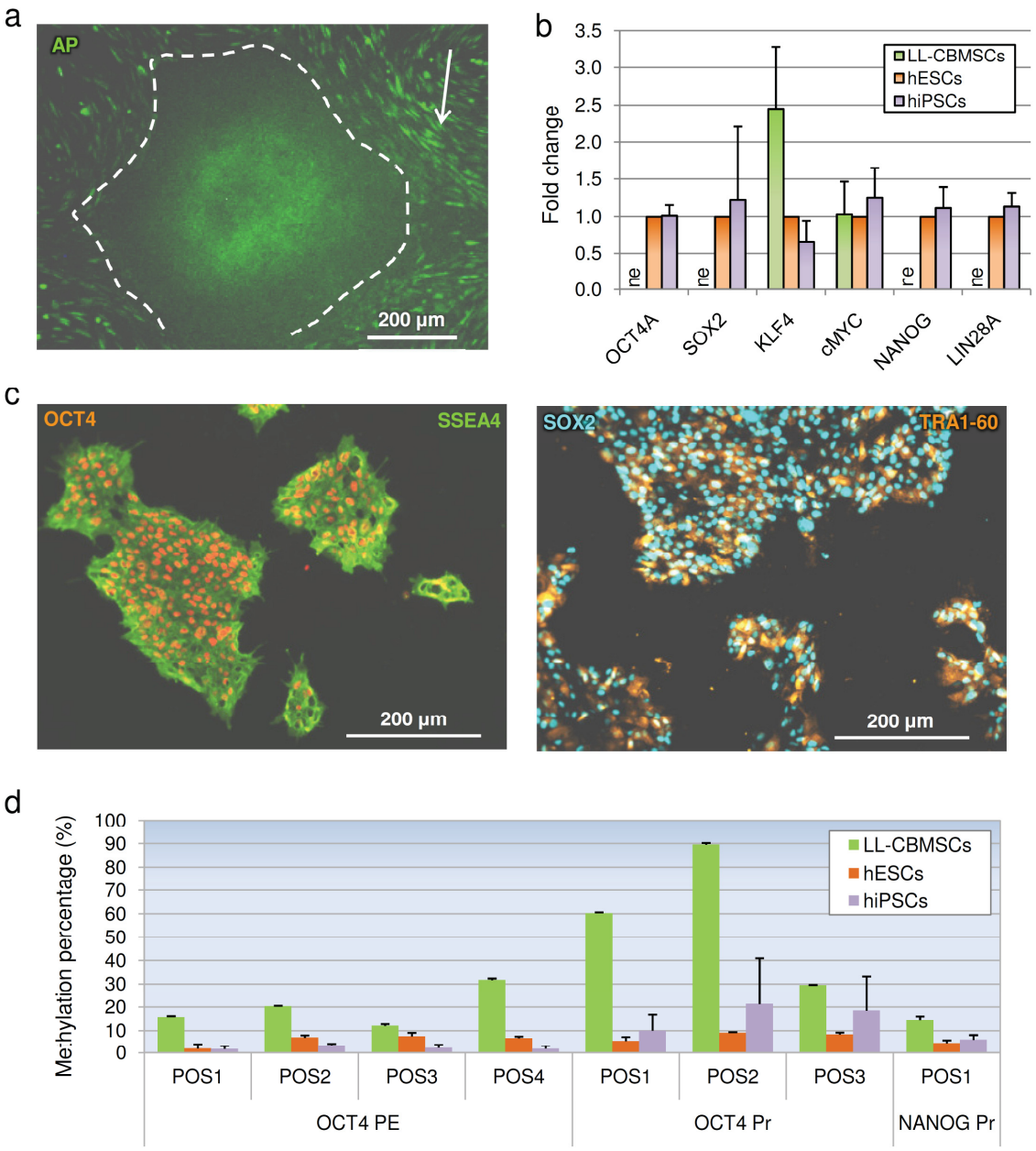

Figure 4.3. Stemness properties of human induced pluripotent stem cells (hiPSCs). In a), alkaline phosphatase (AP)-live staining detected AP activity in hiPSC colonies (dashed line), but also in parental non-reprogrammed cells, indicated by the arrow. In b), Real Time qRT-PCR revealed strong expression of pluripotency network-related genes, normalized to human embryonic stem cells (hESCs), as pluripotent positive control. Mean (n=3) with standard deviation is presented; ne, not expressed. In c), protein expression of typical pluripotency markers was assessed by immunofluorescence. Complete modification of the epigenetic landscape of NANOG and OCT4 regulatory regions after reprogramming was investigated by pyrosequencing of bisulfite-treated DNA (d); POS, position; PE, proximal enhancer; Pr, promoter.

Second, the expression of key pluripotency network-related genes was investigated by Real Time qRT-PCR, compared to parental LL-CBMSCs as negative control, and to a pluripotent stem cell line as positive control (Fig. 3.4, b). The established hiPSC lines showed increased gene expression for *OCT4* (absent in parental cells) and *SOX2* (absent in parental cells), two well-known pluripotency markers; *KLF4* was more expressed in parental cells (5-fold change), consistently with other reports [181], while *cMYC* was expressed at similar levels. More importantly, also *NANOG* (absent in parental cells) and *LIN28A* (absent in parental cells), not present in the cocktail of exogenously encoded reprogramming factors, showed a gene expression similar to that of the pluripotent control. This clearly indicates that the expression of exclusive pluripotency-associated genes was switched on at the endogenous level.

Third, to detect expression of pluripotency-associated markers at the protein level, immunofluorescence analyses were performed on undifferentiated hiPSC colonies (Fig. 4.3, c). Both OCT4/SSEA4 and SOX2/TRA1-60 double stainings revealed strong protein expression. Finally, the epigenetic state of crucial gene regulatory regions was addressed on hiPSC bisulfite-treated DNA by pyrosequencing (Fig. 4.3, d), compared to LL-CBMSCs as negative control, and to a pluripotent stem cell line as positive control. The results showed complete methylation remodeling for CpG islands in various positions along *OCT4* promoter and proximal enhancer sequences. The same was found for *NANOG* promoter (Fig. 4.3, d), further confirming fully acquisition of pluripotent features for LL-CBMSCs following reprogramming.

Finally, hiPSC differentiation properties were investigated to complete the characterization of the cell lines generated. Protein marker expression for derivatives of the three germ layers was assessed by immunofluorescence, after *in vitro* differentiation protocols were applied (Fig. 4.4). The hiPSCs could generate neural cell adhesion molecule (NCAM)-positive neurectodermal cells (Fig. 4.4, a), α-smooth muscle actin (α-SMA)-positive mesodermal cells (Fig. 4.4, b), and α-fetoprotein (AFP)-positive endodermal cells (Fig. 4.4, c).

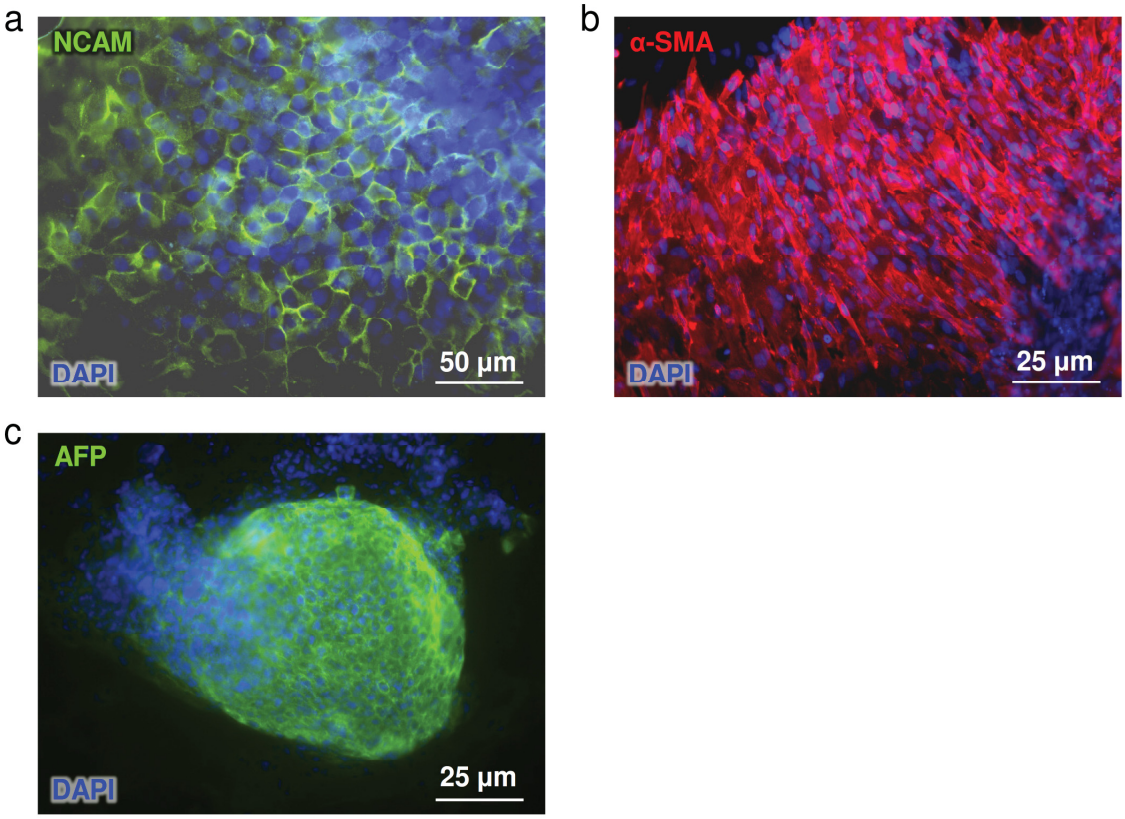

Figure 4.4. Differentiation of induced pluripotent stem cells into derivatives of the three germ layers. The induced pluripotent stem cells underwent *in vitro* differentiation into derivatives of the three germ layers. Protein expression of typical ectodermal (a), mesodermal (b) and endodermal (c) markers was assessed by immunofluorescence. DAPI, 4',6-diamidin-2-fenilindolo; NCAM, neural cell adhesion molecule; α-SMA, α-smooth muscle actin; AFP, α-fetoprotein.

4.2.2 Extracellular vesicles as a new feature of pluripotent stem cell biology

To investigate if hiPSCs still preserved the capacity to produce extracellular vesicles (EVs), the same characterization workflow used for LL-CBMSC-EVs in Chapter 3 was implemented. Thanks to scanning electron microscopy, the production of EVs by hiPSCs was confirmed. Also for hiPSCs, EVs were detected as outward structures protruding from the cell surface (Fig. 4.5, a). Concerning EV secretion, it was located at peripheral protrusions of the plasma membrane, indicating that hiPSCs, as well as LL-CBMSCs, need space to outgrow and release EVs (Fig. 4.5, b). Afterwards, EV size was assessed by nanoparticle tracking analysis (NTA), which detected a mean size of 256 nm (n=5; standard deviation (SD)=66). Again, this particle size range indicates absence of apoptotic bodies (1-5 µm).

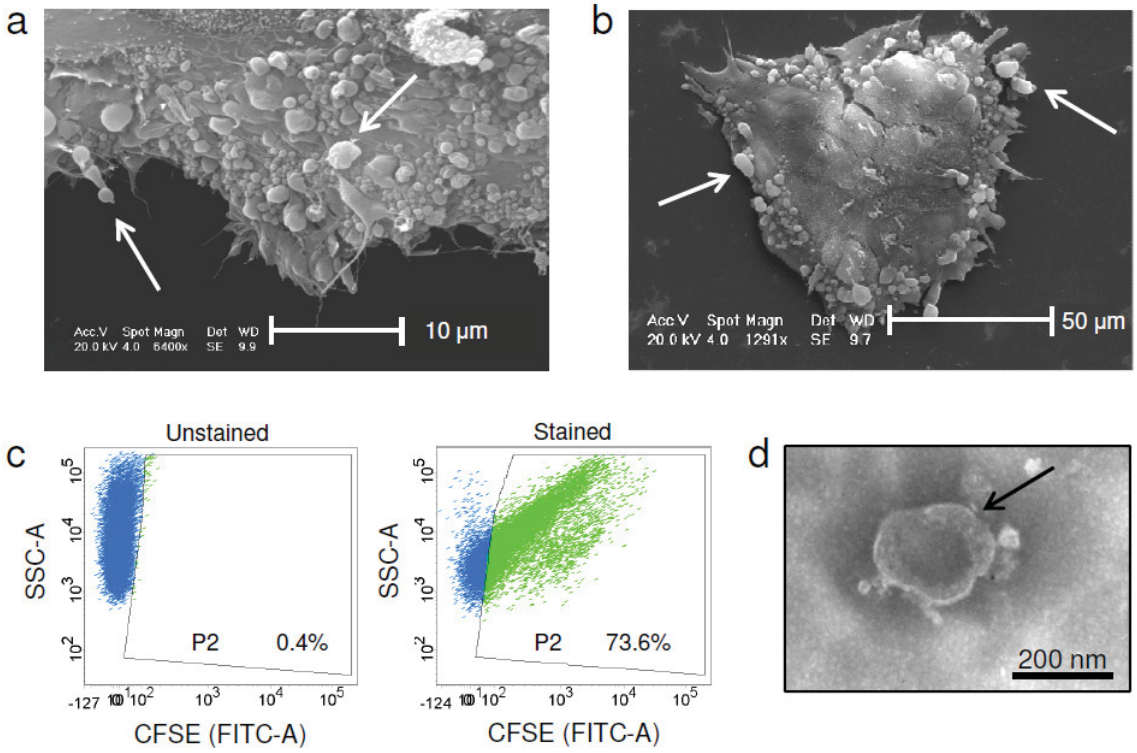

Figure 4.5. Characterization of extracellular vesicles (EVs) from induced pluripotent stem cells. EVs were recognized by scanning electron microscopy as outward structures protruding from the cell surface (a); representative EVs are indicated by arrows. In b), an entire induced pluripotent stem cell (hiPSC) colony is shown; representative EVs are indicated by arrows. Flow cytometry analysis (c) revealed positivity for carboxyfluorescein ester (CFSE), which produced fluorescence in the fluorescein isothiocyanate channel (FITC-A) (P2), demonstrating that hiPSC-EVs are intact cytoplasm containing membrane-enclosed particles; SSC-A, side scatter. Transmission electron microscopy (d) visualized the ultrastructural morphology of isolated EVs; the intact membrane of a representative EV is indicated by the arrow.

Quantification of EVs by NTA revealed that hiPSCs produced a mean of 28 billion EVs per Petri dish (100mm) per day (n=5; SD=12). Integrity of EVs was investigated by carboxyfluorescein diacetate succinimidyl ester (CFDA-SE) staining, whose principle was explained in paragraph 3.2. Flow cytometry analysis revealed that >70% of the detected events were carboxyfluorescein succinimidyl ester (CFSE) positive, which indicated that they were intact EVs (Fig. 4.5, c); in addition, 50% of CFSE-positive EVs also expressed CD63 and CD81 surface markers. Lastly, transmission electron microscopy images showed a morphology consistent with pure EV preparations (Fig. 4.5, d). Importantly, very recently, other laboratories reported the generation of EVs by pluripotent stem cells [182-187].

4.3 Stem cell extracellular vesicle miRNome load

In the recent literature, extracellular vesicles (EVs) were shown to shuttle preferentially small RNA species (see paragraph 1.3.1). Nevertheless, no complete miRNome analysis has been attempted so far for EVs generated by long living (LL)-cord blood (CB) multipotent mesenchymal stromal cells (MSCs) and human induced pluripotent stem cells (hiPSCs). This is of crucial importance, as the few reports trying to elucidate EV molecular mechanisms of action underlined the pivotal role of miRNAs. To address this point, a complete miRNome analysis was performed on EVs harvested from hiPSCs, LL-CBMSCs and a pluripotent stem cell control. The profiling was performed exploiting a Real Time PCR-array system covering 754 human miRNAs, whose sequences were derived from miRBase version 14 database (see Appendix III.b for complete protocols). First, an analysis of stem cell source-unique EV miRNAs was performed on raw PCR amplification data, selecting the 150 sequences (top 150) with the highest output signal (Fig. 4.6, a). Interestingly, the majority of miRNAs present in LL-CBMSC-EVs were also found in hiPSC-EVs (87 common miRNAs), consistently with the pluripotent control. Only 16 miRNAs were found to be exclusively incorporated into hiPSC-EVs, while LL-CBMSC-EVs showed 53 specific miRNA sequences. Focusing on the ten most incorporated miRNAs, hiPSC-EVs showed a pattern identical to that of the pluripotent control EVs (Fig. 4.6, b). This can be considered a further confirmation of a successful reprogramming, as these miRNAs belonged to miRNA families known to have a role in the maintenance of pluripotency. For instance, the miRNA302/367 cluster (miR-367,-302a, b, c and d) is essential for *OCT4* expression and it supports reprogramming [188-191]. The other miRNAs belonged to the miRNA17/92 (miR-17, -18, -19a, -20a, -19b1 and -92a-1) and 106a/363 (miR-106a, -18b, -20b, -19b-2 -92a-2, and -363) clusters, which are implicated in control of cell proliferation and embryonic development [192-194]. On the other hand, LL-CBMSC-EV miR-125b and -21 were recently shown to be shuttled in mouse EVs, which exerted wound healing properties [195]. Furthermore, miR-125b and -24 were demonstrated to have a role in differentiation and self-renewal of MSCs [196, 197]. Intriguingly, miR-221 was detected in rat MSC-EVs, through which it contributed to cardioprotection during hypoxia *in vitro* [198].

a

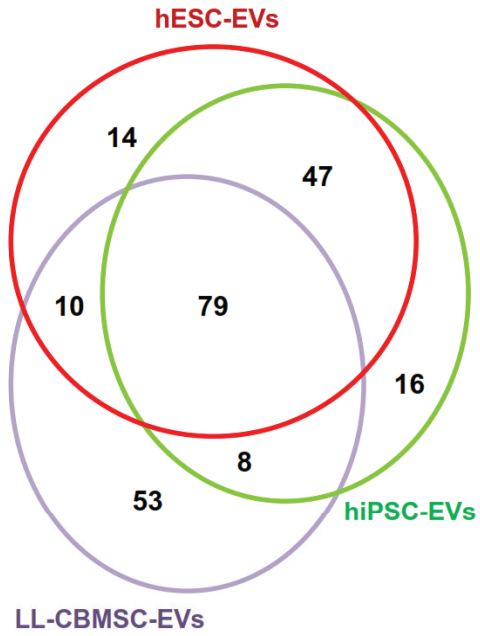

b

EV source		
LL-CBMSCs	**hESCs**	**hiPSCs**
miR-24	miR-367	miR-367
miR-125b	miR-302b	miR-20a
miR-221	miR-20a	miR-302a
miR-222	miR-302a	miR-302d
miR-100	miR-19b	miR-92a
miR-99a	miR-92a	miR-302b
miR-31	miR-106a	miR-19b
miR-21	miR-17	miR-106a
miR-1274B	miR-302c	miR-302c
miR-20a	miR-302d	miR-17

c

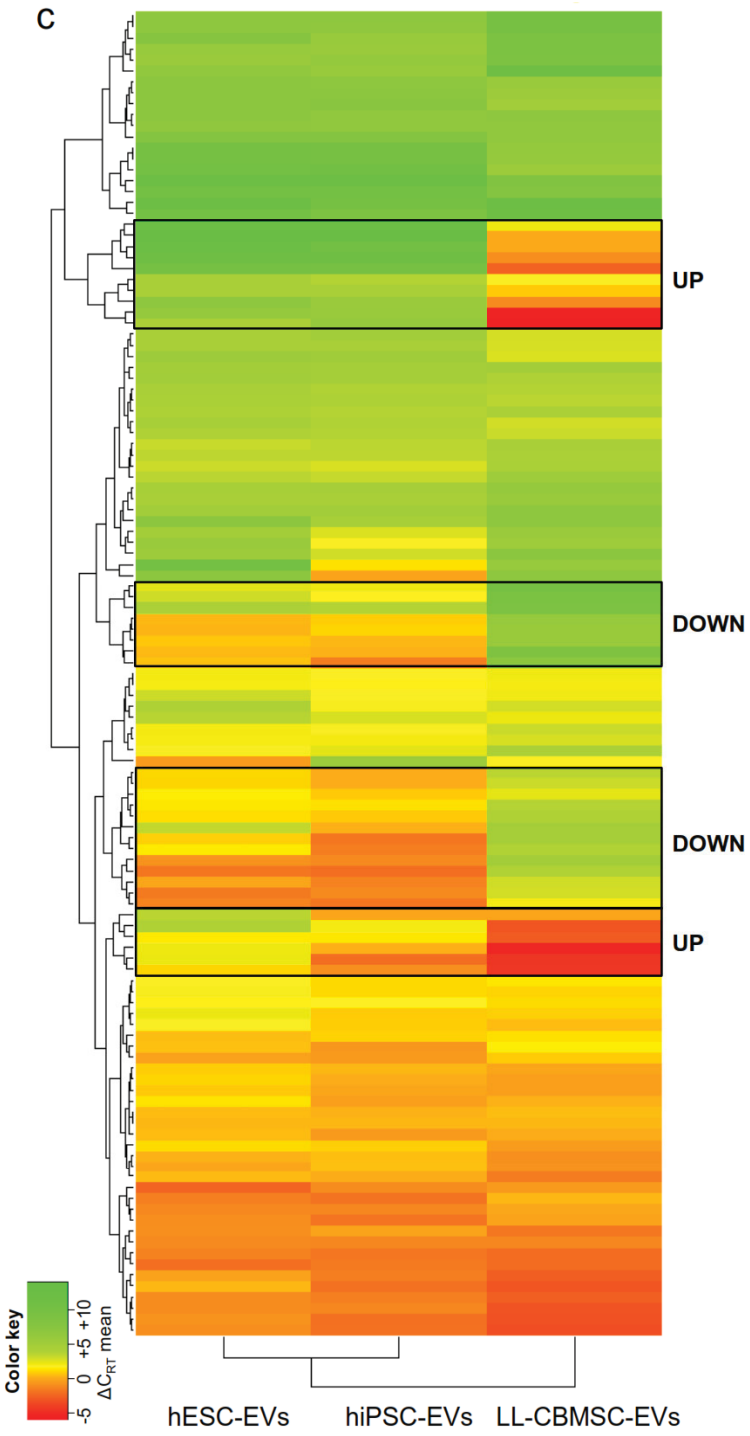

d

KEGG pathways UP	p-value	KEGG pathways DOWN	p-value
Prolactin signaling pathway	1.2^(-6)	Fatty acid biosynthesis	<1^(-325)
Wnt signaling pathway	2.5^(-5)	Steroid biosynthesis	<1^(-325)
Endocytosis	0.0010	ECM-receptor interaction	<1^(-325)
Oocyte meiosis	0.0138	Fatty acid metabolism	1.1^(-16)
Signaling pathways regulating pluripotency of stem cells	0.0183	Mucin type O-Glycan biosynthesis	1.4^(-7)

Figure 4.6. Stem cell extracellular vesicle (EV) miRNome. EVs were characterized for their miRNome load. In a), a Venn diagram shows the distribution of common and unique miRNAs among the three EV stem cell sources. In table b) the first ten most incorporated miRNAs for each EV stem cell source are listed. The heatmap in c) represent the fold changes in miRNA EV incorporation; the horizontal dendrogram clusters miRNAs for similar amplification patterns, the vertical dendrogram clusters EV stem cell source for similar miRNA incorporation; the legend (color key) shows the fold change range (red for less incorporated miRNAs, green for more incorporated miRNAs). The miRPath version 3 bioinformatic tool was used to identify significantly enriched cellular pathways of the Kyoto Encyclopedia of Genes and Genomes (KEGG) database for the differentially expressed miRNA classes (d); only Tarbase database of experimentally validated miRNAs was considered. Statistics: pathway union by Fisher's exact test (hypergeometric distribution) enrichment analysis method with false discovery rate correction; the class-specific disease-unrelated top 5 ranked pathways are reported.

Second, the miRNA fold change data plotted in a heatmap, by R statistical software, revealed two classes of more incorporated (UP) and two classes of less incorporated (DOWN) hiPSC-EV miRNAs (Fig. 4.6, c). The cellular pathways targeted by UP and DOWN classes of differentially expressed miRNAs were addressed by interrogation of the miRTarBase database, which uses only experimentally validated miRNAs (Fig. 4.6, d). The UP classes were involved, among others, in regulation of pluripotency in stem cells and in Wnt signaling pathway, also important for pluripotent stem cell specification and proliferation [199]. The DOWN classes revealed major associations with fatty acid metabolism and with adherence features. This result was consistent with the stemness properties of hiPSCs and LL-CBMSCs, since pluripotent stem cell metabolism relies more on glycolysis than fatty acid oxidation [200], while mesenchymal stromal cells are known to express a wide range of adhesion molecules [201].

To conclude, even though the heatmap-associated hierarchical clustering analysis grouped hiPSC-EVs and the pluripotent control together, this was due to differences in the EV incorporation relative amount. Notably, the EV miRNome load was largely maintained following reprogramming, since the majority of the top 150 miRNAs were common between the hiPSC-EVs and LL-CBMSC-EVs.

4.4 Conclusions

The reprogramming of long living (LL)-cord blood (CB) multipotent mesenchymal stromal cells (MSCs) was proved feasible. Interestingly, no feeder cells were used, guaranteeing a more straightforward and unbiased xeno-free process. This was due to the feeder properties of non-reprogrammed LL-CBMSCs in culture. Moreover, a minimal immunophenotype panel composed of HLA-ABC and CD73 was proposed in order to assess successful MSC reprogramming. The induced pluripotent stem cell (hiPSC) lines generated were characterized successfully for stemness and pluripotency features, indicating that a complete reprogramming process was achieved.

Importantly for this research and for a possible therapeutic application of hiPSC-EVs, reprogramming preserved secretion of extracellular vesicles (EVs) with physical properties similar to those of parental LL-CBMSCs. Noteworthy, the EV miRNome load was largely maintained, which represents a prerequisite to envision a switch from LL-CBMSC-EV to hiPSC-EV use.

Chapter 5

Stem cell extracellular vesicles for neuroprotection

5.1 Motivations for an *ex vivo* model of brain ischemia

In Chapter 3, the anti-apoptotic and anti-inflammatory properties of LL-CBMSC secretome were presented, and the potential of extracellular vesicles (EVs) as therapeutic agents was also explored in an *in vitro* model of acute damage. Focusing on the development of EV-based therapies, pathological conditions for which ready-to-use therapeutics and a rapid administration is essential appeared the most suitable areas of clinical application. In this context, acute brain ischemia has a very limited therapeutic window of 3-6 hours for tissue plasminogen activator treatment [202]. Moreover, it is the second leading cause of death and dementia, and the first cause of disability in adult humans, with a global incidence of 76-119 cases per 100,000 inhabitants per year [203, 204]. This pathological condition occurs when blood is not flowing sufficiently to the brain to meet its metabolic demand, causing hypoxia, lack of nutrients, and, as a consequence, death of neural cells. Importantly, a successful therapy for acute brain ischemia could be beneficial also for other organs subject to the same risk, such as kidney, skeletal muscles, heart and lungs.

In order to study EV potential in acute brain ischemia treatment, an *ex vivo* model was exploited. This kind of model has the advantage of higher control over the experimental conditions and less variability. In addition, it is more suitable to study the mechanism of action of a therapeutic approach, compared to *in vivo* models of sensorimotor and cognitive deficits, because molecular and cellular events may be investigated at the tissue and cellular level (*e.g.*: signaling pathways, cell viability, tissue secretion in response to damage).

5.2 Extracellular vesicle-driven damage recovery

Ischemic damage was induced in organotypic mouse brain slices by a standard oxygen and glucose deprivation (OGD) culture condition (complete experimental schematic in figure 5.1; see Appendix III.c for detailed protocols). This kind of insult mimics the sudden lack of oxygen and nutrients in the ischemic brain, which leads to metabolic and oxidative stress, and eventually to inflammation and tissue necrosis. Hence, all these different aspects of ischemia-driven injury were addressed to investigate if EV-based treatments could be of any therapeutic use. Briefly, the experimental conditions were:

- Undamaged brain slices (positive control, n=12);
- OGD-damaged brain slices (negative control, n=12);
- LL-CBMSCs in co-culture with damaged brain slices (co-culture, n=12);
- LL-CBMSC-EV treated damaged brain slices, one-fold dose (CB-EV[1], n=12);
- hiPSC-EV treated damaged brain slices, one-fold dose (hiPSC-EV[1], n=12);
- hiPSC-EV treated damaged brain slices, two-fold dose (hiPSC-EV[2], n=12);
- PKH26-labelled LL-CBMSC-EV treated damaged brain slices (n=2);
- PKH26-labelled hiPSC-EV treated damaged brain slices (n=2).

The one-fold dose consisted in 2.4 billion EVs per brain slice and it was determined based on an estimation of EV production by LL-CBMSCs in co-culture. A direct comparison between LL-CBMSC- and hiPSC-EVs was planned in order to assess if and how much reprogramming had affected EV protective properties; to detect any dose-response phenomenon, the two-fold dose was also used. EV administration was repeated for two subsequent days, based on the assumption that LL-CBMSCs in co-culture would constantly generate new EVs. In addition, EV membranes were labelled with PKH26 to investigate if fusion with the target tissue had taken place during the treatments.

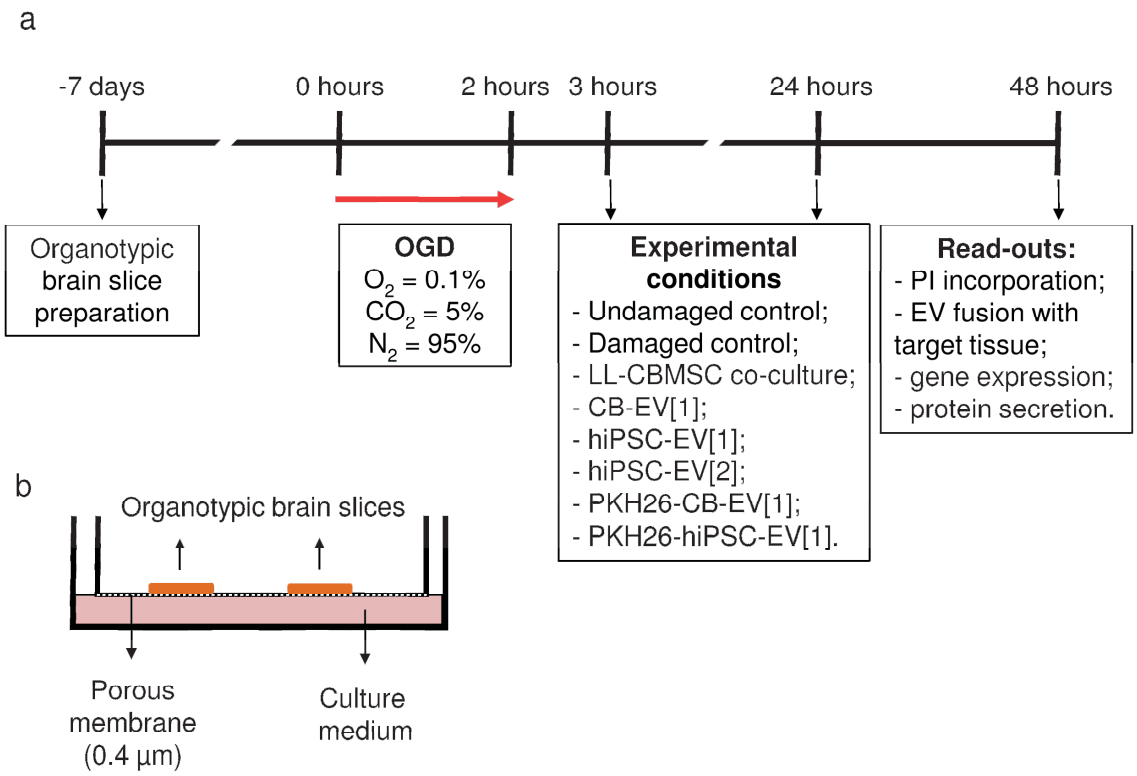

Figure 5.1. Experimental schematic. In a), the experimental protocol is summarized. Mouse brain slices were prepared 1 week before the injury induction and they were maintained in culture in 6-well plates. Each well contained a transwell permeable to particles <400 nm in size; n=2 brain slices were used per transwell (b). Ischemic-like oxygen and glucose deprivation (OGD) insult consisted in a 2 hour incubation at 0.1% O_2, 0% glucose, followed by 1 hour of reoxygenation and nutrient availability. Then, LL-CBMSC co-culture or extracellular vesicle (EV) administrations were performed; EVs were administered also 24 hours *post*-OGD. At 48 hours *post*-OGD, tissue necrosis rescue and EV fusion with the target tissue were assessed, and samples for gene expression and secretion analysis were collected. PI, propidium iodide; CB-EV[1], one-fold dose LL-CBMSC-EV treatment; hiPSC-EV[1], one-fold dose hiPSC-EV treatment; hiPSC-EV[2], two-fold dose hiPSC-EV treatment; PKH26, PHK26-labelled EVs.

At 48 hours *post*-OGD insult, the effectiveness of the applied treatments was addressed by the evaluation of cell necrosis, which is one endpoint of the ischemic cascade. Necrotic cells in the brain tissue were quantified by propidium iodide (PI) incorporation. Strikingly, all the treatments rescued cell mortality, showing statistically significant reductions in PI signal, measured by fluorescence microscopy. In particular, all stem cell EV-based treatments demonstrated a neuroprotective effect equal to that of LL-CBMSC co-culture. Yet, the most effective treatment among them was CB-EV[1], which resulted in a statistically significant lower PI incorporation only if compared to hiPSC-EV[1]. Nonetheless, also hiPSC-EVs possessed relevant neuroprotective properties, which were more evident for hiPSC-EV[2].

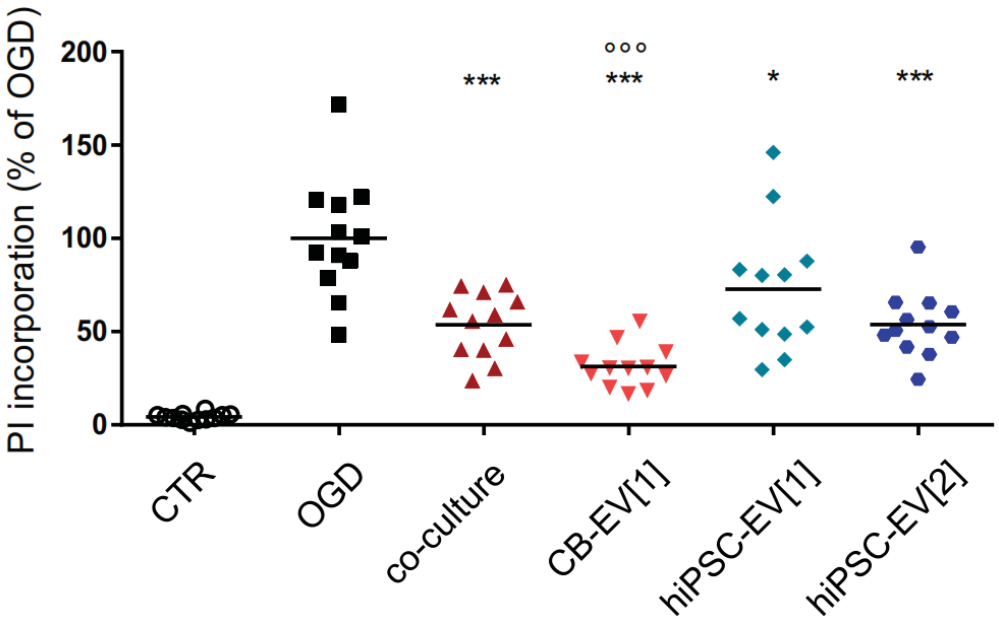

Figure 5.2. Necrosis upon oxygen and glucose deprivation (OGD)-driven injury. Necrotic cells were quantified by propidium iodide (PI) staining. The results are presented as percentage of untreated OGD negative control (% of OGD). Statistical analysis: one-way ANOVA, followed by Tukey post-test, after normality was assessed by Kolmogorov-Smirnov test; ***$p<0.001$, *$p<0.05$, for all experimental conditions compared to OGD group; °°°$p<0.001$, for CB-EV[1] compared to hiPSC-EV[1] conditions; n=12 for each experimental group. CTR, undamaged positive control; OGD, damaged untreated negative control; co-culture, damaged brain slices in co-culture with LL-CBMSCs; CB-EV[1], damaged brain slices treated with one-fold dose LL-CBMSC-EVs; hiPSC-EV[1], damaged brain slices treated with one-fold dose hiPSC-EVs; hiPSC-EV[2], damaged brain slices treated with two-fold dose hiPSC-EVs.

At 48 hours *post*-OGD, PKH26-labelled EV presence within the brain slices was addressed by fluorescence microscopy (Fig 5.2, a, b and b). The EV signals were detected as bright fluorescent spots, located especially at tissue slice borders.

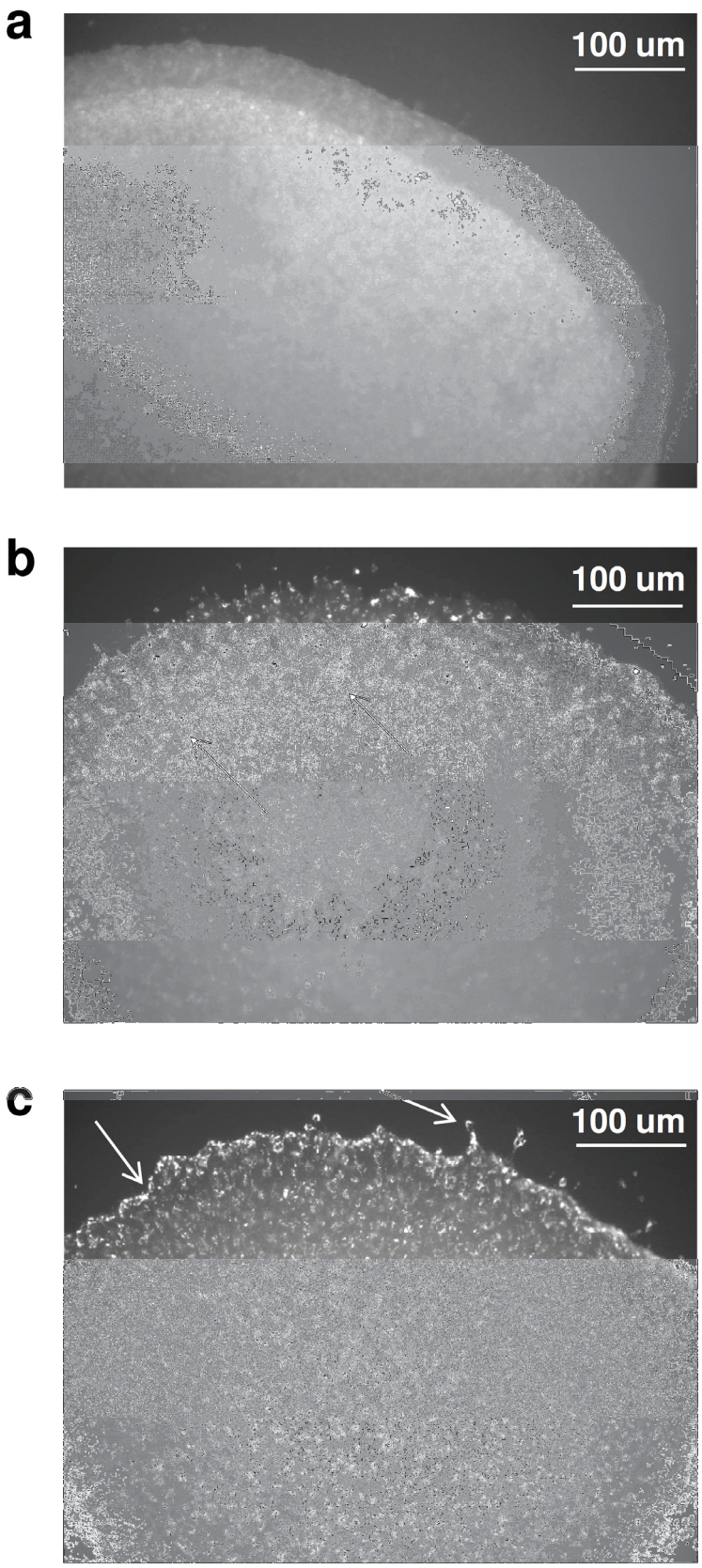

Figure 5.3. Fusion of extracellular vesicles (EVs) with brain tissue cells. In a), a representative brain slice which did not receive PKH26-labelled EVs is shown. PKH26-labelled LL-CBMSC- (b) or hiPSC- (c) EV treated brain slices show positivity for fluorescence, clearly higher than the autofluorescence background; the arrows indicate representative PKH26-positive spots.

The next step was to evaluate which cell type was damaged by the OGD insult and if the treatments could have a beneficial effect on them. The presence of specific neural cell types was assessed at the transcriptional level by Real Time qRT-PCR analysis performed on markers typical of neurons (*Map2*), endothelial cells (*Cd31*), microglia (*Cd11b*), and astrocytes (*Gfap*). Neurons and astrocytes were affected by the OGD insult, as shown by a statistically significant reduction of the respective marker mRNA transcripts, whereas endothelial cells and microglia did not (Fig. 5.4, a, b, c and d). Importantly, astrocyte marker mRNA level was rescued in all treatments, indicating that this cell type is the main therapeutic target of stem cells and stem cell-EVs. Notably, the co-culture treatment showed only a partial and not significant rescue.

The expression of anti-apoptotic (*Bcl2*) and pro-apoptotic (*Bax*) genes was also investigated to evaluate if a modulation of apoptosis by the treatments had played a role in the observed neuroprotection. Unfortunately, no treatment revealed increased expression of *Bcl2* or decreased expression of *Bax*, compared to untreated control (Fig. 5.4, e and f). The same approach was used to address if the treatments promoted proliferation, but, also in this case, no significant fluctuations in *Mki67* and *Pcna* gene expression was observed, compared to OGD negative control (Fig. 5.4, g and h). Instead, undamaged positive control brain slices showed statistically significant lower *Mki67* and *Pcna* mRNA levels, compared to the other experimental conditions. This suggested that in this *ex vivo* model the OGD insult *per se*, followed by reoxygenation and glucose availability, induced transcription of these genes, maybe as an endogenous response to injury. Yet, a significant difference was identified between the co-culture condition, compared to hiPSC-EV[2], hinting at a higher stimulation of proliferation by the latter treatment. The gene expression of growth factors crucial for ischemia-triggered injury recovery was also assessed: brain-derived neurotrophic factor (*Bdnf*) [205] and vascular endothelial growth factor A (*Vegfa*) [206]. The transcript levels were significantly lower than those of the undamaged positive control were. Notwithstanding, both hiPSC-EV[1] and [2] treatments demonstrated significantly higher *Vegfa* mRNA levels, compared to the co-culture condition (Fig. 5.4, i and j).

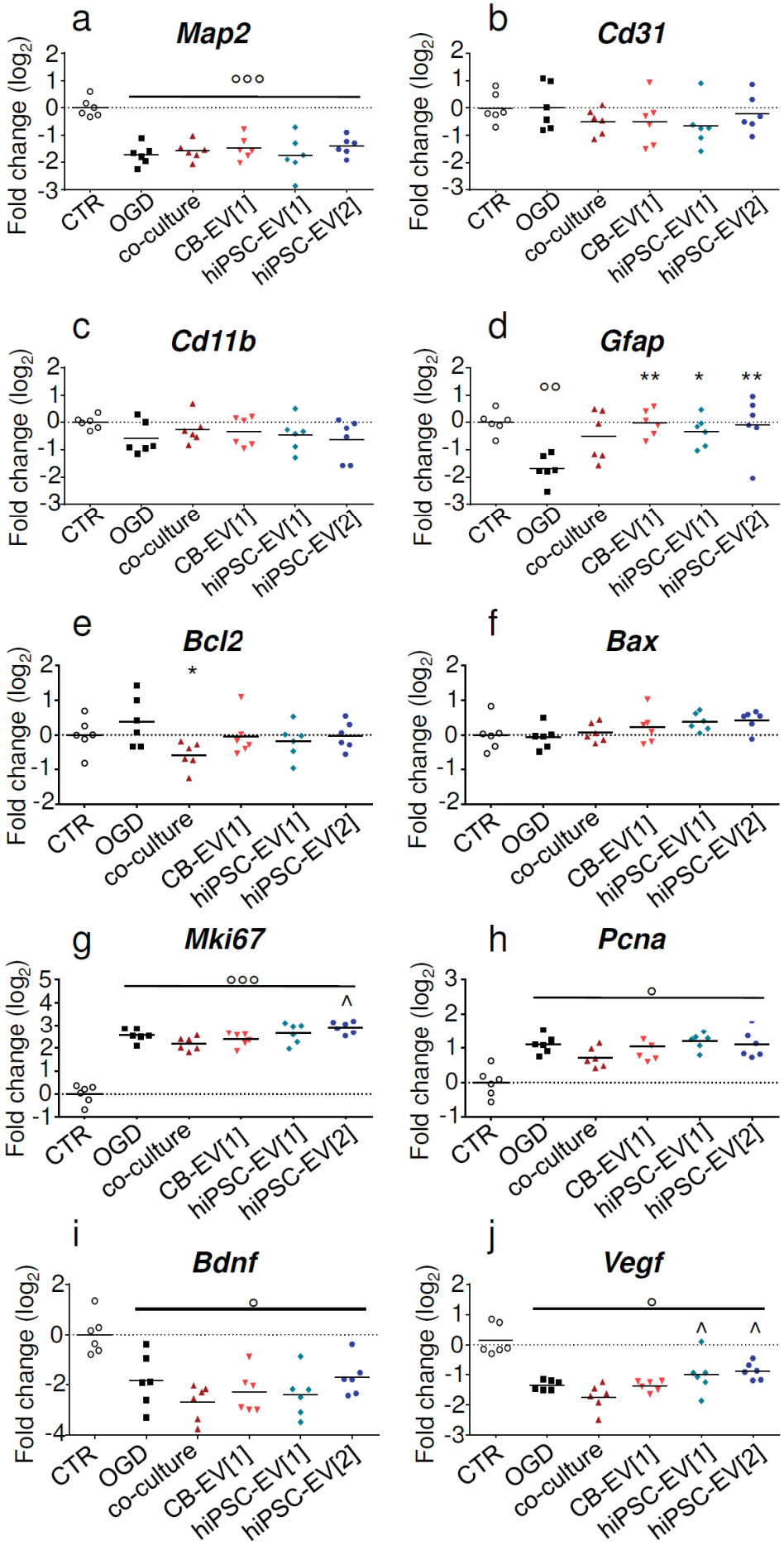
a
Map2
b
Cd31
c
Cd11b
d
Gfap
e
Bcl2
f
Bax
g
Mki67
h
Pcna
i
Bdnf
j
Vegf
Fold change (log2)
CTR
OGD
co-culture
CB-EV[1]
hiPSC-EV[1]
hiPSC-EV[2]

Figure 5.4. Effects on apoptosis, proliferation and production of growth factors. Cell type marker- (a, b, c and d), apoptosis- (e and f), proliferation- (g and h) and growth factor- (i and j) related gene mRNA levels are presented as log_2 of the fold change, normalized to undamaged positive control (CTR). Statistical analysis: one-way ANOVA, followed by Tukey post-test, after normality was assessed by Kolmogorov-Smirnov test; n=6 for each experimental group; °°°p<0.001, °°p<0.01, °p<0.05, compared to CTR; **p<0.01, *p<0.05, compared to oxygen and glucose deprivation (OGD) damaged untreated negative control; ^p<0.05, compared to damaged brain slices in co-culture with LL-CBMSC (co-culture) condition. CB-EV[1], damaged brain slices treated with one-fold LL-CBMSC-EVs; hiPSC-EV[1], damaged brain slices treated with one-fold hiPSC-EVs; hiPSC-EV[2], damaged brain slices treated with two-fold hiPSC-EVs.

Finally, the metabolic and oxidative stress consequences of the OGD insult were investigated. To this purpose, the culture medium levels of ATP, adenosine and glutamate metabolites (mediators of ischemic damage), malondialdehyde (lipid peroxidation marker), superoxide dismutase and glutathione (anti-oxidant molecules) were measured, by colorimetric or fluorescence reaction-based assays. Unfortunately, none of the aforementioned molecules were detected. It is likely that to appreciate, if any, a modulation of these parameters, a technique allowing a lower detection limit should have been used (*e.g.*: mass spectrometry).

5.3 Tissue modulation as stem cell extracellular vesicle mechanism of action

Based on the previously assessed anti-inflammatory properties of LL-CBMSCs, which could be relevant in the context of brain ischemia, modulation of inflammatory cytokines secreted by brain slices in the culture medium was investigated by multiplexed ELISA. The levels of INFγ, IL1β, IL2, IL6, IL10, IL12p70, IL17 and TNFα were simultaneously measured for positive and negative controls, and for co-culture, CB-EV[1] and hiPSC-EV[2] treatments. Intriguingly, detectable levels of secreted protein were found for TNFα and IFNγ. This was a very relevant result, because microglia-produced TNFα is one major mediator of *post*-ischemic early phase inflammation and it is responsible for many aspects of it [207, 208]. Furthermore, $CD4^+$ Th1 lymphocyte-produced IFNγ is involved in late phase ischemic events [209], and it is a potent inducer of TNFα, thus promoting amplification and maintenance of neuroinflammation [210, 211]. Going into details, TNFα and INFγ secreted protein levels underwent statistically significant increases in OGD condition, compared to undamaged control (Fig. 5.5, a and b). Surprisingly, all treatment conditions showed a statistically significant reduction of TNFα, compared to OGD condition. The effect was so dramatic as to significantly decrease the protein levels below the undamaged control condition by a two-fold change. In addition, CB-EV[1] treatment showed a significant lower reduction of TNFα, compared to the co-culture condition. Concerning INFγ, decreased levels of secreted protein were observed in all treatments, compared to the negative control; statistically significant results were obtained for CB-EV[1] and for hiPSC-EV[2], with the latter demonstrating a stronger action, but not for the co-culture condition. Both TNFα and INFγ results indicated that complete rescue of these two crucial ischemia-driven injury parameters was achieved by the EV-based treatments.

a

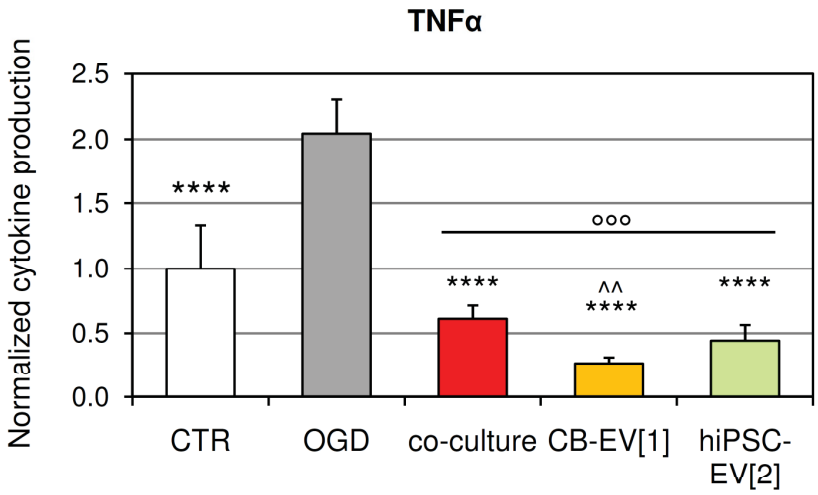

b

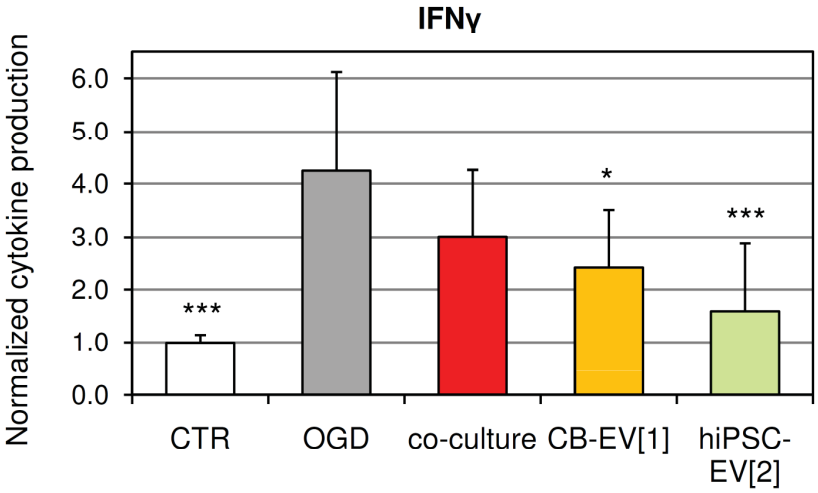

c

	Top 150 rank		Validation	
	EV source		Organism	
TNFα	***LL-CBMSCs***	***hiPSCs***	***Human***	***Mouse***
miR-125b-5p	2	60		x
miR-130a	44	15	x	
miR-19a-3p	87	28	x	x
miR-203	n.p.	103	x	
INFγ	***LL-CBMSCs***	***hiPSCs***	***Human***	***Mouse***
miR-24-3p	1	25	x	
miR-409-3p	13	n.p.	x	
miR-27a-3p	33	97	x	
miR-143-3p	49	n.p.	x	
miR-181a-5p	55	n.p.	x	
miR-16-5p	61	50	x	
miR-26b-5p	71	76	x	
miR-29b-3p	81	126	x	
miR-125a-5p	83	n.p.	x	
miR-15b-5p	85	41	x	
miR-146a-5p	98	145		x
miR-15a-5p	146	146	x	

Figure 5.5. Modulation of inflammatory cytokines. Tumor necrosis factor α (TNFα) (a) or interferon γ (INFγ) (b) protein levels are shown, normalized to undamaged positive control (CTR); mean and standard deviation is presented. Statistical analysis: one-way ANOVA, followed by Tukey post-test, after normality was assessed by Kolmogorov-Smirnov test; n=4 for CTR, n=5 for LL-CBMSC co-culture treatment (co-culture), n=6 for all other experimental conditions; °°°p<0.001, compared to CTR; ****p<0.0001; ***p<0.001; *p<0.05, compared to oxygen and glucose deprivation (OGD) damaged untreated negative control; ^^p<0.01, compared to the co-culture condition. In c), the table summarizes TNFα and INFγ transcript-targeting miRNAs; ranks among total incorporated miRNAs, and validation in human or mouse cells are specified; n.p., not present. CB-EV[1], one-fold dose LL-CBMSC-EV treatment; hiPSC-EV[2], two-fold dose hiPSC-EV treatment.

Following the working hypothesis presented in paragraph 4.3, the possibility of a functional role for miRNAs in this context was explored. Out of the top 150 ranked LL-CBMSC EV-incorporated miRNAs, 15 were found to target TNFα or INFγ mRNA transcripts, by interrogation of the miRTarBase database of experimentally validated miRNAs (Fig. 5.5, c). With regard to hiPSC-EVs, the result was 12 out of 150 top ranked miRNAs. Among them, TNFα transcript-targeting miR-125b-5p, miR-130a-3p and miR-19a-3p were present in both stem cell EVs, as well as INFγ transcript-targeting miR-146a-5p, miR-15a-5p, miR-15b-5p, miR-16-5p, miR-24-3p, miR-26b-5p, miR-27a-3p and miR-29b-3p. Interestingly, miR-24-3p and miR-125b-5p were the two most enriched miRNAs in LL-CBMSC-EVs, nonetheless, they were also present in hiPSC-EVs, ranked 25th and 60th, respectively. Thus, different stem cell-EV miRNA bioavailability could explain the different efficacies observed in the rescue of OGD-driven injury and the dose-response phenomenon verified for hiPSC-EVs. Yet, further and more focused experiments are needed to address these questions.

5.4 Conclusions

Stem cell extracellular vesicles (EVs) were shown to exert effectively neuroprotection in an organotypic *ex vivo* model of acute brain ischemia, reducing considerably the entity of tissue necrosis. The mechanism unveiled in this context counteracts brain injury via the modulation of the damaged tissue environment to establish a pro-regenerative milieu. Noteworthy, the *ex vivo* model mimicked very well an acute phase brain ischemia inflammatory response. This confirmed its validity to assess the efficacy of the developed EV-based treatments in the very early stages of the pathology. Intriguingly, EVs demonstrated anti-inflammatory properties equal to those of LL-CBMSCs. This suggests that EVs are carriers of the same stem cell regenerating clues able to modulate inflammation. Going into detail, the action of EVs was described on tumor necrosis factor α (TNFα), a pleiotropic peptide involved in inflammation- and immune-related activities, which plays a role not only in ischemia, but also in brain trauma and cerebral infection [207, 212, 213]. In addition, EV-based treatments targeted also interferon γ, whose capacity to activate innate and adaptive immune responses can act in concert with TNFα to establish chronic inflammation through a positive regulatory loop found in many neurological diseases [210, 211, 214-216]. Therefore, a larger area of application for the developed therapeutic approach could be considered, after the mechanism of action is validated also in other pathological contexts.

Chapter 6

Perspectives of extracellular vesicle-based therapeutics

Very recently, research on multipotent mesenchymal stromal cell (MSC) mechanism of action (MoA) in regenerative medicine approaches shifted its focus from secreted proteins to the generation of extracellular vesicles (EVs) [33, 63]. Consequently, an increasing amount of reports started to point at EVs as cell-derived vehicles responsible of the transfer of regenerative and protective information to injured tissues [34, 109]. In this frame, EVs are becoming one of the central players in MSC MoA, suggesting that a cellular-to-vesicular therapeutic paradigm switch can be feasible and promising. EVs could be produced in larger amounts, compared to MSCs, and stocked in a drug-like ready-to-use formulation. This will guarantee feasibility of clinical application in pathological contexts where rapidity is essential, which is something that cell therapy strategies currently cannot achieve. Hence, the idea of this PhD project was to develop a stem cell-based albeit cell-free regenerative approach.

Pivotal in the development of EV-based therapeutic approaches is the choice of the cell source. To address this issue, a mediation between the biological features of the cell source, the EV therapeutic properties and the scalability of the process at the industrial level should be done. Thus, the optimal cell source would allow limitless production of clinically relevant EVs able to recapitulate MSC regenerative potential. For this research, long living (LL)-MSCs isolated from a birth-associated tissue such as cord blood (CB) were chosen as EV source over MSCs derived from adult tissues (*e.g.*: bone marrow), which show age-related senescent features [46, 138, 139, 141, 142, 166].

Yet, from an industrial perspective, immortalized cell lines could be a more convenient EV source, compared to more heterogeneous and life span-limited primary cells. In this PhD work, the reprogramming technique was implemented as a tool to obtain LL-CBMSC-derived immortal cell lines preserving the original EV features. In this context, future studies assessing the safety of EV-based therapies will be necessary, with a focus on possible tumorigenic risks and on the feasibility of allogeneic clinical approaches.

A potential drawback of EV-based therapies would be the loss of the dynamic stimulus-response nature of living systems, as MSCs are. This crucial issue could be overcome "pushing" MSCs to generate EVs enriched in specific contents. A variety of means could be used to reach such a goal, such as specific culture conditions (*e.g.*: hypoxia, cytokine or small molecule administration), or also growth substrate control (*e.g.*: 2D versus 3D culture systems, growth surface patterning/stiffness control). The modulation of these cell culture aspects was already proved useful to reshape MSC secretome composition [217-219], therefore could be effective also with regard to EV cargo.

Another option, that is genetic engineering, could allow directed incorporation of specific proteins and RNA molecules into EVs, following their forced expression in parental cells. Essential to this highly refined control of the EV-load is the full comprehension of the cellular mechanisms leading to protein- and RNA-specific sorting into EVs. A lot of information that could be useful to this purpose is already available at online databases collecting data on the molecular content and other features of EVs, generated from different organisms, sources or under different culture conditions (*e.g.*: ExoCarta, Vesiclepedia, EVpedia, Microvesicles).

In this doctoral thesis, the developed EV-based regenerative approach was shown to be effective in the protection of neural tissue, in an *ex vivo* model of brain ischemia. Focusing on the MoA of this therapeutic strategy, the working hypothesis is that EVs acted as carriers of bioactive molecules able to modulate the *post*-ischemic inflammatory environment.

Many molecular aspects of the observed neuroprotective effect still have to be unveiled, yet, from the definition of the stem cell-EV miRNome, it could be speculated that EV-shuttled miRNAs may participate in the establishment of a pro-regenerative milieu.

Stem cell-EV miRNAs would be released into pro-inflammatory cytokine-secreting cells (*i.e.*: microglia and astrocytes) of the damaged tissue, upon fusion of EVs with the plasma membrane. Once inside the cell, a subset of specific miRNAs (*e.g.*: miR-125b-5p and miR-24-3p) could directly repress TNFα and INFγ transcript translation. In this way, extracellular levels of pro-inflammatory cytokines would be decreased, contributing to the exit from the positive regulatory loops leading to chronic inflammation, as depicted in figure 6.1.

In the proposed model (modified from [209]), four pro-inflammatory loops could be interrupted by the EV-shuttled miRNAs. First, TNFα acts on TNFα receptor 1 (TNF-R1) in an autocrine fashion, which leads to more TNFα secretion and glutamate release by microglia and astrocytes [220]; in turn, glutamate-stimulated group 2 metabotropic glutamate receptor (mGluR2) further induces TNFα release from microglia [221]. Second, TNFα increases glutamate release by astrocytes, too, and concomitantly reduces glutamate uptake, by the downregulation of astrocytic glutamate transporter (human EAAT1/murine GLAST and human EAAT2/murine GLT1) mRNA levels [222]. Third, INFγ acts on microglia in a paracrine fashion, which sustains TNFα extracellular levels and promotes immune system cell infiltration and amplification of inflammation [210, 211]. Fourth, TNFα leads to increased permeability of ionotropic N-Methyl-D-aspartic acid (NMDA) [223] and α-amino-3-hydroxy-5-methyl-4-isoxazolepropionic acid (AMPA) excitatory receptors [224] and to decreased membrane surface levels of γ-aminobutyric acid inhibitory receptor A ($GABA_A$-R) [225, 226], leading to increased synaptic excitatory/inhibitory ratio and excessive calcium entry, which induces neuronal death; in turn, dying neurons amplify the injury signals maintaining microglial cells in an active state [227].

In addition, stem cell EVs may also counteract direct promotion of TNF-R1-associated DEATH domain (TRADD)-mediated apoptosis by TNFα signaling [208]. It is worth noting that TNF-R1 stimulation also leads to the activation of NF-kB protein complex, a transcription factor sequestered in an inhibited state in the cytoplasm. Activated NF-kB can translocate into the nucleus and there it regulates the cellular response to a variety of stimuli (*e.g.*: stress, cytokine signaling, free radicals, infections) [228]. The genes controlled by NF-kB can turn on anti-apoptotic pathways and growth factor genes, such as *BDNF* and *NGF*, but also increase TNF-R1 and TNFα production as well [229].

On balance, this endogenous cellular response is insufficient to resolve ischemia-triggered injury. Finally, the protection exerted on astrocytes would allow more glutamate uptake from the injured tissue environment; therefore, TNFα release would be even more reduced, lacking one of its positive regulatory loops.

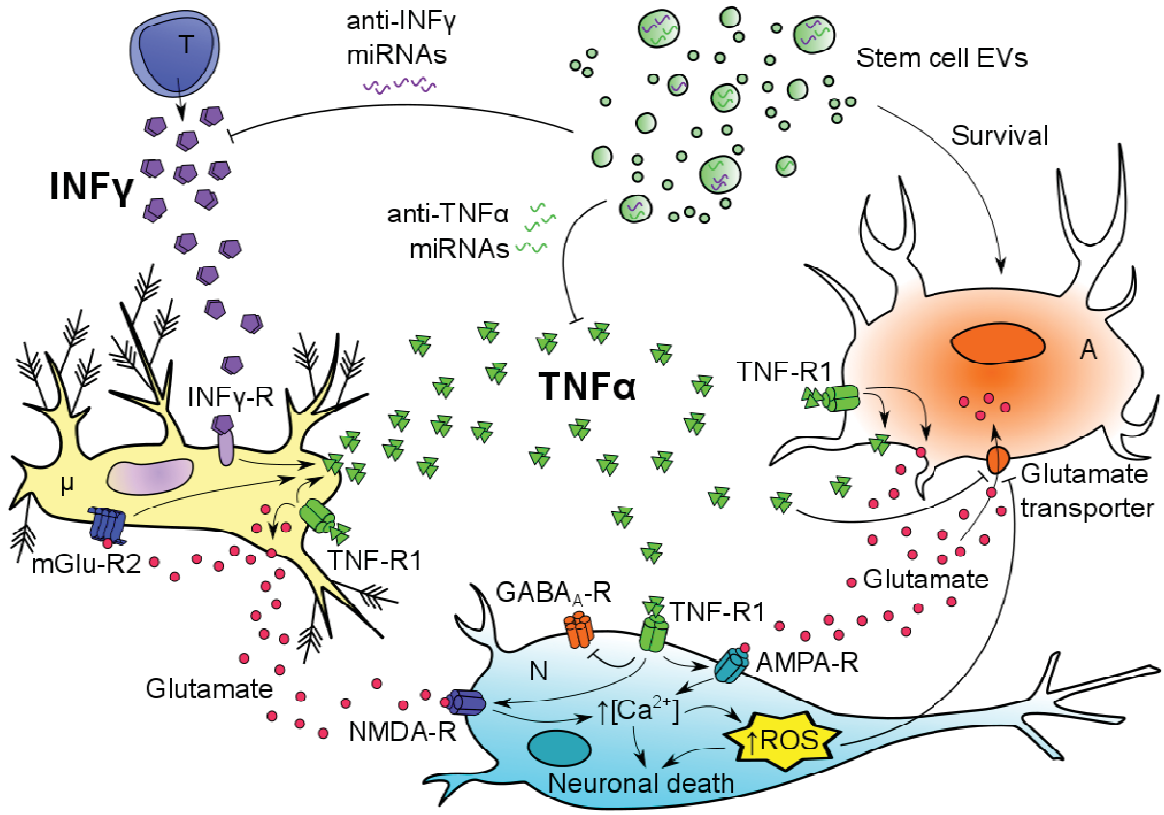

Figure 6.1. Working model: stem cell extracellular vesicles (EVs) disrupt positive regulatory loops to avoid chronic inflammation. After glial cells sense early signs of neuronal stress, an inflammatory response is activated, leading to glutamate release and secretion of tumor necrosis factor α (TNFα). This first cellular process is followed by the establishment of positive regulatory loops at the tissue level, involving also late-phase inflammatory responses, such as interferon γ (INFγ) secretion by infiltrated immune cells. In this way, inflammation is sustained and amplified, which is highly detrimental for tissue regeneration. Stem cell EVs were shown to reduce TNFα and INFγ extracellular levels, and to promote astrocyte survival, which are crucial players in the control of extracellular glutamate levels. Therefore, in the proposed model, stem cell EVs may modulate pro-inflammatory regulatory loops, contributing to the establishment of a pro-regenerative environment. A role of EV-shuttled miRNAs as molecular mediators of this effect is here hypothesized. T, T lymphocyte; TNFα-R1, TNFα receptor 1; INFγ-R, INFγ receptor; μ, microglia; mGlu-R2, group 2 metabotropic glutamate receptor; NMDA-R, N-Methyl-D-aspartic acid receptor; AMPA-R, α-amino-3-hydroxy-5-methyl-4-isoxazolepropionic acid receptor; GABA$_A$-R, γ-aminobutyric acid receptor A; N, neuron; ROS, reactive oxygen species; Ca^{2+}, free calcium; A, astrocyte.

In conclusion, it seems that such a complex dysfunctional crosstalk, herein partially described in aspects related to the present PhD work, would be more easily corrected toward a regenerative resolution if counteracted from many directions at a time. In this research project, an anti-inflammatory role for stem cell EVs was demonstrated, and a possible role for shuttled miRNAs was proposed. Yet, EVs may have exerted a beneficial effect through the action of other biomolecules as well, such as surface-exposed proteins or receptors, which could interact with the plasma membrane of target tissue cells to initiate intracellular signal transduction pathways. In addition, EVs could shuttle also metabolites, which were recently demonstrated to be neuroprotective in the same *ex vivo* model of brain ischemia [230]. This is very intriguing, because the primary consequences of ischemia are manifested at the metabolic level, so that an EV-based metabolic rescue appears an additional therapeutic option to investigate. All considered, the action of stem cell EVs could not only modulate both early-phase innate and late-phase acquired immune mechanisms, but also other aspects of ischemic injury (*i.e.*: metabolic and oxidative stress). As a final consideration, the described interplay involving microglia, T lymphocytes, astrocytes and neurons is common to many other neural pathological conditions (*e.g.*: multiple sclerosis, Parkinson's disease), therefore, it appears of extreme interest to assess if the herein presented EV-based therapeutic approach may be of any use in such diseases.

Conclusions

The aim of this doctoral project was the development of a stem cell-based albeit cell-free regenerative approach. The ratio behind this choice was to meet the need of a therapeutic strategy matching stem cell regenerative features, without the disadvantages of working with living cells.

For this purpose, multipotent mesenchymal stromal cells (MSCs), which already demonstrated relevant anti-inflammatory, anti-apoptotic and immunomodulatory paracrine properties at the clinical level, were used. Furthermore, giving the high interest arisen around extracellular vesicles (EVs), as cellular secretion products mimicking paracrine properties of parental cell sources, they were chosen as candidate carriers of MSC regenerative information.

In order to isolate MSCs, different cell sources were considered. In line with other reports, MSCs from adult sources (*i.e.*: adipose tissue, bone marrow) were shown to possess senescent-like features (e.g.: IGF1 secretion), compared to MSCs from perinatal sources (*i.e.*: birth-associated tissues). Thus, cord blood (CB) was chosen as MSC source, also in reason of advantages related to the already existing network of banks collecting CB units for clinical purposes. From the dissection of the CB stromal component, a protocol for the isolation of long-living (LL)-CBMSCs was defined, relying on the use of telomere length as predictive parameter of culture outcome. In addition, the feasibility of high efficiency CBMSC isolation rate by an improved procedure was described, solving one major issue in CBMSC clinical translation.

In vitro and *in vivo* anti-inflammatory and anti-apoptotic paracrine properties of LL-CBMSCs were shown in different models of tissue injury. This broad tissue protective mechanism was demonstrated to be rooted on the modulation of inflammation. Specifically, LL-CBMSCs were able to recruit macrophages *in vivo* in an injured tissue and to skew their phenotype to an Arg I-producing anti-inflammatory M2 one. Furthermore, LL-CBMSCs reduced extracellular levels of pro-inflammatory cytokines (*e.g.*: TNFα and INFγ), while increasing those of anti-apoptotic growth factors (*e.g.*: HGF and FGF), after cell acute damage. These were considered crucial features of LL-CBMSCs, as reduced inflammation facilitates tissue regeneration in many pathological contexts. More importantly, LL-CBMSCs were shown to generate EVs capable to recapitulate the parental cell paracrine ability to rescue cell viability after acute damage.

Then, the reprogramming technology was shown to be a feasible engineering solution to immortalize LL-CBMSCs, avoiding permanent modification of the genome caused by integration of viral DNA. In spite of the induction of pluripotency in LL-CBMSCs, thoroughly assessed addressing both stemness and pluripotency features of the generated human induced pluripotent stem cell (hiPSC) lines, the secretion of EVs with characteristics similar to those of the unreprogrammed cells was preserved. Noteworthy, LL-CBMSC-EV miRNome was defined for the first time and it was shown to be largely maintained in hiPSC-EVs, as a novel feature of pluripotent stem cell biology to be further elucidated. Yet, this result was crucial to envision EV therapeutic approaches based on hiPSC-EVs, since miRNAs are, at the present knowledge, central players in EV-mediated mechanisms of action.

Eventually, for the first time stem cell EVs were shown to exert effectively neuroprotection in an organotypic *ex vivo* model of acute brain ischemia, used as a proof-of-concept to challenge the therapeutic potentiality of EVs. The EV-based regenerative approach reduced significantly ischemia-driven tissue necrosis. Remarkably, a major effect was detected for astrocytes, a glial cell type involved in the support of neuronal activity, but also in neural tissue regeneration following injury [231-234].

The mechanism unveiled in this context counteracts brain injury via the modulation of the damaged tissue environment to establish a pro-regenerative milieu. Noteworthy, the *ex vivo* model mimicked very well an early acute brain ischemia inflammatory response. Thus, the therapeutic potential of the developed EV-based treatment in the very first stage of the pathology was assessed.

Going into detail, a previously unreported action of EVs was described on tumor necrosis factor α (TNFα), a pleiotropic peptide involved in inflammation- and immune-related activities, which plays a role not only in ischemia, but also in brain trauma and cerebral infection [207, 212, 213]. In addition, the EV-based treatments targeted also interferon γ, whose capacity to activate innate and adaptive immune responses can act in concert with TNFα to establish chronic inflammation through a positive regulatory loop, also in many other neurological diseases [210, 211, 214-216]. Therefore, a larger area of application for the developed therapeutic approach could be considered, after the mechanism of action is validated also in the other pathological contexts.

Bibliography

1. Nagpal, A., et al., *Stem cell therapy clinical research: A regulatory conundrum for academia.* Adv Drug Deliv Rev, 2016.
2. Ratcliffe, E., et al., *Current status and perspectives on stem cell-based therapies undergoing clinical trials for regenerative medicine: case studies.* Br Med Bull, 2013. **108**: p. 73-94.
3. Ho, A.D., W. Wagner, and W. Franke, *Heterogeneity of mesenchymal stromal cell preparations.* Cytotherapy, 2008. **10**(4): p. 320-30.
4. Jones, E. and R. Schafer, *Where is the common ground between bone marrow mesenchymal stem/stromal cells from different donors and species?* Stem Cell Res Ther, 2015. **6**: p. 143.
5. Phinney, D.G., *Functional heterogeneity of mesenchymal stem cells: implications for cell therapy.* J Cell Biochem, 2012. **113**(9): p. 2806-12.
6. Assoni, A.F., et al., *Different donors Mesenchymal Stromal Cells secretomes reveal heterogeneous profile of relevance for therapeutic use.* Stem Cells Dev, 2016.
7. Sammour, I., et al., *The Effect of Gender on Mesenchymal Stem Cell (MSC) Efficacy in Neonatal Hyperoxia-Induced Lung Injury.* PLoS One, 2016. **11**(10): p. e0164269.
8. Morigi, M., et al., *Life-sparing effect of human cord blood-mesenchymal stem cells in experimental acute kidney injury.* Stem Cells, 2010. **28**(3): p. 513-22.
9. Pierro, M., et al., *Short-term, long-term and paracrine effect of human umbilical cord-derived stem cells in lung injury prevention and repair in experimental bronchopulmonary dysplasia.* Thorax, 2013. **68**(5): p. 475-84.
10. Zanier, E.R., et al., *Human umbilical cord blood mesenchymal stem cells protect mice brain after trauma.* Crit Care Med, 2011. **39**(11): p. 2501-10.
11. Bronckaers, A., et al., *Mesenchymal stem/stromal cells as a pharmacological and therapeutic approach to accelerate angiogenesis.* Pharmacol Ther, 2014. **143**(2): p. 181-96.
12. Ho, M.S., S.H. Mei, and D.J. Stewart, *The Immunomodulatory and Therapeutic Effects of Mesenchymal Stromal Cells for Acute Lung Injury*

and Sepsis. J Cell Physiol, 2015. **230**(11): p. 2606-17.

13. Teixeira, F.G., et al., *Mesenchymal stem cells secretome: a new paradigm for central nervous system regeneration?* Cell Mol Life Sci, 2013. **70**(20): p. 3871-82.
14. Bruno, S., M.C. Deregibus, and G. Camussi, *The secretome of mesenchymal stromal cells: Role of extracellular vesicles in immunomodulation.* Immunol Lett, 2015. **168**(2): p. 154-8.
15. Konala, V.B., et al., *The current landscape of the mesenchymal stromal cell secretome: A new paradigm for cell-free regeneration.* Cytotherapy, 2016. **18**(1): p. 13-24.
16. Merino-Gonzalez, C., et al., *Mesenchymal Stem Cell-Derived Extracellular Vesicles Promote Angiogenesis: Potencial Clinical Application.* Front Physiol, 2016. **7**: p. 24.
17. Mason, C. and P. Dunnill, *A brief definition of regenerative medicine.* Regen Med, 2008. **3**(1): p. 1-5.
18. Kaiser, L.R., *The future of multihospital systems.* Top Health Care Financ, 1992. **18**(4): p. 32-45.
19. Satoh, A., K. Mitogawa, and A. Makanae, *Regeneration inducers in limb regeneration.* Dev Growth Differ, 2015. **57**(6): p. 421-9.
20. Rosenthal, L.J., M.A. Reiner, and M.A. Bleicher, *Nonoperative management of distal fingertip amputations in children.* Pediatrics, 1979. **64**(1): p. 1-3.
21. Huppert, S.S. and K.M. Campbell, *Emerging advancements in liver regeneration and organogenesis as tools for liver replacement.* Curr Opin Organ Transplant, 2016. **21**(6): p. 581-587.
22. Pearce, K.F., et al., *Regulation of advanced therapy medicinal products in Europe and the role of academia.* Cytotherapy, 2014. **16**(3): p. 289-97.
23. Zhao, K., et al., *Immunomodulation effects of mesenchymal stromal cells on acute graft-versus-host disease after hematopoietic stem cell transplantation.* Biol Blood Marrow Transplant, 2015. **21**(1): p. 97-104.
24. HoWangYin, K.Y., et al., *HIF-prolyl hydroxylase 2 inhibition enhances the efficiency of mesenchymal stem cell-based therapies for the treatment of critical limb ischemia.* Stem Cells, 2014. **32**(1): p. 231-43.
25. Kwon, S., et al., *Anti-apoptotic Effects of Human Wharton's Jelly-derived Mesenchymal Stem Cells on Skeletal Muscle Cells Mediated via Secretion*

of XCL1. Mol Ther, 2016. **24**(9): p. 1550-60.

26. Wang, P., et al., *Effects and safety of allogenic mesenchymal stem cell intravenous infusion in active ankylosing spondylitis patients who failed NSAIDs: a 20-week clinical trial.* Cell Transplant, 2014. **23**(10): p. 1293-303.
27. Phinney, D.G. and D.J. Prockop, *Concise review: mesenchymal stem/multipotent stromal cells: the state of transdifferentiation and modes of tissue repair--current views.* Stem Cells, 2007. **25**(11): p. 2896-902.
28. Bianco, P., *Reply to MSCs: science and trials.* Nat Med, 2013. **19**(7): p. 813-4.
29. Bianco, P., *"Mesenchymal" stem cells.* Annu Rev Cell Dev Biol, 2014. **30**: p. 677-704.
30. Bianco, P., et al., *The meaning, the sense and the significance: translating the science of mesenchymal stem cells into medicine.* Nat Med, 2013. **19**(1): p. 35-42.
31. Mastri, M., H. Lin, and T. Lee, *Enhancing the efficacy of mesenchymal stem cell therapy.* World J Stem Cells, 2014. **6**(2): p. 82-93.
32. Rizk, M., et al., *Heterogeneity in Studies of Mesenchymal Stromal Cells to Treat or Prevent Graft-versus-Host Disease: A Scoping Review of the Evidence.* Biol Blood Marrow Transplant, 2016. **22**(8): p. 1416-23.
33. Rani, S., et al., *Mesenchymal Stem Cell-derived Extracellular Vesicles: Toward Cell-free Therapeutic Applications.* Mol Ther, 2015. **23**(5): p. 812-23.
34. Yanez-Mo, M., et al., *Biological properties of extracellular vesicles and their physiological functions.* J Extracell Vesicles, 2015. **4**: p. 27066.
35. Owen, M. and A.J. Friedenstein, *Stromal stem cells: marrow-derived osteogenic precursors.* Ciba Found Symp, 1988. **136**: p. 42-60.
36. Thomson, J.A., et al., *Embryonic stem cell lines derived from human blastocysts.* Science, 1998. **282**(5391): p. 1145-7.
37. Lalu, M.M., et al., *Efficacy and safety of mesenchymal stromal cells in preclinical models of acute lung injury: a systematic review protocol.* Syst Rev, 2014. **3**: p. 48.
38. Klimczak, A. and U. Kozlowska, *Mesenchymal Stromal Cells and Tissue-Specific Progenitor Cells: Their Role in Tissue Homeostasis.* Stem Cells Int, 2016. **2016**: p. 4285215.

39. Crisan, M., et al., *A perivascular origin for mesenchymal stem cells in multiple human organs.* Cell Stem Cell, 2008. **3**(3): p. 301-13.
40. Ramsauer, M., D. Krause, and R. Dermietzel, *Angiogenesis of the blood-brain barrier in vitro and the function of cerebral pericytes.* Faseb j, 2002. **16**(10): p. 1274-6.
41. Daneman, R., et al., *Pericytes are required for blood-brain barrier integrity during embryogenesis.* Nature, 2010. **468**(7323): p. 562-6.
42. Murray, I.R., et al., *Skeletal and cardiac muscle pericytes: Functions and therapeutic potential.* Pharmacol Ther, 2016.
43. Bunnell, B.A., et al., *Adipose-derived stem cells: isolation, expansion and differentiation.* Methods, 2008. **45**(2): p. 115-20.
44. Erices, A., P. Conget, and J.J. Minguell, *Mesenchymal progenitor cells in human umbilical cord blood.* Br J Haematol, 2000. **109**(1): p. 235-42.
45. Seshareddy, K., D. Troyer, and M.L. Weiss, *Method to isolate mesenchymal-like cells from Wharton's Jelly of umbilical cord.* Methods Cell Biol, 2008. **86**: p. 101-19.
46. Bajek, A., et al., *Does aging of mesenchymal stem cells limit their potential application in clinical practice?* Aging Clin Exp Res, 2012. **24**(5): p. 404-11.
47. Qi, X., et al., *Exosomes Secreted by Human-Induced Pluripotent Stem Cell-Derived Mesenchymal Stem Cells Repair Critical-Sized Bone Defects through Enhanced Angiogenesis and Osteogenesis in Osteoporotic Rats.* Int J Biol Sci, 2016. **12**(7): p. 836-49.
48. Zhang, B., et al., *Mesenchymal stem cells secrete immunologically active exosomes.* Stem Cells Dev, 2014. **23**(11): p. 1233-44.
49. Caron, I., et al., *A new three dimensional biomimetic hydrogel to deliver factors secreted by human mesenchymal stem cells in spinal cord injury.* Biomaterials, 2016. **75**: p. 135-47.
50. Timmers, L., et al., *Reduction of myocardial infarct size by human mesenchymal stem cell conditioned medium.* Stem Cell Res, 2007. **1**(2): p. 129-37.
51. Lee, R.H., et al., *Intravenous hMSCs improve myocardial infarction in mice because cells embolized in lung are activated to secrete the anti-inflammatory protein TSG-6.* Cell Stem Cell, 2009. **5**(1): p. 54-63.
52. Chargaff, E. and R. West, *The biological significance of the thromboplastic*

protein of blood. J Biol Chem, 1946. **166**(1): p. 189-97.

53. Wolf, P., *The nature and significance of platelet products in human plasma.* Br J Haematol, 1967. **13**(3): p. 269-88.
54. Anderson, H.C., *Vesicles associated with calcification in the matrix of epiphyseal cartilage.* J Cell Biol, 1969. **41**(1): p. 59-72.
55. Dalton, A.J., *Microvesicles and vesicles of multivesicular bodies versus "virus-like" particles.* J Natl Cancer Inst, 1975. **54**(5): p. 1137-48.
56. Ronquist, G., et al., *An Mg2+ and Ca2+-stimulated adenosine triphosphatase in human prostatic fluid: part I.* Andrologia, 1978. **10**(4): p. 261-72.
57. Taylor, D.D., H.D. Homesley, and G.J. Doellgast, *Binding of specific peroxidase-labeled antibody to placental-type phosphatase on tumor-derived membrane fragments.* Cancer Res, 1980. **40**(11): p. 4064-9.
58. Harding, C., J. Heuser, and P. Stahl, *Endocytosis and intracellular processing of transferrin and colloidal gold-transferrin in rat reticulocytes: demonstration of a pathway for receptor shedding.* Eur J Cell Biol, 1984. **35**(2): p. 256-63.
59. Raposo, G., et al., *B lymphocytes secrete antigen-presenting vesicles.* J Exp Med, 1996. **183**(3): p. 1161-72.
60. Kalra, H., et al., *Comparative proteomics evaluation of plasma exosome isolation techniques and assessment of the stability of exosomes in normal human blood plasma.* Proteomics, 2013. **13**(22): p. 3354-64.
61. Tauro, B.J., et al., *Comparison of ultracentrifugation, density gradient separation, and immunoaffinity capture methods for isolating human colon cancer cell line LIM1863-derived exosomes.* Methods, 2012. **56**(2): p. 293-304.
62. Colombo, M., G. Raposo, and C. Thery, *Biogenesis, secretion, and intercellular interactions of exosomes and other extracellular vesicles.* Annu Rev Cell Dev Biol, 2014. **30**: p. 255-89.
63. Kalra, H., G.P. Drummen, and S. Mathivanan, *Focus on Extracellular Vesicles: Introducing the Next Small Big Thing.* Int J Mol Sci, 2016. **17**(2): p. 170.
64. Gonzales, P.A., et al., *Large-scale proteomics and phosphoproteomics of urinary exosomes.* J Am Soc Nephrol, 2009. **20**(2): p. 363-79.

65. Jeppesen, D.K., et al., *Quantitative proteomics of fractionated membrane and lumen exosome proteins from isogenic metastatic and nonmetastatic bladder cancer cells reveal differential expression of EMT factors.* Proteomics, 2014. **14**(6): p. 699-712.
66. Ostergaard, O., et al., *Quantitative proteome profiling of normal human circulating microparticles.* J Proteome Res, 2012. **11**(4): p. 2154-63.
67. Escrevente, C., et al., *Interaction and uptake of exosomes by ovarian cancer cells.* BMC Cancer, 2011. **11**: p. 108.
68. Witwer, K.W., et al., *Standardization of sample collection, isolation and analysis methods in extracellular vesicle research.* J Extracell Vesicles, 2013. **2**.
69. Bobrie, A. and C. Thery, *Exosomes and communication between tumours and the immune system: are all exosomes equal?* Biochem Soc Trans, 2013. **41**(1): p. 263-7.
70. Tauro, B.J., et al., *Two distinct populations of exosomes are released from LIM1863 colon carcinoma cell-derived organoids.* Mol Cell Proteomics, 2013. **12**(3): p. 587-98.
71. Colombo, M., et al., *Analysis of ESCRT functions in exosome biogenesis, composition and secretion highlights the heterogeneity of extracellular vesicles.* J Cell Sci, 2013. **126**(Pt 24): p. 5553-65.
72. Aatonen, M.T., et al., *Isolation and characterization of platelet-derived extracellular vesicles.* J Extracell Vesicles, 2014. **3**.
73. Batagov, A.O. and I.V. Kurochkin, *Exosomes secreted by human cells transport largely mRNA fragments that are enriched in the 3'-untranslated regions.* Biol Direct, 2013. **8**: p. 12.
74. Chen, T.S., et al., *Mesenchymal stem cell secretes microparticles enriched in pre-microRNAs.* Nucleic Acids Res, 2010. **38**(1): p. 215-24.
75. Baj-Krzyworzeka, M., et al., *Tumour-derived microvesicles carry several surface determinants and mRNA of tumour cells and transfer some of these determinants to monocytes.* Cancer Immunol Immunother, 2006. **55**(7): p. 808-18.
76. Nazarenko, I., et al., *Cell surface tetraspanin Tspan8 contributes to molecular pathways of exosome-induced endothelial cell activation.* Cancer Res, 2010. **70**(4): p. 1668-78.

77. Perez-Hernandez, D., et al., *The intracellular interactome of tetraspanin-enriched microdomains reveals their function as sorting machineries toward exosomes.* J Biol Chem, 2013. **288**(17): p. 11649-61.
78. Capraro, B.R., et al., *Curvature sensing by the epsin N-terminal homology domain measured on cylindrical lipid membrane tethers.* J Am Chem Soc, 2010. **132**(4): p. 1200-1.
79. Batagov, A.O., V.A. Kuznetsov, and I.V. Kurochkin, *Identification of nucleotide patterns enriched in secreted RNAs as putative cis-acting elements targeting them to exosome nano-vesicles.* BMC Genomics, 2011. **12 Suppl 3**: p. S18.
80. Villarroya-Beltri, C., et al., *Sumoylated hnRNPA2B1 controls the sorting of miRNAs into exosomes through binding to specific motifs.* Nat Commun, 2013. **4**: p. 2980.
81. Heijnen, H.F., et al., *Activated platelets release two types of membrane vesicles: microvesicles by surface shedding and exosomes derived from exocytosis of multivesicular bodies and alpha-granules.* Blood, 1999. **94**(11): p. 3791-9.
82. Escrevente, C., et al., *Sialoglycoproteins and N-glycans from secreted exosomes of ovarian carcinoma cells.* PLoS One, 2013. **8**(10): p. e78631.
83. Looze, C., et al., *Proteomic profiling of human plasma exosomes identifies PPARgamma as an exosome-associated protein.* Biochem Biophys Res Commun, 2009. **378**(3): p. 433-8.
84. Barres, C., et al., *Galectin-5 is bound onto the surface of rat reticulocyte exosomes and modulates vesicle uptake by macrophages.* Blood, 2010. **115**(3): p. 696-705.
85. Batista, B.S., et al., *Identification of a conserved glycan signature for microvesicles.* J Proteome Res, 2011. **10**(10): p. 4624-33.
86. Liang, Y., et al., *Complex N-linked glycans serve as a determinant for exosome/microvesicle cargo recruitment.* J Biol Chem, 2014. **289**(47): p. 32526-37.
87. Menck, K., et al., *Tumor-derived microvesicles mediate human breast cancer invasion through differentially glycosylated EMMPRIN.* J Mol Cell Biol, 2015. **7**(2): p. 143-53.
88. Atai, N.A., et al., *Heparin blocks transfer of extracellular vesicles between*

donor and recipient cells. J Neurooncol, 2013. **115**(3): p. 343-51.

89. Christianson, H.C., et al., *Cancer cell exosomes depend on cell-surface heparan sulfate proteoglycans for their internalization and functional activity.* Proc Natl Acad Sci U S A, 2013. **110**(43): p. 17380-5.
90. Feng, D., et al., *Cellular internalization of exosomes occurs through phagocytosis.* Traffic, 2010. **11**(5): p. 675-87.
91. Fitzner, D., et al., *Selective transfer of exosomes from oligodendrocytes to microglia by macropinocytosis.* J Cell Sci, 2011. **124**(Pt 3): p. 447-58.
92. Morelli, A.E., et al., *Endocytosis, intracellular sorting, and processing of exosomes by dendritic cells.* Blood, 2004. **104**(10): p. 3257-66.
93. Thery, C., M. Ostrowski, and E. Segura, *Membrane vesicles as conveyors of immune responses.* Nat Rev Immunol, 2009. **9**(8): p. 581-93.
94. Laulagnier, K., et al., *PLD2 is enriched on exosomes and its activity is correlated to the release of exosomes.* FEBS Lett, 2004. **572**(1-3): p. 11-4.
95. Laulagnier, K., et al., *Mast cell- and dendritic cell-derived exosomes display a specific lipid composition and an unusual membrane organization.* Biochem J, 2004. **380**(Pt 1): p. 161-71.
96. Parolini, I., et al., *Microenvironmental pH is a key factor for exosome traffic in tumor cells.* J Biol Chem, 2009. **284**(49): p. 34211-22.
97. Subra, C., et al., *Exosome lipidomics unravels lipid sorting at the level of multivesicular bodies.* Biochimie, 2007. **89**(2): p. 205-12.
98. Saunderson, S.C., et al., *CD169 mediates the capture of exosomes in spleen and lymph node.* Blood, 2014. **123**(2): p. 208-16.
99. Hao, S., et al., *Mature dendritic cells pulsed with exosomes stimulate efficient cytotoxic T-lymphocyte responses and antitumour immunity.* Immunology, 2007. **120**(1): p. 90-102.
100. Simons, M. and G. Raposo, *Exosomes--vesicular carriers for intercellular communication.* Curr Opin Cell Biol, 2009. **21**(4): p. 575-81.
101. Nolte-'t Hoen, E.N., et al., *Activated T cells recruit exosomes secreted by dendritic cells via LFA-1.* Blood, 2009. **113**(9): p. 1977-81.
102. Willekens, F.L., et al., *Liver Kupffer cells rapidly remove red blood cell-derived vesicles from the circulation by scavenger receptors.* Blood, 2005. **105**(5): p. 2141-5.
103. Takahashi, Y., et al., *Visualization and in vivo tracking of the exosomes of*

murine melanoma B16-BL6 cells in mice after intravenous injection. J Biotechnol, 2013. **165**(2): p. 77-84.

104. Clayton, A., et al., *Antigen-presenting cell exosomes are protected from complement-mediated lysis by expression of CD55 and CD59.* Eur J Immunol, 2003. **33**(2): p. 522-31.
105. Lener, T., et al., *Applying extracellular vesicles based therapeutics in clinical trials - an ISEV position paper.* J Extracell Vesicles, 2015. **4**: p. 30087.
106. Del Fattore, A., et al., *Immunoregulatory Effects of Mesenchymal Stem Cell-Derived Extracellular Vesicles on T Lymphocytes.* Cell Transplant, 2015. **24**(12): p. 2615-27.
107. Lai, R.C., et al., *Exosome secreted by MSC reduces myocardial ischemia/reperfusion injury.* Stem Cell Res, 2010. **4**(3): p. 214-22.
108. Kilpinen, L., et al., *Extracellular membrane vesicles from umbilical cord blood-derived MSC protect against ischemic acute kidney injury, a feature that is lost after inflammatory conditioning.* J Extracell Vesicles, 2013. **2**.
109. Tetta, C., et al., *The role of microvesicles in tissue repair.* Organogenesis, 2011. **7**(2): p. 105-15.
110. Favaro, E., et al., *Human mesenchymal stem cells and derived extracellular vesicles induce regulatory dendritic cells in type 1 diabetic patients.* Diabetologia, 2016. **59**(2): p. 325-33.
111. De Luca, L., et al., *MiRNAs and piRNAs from bone marrow mesenchymal stem cell extracellular vesicles induce cell survival and inhibit cell differentiation of cord blood hematopoietic stem cells: a new insight in transplantation.* Oncotarget, 2016. **7**(6): p. 6676-92.
112. Xie, H., et al., *Mesenchymal Stem Cell-Derived Microvesicles Support Ex Vivo Expansion of Cord Blood-Derived CD34(+) Cells.* Stem Cells Int, 2016. **2016**: p. 6493241.
113. Gai, C., et al., *Extracellular vesicle-mediated modulation of angiogenesis.* Histol Histopathol, 2016. **31**(4): p. 379-91.
114. Pascucci, L., et al., *Paclitaxel is incorporated by mesenchymal stromal cells and released in exosomes that inhibit in vitro tumor growth: a new approach for drug delivery.* J Control Release, 2014. **192**: p. 262-70.
115. Wen, S., et al., *Mesenchymal stromal cell-derived extracellular vesicles rescue radiation damage to murine marrow hematopoietic cells.* Leukemia,

2016. **30**(11): p. 2221-2231.

116. Doeppner, T.R., et al., *Extracellular Vesicles Improve Post-Stroke Neuroregeneration and Prevent Postischemic Immunosuppression.* Stem Cells Transl Med, 2015. **4**(10): p. 1131-43.
117. Ophelders, D.R., et al., *Mesenchymal Stromal Cell-Derived Extracellular Vesicles Protect the Fetal Brain After Hypoxia-Ischemia.* Stem Cells Transl Med, 2016. **5**(6): p. 754-63.
118. Lee, J.Y., et al., *Microvesicles from brain-extract-treated mesenchymal stem cells improve neurological functions in a rat model of ischemic stroke.* Sci Rep, 2016. **6**: p. 33038.
119. Collino, F., et al., *AKI Recovery Induced by Mesenchymal Stromal Cell-Derived Extracellular Vesicles Carrying MicroRNAs.* J Am Soc Nephrol, 2015. **26**(10): p. 2349-60.
120. Nassar, W., et al., *Umbilical cord mesenchymal stem cells derived extracellular vesicles can safely ameliorate the progression of chronic kidney diseases.* Biomater Res, 2016. **20**: p. 21.
121. Wang, Y., et al., *Influence of erythropoietin on microvesicles derived from mesenchymal stem cells protecting renal function of chronic kidney disease.* Stem Cell Res Ther, 2015. **6**: p. 100.
122. Zhang, G., et al., *Mesenchymal Stromal Cell-Derived Extracellular Vesicles Protect Against Acute Kidney Injury Through Anti-Oxidation by Enhancing Nrf2/ARE Activation in Rats.* Kidney Blood Press Res, 2016. **41**(2): p. 119-28.
123. Gallo, S., et al., *Stem Cell-Derived, microRNA-Carrying Extracellular Vesicles: A Novel Approach to Interfering with Mesangial Cell Collagen Production in a Hyperglycaemic Setting.* PLoS One, 2016. **11**(9): p. e0162417.
124. Yin, G., et al., *Role of Microvesicles From Bone Marrow Mesenchymal Stem Cells in Acute Pancreatitis.* Pancreas, 2016. **45**(9): p. 1282-1293.
125. Monsel, A., et al., *Therapeutic Effects of Human Mesenchymal Stem Cell-derived Microvesicles in Severe Pneumonia in Mice.* Am J Respir Crit Care Med, 2015. **192**(3): p. 324-36.
126. Yu, B., et al., *Exosomes derived from MSCs ameliorate retinal laser injury partially by inhibition of MCP-1.* Sci Rep, 2016. **6**: p. 34562.

127. Nong, K., et al., *Hepatoprotective effect of exosomes from human-induced pluripotent stem cell-derived mesenchymal stromal cells against hepatic ischemia-reperfusion injury in rats.* Cytotherapy, 2016. **18**(12): p. 1548-1559.
128. Suzuki, E., et al., *Stem cell-derived exosomes as a therapeutic tool for cardiovascular disease.* World J Stem Cells, 2016. **8**(9): p. 297-305.
129. Lorincz, A.M., et al., *Effect of storage on physical and functional properties of extracellular vesicles derived from neutrophilic granulocytes.* J Extracell Vesicles, 2014. **3**: p. 25465.
130. Akers, J.C., et al., *Optimizing preservation of extracellular vesicular miRNAs derived from clinical cerebrospinal fluid.* Cancer Biomark, 2016. **17**(2): p. 125-32.
131. Wood, M.J., A.J. O'Loughlin, and L. Samira, *Exosomes and the blood-brain barrier: implications for neurological diseases.* Ther Deliv, 2011. **2**(9): p. 1095-9.
132. Alvarez-Erviti, L., et al., *Delivery of siRNA to the mouse brain by systemic injection of targeted exosomes.* Nat Biotechnol, 2011. **29**(4): p. 341-5.
133. Skog, J., et al., *Glioblastoma microvesicles transport RNA and proteins that promote tumour growth and provide diagnostic biomarkers.* Nat Cell Biol, 2008. **10**(12): p. 1470-6.
134. Liu, L., et al., *From blood to the brain: can systemically transplanted mesenchymal stem cells cross the blood-brain barrier?* Stem Cells Int, 2013. **2013**: p. 435093.
135. Yi, Q., et al., *Analysis of Senescence-Related Differentiation Potentials and Gene Expression Profiles in Human Dental Pulp Stem Cells.* Cells Tissues Organs, 2016.
136. Jin, H.J., et al., *Comparative analysis of human mesenchymal stem cells from bone marrow, adipose tissue, and umbilical cord blood as sources of cell therapy.* Int J Mol Sci, 2013. **14**(9): p. 17986-8001.
137. Yang, H.J., et al., *The stem cell potential and multipotency of human adipose tissue-derived stem cells vary by cell donor and are different from those of other types of stem cells.* Cells Tissues Organs, 2014. **199**(5-6): p. 373-83.
138. Duscher, D., et al., *Aging disrupts cell subpopulation dynamics and*

diminishes the function of mesenchymal stem cells. Sci Rep, 2014. **4**: p. 7144.

139. Wu, L.W., et al., *Donor age negatively affects the immunoregulatory properties of both adipose and bone marrow derived mesenchymal stem cells.* Transpl Immunol, 2014. **30**(4): p. 122-7.
140. Bruna, F., et al., *Regenerative Potential of Mesenchymal Stromal Cells: Age-Related Changes.* Stem Cells Int, 2016. **2016**: p. 1461648.
141. Guillot, P.V., et al., *Human first-trimester fetal MSC express pluripotency markers and grow faster and have longer telomeres than adult MSC.* Stem Cells, 2007. **25**(3): p. 646-54.
142. Choumerianou, D.M., et al., *Comparative study of stemness characteristics of mesenchymal cells from bone marrow of children and adults.* Cytotherapy, 2010. **12**(7): p. 881-7.
143. Siegel, G., et al., *Phenotype, donor age and gender affect function of human bone marrow-derived mesenchymal stromal cells.* BMC Med, 2013. **11**: p. 146.
144. Mattar, P. and K. Bieback, *Comparing the Immunomodulatory Properties of Bone Marrow, Adipose Tissue, and Birth-Associated Tissue Mesenchymal Stromal Cells.* Front Immunol, 2015. **6**: p. 560.
145. Stimpson, K.M., et al., *Nucleolar organization, ribosomal DNA array stability, and acrocentric chromosome integrity are linked to telomere function.* PLoS One, 2014. **9**(3): p. e92432.
146. Feijoo, P., et al., *Telomere-dependent genomic integrity: evolution of the fusion-bridge-breakage cycle concept.* Curr Pharm Des, 2014. **20**(41): p. 6375-85.
147. Bosch, J., et al., *Distinct differentiation potential of "MSC" derived from cord blood and umbilical cord: are cord-derived cells true mesenchymal stromal cells?* Stem Cells Dev, 2012. **21**(11): p. 1977-88.
148. Hass, R., et al., *Different populations and sources of human mesenchymal stem cells (MSC): A comparison of adult and neonatal tissue-derived MSC.* Cell Commun Signal, 2011. **9**: p. 12.
149. Sousa, B.R., et al., *Human adult stem cells from diverse origins: an overview from multiparametric immunophenotyping to clinical applications.* Cytometry A, 2014. **85**(1): p. 43-77.

150. Goridis, C. and J.F. Brunet, *NCAM: structural diversity, function and regulation of expression.* Semin Cell Biol, 1992. **3**(3): p. 189-97.
151. Cuthbert, R.J., et al., *Examining the feasibility of clinical grade CD271+ enrichment of mesenchymal stromal cells for bone regeneration.* PLoS One, 2015. **10**(3): p. e0117855.
152. Ghazanfari, R., et al., *Human Non-hematopoietic CD271pos/CD140alow/neg Bone Marrow Stroma Cells Fulfill Stringent Stem Cell Criteria in Serial Transplantations.* Stem Cells Dev, 2016.
153. Yang, J., M. Anzo, and P. Cohen, *Control of aging and longevity by IGF-I signaling.* Exp Gerontol, 2005. **40**(11): p. 867-72.
154. Taormina, G. and M.G. Mirisola, *Longevity: epigenetic and biomolecular aspects.* Biomol Concepts, 2015. **6**(2): p. 105-17.
155. Hsiao, E.Y. and P.H. Patterson, *Placental regulation of maternal-fetal interactions and brain development.* Dev Neurobiol, 2012. **72**(10): p. 1317-26.
156. Kanda, J., et al., *Impact of graft-versus-host disease on outcomes after unrelated cord blood transplantation.* Leukemia, 2016.
157. Lee, M., et al., *Low immunogenicity of allogeneic human umbilical cord blood-derived mesenchymal stem cells in vitro and in vivo.* Biochem Biophys Res Commun, 2014. **446**(4): p. 983-9.
158. Bieback, K., et al., *Critical parameters for the isolation of mesenchymal stem cells from umbilical cord blood.* Stem Cells, 2004. **22**(4): p. 625-34.
159. Zhang, X., et al., *Isolation and characterization of mesenchymal stem cells from human umbilical cord blood: reevaluation of critical factors for successful isolation and high ability to proliferate and differentiate to chondrocytes as compared to mesenchymal stem cells from bone marrow and adipose tissue.* J Cell Biochem, 2011. **112**(4): p. 1206-18.
160. Markov, V., et al., *Identification of cord blood-derived mesenchymal stem/stromal cell populations with distinct growth kinetics, differentiation potentials, and gene expression profiles.* Stem Cells Dev, 2007. **16**(1): p. 53-73.
161. Chang, Y.J., et al., *Characterization of two populations of mesenchymal progenitor cells in umbilical cord blood.* Cell Biol Int, 2006. **30**(6): p. 495-9.
162. Kogler, G., et al., *A new human somatic stem cell from placental cord blood*

with intrinsic pluripotent differentiation potential. J Exp Med, 2004. **200**(2): p. 123-35.

163. Sun, H.P., et al., *Human umbilical cord blood-derived stromal cells are superior to human umbilical cord blood-derived mesenchymal stem cells in inducing myeloid lineage differentiation in vitro.* Stem Cells Dev, 2012. **21**(9): p. 1429-40.
164. Laitinen, A. and J. Laine, *Isolation of mesenchymal stem cells from human cord blood.* Curr Protoc Stem Cell Biol, 2007. **Chapter 2**: p. Unit 2A.3.
165. Udagawa, N., et al., *Origin of osteoclasts: mature monocytes and macrophages are capable of differentiating into osteoclasts under a suitable microenvironment prepared by bone marrow-derived stromal cells.* Proc Natl Acad Sci U S A, 1990. **87**(18): p. 7260-4.
166. Wagner, W., et al., *Aging and replicative senescence have related effects on human stem and progenitor cells.* PLoS One, 2009. **4**(6): p. e5846.
167. Kern, S., et al., *Comparative analysis of mesenchymal stem cells from bone marrow, umbilical cord blood, or adipose tissue.* Stem Cells, 2006. **24**(5): p. 1294-301.
168. Ragni, E., et al., *Adipogenic potential in human mesenchymal stem cells strictly depends on adult or foetal tissue harvest.* Int J Biochem Cell Biol, 2013. **45**(11): p. 2456-66.
169. Gupta, K., et al., *VEGF prevents apoptosis of human microvascular endothelial cells via opposing effects on MAPK/ERK and SAPK/JNK signaling.* Exp Cell Res, 1999. **247**(2): p. 495-504.
170. Kim, H.R., et al., *FGF-2 inhibits TNF-alpha mediated apoptosis through upregulation of Bcl2-A1 and Bcl-xL in ATDC5 cells.* BMB Rep, 2012. **45**(5): p. 287-92.
171. Xiao, G.H., et al., *Anti-apoptotic signaling by hepatocyte growth factor/Met via the phosphatidylinositol 3-kinase/Akt and mitogen-activated protein kinase pathways.* Proc Natl Acad Sci U S A, 2001. **98**(1): p. 247-52.
172. Ying, W.Z., H.G. Zhang, and P.W. Sanders, *EGF receptor activity modulates apoptosis induced by inhibition of the proteasome of vascular smooth muscle cells.* J Am Soc Nephrol, 2007. **18**(1): p. 131-42.
173. Ekdahl, C.T., et al., *Inflammation is detrimental for neurogenesis in adult brain.* Proc Natl Acad Sci U S A, 2003. **100**(23): p. 13632-7.

174. Fitch, M.T. and J. Silver, *CNS injury, glial scars, and inflammation: Inhibitory extracellular matrices and regeneration failure.* Exp Neurol, 2008. **209**(2): p. 294-301.
175. Monje, M.L., H. Toda, and T.D. Palmer, *Inflammatory blockade restores adult hippocampal neurogenesis.* Science, 2003. **302**(5651): p. 1760-5.
176. Schlaeger, T.M., et al., *A comparison of non-integrating reprogramming methods.* Nat Biotechnol, 2015. **33**(1): p. 58-63.
177. Shu, X. and D. Pei, *The function and regulation of mesenchymal-to-epithelial transition in somatic cell reprogramming.* Curr Opin Genet Dev, 2014. **28**: p. 32-7.
178. Zhan, X., et al., *Cells derived from human umbilical cord blood support the long-term growth of undifferentiated human embryonic stem cells.* Cloning Stem Cells, 2008. **10**(4): p. 513-22.
179. Li, C., et al., *Genetic heterogeneity of induced pluripotent stem cells: results from 24 clones derived from a single C57BL/6 mouse.* PLoS One, 2015. **10**(3): p. e0120585.
180. Stefkova, K., J. Prochazkova, and J. Pachernik, *Alkaline phosphatase in stem cells.* Stem Cells Int, 2015. **2015**: p. 628368.
181. Zaehres, H., et al., *Induction of pluripotency in human cord blood unrestricted somatic stem cells.* Exp Hematol, 2010. **38**(9): p. 809-18, 818.e1-2.
182. Bobis-Wozowicz, S., et al., *Human Induced Pluripotent Stem Cell-Derived Microvesicles Transmit RNAs and Proteins to Recipient Mature Heart Cells Modulating Cell Fate and Behavior.* Stem Cells, 2015. **33**(9): p. 2748-61.
183. Katsman, D., et al., *Embryonic stem cell-derived microvesicles induce gene expression changes in Muller cells of the retina.* PLoS One, 2012. **7**(11): p. e50417.
184. Khan, M., et al., *Embryonic stem cell-derived exosomes promote endogenous repair mechanisms and enhance cardiac function following myocardial infarction.* Circ Res, 2015. **117**(1): p. 52-64.
185. Ratajczak, J., et al., *Embryonic stem cell-derived microvesicles reprogram hematopoietic progenitors: evidence for horizontal transfer of mRNA and protein delivery.* Leukemia, 2006. **20**(5): p. 847-56.
186. Wang, Y., et al., *Exosomes/microvesicles from induced pluripotent stem*

cells deliver cardioprotective miRNAs and prevent cardiomyocyte apoptosis in the ischemic myocardium. Int J Cardiol, 2015. **192**: p. 61-9.

187. Zhou, J., et al., *Characterization of Induced Pluripotent Stem Cell Microvesicle Genesis, Morphology and Pluripotent Content.* Sci Rep, 2016. **6**: p. 19743.
188. Hu, S., et al., *MicroRNA-302 increases reprogramming efficiency via repression of NR2F2.* Stem Cells, 2013. **31**(2): p. 259-68.
189. Liao, B., et al., *MicroRNA cluster 302-367 enhances somatic cell reprogramming by accelerating a mesenchymal-to-epithelial transition.* J Biol Chem, 2011. **286**(19): p. 17359-64.
190. Lipchina, I., L. Studer, and D. Betel, *The expanding role of miR-302-367 in pluripotency and reprogramming.* Cell Cycle, 2012. **11**(8): p. 1517-23.
191. Subramanyam, D., et al., *Multiple targets of miR-302 and miR-372 promote reprogramming of human fibroblasts to induced pluripotent stem cells.* Nat Biotechnol, 2011. **29**(5): p. 443-8.
192. Jevnaker, A.M., et al., *Expression of members of the miRNA17-92 cluster during development and in carcinogenesis.* J Cell Physiol, 2011. **226**(9): p. 2257-66.
193. Kumar, P., et al., *The c-Myc-regulated microRNA-17~92 (miR-17~92) and miR-106a~363 clusters target hCYP19A1 and hGCM1 to inhibit human trophoblast differentiation.* Mol Cell Biol, 2013. **33**(9): p. 1782-96.
194. Mendell, J.T., *miRiad roles for the miR-17-92 cluster in development and disease.* Cell, 2008. **133**(2): p. 217-22.
195. Geiger, A., A. Walker, and E. Nissen, *Human fibrocyte-derived exosomes accelerate wound healing in genetically diabetic mice.* Biochem Biophys Res Commun, 2015. **467**(2): p. 303-9.
196. Huang, K., et al., *MicroRNA-125b regulates osteogenic differentiation of mesenchymal stem cells by targeting Cbfbeta in vitro.* Biochimie, 2014. **102**: p. 47-55.
197. Zhao, W., et al., *MicroRNA-24 Regulates Osteogenic Differentiation via Targeting T-Cell Factor-1.* Int J Mol Sci, 2015. **16**(5): p. 11699-712.
198. Yu, B., et al., *Cardiomyocyte protection by GATA-4 gene engineered mesenchymal stem cells is partially mediated by translocation of miR-221 in microvesicles.* PLoS One, 2013. **8**(8): p. e73304.

199. Miki, T., S.Y. Yasuda, and M. Kahn, *Wnt/beta-catenin signaling in embryonic stem cell self-renewal and somatic cell reprogramming.* Stem Cell Rev, 2011. **7**(4): p. 836-46.
200. Teslaa, T. and M.A. Teitell, *Pluripotent stem cell energy metabolism: an update.* Embo j, 2015. **34**(2): p. 138-53.
201. Minguell, J.J., A. Erices, and P. Conget, *Mesenchymal stem cells.* Exp Biol Med (Maywood), 2001. **226**(6): p. 507-20.
202. Medcalf, R.L., *Plasminogen activation-based thrombolysis for ischaemic stroke: the diversity of targets may demand new approaches.* Curr Drug Targets, 2011. **12**(12): p. 1772-81.
203. Feigin, V.L., et al., *Epidemiology of ischaemic stroke and traumatic brain injury.* Best Pract Res Clin Anaesthesiol, 2010. **24**(4): p. 485-94.
204. Thrift, A.G., et al., *Global stroke statistics.* Int J Stroke, 2016.
205. Berretta, A., Y.C. Tzeng, and A.N. Clarkson, *Post-stroke recovery: the role of activity-dependent release of brain-derived neurotrophic factor.* Expert Rev Neurother, 2014. **14**(11): p. 1335-44.
206. Yang, J.P., H.J. Liu, and X.F. Liu, *VEGF promotes angiogenesis and functional recovery in stroke rats.* J Invest Surg, 2010. **23**(3): p. 149-55.
207. Bokhari, F.A., et al., *TNF-alpha: a risk factor for ischemic stroke.* J Ayub Med Coll Abbottabad, 2014. **26**(2): p. 111-4.
208. Sethu, S. and A.J. Melendez, *New developments on the TNFalpha-mediated signalling pathways.* Biosci Rep, 2011. **31**(1): p. 63-76.
209. Olmos, G. and J. Llado, *Tumor necrosis factor alpha: a link between neuroinflammation and excitotoxicity.* Mediators Inflamm, 2014. **2014**: p. 861231.
210. Mir, M., et al., *Complementary roles of tumor necrosis factor alpha and interferon gamma in inducible microglial nitric oxide generation.* J Neuroimmunol, 2008. **204**(1-2): p. 101-9.
211. Vila-del Sol, V., C. Punzon, and M. Fresno, *IFN-gamma-induced TNF-alpha expression is regulated by interferon regulatory factors 1 and 8 in mouse macrophages.* J Immunol, 2008. **181**(7): p. 4461-70.
212. Francisco, N.M., et al., *TNF-dependent regulation and activation of innate immune cells are essential for host protection against cerebral tuberculosis.* J Neuroinflammation, 2015. **12**: p. 125.

213. Tuttolomondo, A., R. Pecoraro, and A. Pinto, *Studies of selective TNF inhibitors in the treatment of brain injury from stroke and trauma: a review of the evidence to date.* Drug Des Devel Ther, 2014. **8**: p. 2221-38.
214. Belkhelfa, M., et al., *IFN-gamma and TNF-alpha are involved during Alzheimer disease progression and correlate with nitric oxide production: a study in Algerian patients.* J Interferon Cytokine Res, 2014. **34**(11): p. 839-47.
215. Cavalcanti, Y.V., et al., *Role of TNF-Alpha, IFN-Gamma, and IL-10 in the Development of Pulmonary Tuberculosis.* Pulm Med, 2012. **2012**: p. 745483.
216. Munoz-Fernandez, M.A. and M. Fresno, *The role of tumour necrosis factor, interleukin 6, interferon-gamma and inducible nitric oxide synthase in the development and pathology of the nervous system.* Prog Neurobiol, 1998. **56**(3): p. 307-40.
217. Chang, C.P., et al., *Hypoxic preconditioning enhances the therapeutic potential of the secretome from cultured human mesenchymal stem cells in experimental traumatic brain injury.* Clin Sci (Lond), 2013. **124**(3): p. 165-76.
218. Ranganath, S.H., et al., *Controlled Inhibition of the Mesenchymal Stromal Cell Pro-inflammatory Secretome via Microparticle Engineering.* Stem Cell Reports, 2016. **6**(6): p. 926-39.
219. Silva, N.A., et al., *Modulation of bone marrow mesenchymal stem cell secretome by ECM-like hydrogels.* Biochimie, 2013. **95**(12): p. 2314-9.
220. Kuno, R., et al., *Autocrine activation of microglia by tumor necrosis factor-alpha.* J Neuroimmunol, 2005. **162**(1-2): p. 89-96.
221. Taylor, D.L., et al., *Stimulation of microglial metabotropic glutamate receptor mGlu2 triggers tumor necrosis factor alpha-induced neurotoxicity in concert with microglial-derived Fas ligand.* J Neurosci, 2005. **25**(11): p. 2952-64.
222. Pickering, M., D. Cumiskey, and J.J. O'Connor, *Actions of TNF-alpha on glutamatergic synaptic transmission in the central nervous system.* Exp Physiol, 2005. **90**(5): p. 663-70.
223. Jara, J.H., et al., *Tumor necrosis factor alpha stimulates NMDA receptor activity in mouse cortical neurons resulting in ERK-dependent death.* J Neurochem, 2007. **100**(5): p. 1407-20.
224. Bliss, R.M., et al., *Tumor necrosis factor-alpha (TNF-alpha) augments*

AMPA-induced Purkinje neuron toxicity. Brain Res, 2011. **1386**: p. 1-14.

225. Pribiag, H. and D. Stellwagen, *TNF-alpha downregulates inhibitory neurotransmission through protein phosphatase 1-dependent trafficking of GABA(A) receptors.* J Neurosci, 2013. **33**(40): p. 15879-93.
226. Stellwagen, D., et al., *Differential regulation of AMPA receptor and GABA receptor trafficking by tumor necrosis factor-alpha.* J Neurosci, 2005. **25**(12): p. 3219-28.
227. Perez-Capote, K., J. Serratosa, and C. Sola, *Excitotoxic and apoptotic neuronal death induce different patterns of glial activation in vitro.* J Neurochem, 2005. **94**(1): p. 226-37.
228. Ridder, D.A. and M. Schwaninger, *NF-kappaB signaling in cerebral ischemia.* Neuroscience, 2009. **158**(3): p. 995-1006.
229. Li, X. and G.R. Stark, *NFkappaB-dependent signaling pathways.* Exp Hematol, 2002. **30**(4): p. 285-96.
230. Pischiutta, F., et al., *Protection of Brain Injury by Amniotic Mesenchymal Stromal Cell-Secreted Metabolites.* Crit Care Med, 2016. **44**(11): p. e1118-e1131.
231. Abeysinghe, H.C., et al., *Modulating Astrocyte Transition after Stroke to Promote Brain Rescue and Functional Recovery: Emerging Targets Include Rho Kinase.* Int J Mol Sci, 2016. **17**(3): p. 288.
232. Filous, A.R. and J. Silver, *"Targeting astrocytes in CNS injury and disease: A translational research approach".* Prog Neurobiol, 2016. **144**: p. 173-87.
233. Kiray, H., et al., *The multifaceted role of astrocytes in regulating myelination.* Exp Neurol, 2016. **283**(Pt B): p. 541-9.
234. Magnusson, J.P. and J. Frisen, *Stars from the darkest night: unlocking the neurogenic potential of astrocytes in different brain regions.* Development, 2016. **143**(7): p. 1075-86.

Appendix

I. Published literature

a. Dissection of the cord blood stromal component reveals predictive parameters for culture outcome

b. A chemically defined medium-based strategy to efficiently generate clinically relevant cord blood mesenchymal stromal colonies

c. A new three dimensional biomimetic hydrogel to deliver factors secreted by human mesenchymal stem cells in spinal cord injury

d. Angiogenic and anti-inflammatory properties of mesenchymal stem cells from cord blood: soluble factors and extracellular vesicles for cell regeneration

STEM CELLS AND DEVELOPMENT
Volume 24, Number 1, 2015

DOI: 10.1089/scd.2014.0160

Dissection of the Cord Blood Stromal Component Reveals Predictive Parameters for Culture Outcome

Mario Barilani,[1,2] Cristiana Lavazza,[1] Mariele Viganò,[1] Tiziana Montemurro,[1] Valentina Boldrin,[1] Valentina Parazzi,[1] Elisa Montelatici,[1] Mariacristina Crosti,[3] Monica Moro,[3] Rosaria Giordano,[1] and Lorenza Lazzari[1]

In regenerative medicine, human cord blood-derived multipotent mesenchymal stromal cells (CBMSCs) stand out for their biological peculiarities demonstrated in in vitro and in vivo preclinical studies. Here, we present our 9-year experience for the consistent isolation of CBMSCs. Although nearly one CB unit out of two retains the potential to give rise to MSC colonies, only 46% of them can be cultured till low passages ($P \geq 4$), but one-fourth of those reaches even higher passages ($P \geq 8$). Subsequent characterization for morphological, clonal, differentiation, and proliferation properties revealed two divergent CBMSC behaviors. In particular, a cumulative population doublings cut-off (CPD = 15) was identified that undoubtedly distinguishes two growth curves, and different degrees of commitment toward osteogenesis were observed. These data clearly show the existence of at least two distinct CBMSC subsets: one mainly short-living and less proliferative (SL-CBMSCs), the other long-living, with higher growth rate, and, very importantly, with significantly ($P \leq 0.01$) longer telomere (LL-CBMSCs). Moreover, significant differences in the immunoprofile before seeding were found among CB units giving rise to LL-CBMSCs or SL-CBMSCs or showing no colony formation. Finally, all the aforementioned results provided a peculiar and useful set of parameters potentially predictive for CBMSC culture outcome.

Introduction

In the past decades, multipotent mesenchymal stromal cells (MSCs) have been widely studied for their therapeutic properties and have gained a primary role in the field of cell therapy and regenerative medicine (http://clinicaltrials.gov/ct2/results?term=MSC&Search=Search, 03/11/2014). In particular, they have been proposed as a potent tool for the treatment of several diseases characterized by degeneration of affected tissues, but also in other innovative approaches, due to their homing capabilities, immunomodulatory effects, drugstore features, and differentiative potential [1]. These cells were first described in adult tissues [2–4], but in recent years, they have been found in many fetal tissues as well [5–7]. Thus, even if a definition for MSCs has been provided by the International Society for Cellular Therapy (ISCT) [8], this acronym comprises a wide range of cells obtained from various sources that frequently possess different biological characteristics [9–11].

In this context, cord blood-derived multipotent mesenchymal stromal cells (CBMSCs) [6,12] represent a peculiar population since its source is blood and not a solid tissue, and they show higher proliferative capabilities compared with other MSCs [9] and peculiar morphological, differentiative, and trophic properties [13]. Another unique feature of CBMSCs is their low immunogenicity, which makes them suitable for allogenic cell therapies [14–16].

Despite all the promising and intriguing aspects of CBMSCs, translation to the clinic has to face one major obstacle, that is inconsistency of isolation protocols due to the low frequency of these cells in cord blood if compared to other sources [17]. Although a growing number of reports point out experimental and sample conditions for optimal isolation of CBMSCs, the success rate is still controversial and they often require very fresh and abundant cord blood units [18–21]. A further issue that could be related to the low isolation rate is the origin of this stromal population in cord blood. For instance, one of the theories trying to explain the presence of MSCs in various tissues considers pericytes as their direct precursors and a sort of in vivo counterpart [22]. Yet, it is not clear why perivascular cells should abandon their niche and should be circulating in cord blood. In addition, cord blood was reported to give rise to distinct stromal populations in terms of morphology, isolation frequency, proliferation rate, differentiation potentialities, and surface markers [23–26].

[1]Cell Factory, Unit of Cell Therapy and Cryobiology, Fondazione IRCCS Ca' Granda Ospedale Maggiore Policlinico, Milano, Italy.
[2]Department of Industrial Engineering, University of Padova, Padova, Italy.
[3]Istituto Nazionale di Genetica Molecolare (INGM), Milano, Italy.

Starting from these premises, the goal of this work was first of all to summarize our 9-year experience in the field of CBMSCs. Moreover, we wanted to investigate if any parameter existed that could answer to the following questions: do all the CB units have the same potential to produce stromal cells? Does cord blood contain more than one stromal cell population? And finally, can we predict the cultural outcome of cord blood cell samples?

Materials and Methods

Isolation and culture of human cord blood multipotent MSCs

Umbilical cord blood was collected from normal deliveries in a multiple system bag (Machopharma, Mouvax, France) containing 29 mL of citrate phosphate dextrose as anticoagulant. The authors state that this study was performed according to the amended Declaration of Helsinki. In addition, written informed consent has been obtained for all the cord blood units used in the study. Different cell isolation approaches were carried out to obtain CBMSCs. When specified, lysis of red blood cells was performed: an aliquot of sample was diluted 1:9 in lysing buffer 1X (BD Pharm Lyse 10X; BD Biosciences, San Diego, CA), incubated at room temperature for 10 min, and then centrifuged at 1,200 rpm for 8 min. The approaches included:

(a) Samples were seeded as whole blood at 0.5×10^6 total nucleated cells (TNCs)/cm^2.
(b) Alternatively, mononuclear cells (MNCs) from buffy coat were seeded at a density of 0.5×10^6 cells/cm^2. Briefly, whole blood was centrifuged at 1,900 rpm for 15 min, the plasma subsequently discarded, and the buffy coat and a portion of red blood cells collected with a serological pipette, pelleted at 1,200 rpm for 8 min, and resuspended in the complete medium.
(c) Sepax S-100 system (Biosafe, Eysins, Switzerland) was exploited for automated cell separation. CB units were processed directly by the device without external operator manipulation. MNCs were automatically harvested in a bag and subsequently resuspended in the complete medium for seeding at 1×10^6 cells/cm^2.
(d) Another isolation approach was to obtain MSC precursors by immunodepletion using a commercial kit (RosetteSep Mesenchymal Stem Cell enrichment cocktail; StemCell Technologies, Vancouver, BC, Canada) that negatively selects CD3$^+$, CD14$^+$, CD38$^+$, CD19$^+$, glycophorin A, and CD66b$^+$ cells. In summary, we obtained the buffy coat as previously described (b), and the harvested MNCs and a portion of red blood cells were incubated with 50 µL/mL RosetteSep MSC enrichment cocktail for 20 min at room temperature. The sample was then diluted 1:2 with phosphate-buffered saline (PBS; Gibco, Grand Island, NY), ethylenediaminetetraacetic acid (Sigma-Aldrich, St. Louis, MO), and human serum albumin (Kedrion, Lucca, Italy) and separated under standard density gradient conditions (Ficoll Paque Plus 1.077 ± 0.001 g/L; GE Healthcare Europe, Freiburg, Germany). One million cells was collected for the assessment of the immunophenotype, whereas the remaining cells were resuspended in the complete medium and then plated at 1×10^6 cells/cm^2.

The complete medium consisted of alphaMEM-GlutaMAX (Invitrogen, Carlsdad, CA) supplemented with 20% fetal bovine serum (FBS; Biochrom, Berlin, Germany). Cultures were maintained at 37°C in a humidified atmosphere containing 5% CO_2. After 48 h, nonadherent cells were removed and the fresh medium was added; the culture medium was changed every 3 days; nonadherent cells in suspension in the supernatants were collected for immunophenotype assessment. At 80% confluence, the cells were harvested using 25% TrypLE Select 1X (Gibco) and were washed with PBS (Gibco) and subcultured at a concentration of $2–4 \times 10^3$ cells/cm^2. Adherent cells that did not give rise to colonies after 40 days were detached with a scraper and collected for the assessment of the immunophenotype ($n = 10$). Bone marrow-derived (BM) MSCs were obtained as elsewhere reported [27].

Cumulative population doublings

Population doubling (PD) was calculated for each population using the following equation: $PD = \log_{10}(N)/\log_{10}(2)$, where N is the number of cells harvested at the end of the culture/the number of seeded cells. Cumulative PD was calculated adding to the PD of the passage under analysis the PDs of the previous passages.

Morphology analysis

Images of cells in culture were taken with a Nikon Eclipse TS100 microscope. Measurements of the nucleus diameter and of major cell axis ($n = 10$ for each cell type) were acquired and processed with the Media Cybernetics Image-Pro Plus 2 (Media Cybernetics, Rockville, MD). For each cell, the ratio between the two parameters (cell major axis/nucleus diameter) was calculated. This value was considered indicative of cell morphology and used to distinguish more spindle-like cells from those having a more compact shape.

Colony forming unit-fibroblast assay

Two hundred CBMSCs (P4) were plated per 100-mm Petri dish (BD Biosciences) in alphaMEM-GlutaMAX (Invitrogen) supplemented with 20% FBS (Biochrom). Four CBMSCs in duplicate were analyzed [two long-living CBMSCs (LL-CBMSCs) and two short-living CBMSCs (SL-CBMSCs)]. The medium was changed weekly, and after 2 weeks, the cells were washed with PBS (Gibco), fixed with methanol (154903; Sigma-Aldrich), and stained with the carbolic gentian violet solution (Ral diagnostics, Cedex, France). After two washing steps with milliQ-grade water, colonies with diameter bigger than 1–2 mm were counted.

Telomere length assessment

Pellets of CBMSCs at different passages were collected during cell culture and stored at −80°C for subsequent analysis. DNA was extracted with the QIAamp DNA Blood Mini Kit (51104; Qiagen, Hilden, Germany) following the instructions provided. A pool of cells from different CBMSC populations and at different passages was used to build the standard curve by 1:1 serial dilution (100–1.56 ng). Real-time quantitative polymerase chain reaction was performed on a Bio-Rad CFX96 preparing one 96-well plate for telomere and one for single copy reference gene (*36B4*). The experiment outline, the primers, and the reaction mixes were based on the

methodology presented in a recent report [28]. The thermal profile was set up for optimal activity of SsoFast EvaGreen Supermix: enzyme activation at 98°C (30 s), 46 cycles of 95°C (5 s), 54°C (2 min), and a final stage at 62°C (5 s) for telomere assay plate; enzyme activation at 98°C (30 s), 46 cycles of 95°C (5 s), 58°C (1 min), and a final stage at 62°C (5 s) for reference gene assay plate. The analysis of RT data was carried out using Bio-Rad CFX Manager software.

Differentiation into mesodermal lineages and staining of specialized cells

To promote adipogenesis and osteogenesis, commercial media (Lonza, Basel, Switzerland) were used, and the manufacturer's protocols were followed or slightly modified. Five CBMSC populations at different passages (P3–P7) were tested for multipotent differentiative potential.

For adipogenesis, cells were seeded at a density of 2.1×10^4 per cm^2 in alphaMEM-GlutaMAX (Invitrogen) 20% FBS (Biochrom); the medium was changed with fresh one every 2–3 days. When cells reached 100% confluence, three (standard protocol) or five to six (modified protocol) cycles of induction/maintenance were performed; induction step consisted of 7 days in the human MSC adipogenesis induction medium (PT-3102B), with a medium change after 3 days; for the maintenance step, the medium was switched to the human MSC adipogenesis maintenance medium (PT-3102A). The final maintenance cycle lasted 7 days, during which the medium was changed every 2–3 days. Adipogenic differentiation was detected by microscopic observation, and lipid vacuoles were stained with the fresh Oil Red O solution (O0625; Sigma-Aldrich) following the manufacturer's instructions.

For osteogenesis, 3.1×10^3 CBMSC/cm^2 were plated in alphaMEM-GlutaMAX (Invitrogen) plus 20% FBS (Biochrom); the day after the medium was substituted with the human MSC osteogenesis induction medium (PT-3002). The cells were maintained in culture for 3 weeks, with medium changes every 3–4 days.

Calcium deposits were stained with Alizarin Red S (A5533; Sigma-Aldrich). Briefly, cells were washed with PBS (Gibco), fixed for 30 min at 4°C with EtOH (02870-1L-F; Sigma-Aldrich) 70% in water, washed with PBS (Gibco), stained for 15 min at RT with the Alizarin Red S solution, and finally multiple washing steps were performed with PBS (Gibco) putting the cells onto an orbital shaker, until extra staining solution and debris were cleaned out. Images of lipid vacuoles and calcium deposits were acquired on a Nikon Eclipse TS100 microscope.

Gene expression

Isolation of total RNA and real-time quantitative reverse transcription polymerase chain reaction assays for the assessment of adipogenic and osteogenic differentiation were conducted as previously reported [29]. The following primers were used:

FW 5′-CATTCCATTCACAAGAACAGAT-3′, RV 5′-GGCTTATTGTAGAGCTGAGT-3′ (*PPARG*); FW 5′-GGAGCAGTGGGTGCTGAG-3′, RV 5′-AGCTGTAGCAGCAGGAGGTC-3′ (*CFD*); FW 5′-GCTACAGACGAGGACATC-3′, RV 5′-ATATAATCTGGACTGCTTGTG-3′ (*OPN*); FW 5′-TACAAGGTGGTGGGCGGTGAACGA-3′, RV 5′-TGGCGCAGGGGCACAGCAGAC-3′ (*ALP*); FW 5′-CGGAAGACCCCAGTCCAGATCCA-3′, RV 5′-TGCCCTCGGGAGACCTGCAA-3′ (*THY1*); FW 5′-TGTGGGCTCCAAGCAGATGCA-3′, RV 5′-GCAGCAGTTTCTCCAGAGCTGGG-3′ (*RPLP0*); FW 5′-CATAGGAAGCTGGGAGCAAG-3′, RV 5′-GCCCTCCAATCAGTCTTCTG-3′ (*RPL13alpha*); FW 5′-GCCACGCCAGCTTCGGAGAG-3′, RV 5′-CCGCAGCAAACCGCTTGGGA-3′ (*TBP*); FW 5′-CCGCTGGTGATGACAAGAAAGGGAT-3′, RV 5′-AGGGCCAGACCCAGTCTGATAGGA-3′ (*YHWAZ*).

Flow cytometry

The previously described collected cell samples were characterized by flow cytometry. A total of three CB immunodepleted buffy coat samples for each possible cell culture outcome were analyzed, and at least three measurements per marker were taken for each sample. Cells were washed with PBS (Gibco), centrifuged at 1,200 rpm for 8 min, and resuspended in PBS (Gibco) plus 2% FBS (Biochrom) or washed in PBS (Gibco) for 20 min at RT and then incubated in the dark with the following mixes of directly coupled mouse anti-human fluorochrome-conjugated antibodies: CD45-FITC (21270453X2; Miltenyi Biotec, Bergisch Gladbach, Germany), CD73-PE (550257; BD Biosciences), CD34-PE-Cy5 (A07777; Beckman Coulter, Brea, CA), CD117-PE-Cy7 (PNIM3698; Beckman Coulter), CD90-APC (559869; BD Biosciences), CD146-APC-Cy7 (5050-B100T; BioCytex, Marseille, France), CD105-Pacific Blue (PB298T100; Exbio, Vestec, Czech Republic) for the first mix; CD31-FITC (555445; BD Biosciences), CD144-PE (PNA07481; Beckman Coulter), CD34-PE-Cy5 (Beckman Coulter), CD117-PE-Cy7 (Beckman Coulter), CD133-APC (130-092-880; Miltenyi Biotec), CD146-APC-Cy7 (BioCytex), CD45-Pacific Blue (130092880; Miltenyi Biotec) for the second mix; alphaSMA-FITC (F3777; Sigma-Aldrich), PDGFRB-PE (FAB1263P; R&D System, Minneapolis, MN), CD90-PE-Cy5 (PNIM3703; Beckman Coulter), CD34-PE-Cy7 (A21691; Beckman Coulter), CD45-APC (21270456X2; ImmunoTools, Friesoythe, Germany), CD146-APC-Cy7 (BioCytex), CD105-Pacific Blue (Exbio) for the third mix; NG2-PE (PNIM3454U; Beckman Coulter), CD56-PE-Cy5 (555517; BD Biosciences), CD117-PE-Cy7 (Beckman Coulter), CD133-APC (Miltenyi Biotec), CD146-APC-Cy7 (BioCytex), CD45-Pacific Blue (Miltenyi Biotec) for the fourth mix; CD31-FITC (BD Biosciences), CD146-APC-Cy7 (BioCytex), CD45-Pacific Blue (Miltenyi Biotec) for the fifth mix. After staining, the cells were washed once with PBS (Gibco) containing 0.1% bovine serum albumin (Kedrion). At least 100,000 events were acquired with a FACSCanto II (BD Biosciences), and isotype-matched mouse immunoglobulins were used as controls under the same conditions. Plots of CD45- cells were generated using FlowJo analysis software v8.8.7 (Tree Star, Ashland, OR).

Statistical analysis

A normality test based on Z-score formula (www.seeingstatistics.com, 03/11/2014) was used to calculate the probability for every data set to be normally distributed. The Student's *t*-test was applied to compare means (www.graphpad.com, 03/11/2014) only for groups with an assessed probability of $\geq 70\%$.

Results and Discussion

During the past 9 years, the R&D section of our facility (Cell Factory ''Franco Calori'') has been extensively investigating and setting up protocols for efficient isolation, culture, and characterization of stromal cells from cord blood, given the large availability of discarded CB units not matching the requirements for transplantation purposes at the affiliated Milano Cord Blood Bank (MICB). In addition, cord blood is widely recognized as hematopoietic stem/progenitor source and the possible identification of CB stromal cells of mesodermal origin is an intriguing issue to address. Extensive characterization of MSCs obtained from CB as multipotent cells, including trilineage differentiation, immunophenotyping, and hematopoietic support, has been performed by various research groups [13].

A total of 264 CB samples were processed. Units were not manipulated if the time from delivery to sample collection was greater than 48 h. In the event of hemolysis or the presence of clots detected during any step of the isolation protocol, the procedure was not completed and the sample not included in the study. Importantly, to evaluate whether we had successfully processed a cord blood unit, we considered the appearance of colonies composed by at least 10 fibroblastic-like cells as the positive event, in accordance to previous studies [18]. This standard was adopted to facilitate the assessment of colony formation within the context of CB primary cell cultures, characterized by a mixed cell environment as described below.

Definition of a standard protocol for the isolation of stromal cells from human cord blood

In a first step of our study, three isolation strategies were implemented and 25 CB units were processed. We obtained some initial encouraging results but with a quite low rate of successful events. Nonetheless, we observed colony formation from unprocessed whole blood (2 positive events out of 10 processed units), untreated MNCs from buffy coat (3 out of 9), and Sepax-separated cord blood cells (1 out of 6). In five experiments with whole blood and four with buffy coat, we investigated if red blood cell lysis could be useful to improve MSC attachment [26,30]. In our case, the lysis did not facilitate the appearance of colonies as none of the isolations presented a positive result. It is possible that the treatment and subsequent centrifugations caused loss of crucial progenitor cells.

After these preliminary results, we adopted a fourth methodological approach consisting of the immunodepletion of nonmesenchymal populations from CB buffy coat. The ratio behind this choice was again to eliminate adherent and nonadherent ''contaminant'' cell types, which could make more difficult for a stromal progenitor cell to attach to the culture surface and to form a colony [21,30]. Among the adherent portion of ''contaminant'' cells, we observed spindle-shaped cells with short stretched extensions and osteoclast-like cells with very large cytoplasm, frequently showing more than one nuclei (Fig. 1A, B).

Isolation efficiency of stromal clones and establishment of primary culture

In the second group of experiments, 243 CB units were processed, obtaining colonies of stromal cells in nearly 40% of them (Fig. 1C). The appearance of colonies occurred with a median of 16 days after seeding, from a minimum of 4 days to a maximum of 64. The majority of them (90%) were detected within 4 weeks from seeding. It is worth noting that clones appeared after 40 days represented only 2% of total

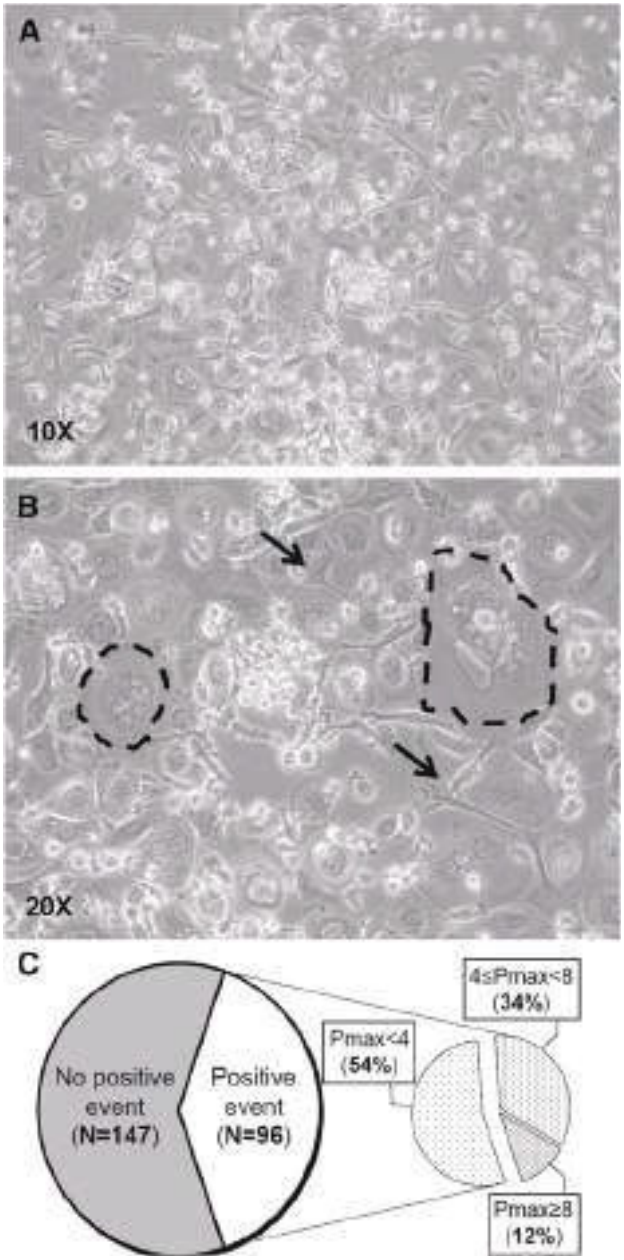

FIG. 1. Establishment of CBMSC cell cultures. In T0 culture, it is frequent to observe adherent cells showing different morphologies that we do not recognize as MSCs **(A)**. Among them, **(B)** nonproliferating fibroblast-like cells (indicated by *arrows*) and polynucleated (two to seven distinguishable nuclei) cells with a very large cytoplasm (*dashed circles*). **(C)** The *pie chart at the left* represents total isolation experiments relying on immunodepletion of nonmesenchymal cells; the *right pie chart* summarizes culture outcomes of CB units that gave rise to primary colonies of stromal cells (positive events). CBMSCs, cord blood-derived multipotent mesenchymal stromal cells; MSCs, mesenchymal stromal cells.

colonies and that they were not able to reach confluence at passage 1. Therefore, after these considerations, we defined 40 days as the detection time of colony appearance; adherent cells from CB cultures exceeding this detection time were used for the immunophenotype characterization. Notably, even if the morphology of the cells forming the colonies was fibroblastic-like and similar to that of bone marrow MSCs, CBMSCs were smaller and less spindle shaped. Upon appearance of a colony, we chose not to wait till high confluence before the first trypsinization in order not to cause stress to the ''newly born'' cells but to detach the cells when still actively dividing. Thus, the first passage came after a median of 22 days after seeding, approximately a week after the detection of the colony; CBMSC morphology is shown in Fig. 2A.

To pass subconfluent cells once a week, we fixed optimal seeding density from 2,000 to 4,000 cells/cm^2. In addition, we observed that during the first trypsinization, a good portion of osteoclast-like cells remained attached to the plastic surface, showing spiky cytoplasm extroflessions. Thus, it is recommended to perform the first passage in a gentle manner in order not to detach unwished cells and favor the formation of as homogeneous as possible stromal populations. In fact, it is also important to underline that especially during the first passages (P1–P3) stromal cells present a high degree of heterogeneity [31,32]. Therefore, it is possible that a stochastic selection of a certain subset among this mixed population could alter the outcome of the long-term culture. As a consequence, cell suspensions should be handled with great attention to maintain them homogeneous, without altering their supposedly mixed composition.

Long-term follow-up of CBMSC populations

Focusing on long-term CBMSC culture, we obtained the most interesting and challenging results (Fig. 1C). Even if about 46% of clones gave rise to CBMSC populations that could reach at least passage 4, among them only one-fourth went on growing till, or beyond, passage 8 before entering a senescent state and arresting proliferation. More interestingly, we could visualize two main types of growth curves: the first one having higher CPD values, over 15 and in few cases more than 30 (Fig. 2C); the second one with lower CPD peaks (≤ 15) (Fig. 2D). The two groups start changing their growth trend around passage 5, after which cell populations belonging to the second group tend to reach plateau (Fig. 2D). These two behaviors in fact correlate in a certain extent with longevity

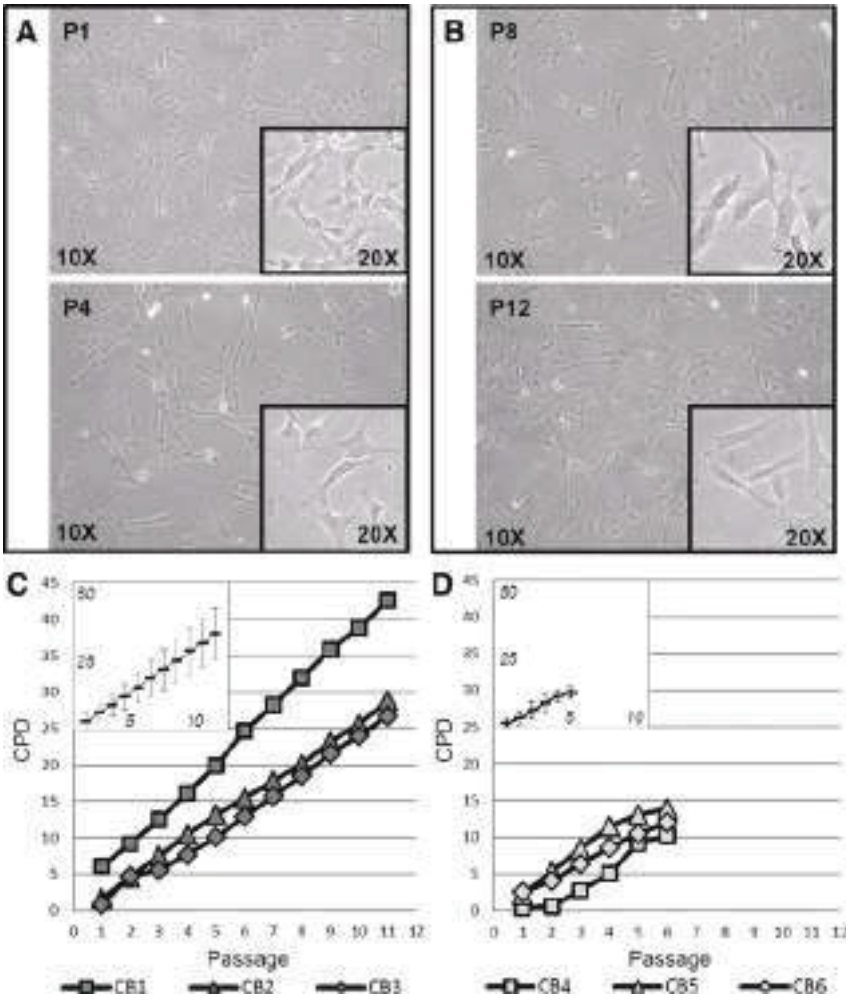

FIG. 2. CBMSC morphology and growth kinetics. Adherent and proliferative cells isolated from processed CB units possess distinct morphology and cell shape. The images were taken from a representative CBMSC population and show subconfluent cells at early passages (P1, P4; **A**) and in long-term culture (P8, P12; **B**) at the indicated magnitudes. Representative growth trends of CBMSCs grouped by similar CPD values (*vertical axis*) and longevity (*horizontal axis*) are presented in (**C, D**). In the *boxes*, the means (*black rectangle*) and deviation standards (*vertical bars*) of CPDs for each passage are also shown. The values obtained fitted almost perfectly with a linear function in the case of LL-CBMSCs ($y = 3.0x - 0.3$), whereas in the case of SL-CBMSCs, the growth was slower at the beginning and the arrest was gradual starting from the last passages, so that the mean CPD values better fitted a polynomial curve ($y = -0.1x^3 + 1.1x^2 - 0.9x + 1.6$). CPD, cumulative population doublings cut-off; LL-CBMSCs, long-living CBMSCs; SL-CBMSCs, short-living CBMSCs.

and, in general, with ''young'' or nonstressed phenotype after long-term cell culture. Specifically, all the populations of the first group, which we decided to refer to as LL-CBMSCs, possess a healthy and prevalently nonsenescent morphology till high passages (P8 or over, till P13), as shown in Fig. 2B. In contrast, stromal populations showing lower CPD values, which we named SL-CBMSCs, arrest their growth around passage 5.

Unlike bone marrow MSCs, for which donor age heavily influence their growth and stemness properties [33,34], those isolated from cord blood are all of fetal, or neonatal, origin. Thus, the differences between LL-CBMSCs and SL-CBMSCs cannot be explained in terms of donor age, whereas a likely possibility is that the two represent indeed distinct stromal populations.

Biological characterization of LL-CBMSCs and SL-CBMSCs: morphology, cloning properties, and telomere length

Since we noted differences in cell shape during cell culture, we wondered if we could distinguish the different cell types by means of morphology parameters. We performed a comparative analysis between BMMSCs and CBMSCs that after long-term culture were recognized as LL-CBMSCs or SL-CBMSCs. Two parameters, cell major axis and nucleus diameter, were measured using images of the cultures at passage 4. This retrospective analysis revealed that CBMSCs present lower cell major axis/nucleus diameter ratio compared with BMMSCs and that within CBMSC populations LL-CBMSCs are the cells with the lowest value (Fig. 3A–D).

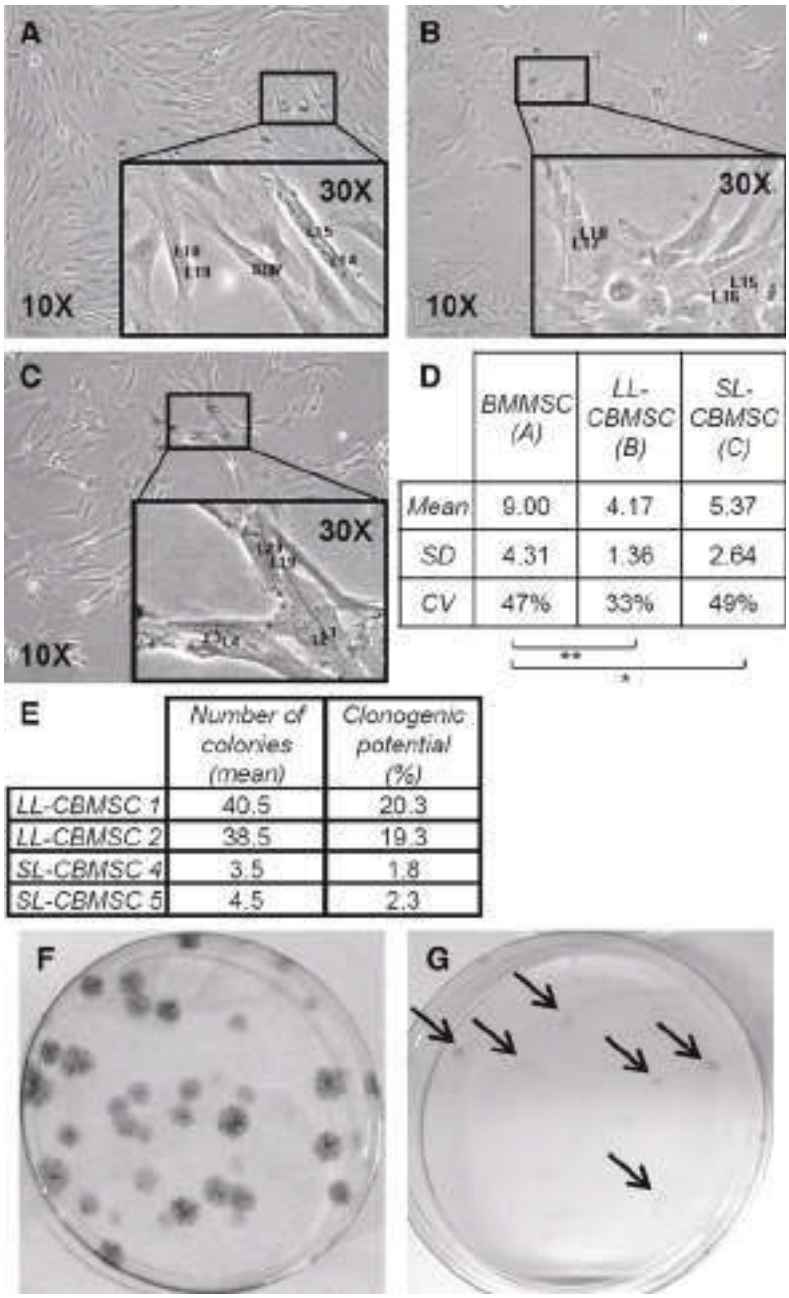

FIG. 3. Cell shape comparison and clonogenic properties. Panels **(A)**, **(B),** and **(C)** and magnified areas (*black rectangles*) represent some MSC morphologies at passage 4. BMMSCs **(A)** possess significantly higher cell major axis/nucleus diameter ratio compared with LL-CBMSCs **(B)** and SL-CBMSCs **(C)** **(D**, see table for mean values). LL-CBMSCs compared to SL-CBMSCs seem to have a lower ratio even if no statistical significance was found. **(E)** Table summarizes the mean number of colonies (CFU-Fs) and related clonogenic potential (percentage of clonogenic cells) for two LL-CBMSC and two SL-CBMSC populations at passage 4. **(F, G)** Images of LL-CBMSC- and SL-CBMSC-derived CFU-Fs, respectively. LL-CBMSC colonies are bigger and more easily detectable compared to SL-CBMSCs, whose colonies are very small and difficult to detect (indicated by *arrows*). $*P \leq 0.05$; $**P \leq 0.01$. CFU-Fs, colony forming unit-fibroblasts.

In addition, the coefficient of variation (relative standard deviation) for calculated ratios in the case of LL-CBMSCs (33%) is the lowest, indicating that they are a more homogeneous population in terms of morphology characteristics if compared with SL-CBMSCs (49%) and BMMSCs (47%).

Concerning heterogeneity of MSC populations, we wondered if established LL-CBMSCs and SL-CBMSCs could also present differences in the clonogenic progenitor content. A retrospective analysis of colony forming unit-fibroblast assay data was performed to address this issue, and indeed, a strong difference in terms of number and morphology of colonies was observed: LL-CBMSCs retained a higher clonogenic potential, whereas SL-CBMSCs almost lacked it (Fig. 3, table E). In addition, colonies from LL-CBMSC populations covered larger areas and the cell density was clearly higher so that they were easily detected and counted (Fig. 3F, G).

From the observation that one major difference between LL-CBMSCs and SL-CBMSCs is lifespan, and since lifespan is related to telomere length [35], we investigated if longer telomeres could be a feature of LL-CBMSCs compared with SL-CBMSCs. Our results showed that passage 1 LL-CBMSCs possess telomeres that can be even 12 times longer than those of SL-CBMSCs (Fig. 4A). This significantly superior telomere length is shortened by a half during the first passage, whereas shorter SL-CBMSC telomeres do not change drastically their length during cell culture. Moreover, LL-CBMSC telomere length decreases gradually through various passages, and only at high passages becomes comparable to that of low passage SL-CBMSCs (Fig. 4A). Thus, telomere length could be a useful parameter to predict the culture outcome of a passage 1 CBMSC population. A longer telomere will indicate the probable establishment of LL-CBMSCs, whereas from a short telomere, SL-CBMSCs derivation is to be expected.

Differentiation into adipocytes and osteocytes

Previous reports [24,25,36] described differences in adipogenic and osteogenic potentials for distinct CB stromal populations. To verify if this could also distinguish LL-CBMSCs from SL-CBMSCs, both populations were induced to differentiate into mesodermal mature cells.

Adipogenic differentiation induced by the standard protocol failed to produce large fat deposits, with very few cells showing little cytoplasmic droplets (data not shown). Instead, following a modified protocol, lipid vacuoles began to appear between 3 and 4 weeks; nonetheless, also in this case, only few CBMSCs presented large Oil Red O-positive deposits, even if molecular analysis confirmed the presence of adipocytes in the culture (Fig. 4B). These experimental tricks may suggest that CBMSCs are less prone than MSCs from other sources to give rise to adipose tissue-differentiated cell types. In this regard, differences at molecular level between CBMSCs and BMMSCs that explain this behavior during adipogenic induction have been recently elucidated [10]. CBMSCs could lack in some measure adipogenic potential or either their being ''fetal'' cells implies also a more immature state that necessitates longer or ad hoc differentiation protocols. It has been proposed that *DLK1*, a gene encoding a protein involved in adipogenesis, could act as a molecular marker distinguishing CBMSCs from unrestricted somatic stem cells (USSCs) [36]. In this model, *DLK1* is highly expressed in USSCs, inhibiting differentiation into adipocytes and correlating to high proliferative potential

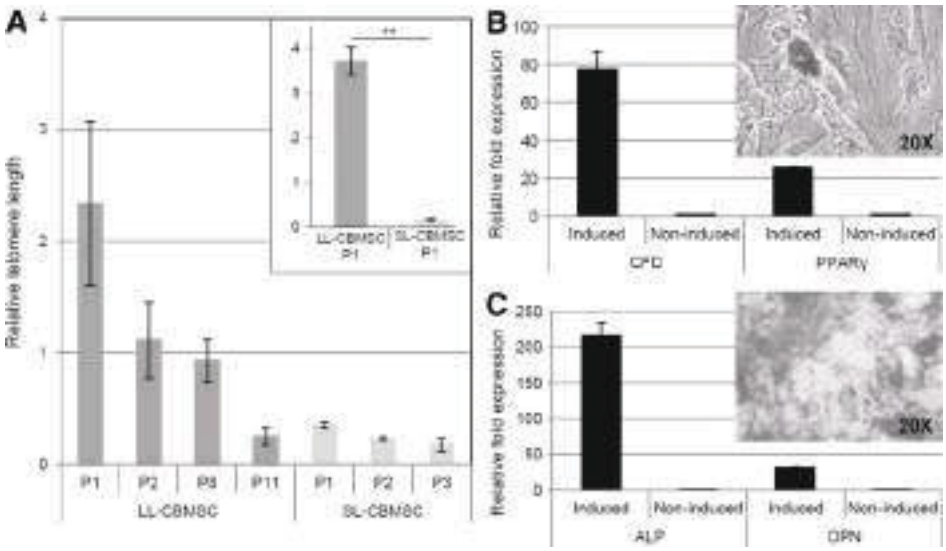

FIG. 4. Mean telomere length at different passages for three LL-CBMSCs and three SL-CBMSCs with related SEM values (*black bars*) is shown in **(A)**. In the *box*, representative passage 1 LL-CBMSCs and SL-CBMSCs show dramatic differences in telomere length (standard deviation represented with *black bars*). Differentiation properties of a representative CBMSC population are shown in **(B, C)**. Oil Red O solution stains lipid vacuoles of mature adipocytes **(B)**; Alizarin Red S stains calcium deposits produced by CBMSC-derived osteocytes **(C)**. Molecular data confirmed the differentiation of induced compared with noninduced CBMSCs: increased expression of *CFD* (78-folds) and *PPARgamma* (26-folds) (housekeeping genes: *TBP* and *YHWAZ*) for adipogenesis **(B)**, whereas high expression levels of *ALP* (216-folds) and *OPN* (32-folds) genes (house-keeping genes: *RPLP0* and *RPL13alpha*) assessed osteogenic differentiation **(C)**. Standard deviation represented with *black bars* when visible. $^{**}P \leq 0.01$.

compared to less proliferative and adipogenesis-competent CBMSCs, for which *DLK1* is less expressed or absent. We also analyzed this gene and found variability in relative expression between different batches of CBMSCs, even if with C_t values not reliable (>36), but no consistent differences were observed between SL- and LL-CBMSCs (data not shown). Moreover, we did not detect any major difference in adipogenic potential between CBMSCs, but a general lack of abundant lipid droplets, as others similarly reported [18]. This is also in contrast with the reports suggesting higher adipogenic properties for less frequent and at times more proliferative subsets of spindle-shaped CB stromal cells [24,25].

On the other hand, calcium deposits appeared very soon (7 days after switch to the differentiation medium) in cultured cells undergoing osteogenesis. The formation of Alizarin Red S-positive deposits and molecular analysis assessed the differentiation of both LL-CBMSCs and SL-CBMSCs into osteocytes (Fig. 4C). Macrodifferences in the extent of mineralization were observed, with larger and more strongly stained deposits in cells from LL-CBMSC populations.

Although all these data identify the isolated cells as multipotent MSCs, great discrepancies with previous reports concerning their precise differentiation potentials remain. These inconsistencies could be caused by differences in the isolation methodologies, differentiation protocols and also by the lack of unequivocal criteria or markers for the isolation and definition of the distinct subsets of stromal populations.

Characteristics of CB units

Cord blood unit characteristics were considered as potential predictive parameters of cell culture outcome and thus analyzed in terms of TNC content, time from collection to processing, and total volume (blood plus anticoagulant). Also gender and gestational age were considered, but this analysis did not show any interesting result, as already reported in the literature [18,21]. For this analysis, 146 blood units were analyzed: 65 presented positive events after the immunodepletion approach, whereas the other 81 did not.

The percentage of monocytes (median) in whole cord blood units giving rise to LL-CBMSCs was lower, but not statistically significant, if compared with those giving rise to SL-CBMSCs or not showing any positive event (Fig. 5A). As clearly evident from the wider range of monocyte percentages in CB units giving rise to SL-CBMSCs and no positive event, we can suggest that those samples having a monocyte percentage higher than 10% should not be processed, or effective methodologies for monocyte depletion should be considered. The fact that monocytes could act as a sort of inhibiting

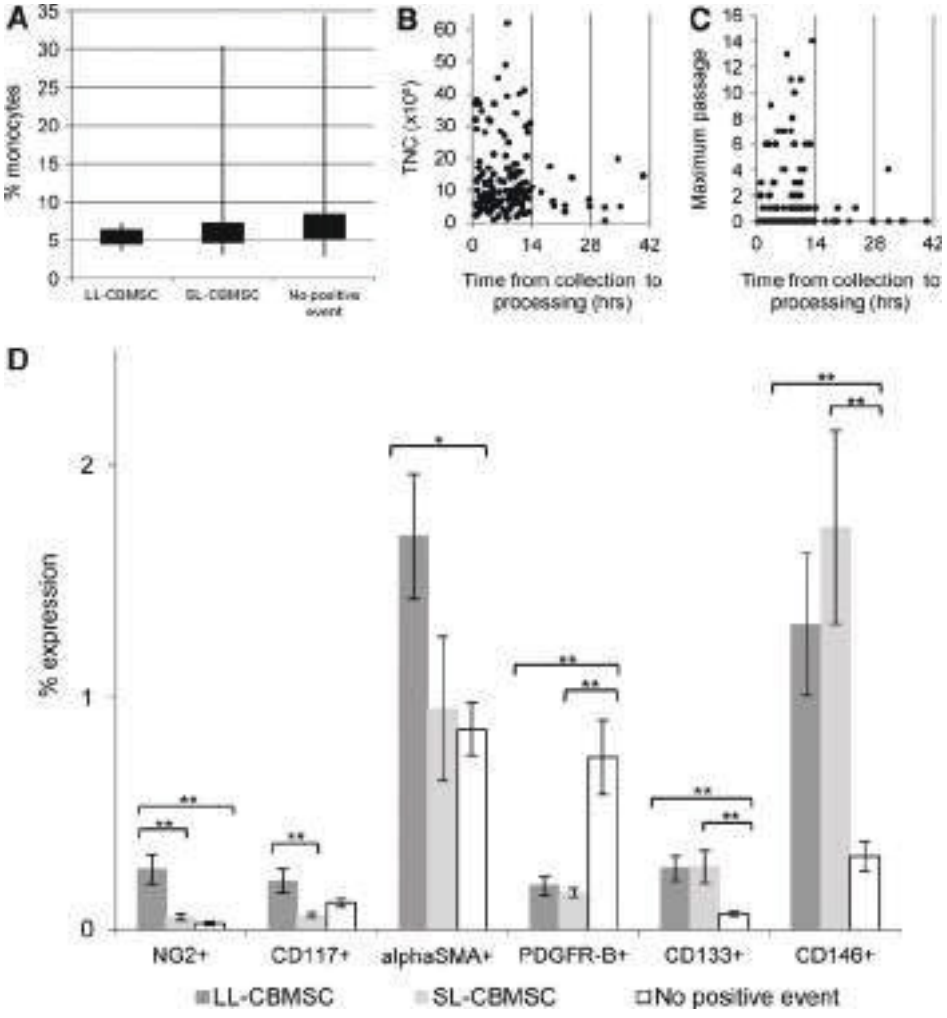

FIG. 5. CB unit characteristics. **(A)** The percentage of monocytes was lower in CB units that gave rise to LL-CBMSCs (median = 5.0; min = 3.6; max = 7.4; $n = 7$), compared with those giving rise to SL-CBMSCs (median = 6.0; min = 3.1; max = 30.4; $n = 49$) or units for which no positive event was observed (median = 6.5; min = 2.9; max = 34.4; $n = 81$). The *black rectangles* cover the portion of values between the first and third quantiles, whereas the *bars* represent the range of values from minimum to maximum. No statistical significance was observed. **(B, C)** No correlation between total nucleated cells (TNCs) recovered after immunodepletion or maximum passage and time from collection to processing. Positivity of immunodepleted CB cells before seeding for single surface markers is shown in **(D)**. Percentages of expression reported in the graph are the mean with associated SEM (*black bars*). $^*P \leq 0.05$; $^{**}P \leq 0.01$.

population in respect to colony formation and establishment of SL- and LL-CBMSCs is in accordance with the concept already discussed of steric hindrance exerted by "contaminant" adherent cell types. In fact, it has been demonstrated that monocytes/macrophages can fuse in vivo to form polynucleated cells spreading over large areas and recognized as osteoclast-like cells [37,38]. It is possible that the cocktail we use for immunodepletion of hematopoietic lineages fails to work properly when monocytes or macrophages are very abundant in the cord blood unit.

Relevance of time from collection to processing was considered in relation to other two parameters: TNC recovered postprocessing and maximum passage reached by CBMSCs when cell culture could be established (Fig. 5B, C). Even if there was no correlation between these parameters, we ascertained that the majority (90%) of the units that could not give rise to colonies had a median value for time from the collection of 18 h and 20 min, which dropped to 13 h and 9 min for CB units that had given rise to stromal colonies. This confirms previous reports [18,21] and indicates that it is advisable to process a CB unit when time from collection is less than 14 h. We can speculate that since CB is the only nonsolid MSC source, the few stromal progenitors circulating in this blood need to adhere to a solid substrate as soon as possible to activate molecular mechanisms for survival and maintenance of their MSC features [39–41].

We also evaluated the influence of sample volume on isolation of stromal cells. We found that among the 146 analyzed CB units, the median values varied from 89 mL (range: 34–127 mL) for units that presented no positive event to 100 mL (range: 87–129 mL) for units that formed SL-CBMSCs and 110 mL (range: 89–121 mL) for units giving rise to LL-CBMSCs. This suggests that sample volume could be a parameter to consider for efficient isolation of adherent clones, as already reported [18]. We believe that the importance of sample volume could be related to the stem/progenitor cell frequency in CB. Even if it is not yet clear and unequivocal which is the complete phenotype that identify the stromal cell circulating in cord blood, based on our herein reported experience we could assume that a higher blood volume contains a higher number of stromal stem/progenitor cells.

Immunophenotypic characterization

Samples at different steps were extensively characterized for the expression of hematopoietic, endothelial, perivascular, and mesenchymal surface markers: immunodepleted CB buffy coat before seeding, nonadherent cells after the first medium change, and nonclonogenic adherent cells after 40 days of culture.

In the case of immunodepleted buffy coat, the analysis revealed distinctive immunoprofiles associated with different cell culture outcomes. In fact, when considering positivity for a single cell marker, we detected some intriguing differences between samples not giving rise to positive event, SL-CBMSCs or LL-CBMSCs. The most evident and significant differences were found for NG2, highly expressed in samples giving rise to LL-CBMSCs, and for PDGFR-B, more expressed in samples for which no positive event was observed. Moreover, CD133 and CD146 were associated to samples giving rise to both LL-CBMSCs and SL-CBMSCs, whereas they were significantly less expressed in samples not showing positive events. In addition, alphaSMA$^+$ and CD117$^+$ cells were significantly more present in LL-CBMSC-related samples than no positive event and SL-CBMSC-related ones, respectively (Fig. 5D).

The immunophenotype of nonadherent contaminant cells did not give relevant results, whereas the nonclonogenic adherent fraction revealed high expression (with a maximum of 90%) of CD105 and CD45 and no presence of CD90-positive cells, both indicating the strong presence of mature endothelial cells.

Conclusion

All the reported data support, if still necessary, the concept that multipotent MSCs can be isolated from cord blood, even if at low frequency. In addition, we observed two alternative and specific behaviors of CBMSCs in cell culture, which could identify two distinct stromal populations circulating in cord blood, with different biological properties. We named them LL-CBMSCs and SL-CBMSCs based on differences in observed lifespan. Our findings induced us to consider LL-CBMSCs "better" CBMSCs, in reason of their nonsenescent morphology even after extensive culture, longer telomeres, higher proliferation rate, and osteogenic potential when compared with SL-CBMSCs. To sum up, LL-CBMSCs should possess a maximum CPD value over 15, pass the passage 5–6 limit, have a nonstressed and juvenile morphology till at least passage 8, with a steady and almost linear growth curve before entering a senescent state.

In conclusion, low frequency in cord blood of CBMSC progenitors drastically reduces isolation rate compared to other sources and could prevent from widening scientific knowledge about these cells. On the other hand, this low frequency could paradoxically shed lights on the reason why these stromal cells are present in cord blood. Our hypothesis is that it could be the result of flushing of blood coming from fetal organs. From this point of view, LL-CBMSCs and SL-CBMSCs could simply derive from different compartments of the fetus, that is, fetal liver or bone marrow, and for this reason, they show dissimilar biological properties. Otherwise, another interesting hypothesis could be that LL-CBMSC and SL-CBMSC behavior in culture may reflect different developmental stages of the same cell population. Moreover, these hypotheses concerning CBMSC derivation are not in contrast with the innovative theory of the perivascular origin of MSCs [22], but further in vivo studies should be done to unveil the origin of these populations [42].

Recently, it was hypothesized that replicative senescence of stem cells cultured in vitro could reflect their in vivo properties [43]. In fact, the aging process is characterized by impaired regenerative capabilities and it has been proposed that this is also related to less effective or absent adult stem cell functionalities [44,45]. This has prompted some researchers to consider lifespan shown during cell culture as a potency assay informative of stem cell therapeutic potentialities [46]. Moreover, if an allogeneic cell therapy context is envisioned for CBMSCs, there is strong need for healthy and proliferative cells able to sustain the requested scaling-up to reach clinically relevant cell doses [34]. All together, these considerations suggest that all the efforts in the CBMSC field should be addressed to isolate LL-CBMSCs, the most promising cord blood stromal population for regenerative medicine application, based on the presented results. Therefore, since we strongly believe in the high therapeutic

potentialities of CBMSCs [47–49], herein we proposed a sort of ''recipe'' containing useful and effective parameters predictive of CBMSC culture outcome, defined through the dissection of the CB stromal cellular component.

And now back to our Introduction and to our questions. ''Do all the CB units have the same potential to produce stromal cells?'': unfortunately they do not. ''Does cord blood contain more than one stromal cell population?'': fortunately they do. ''Can we predict the cultural outcome of cord blood cell samples?'': maybe now we can.

Acknowledgments

The authors thank all the researchers working at our facility Cell Factory for their critical advices during the laboratory meetings. We are also grateful to the Milano Cord Blood group for their help in providing cord blood units. In addition, special mention must be made to all the colleagues who have worked on this project over the last few years: Viviana Lo Cicero, Gabriella Andriolo, Gabriella Spaltro, and Francesca Chelli.

This work was partially supported by funds from Regione Lombardia (PB 0098), from Ministero della Salute Italiano (''Young Researchers'' grants: R.F.G.R. 2010-2318448, R.F.G.R. 2010-2312573), and from European Union's Seventh Programme (Grant Agreement Number 241879).

Author Disclosure Statement

No competing financial interests exist. This work was part of the PhD project of Mario Barilani for the PhD School in Biosciences and Biotechnology - curriculum Cell Biology of the University of Padoa.

References

1. Di Trapani M, G Bassi, M Ricciardi, E Fontana, F Bifari, L Pacelli, L Giacomello, M Pozzobon, F Féron, et al. (2013). Comparative study of immune regulatory properties of stem cells derived from different tissues. Stem Cells Dev 22:2990–3002.
2. Owen M and AJ Friedenstein. (1988). Stromal stem cells: marrow-derived osteogenic precursors. Ciba Found Symp 136:42–60.
3. Zuk PA, M Zhu, H Mizuno, J Huang, JW Futrell, AJ Katz, P Benhaim, HP Lorenz and MH Hedrick. (2001). Multilineage cells from human adipose tissue: implications for cell-based therapies. Tissue Eng 7:211–228.
4. Gronthos S, M Mankani, J Brahim, PG Robey and S Shi. (2000). Postnatal human dental pulp stem cells (DPSCs) in vitro and in vivo. Proc Natl Acad Sci U S A 97:13625–13630.
5. McElreavey KD, AI Irvine, KT Ennis and WH Mc Lean. (1991). Isolation, culture and characterisation of fibroblast-like cells derived from the Wharton's jelly portion of human umbilical cord. Biochem Soc Trans 19:29S.
6. Erices A, P Conget and JJ Minguell. (2000). Mesenchymal progenitor cells in human umbilical cord blood. Br J Haematol 109:235–242.
7. Igura K, X Zhang, K Takahashi, A Mitsuru, S Yamaguchi and TA Takashi. (2004). Isolation and characterization of mesenchymal progenitor cells from chorionic villi of human placenta. Cytotherapy 6:543–553.
8. Dominici M, K Le Blanc, I Mueller, I Slaper-Cortenbach, F Marini, D Krause, R Deans, A Keating, DJ Prockop and Horwitz E. (2006). Minimal criteria for defining multipotent mesenchymal stromal cells. The International Society for Cellular Therapy position statement. Cytotherapy 8:315–317.
9. Jin HJ, YK Bae, M Kim, SJ Kwon, HB Jeon, SJ Choi, SW Kim, YS Yang, W Oh and JW Chang. (2013). Comparative analysis of human mesenchymal stem cells from bone marrow, adipose tissue, and umbilical cord blood as sources of cell therapy. Int J Mol Sci 14:17986–18001.
10. Ragni E, M Viganò, V Parazzi, T Montemurro, E Montelatici, C Lavazza, S Budelli, S Vecchini, P Rebulla, R Giordano and L Lazzari. (2013). Adipogenic potential in human mesenchymal stem cells strictly depends on adult or foetal tissue harvest. Int J Biochem Cell Biol 45:2456–2466.
11. Hoogduijn MJ, MG Betjes and CC Baan. (2014). Mesenchymal stromal cells for organ transplantation: different sources and unique characteristics? Curr Opin Organ Transplant 19:41–46.
12. Goodwin HS, AR Bicknese, SN Chien, BD Bogucki, CO Quinn and DA Wall. (2001). Multilineage differentiation activity by cells isolated from umbilical cord blood: expression of bone, fat, and neural markers. Biol Blood Marrow Transplant 7:581–588.
13. Flynn A, F Barry and T O'Brien. (2007). UC blood-derived mesenchymal stromal cells: an overview. Cytotherapy 9: 717–726.
14. Stubbendorff M, T Deuse, X Hua, TT Phan, K Bieback, K Atkinson, TH Eiermann, J Velden, C Schröder, et al. (2013). Immunological properties of extraembryonic human mesenchymal stromal cells derived from gestational tissue. Stem Cells Dev 22:2619–2629.
15. Wang M, Y Yang, D Yang, F Luo, W Liang, S Guo and J Xu. (2009). The immunomodulatory activity of human umbilical cord blood-derived mesenchymal stem cells in vitro. Immunology 126:220–232.
16. Riordan NH, K Chan, AM Marleau and TE Ichim. (2007). Cord blood in regenerative medicine: do we need immune suppression? J Transl Med 5:8.
17. Bieback K, S Kern, A Kocaömer, K Ferlik and P Bugert. (2008). Comparing mesenchymal stromal cells from different human tissues: bone marrow, adipose tissue and umbilical cord blood. Biomed Mater Eng 18:S71–S76.
18. Zhang X, M Hirai, S Cantero, R Ciubotariu, L Dobrila, A Hirsh, K Igura, Satoh H, Yokomi I, et al. Isolation and characterization of mesenchymal stem cells from human umbilical cord blood: reevaluation of critical factors for successful isolation and high ability to proliferate and differentiate to chondrocytes as compared to mesenchymal stem cells from bone marrow and adipose tissue. J Cell Biochem 112:1206–1218.
19. Laitinen A, J Nystedt and S Laitinen. (2011). The isolation and culture of human cord blood-derived mesenchymal stem cells under low oxygen conditions. Methods Mol Biol 698:63–73.
20. Sibov TT, P Severino, LC Marti, LF Pavon, DM Oliveira, PR Tobo, AH Campos, AT Paes, E Amaro, L Gamarra and CA Moreira-Filho. (2012). Mesenchymal stem cells from umbilical cord blood: parameters for isolation, characterization and adipogenic differentiation. Cytotechnology 64:511–521.
21. Bieback K, S Kern, H Klüter and H Eichler. (2004). Critical parameters for the isolation of mesenchymal stem cells from umbilical cord blood. Stem Cells 22(4):625–634.
22. Crisan M, S Yap, L Casteilla, CW Chen, M Corselli, TS Park, G Andriolo, B Sun, B Zheng, et al. (2008). A perivascular origin for mesenchymal stem cells in multiple human organs. Cell Stem Cell 3:301–313.

23. Sun HP, X Zhang, XH Chen, C Zhang, L Gao, YM Feng, XG Peng and L Gao. (2012). Human umbilical cord blood-derived stromal cells are superior to human umbilical cord blood-derived mesenchymal stem cells in inducing myeloid lineage differentiation in vitro. Stem Cells Dev 21:1429–1440.
24. Markov V, K Kusumi, MG Tadesse, DA William, DM Hall, V Lounev, A Carlton, J Leonard, RI Cohen, EF Rappaport and B Saitta. (2007). Identification of cord blood-derived mesenchymal stem/stromal cell populations with distinct growth kinetics, differentiation potentials, and gene expression profiles. Stem Cells Dev 16:53–73.
25. Chang YJ, CP Tseng, LF Hsu, TB Hsieh and SM Hwang. (2006). Characterization of two populations of mesenchymal progenitor cells in umbilical cord blood. Cell Biol Int 30:495–499.
26. Kögler G, S Sensken, JA Airey, T Trapp, M Müschen, N Feldhahn, S Liedtke, RV Sorg, J Fischer, et al. (2004). A new human somatic stem cell from placental cord blood with intrinsic pluripotent differentiation potential. J Exp Med 200:123–135.
27. Ragni E, T Montemurro, E Montelatici, C Lavazza, M Viganò, P Rebulla, R Giordano and L Lazzari. (2013). Differential microRNA signature of human mesenchymal stem cells from different sources reveals an ''environmental-niche memory'' for bone marrow stem cells. Exp Cell Res 319:1562–1574.
28. Samsonraj RM, M Raghunath, JH Hui, L Ling, V Nurcombe and SM Cool. (2013). Telomere length analysis of human mesenchymal stem cells by quantitative PCR. Gene 519:348–355.
29. Ragni E, M Viganò, P Rebulla, R Giordano and L Lazzari. (2013). What is beyond a qRT-PCR study on mesenchymal stem cell differentiation properties: how to choose the most reliable housekeeping genes. J Cell Mol Med 17:168–180.
30. Laitinen A and J Laine. (2007). Isolation of mesenchymal stem cells from human cord blood. Curr Protoc Stem Cell Biol 2: 2A.3
31. Phinney DG. (2012). Functional heterogeneity of mesenchymal stem cells: implications for cell therapy. J Cell Biochem 113:2806–2812.
32. Ho AD, W Wagner and W Franke. (2008). Heterogeneity of mesenchymal stromal cell preparations. Cytotherapy 10: 320–330.
33. Siegel G, T Kluba, U Hermanutz-Klein, K Bieback, H Northoff and R Schäfer. (2013). Phenotype, donor age and gender affect function of human bone marrow-derived mesenchymal stromal cells. BMC Med 11:146.
34. Bajek A, M Czerwinski, J Olkowska, N Gurtowska, T Kloskowski and T Drewa. (2012). Does aging of mesenchymal stem cells limit their potential application in clinical practice? Aging Clin Exp Res 24:404–411.
35. Mikhelson VM and IA Gamaley. (2012). Telomere shortening is a sole mechanism of aging in mammals. Curr Aging Sci 5:203–208.
36. Kluth SM, A Buchheiser, AP Houben, S Geyh, T Krenz, TF Radke, C Wiek, H Hanenberg, P Reinecke, P Wernet and G Kögler. (2010). DLK-1 as a marker to distinguish unrestricted somatic stem cells and mesenchymal stromal cells in cord blood. Stem Cells Dev 19:1471–1483.
37. Udagawa N, N Takahashi, T Akatsu, H Tanaka, T Sasaki, T Nishihara, T Koga, TJ Martin and T Suda. (1990). Origin of osteoclasts: mature monocytes and macrophages are capable of differentiating into osteoclasts under a suitable microenvironment prepared by bone marrow-derived stromal cells. Proc Natl Acad Sci U S A 87:7260–7264.
38. Kim YG, CK Lee, JS Oh, SH Kim, KA Kim and B Yoo. (2010). Effect of interleukin-32gamma on differentiation of osteoclasts from $CD14^+$ monocytes. Arthritis Rheum 62:515–523.
39. Zhong X and FJ Rescorla. (2012). Cell surface adhesion molecules and adhesion-initiated signaling: understanding of anoikis resistance mechanisms and therapeutic opportunities. Cell Signal 24:393–401.
40. Stupack DG and DA Cheresh. (2002). Get a ligand, get a life: integrins, signaling and cell survival. J Cell Sci 115:3729–3738.
41. Mathieu PS and EG Loboa. (2012). Cytoskeletal and focal adhesion influences on mesenchymal stem cell shape, mechanical properties, and differentiation down osteogenic, adipogenic, and chondrogenic pathways. Tissue Eng Part B Rev 18:436–444.
42. Murray IR, CC West, WR Hardy, AW James, TS Park, A Nguyen, T Tawonsawatruk, L Lazzari, C Soo and B Péault. (2014). Natural history of mesenchymal stem cells, from vessel walls to culture vessels. Cell Mol Life Sci 71:1353–1374.
43. Wagner W, S Bork, P Horn, D Krunic, T Walenda, A Diehlmann, V Benes, J Blake, FX Huber, et al. (2009). Aging and replicative senescence have related effects on human stem and progenitor cells. PLoS One 4:e5846.
44. Behrens A, van JM Deursen, KL Rudolph and B Schumacher. (2014). Impact of genomic damage and ageing on stem cell function. Nat Cell Biol 16:201–207.
45. López-Otín C, MA Blasco, L Partridge, M Serrano and G Kroemer. (2013). The hallmarks of aging. Cell 153:1194–1217.
46. Wagner W, AD Ho and M Zenke. (2010). Different facets of aging in human mesenchymal stem cells. Tissue Eng Part B Rev 16:445–453.
47. Pierro M, L Ionescu, T Montemurro, A Vadivel, G Weissmann, G Oudit, D Emery, S Bodiga, F Eaton, et al. (2013). Short-term, long-term and paracrine effect of human umbilical cord-derived stem cells in lung injury prevention and repair in experimental bronchopulmonary dysplasia. Thorax 68:475–484.
48. Zanier ER, M Montinaro, M Viganò, P Villa, S Fumagalli, F Pischiutta, L Longhi, ML Leoni, P Rebulla, et al. (2011). Human umbilical cord blood mesenchymal stem cells protect mice brain after trauma. Crit Care Med 39:2501–2510.
49. Morigi M, C Rota, T Montemurro, E Montelatici, Lo V Cicero, B Imberti, M Abbate, C Zoja, P Cassis, et al. (2010). Life-sparing effect of human cord blood-mesenchymal stem cells in experimental acute kidney injury. Stem Cells 28:513–522.

Address correspondence to:
Dr. Lorenza Lazzari, PhD
Cell Factory
Unit of Cell Therapy and Cryobiology
Fondazione IRCCS Ca' Granda Ospedale
Maggiore Policlinico
Via F. Sforza 35
20122 Milano
Italy

E-mail: lorenza.lazzari@policlinico.mi.it

Received for publication March 31, 2014
Accepted after revision July 19, 2014
Prepublished on Liebert Instant Online July 21, 2014

Cell Transplantation, Vol. 25, pp. 1501–1514, 2016
Printed in the USA.

0963-6897/16 $90.00 + .00
DOI: http://dx.doi.org/10.3727/096368916X690827
E-ISSN 1555-3892
www.cognizantcommunication.com

A Chemically Defined Medium-Based Strategy to Efficiently Generate Clinically Relevant Cord Blood Mesenchymal Stromal Colonies

Mario Barilani,*† Cristiana Lavazza,* Valentina Boldrin,* Enrico Ragni,* Valentina Parazzi,* Mariacristina Crosti,‡ Elisa Montelatici,* Rosaria Giordano,* and Lorenza Lazzari*

*Cell Factory, Unit of Cell Therapy and Cryobiology,
Fondazione IRCCS Ca' Granda Ospedale Maggiore Policlinico, Milano, Italy
†Department of Industrial Engineering, University of Padova, Padova, Italy
‡Istituto Nazionale di Genetica Molecolare (INGM), Milano, Italy

During the last decade it has been demonstrated that mesenchymal progenitors are present and can be isolated also from cord blood (CB). Recently, we managed to set up a standard protocol allowing the isolation of mesenchymal stromal cells (MSCs) with high proliferative potential and multiple differentiation capabilities, whereas the generation rate of MSC-initiating colonies could still be further improved. Herein, we strikingly succeeded in defining some simple and basic culture conditions based on the use of a chemically defined medium that increased the colony isolation efficiency up to almost 80% of processed CB units. Importantly, this result was achieved irrespective of CB unit white blood cell content and time elapsed from delivery, two limiting parameters involved with processing CB units. Thus, this high efficiency is guaranteed without strict selection of the starting material. In addition, since we are profoundly concerned about how different culture conditions can influence cell behavior, we devoted part of this study to in-depth characterization of the established CB-MSC populations to confirm their stemness features in this novel isolation and culture system. Therefore, an extended study of their immunophenotype, including classical pericytic markers, and a detailed molecular analysis addressing telomere length and also stemness-related microRNA contribution were performed. In summary, we propose a straightforward, extremely efficient, and reliable approach to isolate and expand thoroughly characterized CB-MSCs, even when poor-quality CB units are the only available source, or there is no space for an isolation to fail.

Key words: Cord blood (CB); Cord blood-derived mesenchymal stromal cells (CB-MSCs); Chemically defined medium; Mesenchymal stromal cells (MSCs); Stemness potency assay

INTRODUCTION

Mesenchymal stromal cells (MSCs) are multipotent and represent one of the major players in cell-based clinical trials, and various studies have found that they possess unique therapeutic properties[1,2]. Until now no single mechanism of action has been defined, although the prevailing theory describes MSCs as living drugstores capable of secretion and delivery of numerous cytokines and growth factors to damaged tissues[3], along with vesicular products implicated in many physiological processes[4]. Nonetheless, MSCs also retain the potential to differentiate into mesodermal lineages and specifically into adipocytes, chondrocytes, and osteocytes[5], and this was the characteristic that first drew attention to MSCs as tools in regenerative medicine for tissue repair purposes.

Currently, cord blood (CB) has the undeniable advantage of having a completely safe and noninvasive harvesting procedure. Another advantage that will facilitate extensive use of CB-MSCs in the clinic is the existence of international networks of public and private banks storing thousands of frozen cord blood units (CBUs) that, in the future, could be used for MSC isolation for therapeutic purposes. Like MSCs from other sources, CB-MSCs can also undergo adipogenesis, chondrogenesis, and osteogenesis upon induction[6] and secrete biologically active molecules[7]. Currently, even if several attempts have been made and different methodological approaches have been implemented in order to efficiently isolate stromal cell colonies from CB, high-quality CBUs are often required, specifically with regard to time from collection to processing, white blood cell (WBC) content, and volume[8,9]. For this reason many stem cell researchers have hesitated until now to consider CB-MSCs as a real alternative to bone marrow-derived mesenchymal stromal cells

Received October 2, 2015; final acceptance March 29, 2016. Online prepub date: February 2, 2016.
Address correspondence to Lorenza Lazzari, Ph.D., Cell Factory, Unit of Cell Therapy and Cryobiology, Fondazione IRCCS Ca' Granda Ospedale Maggiore Policlinico, Via F. Sforza 35, 20122 Milano, Italy. Tel: +39 02 5503 4053; Fax: +39 02 5503 2796; E-mail: lorenza.lazzari@policlinico.mi.it

(BM-MSCs). Indeed, this main drawback could represent a huge hurdle, especially when feasibility of translation to the clinic has to be evaluated.

Recently, we described the existence of at least two stromal populations in CB, both capable of differentiation into mesodermal derivatives and both expressing typical MSC surface markers. Nonetheless, marked differences were found with regard to other biological features, such as growth properties including proliferation rate, life span in vitro, and ability to generate colonies under low-density seeding conditions. In addition, a robust statistically significant difference was detected at the molecular level following the analysis of telomere length, which was positively correlated with enhanced growth properties. Thus, we decided to name CB-MSCs endowed with higher proliferation properties and longer telomeres long-living (LL)-CB-MSCs, while we named CB-MSCs showing shorter life span and shorter telomeres short-living (SL)-CB-MSCs. We also proposed LL-CB-MSCs as the best choice in the context of stem cell therapy settings, on the basis of their biological features. For instance, the higher proliferation properties of LL-CB-MSCs allow for obtaining clinically relevant ex vivo cell expansions.

Notwithstanding the crucial advance in the knowledge of these important players in the regenerative medicine field, the establishment of such a population occurred in 12% of total isolated colonies[10]. In order to improve the efficiency of our standard isolation protocol and at the same time to generate CB-MSCs showing the same or improved qualities of LL-CB-MSCs, the main aims of the present study were threefold. First of all, we investigated whether we could provide novel cell culture conditions to improve MSC colony appearance and avoid some of the strict CBU quality requirements. The idea was to offer the best environment to facilitate CB mesenchymal progenitor attachment to a plastic surface, which is considered essential for their survival[11], and also to better support the generation and growth of stromal colonies. Second, considering the great influence of the medium composition on MSC stemness and other biological features[12], we sought to further evaluate the peculiar characteristics of the CB-MSCs cultured under these new conditions to provide more complete information about their effect and on their properties. Finally, we wanted to investigate if such an optimal culture environment could be applied to rescue the SL-CB-MSC phenotype and induce them to adopt the same clinically relevant proliferative properties demonstrated by LL-CB-MSCs in standard culture conditions.

MATERIALS AND METHODS

Isolation of Human CB-MSCs

Human umbilical cord blood (hUCB) was collected in a multiple system bag (Machopharma, Mouvaux, France) containing 29 ml of citrate phosphate dextrose as an anticoagulant. The samples were not included in the study if the presence of clots or hemolysis was detected before or after the implementation of the isolation procedure. The authors state that this study was performed according to the amended Declaration of Helsinki. In addition, written informed consent was obtained from all of the cord blood donors involved in the study, and use of human tissue and cells was approved by the Ethical Committee of our institute, Fondazione IRCCS Ca' Granda Ospedale Maggiore Policlinico. Two standard isolation procedures routinely performed in our laboratory were used for CB-MSC isolation under new culture conditions: a classic BM-MSC isolation protocol and a CB-MSC-tailored one[10]. In the first case, samples were seeded as whole blood at 0.5×10^4 total nucleated cells (TNCs)/cm^2. This protocol is fast and simple, but given the high number of TNCs in the sample, only a small CB fraction (≤4 ml in this study) can be processed, since seeding all CB would imply the use of an excessive and unmanageable number of culture flasks (e.g., for a 20-ml CB sample with 10×10^6 TNCs/ml, a 4,000-cm^2 cell growth area corresponding to more than 50 75-cm^2 flasks would be needed). On the other hand, higher seeding density cannot be applied because red blood cells and adherent white blood cells would heavily interfere with MSC attachment or colony growth. Alternatively, the samples were centrifuged at $680 \times g$ for 15 min, and the plasma was discarded, while the buffy coat (BC) was collected. MSC precursors were obtained by negative immunodepletion of CD3$^+$, CD14$^+$, CD38$^+$, CD19$^+$, glycophorin A, and CD66b$^+$ cells using a commercial kit (RosetteSep Mesenchymal Stem Cell, StemCell Technologies, Vancouver, BC, Canada) followed by density gradient separation. Briefly, for immunodepletion the recovered TNCs were incubated with 50 µl/ml RosetteSep MSC enrichment cocktail for 20 min at room temperature (RT). After incubation, the sample was diluted 1:3 with phosphate-buffered saline (PBS; Gibco, Grand Island, NY, USA), ethylenediaminetetraacetic acid (EDTA; Sigma-Aldrich, St. Louis, MO, USA), and human serum albumin (Kedrion, Barga, Italy) and then separated under standard density gradient conditions (Ficoll Paque Plus 1.077 ± 0.001 g/L; GE Healthcare, Little Chalfont, UK). The ring of immunodepleted mononuclear cells (MNCs) was transferred to a new tube with a Pasteur pipette, washed, and then plated at a concentration of 1×10^6 cells/cm^2. This protocol allows the concentration of CB and its enrichment in MSC progenitors. Thus, all the sample is processed, the undesired and committed cell types are discarded, and a higher seeding density compared to the whole blood protocol can be applied.

In both cases, the sample fractions were suspended in culture medium composed of SPE-IV alone (ABCell-Bio, Paris, France) or supplemented with 20% fetal

bovine serum (FBS; Gibco) and, when specified, with L-glutamine 1× (Gibco), hereafter referred to as complete medium (CM). SPE-IV (ABCell-Bio) is a defined serum-free medium developed for optimal growth support of human MSCs containing 25 ng/ml recombinant human insulin-like growth factor-1 (rh-IGF-1) and 0.33 ng/ml recombinant human-basic fibroblast growth factor (rh-bFGF). Other components, whose exact concentration is not disclosed in detail by the manufacturer, are clinical-grade human albumin, synthetic iron carrier, rh-insulin, nucleosides, L-glutamine, α-monothioglycerol, synthetic lipids, and αMEM. When specified, culture surfaces were coated with 10 μg/cm^2 collagen I–III (ABCell-Bio) for 2 h at RT.

Cell cultures were maintained at 37°C in a humidified atmosphere containing 5% CO_2. After 48 h, nonadherent cells were removed, and fresh medium was added. From that point, culture medium was changed every 3 days and cultures examined for colony appearance everyday. At 80% confluence, the cells were harvested with 25% TrypLE Select 1× (Gibco), washed with PBS (Gibco), and subcultured at a concentration of 1.5×10^3/cm^2. LL-CB-MSCs and SL-CB-MSCs were isolated and cultured as previously reported[10] in the standard medium composed of αMEM-GlutaMAX (Gibco) supplemented with 20% FBS (Gibco) (standard CB-MSC culture control). To ensure proper culture conditions and as a routine quality control in our laboratory, the FBS batches used in this study were previously tested for optimal CB-MSC growth in the aforementioned standard culture conditions.

Cumulative Population Doublings

Population doublings were calculated for each established CB-MSC population using the equation: population doubling (PD) = $\log_{10}(N)/\log_{10}(2)$, where N is the ratio between the number of cells harvested at the end of the culture and the number of seeded cells.

Cumulative PD (CPD) was calculated for each passage as the sum of the current and all the previous PD values.

Colony-Forming Unit-Fibroblast (CFU-F) Assay

Two hundred CB-MSCs were plated per 100-mm Petri dish (BD Biosciences, Franklin Lakes, NJ, USA) in replicate ($n = 2$). The medium was replaced with fresh medium after 1 week; at day 14 the cells were washed with PBS (Gibco), fixed with methanol (154903; Sigma-Aldrich), and stained with carbolic Gentian violet solution (Ral Diagnostics, Cedex, France). After two washing steps with milliQ-grade water, colonies with diameters greater than 1–2 mm were counted by sight.

Morphological Analysis

The morphological parameter calculated as the ratio between cell major axis length and nucleus diameter was considered indicative of cell shape and used to distinguish spindle-like cells from those showing a more compact shape. The two parameters were measured ($n = 10$ for each cell type) with Media Cybernetics Image-Pro Plus 2 (Media Cybernetics, Rockville, MD, USA). Images of cells in culture were taken with a Nikon Eclipse TS100 microscope (Nikon, Tokyo, Japan).

Telomere Length

Telomere length was assessed by real-time qPCR as previously described[13]. Briefly, CB-MSC DNA was extracted from cell pellets stored at −80°C with QIAamp DNA Blood Mini Kit (51104; Qiagen, Hilden, Germany). The telomere sequence and single-copy gene (36B4)-specific amplification reactions were performed in triplicate in 96-well plates on a CFX96 machine (Bio-Rad, Hercules, CA, USA). The data analysis was carried out using CFX Manager software (Bio-Rad). In order to present mean telomere length, the values of each CB-MSC population for each passage were normalized on its passage 0 value, and then the mean was calculated.

Gene Expression

Isolation of total RNA and real-time qRT-PCR assays were conducted in duplicate as previously reported[14]. The following primers were used.

C/EBP-β (FW 5′-GACAAGCACAGCGACGAGTA-3′, RV 5′-AGCTGCTCCACCTTCTTCTG-3′; COL10A1 (FW 5′-ACTCCCAGCACGCAGAATCCA-3′, RV 5′-TGGGCCTTTTATGCCTGTGGGC-3′); MYOD (FW 5′-TGCTCCGACGGCATGATGGAC-3′, RV 5′-GACACCGCCGCACTCTTCCC-3′); PAX3 (FW 5′-GCCCAACCACATCCGCCACA-3′, RV 5′-CTTGGAGACGCAGCCGTGGG-3′); ALP (FW 5′-TACAAGGTGGTGGGCGGTGAACGA-3′, RV 5′-TGGCGCAGGGGCACAGCAGAC-3′); RUNX2 (FW 5′-AACCCACGGCCCTCCCTGAA-3′, RV 5′-CTGTGCCTGCCTGGGGTCTGTA-3′); BDNF (FW 5′-AGGTGAGAAGAGTGATGA-3′, RV 5′-CGGATGTTTGCTTCTTTC-3′); MUSASHI (FW 5′-GCGGCTGTTCGTGTTTTGGG-3′, RV 5′-AATGAGGGAGAGGGAAGCTAAGTG-3′); SOX2 (FW 5′-GGGGGAAAGTAGTTTGCTGCCTCT-3′, RV 5′-TGCCGCCGCCGATGATTGTT-3′); ANGPT1 (FW 5′-AGCAGCCTGATCTTACACGGTGC-3′, RV 5′-GCATCAAACCACCATCCTCCTGT-3′); ICAM-1 (FW 5′-AAGGTGACCGTGAATGTG-3′, RV 5′-GCCTGTTGTAGTCTGTATT-3′); VCAM-1 (FW 5′-TGTCATTGAGGATATTGGAA-3′, RV 5′-TAACTGTATTCTTGGGTGAT-3′); RPLP0 (FW 5′-TGTGGGCTCCAAGCAGATGCA-3′, RV 5′-GCAGCAGTTTCTCCAGAGCTGGG-3′).

Gene expression levels were normalized on RPLP0 "housekeeping" gene expression, following the $2^{\Delta\Delta Ct}$ method. For each CB-MSC population and each analyzed gene, passage 3 expression level was used as baseline.

Flow Cytometry

CB-MSCs were extensively characterized by flow cytometry at passages 3 and 5. Cells were washed with PBS (Gibco), centrifuged at 270×*g* for 8 min and resuspended in PBS (Gibco) plus 2% FBS (Gibco), and then incubated for 20 min in the dark with the following combinations of directly coupled mouse anti-human fluorochrome-conjugated antibodies: CD45-FITC (21270453X2; ImmunoTools, Friesoythe, Germany), CD73-PE (550257; BD), CD90-PE-Cy5 (PNIM3703; Beckman Coulter, Brea, CA, USA), CD117-PE-Cy7 (PNIM3698; Beckman Coulter), CD105-APC (130-094-926; Miltenyi Biotec, Bergisch Gladbach, Germany), CD146-biotin (5050-B100T; BioCytex, Marseille, France) revealed with streptavidin APC-Cy7 (BD) for the first tube; CD31-FITC (555445; BD), CD144-PE (PNA07481; Beckman Coulter), CD34-PE-Cy5 (A07777; Beckman Coulter), CD133-APC (130-092-880; Miltenyi Biotec), CD146-biotin (BioCytex) revealed with streptavidin APC-Cy7 (BD) for the second tube; alphaSMA-FITC (F3777; Sigma-Aldrich), PDGFR-beta-PE (FAB1263P; R&D Systems, Minneapolis, MN, USA), CD146-biotin (BioCytex) revealed with streptavidin APC-Cy7 (BD) for the third tube; NG2-PE (PNIM3454U; Beckman Coulter), CD56-PE-Cy5 (555517; BD) for the fourth tube; SSEA4-FITC (560126; BD), CD271-PE (557196; BD), CD105-APC (Miltenyi Biotec) for the fifth tube. After staining, the cells were washed once with PBS (Gibco) containing 0.1% BSA (Kedrion). Fifty thousand events per sample were acquired with a FACSCanto II (BD) running FACSDiva 6.1.3 software, and isotype-matched mouse immunoglobulins were used as controls under the same conditions. Histograms and plots were generated using FlowJo analysis software v8.8.7 (Tree Star, Ashland, OR, USA). Mean fluorescence intensity (MFI) ratio was calculated as the ratio between sample and control MFI for each marker under analysis. Only MFI ratios greater than 2 were taken into consideration.

Cell Lineage Differentiation

CB-MSCs were induced to differentiate into adipogenic, osteogenic, and chondrogenic cell types. Commercial media (Lonza, Basel, Switzerland) were used following manufacturer's protocols. Adipogenesis was promoted with human MSC adipogenesis induction medium (PT-3102B; Lonza) and human MSC adipogenesis maintenance medium (PT-3102A; Lonza). Lipid vacuoles were stained with Oil red O solution (O0625; Sigma-Aldrich), following manufacturer's instructions. Osteogenic differentiation was induced with human MSC Osteogenic Medium (PT-3002; Lonza). Calcium deposits were stained with Alizarin red S (A5533; Sigma-Aldrich), following manufacturer's instructions. Chondrogenesis was induced with human MSC chondrocyte differentiation medium (PT-3003; Lonza), and the presence of extracellular matrix-producing cells was assessed with Alcian blue staining (B8438; Sigma-Aldrich). Due to high proliferation of CB-MSCs cultured in SPE-IV, initial seeding densities were modified to 0.5×10^3 cells/cm^2, and the induction lasted only 2 weeks. Images of stained cells were taken with a Nikon Eclipse TS100 microscope (Nikon).

MicroRNA Expression Profiling

For miRNA studies, total RNA was isolated using the miRNeasy Mini kit (Qiagen) following manufacturer's instructions. RNA purity was determined by measuring the absorbance A260/A280 in a Nanodrop spectrophotometer. RNA integrity was assessed using electrophoretic techniques. MicroRNA expression profiling was performed in triplicate with an RT^2 miRNA PCR Array System (Qiagen) following the manufacturer's instructions. Briefly, 4 µg of total RNA, including small RNAs like miRNAs, was reverse transcribed into first-strand cDNA using the RT^2 miRNA First Strand Kit. Then the templates were mixed with RT^2 SYBR Green qPCR Master Mix (Qiagen), and 25 µl was aliquoted into each well of the eight 96-well plates containing the 704 predispensed miRNA-specific assays based on the Sanger mirBASE Release 14 (University of Manchester, Manchester, UK). Amplifications were carried out in a Bio-Rad CFX96 Real-Time PCR Detection System instrument (Bio-Rad Laboratories). After amplification, relative expression of each miRNA was determined with the ΔΔCt method using the online software RT^2 Profiler PCR Array Data Analysis version 3.5 (http://pcrdataanalysis.sabiosciences.com/pcr/arrayanalysis.php) and the global mean normalization procedure[5,15,16]. To detect only the reliable amplifications, all the wells giving rise to ambiguous double or flattened amplified product melt curve peaks were removed. In addition, following manufacturer's instructions, an absolute Ct value of 35 was set as the maximum threshold, since low-expressed miRNAs giving rise to high Ct values might be PCR amplification artifacts or miRNA machinery by-products[17]. Then array data of two small RNAs (miR-16 and miR-29b) were confirmed by qPCR using the miScript II RT Kit for cDNA synthesis (Qiagen) and miScript SYBR Green PCR Kit (Qiagen) as per the manufacturer's instructions. Briefly, 1 µg of total RNA was first polyadenylated and then reverse transcribed to generate first-strand cDNA. cDNA was diluted in RNAse-free water and prepared for qPCR with miRNA-specific forward primers (miScript Primer Assay, Qiagen), a universal qPCR primer included in the miScript SYBR Green PCR mix, and SYBR Green reference dye. All reactions were run in a Bio-Rad CFX96 Real-Time PCR Detection System instrument (Bio-Rad Laboratories). Relative miRNA levels were normalized to RSU snRNA, a verified endogenous control. Verified mRNA targets of selected miRNAs were identified using

the miRWalk database (http://www.umm.uni-heidelberg.de)[18]. Final target lists were then uploaded to GeneCodis free software (Centro Nacionál de Biotecnología, Madrid, Spain) for functional interpretation using default filters[19–21].

Statistical Analysis

Nonparametric Kruskal–Wallis tests followed by Dunn's multiple comparisons tests were performed to evaluate CBU characteristics. One-way analysis of variance (ANOVA) followed by Newman–Keuls (mean normalized telomere length) (Fig. 3A) or Tukey's (relative telomere length) (Fig. 3B) multiple comparisons tests were performed to evaluate CB-MSC telomere length after normal distribution of the datasets was verified by a D'Agostino–Pearson omnibus normality test. GraphPad Prism version 6.00 for Windows (www.graphpad.com; GraphPad Software, San Diego, CA, USA) was used to perform all of the previously described statistical analyses. Concerning the miRNA target study, the GeneCodis free software (Centro Nacionál de Biotecnología, Madrid, Spain) was run to find statistically miRNA-dependent enriched biological processes with respect to the entries of the whole human genome[19–21]. A value of $p < 0.05$ was used to determine statistical significance.

RESULTS

Chemically Defined Medium-Based Culture Conditions for the Isolation of Cord Blood Stromal Colonies

A total number of 100 CBUs were processed for this study, and different standard experimental approaches were investigated. The aim was to determine which isolation procedure best supported the generation of stromal colonies from CB under new culture conditions, taking into account efficiency but also feasibility of the procedure (for the complete schematic, see Fig. 1).

In a first series of isolations the importance of the collagen I–III coating was investigated for the optimal use of a chemically defined medium containing, among other bioactive molecules, two important growth factors: IGF-I and bFGF. Whole blood samples versus immunodepleted fractions were compared, and the appearance of the first fibroblastic colony was considered as a positive event. Positive events on coated surfaces were obtained from five whole blood samples (14 total units) and from two immunodepleted fractions (5 total units). On the contrary, without the coating no positive event was observed (5 whole blood samples and 11 immunodepleted fractions) (Fig. 1A).

In a second set of experiments, the addition of a standard percentage of serum was investigated as a possible replacement of the collagen I–III coating, based on the common practice of coating plastic surfaces with serum. In this way, positive events were obtained from three whole blood samples (6 total units) and from 17 immunodepleted fractions (30 total units), representing the most efficient isolation strategy for the experimental conditions reported herein.

The analysis of CBU characteristics demonstrated that the observed results were not biased by major differences between the experimental groups in terms of time elapsed from CB collection to processing (Fig. 1C) or WBC content (Fig. 1D), two crucial parameters for CB-MSC isolation[8,9]. The evaluation of processed sample volume revealed that no statistically significant differences were present within whole blood (WB, WB coating, and WB serum conditions; Fig. 1E) and immunodepleted (ID, ID coating, and ID serum conditions; Fig. 1F) experimental groups.

Following this experimental design, the use of serum as a substitute for collagen I–III coating to culture the CB immunodepleted fraction appeared as the most promising approach to further ameliorate the generation of stromal cell colonies, due to its higher isolation efficiency. Thus, in order to further improve this already relatively high rate of positive events, L-glutamine supplementation as a major energy source for cultured cells was tested in immunodepleted fraction isolation experiments (complete medium) to offer a more favorable environment for colony generation, along with a preference for significantly richer-in-volume (≥20 ml threshold) CBUs compared to the other immunodepleted samples (ID serum and L-glutamine condition; Fig. 1F). Under these conditions, positive events were observed in 79% of the processed samples (23 out of 29 units) (Fig. 1B). Due to this high efficiency, we focused on this method for the isolation and expansion of CB-MSC populations for all of the subsequent studies.

CB-MSC Proliferative Properties

Following the most efficient isolation conditions ($n = 23$ units with positive events), the first colonies of plastic adherent cells appeared reasonably soon [a median of 13 days after seeding (min 5, max 22 days)], with a colony number per processed unit ranging from 1 to 5. Interestingly, there were almost no other "contaminant" adherent cell types, like osteoclast-like or nonproliferative fibroblast-like cells. The first trypsinization occurred with a median of 24 days after seeding (min 7, max 41) and the median number of cells harvested from passage 0 was 0.37×10^6 cells (min 0.05, max 2.59×10^6 cells).

Three CB-MSC populations were established, which were named CB-MSC 1, 2, and 3, each starting from a single colony derived from a distinct CBU (unrelated donors). All three CB-MSC populations were extensively characterized along long-term culture for growth kinetics, immunophenotype, and molecular profile. The CB-MSC growth curves are shown in Figure 2A. For all of the passages, 1,500 cells/cm^2 was the optimal seeding density,

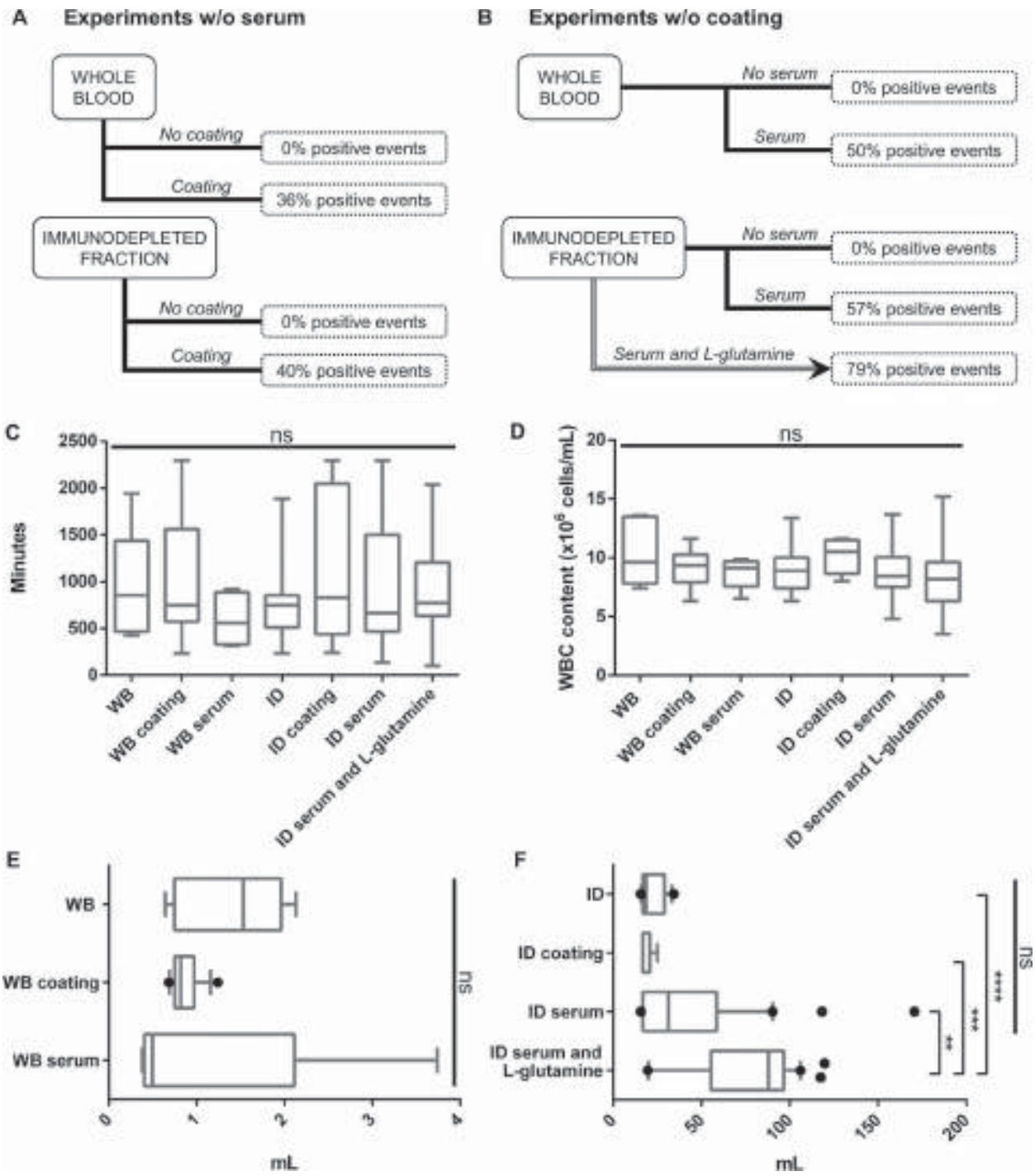

Figure 1. Complete experimental schematic. The two graphs represent isolations performed without (A) or with (B) serum supplementation, and they specify further experimental conditions (diagram branches) and isolation success as percentage (dotted line rectangles). The following CB unit parameters were evaluated for the different whole blood (WB) and immunodepleted fraction (ID) isolation experiments: time from collection to processing (C), WBC content (D), and processed volume (E, F). Box and whisker graphs show 25th and 75th percentiles (plot hinges), median, minimum, and maximum values (C, D) or 10th and 90th percentiles with outside values (E, F). $^{**}p<0.01$; $^{***}p<0.005$; $^{****}p<0.001$; ns = statistically nonsignificant difference.

which allowed us to trypsinize the cells once a week with medium changes every 3–4 days. In two cases (CB-MSC 2 and 3) growth arrest occurred only after reaching a CPD of 75, and only after passage 13, while CB-MSC 1 reached a CPD of 45 and arrested its growth at passage 9. We also noted that the cells proliferated with a constant rate without high fluctuation in terms of population doublings (CB-MSC 1, P1–P9: mean (m)PD = 5.1, standard deviation (SD) = 1.6; CB-MSC 2, P1–P15: mPD = 5.1, SD = 0.7; CB-MSC 3, P1–P13: mPD = 5.8, SD = 1.3), or of days between two subsequent trypsinizations during almost all the culture (a mean of 7 days from P1 to P7 for the three populations; SD = 1.3). If we consider the three CB-MSC populations together from passage 1 to passage 9, the result is a mean growth curve that approximates almost perfectly a linear function, constantly increasing the CPD of 5.6 after every passage (Fig. 2B).

At passage 1, the CFU-F assay was performed, and all the three CB-MSC populations could generate colonies under low-density seeding conditions (a mean of 76 colonies; SD = 35) (Fig. 2C).

CB-MSC Morphology

In order to give quantitative information about cell morphology, two parameters were measured by image analyzer software: diameter of the nucleus and cell major axis. The morphology of CB-MSC 1 (Fig. 2D) was compared with that of LL-CB-MSCs cultured in the standard medium (Fig. 2E). The results are summarized in Figure 2F. Although no statistical significance was observed, the ratio seemed to be lower for CB-MSC 1, as shown by both the mean and median, but concomitantly also presented the greatest degree of variation, as shown by SD and minimum and maximum values. This was consistent with previously reported data[12], comparing CB-MSC morphology of the same population in two different media. No significant differences in cell morphology were observed among CB-MSC 1, 2, and 3 or between LL-CB-MSCs and CB-MSC 2 or 3 (data not shown).

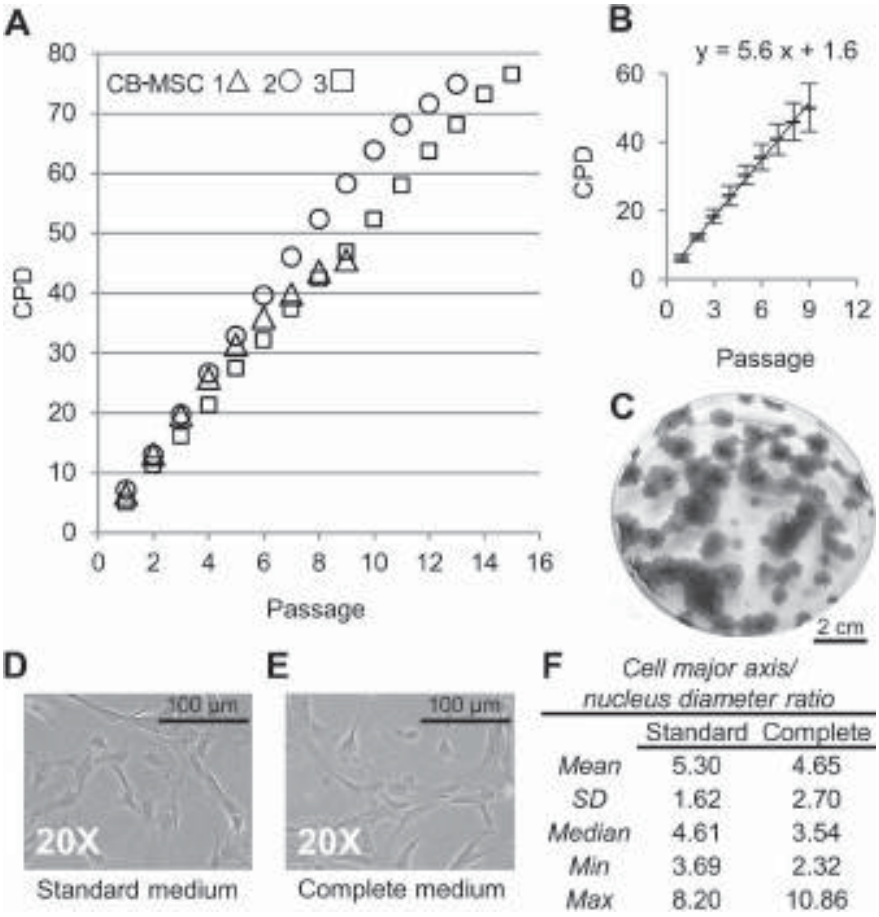

Figure 2. Biological characterization of established CB-MSC populations. Proliferation rate (A) and mean proliferation rate (B) of the three CB-MSC populations. The error bars in (B) represent standard deviation. A representative image of CB-MSC CFU-F is shown (C). (D–F) Morphology study: images of CB-MSCs cultured under standard conditions (D) or relying on the complete medium (E); (F) summarizes the results.

Telomere Length Assessment

To further characterize the CB-MSC populations, telomere length was assessed (Fig. 3A and B). Evaluating the established CB-MSC populations together, a dramatic and significant decrease in mean telomere length was observed from passage 0 to passage 1 (Fig. 3A), after which telomere length was maintained at a constant (statistically nonsignificant differences between P1 and P9 samples). Intriguingly, the CB-MSC populations evaluated separately at passage 0 showed a similar relative telomere length for CB-MSC 2 and 3, while CB-MSC 1 had a telomere length significantly shorter (three times).

Steady-State Gene Expression Profile Along Prolonged Culture

The genes analyzed included typical MSC differentiation markers: C/EBP-β for adipogenesis, COL10A1 for chondrogenesis, and ALP and OSTERIX for osteogenesis. Additionally, genes typically expressed by cells from other lineages, such as neural cells [brain-derived neurotrophic factor (BDNF), MUSASHI, sex-determining region y-box 2 (SOX2)], or implicated in the angiogenic [angiopoietin 1 (ANGPT1), intercellular adhesion molecule 1 (ICAM-1), vascular cell adhesion molecule 1 (VCAM-1)] and myogenic (MYOD, PAX3) processes were considered. The mean gene expression levels of the CB-MSC populations evaluated together revealed stable and mostly unchanged expression along prolonged culture of the majority of the genes taken into consideration (Fig. 3C). The only genes that showed a steady increasing trend in their transcription levels, albeit not significant, were chondrocytic COL10A1 and ANGPT-1, whose expression lead to a threefold difference between P3 and P7 samples.

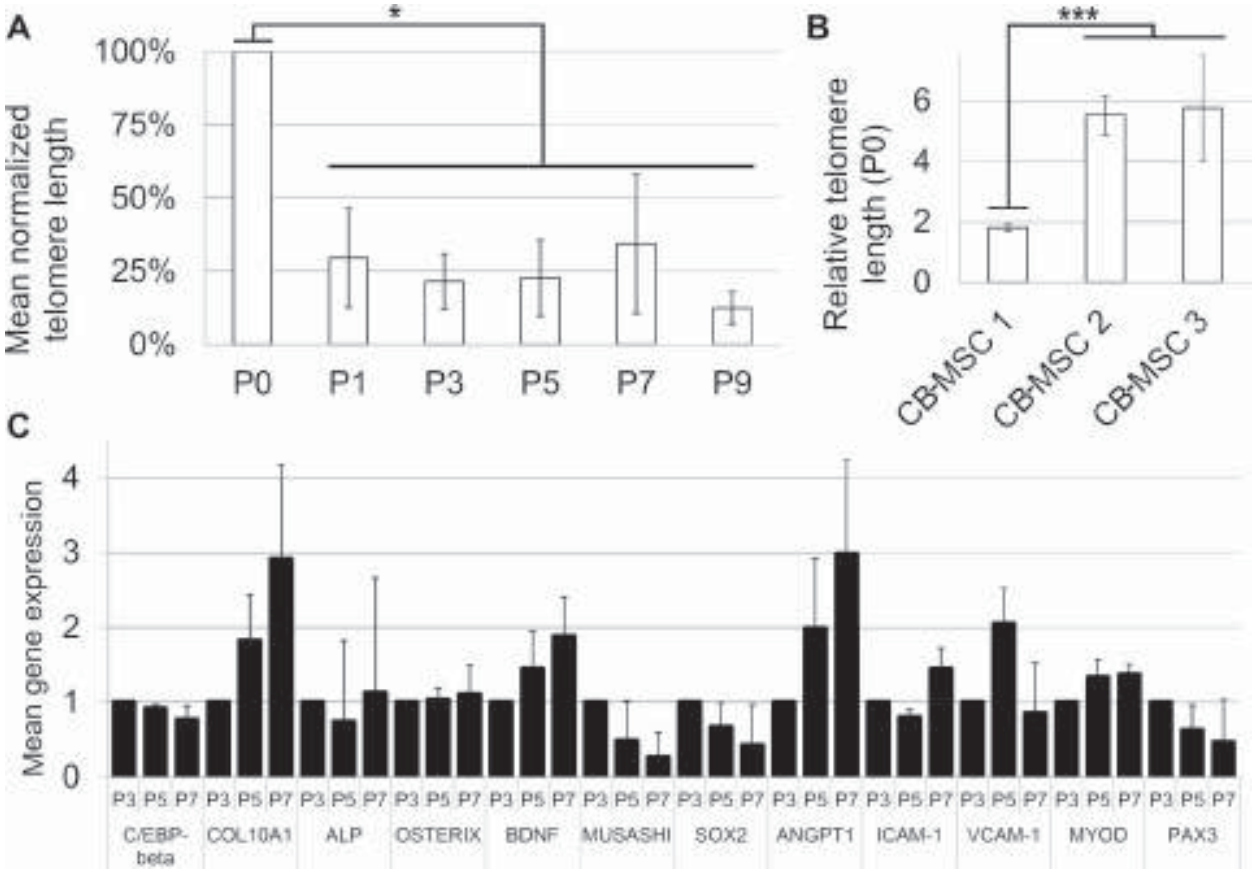

Figure 3. Telomere length. For telomere length analysis, passages 0, 1, 3, 5, 7, and 9 were studied. The histogram in (A) shows the mean value for each passage of the three analyzed CB-MSC populations with the standard deviation. The data are presented as percentage relative to P0 telomere length value. The histograms in (B) show mean value from triplicates of real-time qPCR analysis, again associated with standard deviation. ***$p \leq 0.005$; *$p \leq 0.05$. (C) Steady-state transcription profile. The mRNA levels (P3-5-7) of genes involved in adipogenesis, chondrogenesis, myogenesis, and osteogenesis were taken into consideration. Also the expression of neurotrophic and angiogenetic growth factors as well as neural and endothelial markers was analyzed. The histograms represent mean gene expression of the three CB-MSC populations analyzed, while the error bars show the corresponding standard error of the mean (SEM) values.

Immunophenotype of CB-MSC Populations

All CB-MSCs stained positively for canonical MSC surface markers CD90, CD105, and CD73, whereas they were negative for CD45 and CD34 (Fig. 4A) (data not shown for CB-MSC 3). A deeper analysis with a more extensive surface marker panel was applied to investigate if the observed differences among CB-MSCs in growth properties and passage 0 relative telomere length could correlate with a specific immunophenotype. With this in mind, CB-MSC 1 was compared to CB-MSC 2 at passages 3 and 5. CB-MSC 2 was considered representative of both CB-MSC 2 and 3 behavior, since they shared the same growth characteristics and telomere length. Both populations were strongly positive for CD146. In addition, CB-MSCs were completely negative for CD31, CD133, CD117, and CD144, and almost completely negative for α-smooth muscle actin (α-SMA) and stage-specific embryonic antigen-4 (SSEA4) (Fig. 4A). Concerning platelet-derived growth factor receptor (PDGFR)-β, nerve/glial antigen 2 (NG2), CD56, and CD271 some marked differences were observed (Fig. 4B). PDGFR-β, NG2, and CD56 were more expressed in CB-MSC 2. Mean fluorescence intensity (MFI) ratios summarized in Figure 4C showed a marked difference along passages for PDGFR-β in both populations. The case of CD271 was peculiar since CB-MSC 1 did not express CD271 at passages 3 nor 5, whereas CB-MSC 2 at passage 3 showed a portion of $CD271^+$ cells (MFI ratio = 5.0) corresponding clearly to a distinct subpopulation, as shown in the density plot in Figure 4D. However, this subpopulation was absent at passage 5 (MFI ratio = 1.8).

Maintenance of Differentiation Potential

To evaluate the differentiation potential some changes in the standard protocols were developed. Mostly because the proliferation potential of these CB-MSCs was too high, it was difficult to keep the standard induction protocols without an earlier cell detachment. CB-MSCs were differentiated toward the adipogenic, osteogenic, and chondrogenic lineages. Adipogenesis was confirmed by Oil red O staining of lipid vacuoles (Fig. 4E). Osteogenesis was assessed by Alizarin red S staining, which evidenced the conspicuous production of calcium deposits (Fig. 4F). Chondrogenesis was detected by presence of Alcian blue-positive cells (Fig. 4G). No macroscopic differences in the differentiation capacity toward the adipogenic, osteogenic, and chondrogenic lineages were observed for the three CB-MSC populations at the analyzed passage.

Identification of miRNA Expression Profiles

To unravel whether molecular differences could also be found between CB-MSC 2 and 3, which demonstrated homogenous cell growth, clonogenic properties, telomere length, and molecular signature, a whole-genome comparative gene expression profiling analysis was performed using arrays able to monitor the expression of 704 miRNA sequences. After a quality control procedure, 243 and 244 miRNAs out of the total 704 available sequences were detected in CB-MSC 2 and CB-MSC 3, respectively. In order to exclude potential erroneous miRNA expression changes introduced by handling or technical pitfalls, random individual real-time qRT-PCR reactions on cDNA obtained from two biological replicates of CB-MSC 2 and 3 were performed. Thus, the expression of two miRNAs belonging to unrelated families (miR-16 and -29b), both normalized with the small nuclear RNA RNU6-2 used as a housekeeper, was analyzed, and then the values were compared with those obtained in the arrays (also normalized with RNU6-2). As shown in Figure 5A and B, the independent samples showed consistent values (within twofold modulation) with the array data. We also checked whether the ratios between CB-MSC 2 and CB-MSC 3 in the single PCR amplifications for these two miRNAs were consistent in comparison with the array data and again such values did not show modulations higher than twofold units (Fig. 5C). All of these tests on independently processed and assayed samples confirmed the validity of the proposed array results, although the design of the arrays with single probes leaves open the possibility of few potential technical-dependent miRNA expression variations.

To compare miRNA expression patterns between CB-MSC 2 and 3, a pairwise comparison of the two expression profiles was performed generating a distribution of normalized intensity with a correlation coefficient of 0.96 (Fig. 5D). This finding demonstrates that the two CB-MSCs share a strikingly similar miRNA expression pattern, thus accounting for possible phenotypic and functional overlap. Nevertheless, a deeper characterization was undertaken selecting miRNAs with fourfold or higher differential expression, corresponding to a difference of at least two normalized Ct value units. Distinct molecular signatures were extracted consisting of increased expression of four miRNAs (miR-450a +10.4, miR-369-3p +4.5, miR-10a +4.1, miR-10b +4.1) and downregulation of one miRNA (miR-27a* −4.3) in CB-MSC 2 compared to CB-MSC 3. Notably, none of the differentially expressed miRNAs is among the most expressed ones. In fact, the five most expressed miRNAs are conserved and constant between the two CB-MSCs (miR-21, miR-125b, miR-16, miR-1260, and miR-199-a-3p) with the two most expressed (miR-21 and miR-125b) recently proposed as stem cell markers[22–24]. Next, a gene target identification for the five more differentially modulated miRNAs was performed using miRWalk, a database that presents literature information on experimentally validated miRNA interactions with genes[18]. Mining the miRWalk database, 239 validated targets were

A

	% expression			
	CB-MSC 1		CB-MSC 2	
	P3	P5	P3	P5
CD90	93.6	96.2	99.4	97.9
CD105	100.0	99.9	98.7	99.5
CD73	90.1	99.8	93.5	97.0
CD45	0.0	0.0	0.0	0.0
CD34	0.0	0.0	0.0	0.0
CD117	0.0	0.0	0.0	0.0
CD146	94.4	95.6	73.9	100.0
CD133	0.0	0.0	0.2	0.1
CD144	0.0	0.0	0.0	0.0
CD31	0.0	0.0	0.1	0.0
α-SMA	0.2	0.3	0.0	0.0
SSEA-4	0.1	0.7	0.1	0.7

C

	MFI ratio			
	CB-MSC 1		CB-MSC 2	
	P3	P5	P3	P5
PDGFR-B	9.7	2.0	25.0	6.3
NG2	3.1	2.8	139.7	137.9
CD56	4.4	3.9	69.9	38.0

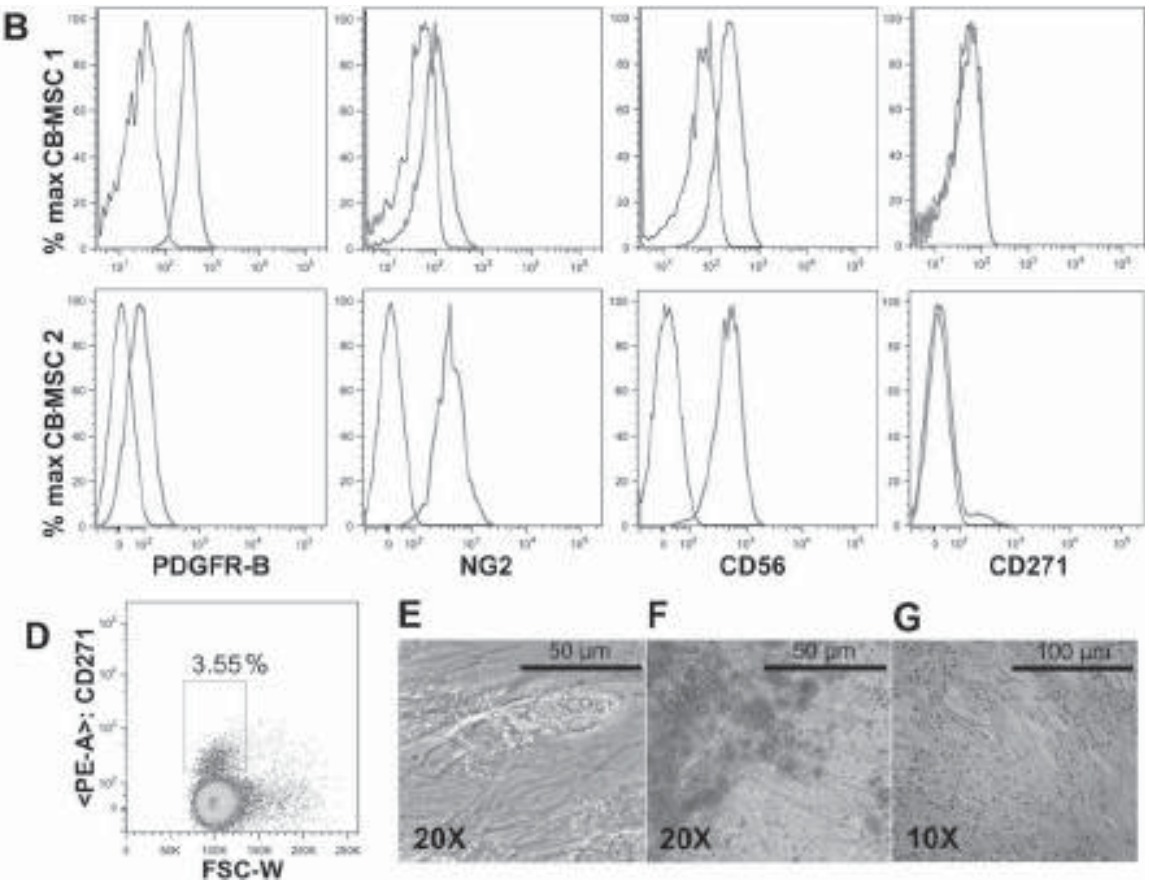

Figure 4. Immunoprofile of CB-MSCs. Classical MSC surface marker panel with percentages of expression (A) for passages 3 and 5 CB-MSCs. Representative histograms (P3) of some novel MSC surface markers show marked differences between the two populations (B). (C) summarizes MFI data for both analyzed passages. The dot plot (D) shows passage 3 $CD271^+$ CB-MSC 2 subpopulation and its percentage within the whole population. In the histograms and in the dot plot, for every plotted event the *y*-axis represents the percentage of maximum expression, while the *x*-axis shows fluorescence intensity on a logarithmic scale. (E–G) Differentiation properties of CB-MSCs. Representative images of CB-MSC-derived fat droplet-producing adipocyte-like cells, calcium deposit-producing osteocyte-like cells, and Alcian blue-positive chondrocyte-like cells are shown, respectively, in (E–G). No significant differences were observed with regard to differentiation capabilities between the different CB-MSC populations.

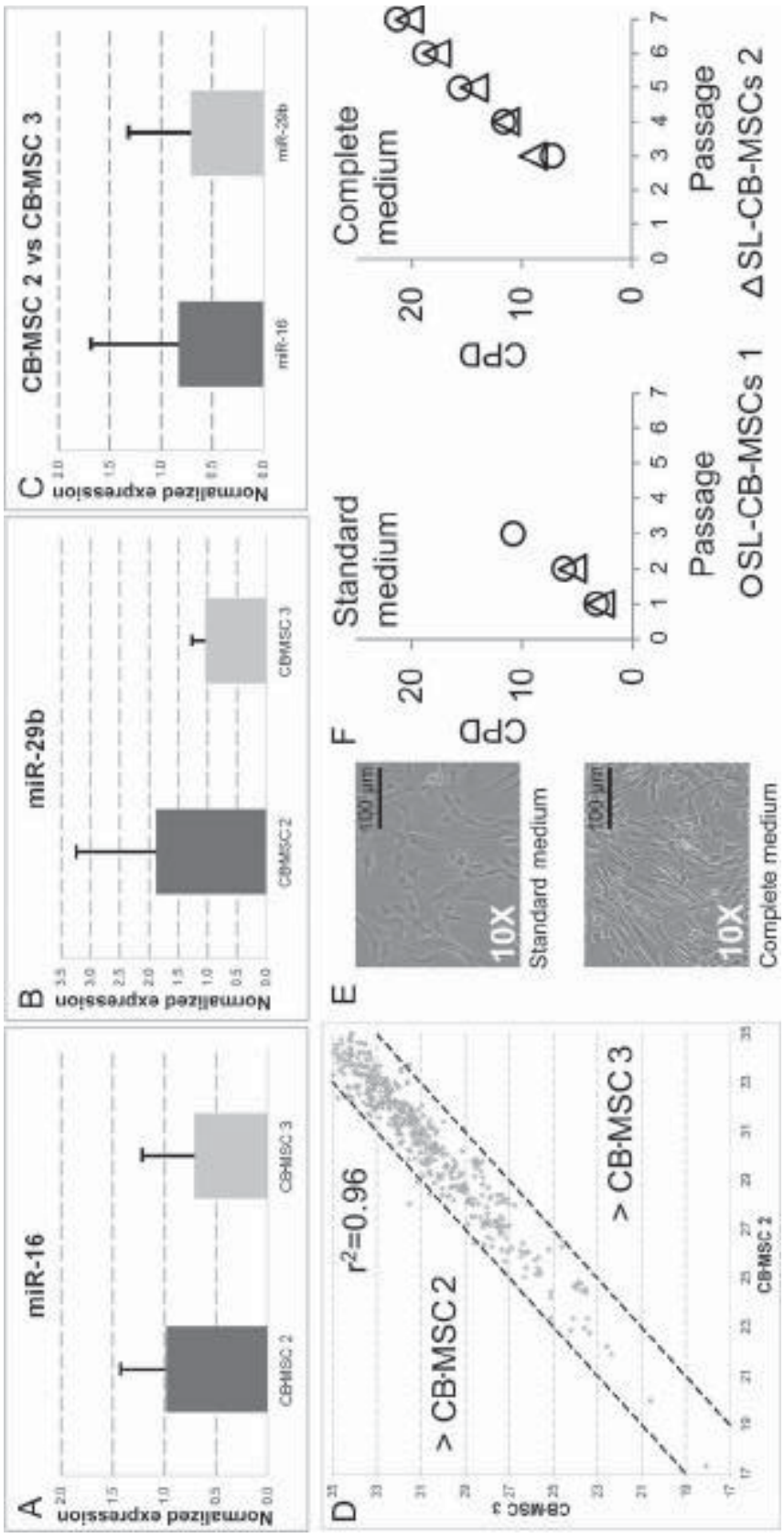

Figure 5. Validation of array data through real-time qRT-PCR on independent samples (A–C). Total RNA isolated from biological replicates of CB-MSC 2 and 3 samples was reverse transcribed and used in real-time qRT-PCR reactions to compare normalized expression levels (*y*-axis) of miR-16 and miR-29b with the normalized values obtained with microRNA arrays set as 1. None of the miRNAs differ by a factor higher than 2 (represented in the graphs by the black lines). Mean values and standard deviations of two independent biological replicates are shown. Comparison of genome-wide miRNA expression profiles (D). Correlation of miRNA expression levels (normalized Ct, *x*- and *y*-axis) between CB-MSC 2 and CB-MSC 3. Dotted lines represent a boundary corresponding to normalized Ct value difference of 2 U (fourfold differential expression). Rescue of short-living phenotype (E, F). Representative morphology of the same SL-CB-MSC population cultured either in standard or complete medium (E). Increased number of passages and CPD shown by SL-CB-MSCs cultured in the complete medium (Complete) and compared to those obtained by the same SL-CB-MSCs grown in the standard medium (Standard) are represented in the two graphs (F). For SL-CB-MSCs cultured in complete medium only the passages after thawing and switch to complete medium are shown.

shown to be regulated by these miRNAs. Then, on the identified genes, the GeneCodis software showed that the two most statistically enriched biological processes were connected with regulation of transcription [from RNA polymerase II promoter—Gene Ontology (GO): 0045944, $p<0.001$; DNA-dependent—GO: 0045893, $p<0.001$], a result in agreement with the most enriched cellular component of the submitted gene products that resulted to be the nucleus (GO: 0005634, $p<0.001$). Finally, such a relationship with gene regulation was supported by the molecular functions uncovered by these regulated genes that appeared to be directly linked with an enrichment in the protein-binding category (GO: 0005515, $p<0.001$), especially associated with DNA-binding transcription factor activity (GO: 0003700, $p<0.001$) and DNA-binding properties (GO: 0043565, $p<0.001$).

Rescue of SL-CB-MSC Short-Living Phenotype

Two SL-CB-MSC populations previously obtained in the standard medium were thawed at passage 2 and cultured in the complete medium to observe whether their short-living phenotype could be rescued. From a morphological point of view the cells grown in the standard medium seemed to possess a more spindle-like versus a more compact morphology, compared to the same cells grown in the complete medium (Fig. 5E). Strikingly, both SL-CB-MSC populations showed an increased life span and higher CPD peaks (from a value of 5.4-10.8 to 20.2-21.3), doubling the maximum number of passages (from P2–3 to P7) in the complete medium compared to the standard one (Fig. 5F). Notwithstanding this ameliorated growth kinetic, they did not reach the same high performances of CB-MSC 2 and 3 of the present study.

DISCUSSION

Over the last years, the clinical use of allogenic CB for hematopoietic stem cell (HSC) transplantation has increased dramatically, and more recently CB was also used as a source of MSCs[25]. Unfortunately, the low frequency of these MSCs in CB and the consequent low isolation efficiency still is a major problem, which keeps this source far from being widely recognized for its possible role in regenerative medicine. In this regard, several attempts and different methodological approaches have been implemented in order to more efficiently isolate MSCs from CB. Notwithstanding, this source still offers some advantages in comparison to the more classical ones, including the easy procurement, the absence of risks to donors, and the reduced risk of transmitting infections[26]. Up until now, one of the crucial CB characteristics that makes CB-MSC isolation feasible is the "freshness" of the CBU (≤2 h from CB collection to processing)[27].

In our laboratory we set up a standard strategy[10] allowing the isolation of long-living (P>7), high proliferative CB-MSCs with multipotent differentiation capabilities (LL-CB-MSCs). Yet, the efficiency of this process should be further improved, especially if clinical application is the final goal. In the last years several commercially available media have been proposed on the market for MSC culture; however, they are mainly developed and tested for MSCs from bone marrow and adipose tissue, whose isolation efficiency is close to 100%. In this context, with respect to the first goal of our work, we succeeded in defining some culture conditions for obtaining CB-MSC colonies at high efficiency, overcoming a major drawback, which hampers a widespread availability of this kind of therapeutic cell. The adopted strategy combines an immunodepletion treatment of CBUs and a chemically defined medium specifically developed for optimal MSC isolation and culture. In this way we also skipped the use of a collagen I–III coating that could possibly make the translation of this system in a clinical-grade setting in some countries more difficult. With this approach and a preference for rich-in-volume samples, the successful rate of CB-MSC colony generation was dramatically improved up to 79%, avoiding strict quality selection of the starting material in terms of cellularity and "freshness." In addition, no osteoclast-like cell contamination, which badly affects the newly born stromal colonies[28], was observed. This could be due to the presence of IGF-1 in the defined medium, which has been demonstrated to reduce monocyte adhesion properties[29]. The same effect was reported also for bFGF, the other growth factor present in the chemically defined medium[30].

The second goal of this work was to investigate the biological features of CB-MSCs obtained in this new isolation and culture system, focusing on growth properties, on the molecular pattern, and also on the protein level. The proliferation curves of the expanded CB-MSCs reached higher CPD peaks in comparison with CB-MSCs isolated and cultured under standard conditions[10], and they showed a stable, linear, and homogeneous growth. Based on the International Society for Cellular Therapy (ISCT) classification[31], the CB-MSCs obtained expressed the classical MSC markers and maintained them during passages and possess multipotent differentiation abilities. The cells were also able to generate colonies under low-density seeding conditions, even if their morphology differed from that of colonies obtained from CB-MSC cultured in standard conditions[10], being more compact and presenting a higher cell density. This again could be ascribed to the synergic action of IGF-1 and bFGF, which add their effect to that of serum growth factors.

Telomere length was dramatically decreased from passage 0 to passage 1, but then was maintained at the same level along culture, suggesting that the medium tested is not sufficient to prevent repetitive telomere sequence loss at the initial phases of the culture establishment, but nonetheless it could play some role in stabilizing its decrease.

Unfortunately, the extreme difficulty to have more than one colony able to give rise to a CB-MSC population from the same CBU has hampered, until now, the ability to perform proper experiments to address this issue, in which standard and novel media effects on telomere length could be compared. Some minor differences were found between the CB-MSC populations. In particular, telomere length dissimilarities correlated with different replicative potentials: CB-MSC 1 presented the shortest telomere and arrested its growth at passage 9, while CB-MSC 2 and 3 showed higher telomere length and could be cultured at least until passage 13.

Moving to an extensive immunophenotype profiling, some noncanonical surface markers were found to be expressed. These surface markers were all classic pericytic markers such as CD146, NG2, CD56, and even the more relevant PDGFR-β[32]. Intriguingly, pericytes have been proposed as the precursors and sort of in vivo counterpart of MSCs[33], so that such an immunophenotype could mirror a CB-MSC state reminiscent of its pericytic precursor.

In addition, CB-MSCs showed very homogenous gene expression profiles. The study revealed stable expression of key genes involved in distinct differentiation pathways, suggesting that the tested medium succeeded in maintaining the CB-MSC cultures in an undifferentiated state. To confirm the homogeneity found at the molecular level between the CB-MSCs endowed with the longest telomeres, we addressed their miRNA signatures using a miRNA array. Interestingly, we observed that in these CB-MSCs the most expressed miRNAs were stemness-related miR-21 and miR-125b[22–24].

Based on our recent report[10] describing two CB-MSC populations distinguished by telomere length and life span, we wondered if the analyzed populations were bona fide SL- and LL-CB-MSCs, even if characterized by growth properties enhanced by a culture medium much richer than the standard one. This hypothesis was substantiated by the "rescue" experiments, as SL-CB-MSCs previously isolated following the standard methodology increased the number of total passages and of population doublings in response to this novel culture system. Nevertheless, the "rescued" SL-CB-MSCs still possessed a shorter life span compared to LL-CB-MSCs, confirming that two distinct stromal populations exist in cord blood irrespective of the culture conditions adopted to isolate or maintain them. It is also true that even the observed partial rescue of the SL-CB-MSC short-living phenotype could represent a relevant effect to take into account when such a population is the only one isolated from a specific CB unit. This is of paramount importance, most of all in the context of private CB banking, where clinically relevant CB-MSC numbers must be obtained necessarily from related or autologous CBUs.

In conclusion, we assessed how medium composition can exert a heavy influence on cell behavior, so that our last message in the bottle is that new media with more complex composition than the standard ones can have advantages on cell culture, although a deep characterization is strongly encouraged to really define how the new culture system may modulate the cells you are dealing with.

ACKNOWLEDGMENTS: The authors would like to thank all the researchers working at our facility Cell Factory for their critical advices during the lab meetings. We are also grateful to the Milano Cord Blood group for their help in providing cord blood units for research. This work was partially supported by funds from Regione Lombardia (PB 0098), from Ministero della Salute Italiano ("Young Researchers" grants: R.F.G.R. 2010-2318448, R.F.G.R. 2010-2312573), and from European Union's Seventh Programme (Grant Agreement No. 241879). This work was part of the Ph.D. project of Mario Barilani for the Ph.D. School in Biosciences and Biotechnology curriculum Cell Biology of the University of Padoa. The authors declare no conflicts of interest.

REFERENCES

1. Wei X, Yang X, Han ZP, Qu FF, Shao L, Shi YF. Mesenchymal stem cells: A new trend for cell therapy. Acta Pharmacol Sin. 2013;34(6):747–54.
2. Das M, Sundell IB, Koka PS. Adult mesenchymal stem cells and their potency in the cell-based therapy. J Stem Cells 2013;8(1):1–16.
3. Caplan AI, Correa D. The MSC: An injury drugstore. Cell Stem Cell 2011;9(1):11–15.
4. Rani S, Ryan AE, Griffin MD, Ritter T. Mesenchymal stem cell-derived extracellular vesicles: Toward cell-free therapeutic applications. Mol Ther. 2015;23(5):812–23.
5. Ragni E, Montemurro T, Montelatici E, Lavazza C, Vigano M, Rebulla P, Giordano R, Lazzari L. Differential microRNA signature of human mesenchymal stem cells from different sources reveals an "environmental-niche memory" for bone marrow stem cells. Exp Cell Res. 2013;319(10):1562–74.
6. Bieback K, Kluter H. Mesenchymal stromal cells from umbilical cord blood. Curr Stem Cell Res Ther. 2007;2(4):310–23.
7. Morigi M, Rota C, Montemurro T, Montelatici E, Lo Cicero V, Imberti B, Abbate M, Zoja C, Cassis P, Longaretti L, Rebulla P, Introna M, Capelli C, Benigni A, Remuzzi G, Lazzari L. Life-sparing effect of human cord blood-mesenchymal stem cells in experimental acute kidney injury. Stem Cells 2010;28(3):513–22.
8. Pham PV, Vu NB, Pham VM, Truong NH, Pham TL, Dang LT, Nguyen TT, Bui AN, Phan NK. Good manufacturing practice-compliant isolation and culture of human umbilical cord blood-derived mesenchymal stem cells. J Transl Med. 2014;12:56.
9. Bieback K, Kern S, Kluter H, Eichler H. Critical parameters for the isolation of mesenchymal stem cells from umbilical cord blood. Stem Cells 2004;22(4):625–34.
10. Barilani M, Lavazza C, Vigano M, Montemurro T, Boldrin V, Parazzi V, Montelatici E, Crosti M, Moro M, Giordano R, Lazzari L. Dissection of the cord blood stromal component reveals predictive parameters for culture outcome. Stem Cells Dev. 2015;24(1):104–14.
11. Zhong X, Rescorla FJ. Cell surface adhesion molecules and adhesion-initiated signaling: understanding of anoikis resistance mechanisms and therapeutic opportunities. Cell Signal. 2012;24(2):393–401.

12. Ragni E, Parazzi V, Crosti M, Moro M, Giordano R, Lazzari L. Diet composition transiently modulates proliferative and potency features of human cord blood-derived mesenchymal stem cells. Int J Biochem Cell Biol. 2014;55:269–78.
13. Samsonraj RM, Raghunath M, Hui JH, Ling L, Nurcombe V, Cool SM. Telomere length analysis of human mesenchymal stem cells by quantitative PCR. Gene 2013;519(2): 348–55.
14. Ragni E, Vigano M, Rebulla P, Giordano R, Lazzari L. What is beyond a qRT-PCR study on mesenchymal stem cell differentiation properties: How to choose the most reliable housekeeping genes. J Cell Mol Med. 2013;17(1):168–80.
15. Vandesompele J, De Preter K, Pattyn F, Poppe B, Van Roy N, De Paepe A, Speleman F. Accurate normalization of real-time quantitative RT-PCR data by geometric averaging of multiple internal control genes. Genome Biol. 2002;3(7):RESEARCH0034.
16. D'Haene B, Mestdagh P, Hellemans J, Vandesompele J. miRNA expression profiling: from reference genes to global mean normalization. Methods Mol Biol. 2012;822: 261–72.
17. Koh W, Sheng CT, Tan B, Lee QY, Kuznetsov V, Kiang LS, Tanavde V. Analysis of deep sequencing microRNA expression profile from human embryonic stem cells derived mesenchymal stem cells reveals possible role of let-7 microRNA family in downstream targeting of hepatic nuclear factor 4 alpha. BMC Genomics 2010;11(Suppl 1):S6.
18. Dweep H, Sticht C, Pandey P, Gretz N. miRWalk–database: Prediction of possible miRNA binding sites by "walking" the genes of three genomes. J Biomed Inform. 2011;44(5):839–47.
19. Carmona-Saez P, Chagoyen M, Tirado F, Carazo JM, Pascual-Montano A. GENECODIS: A web-based tool for finding significant concurrent annotations in gene lists. Genome Biol. 2007;8(1).
20. Nogales-Cadenas R, Carmona-Saez P, Vazquez M, Vicente C, Yang X, Tirado F, Carazo JM, Pascual-Montano A. GeneCodis: Interpreting gene lists through enrichment analysis and integration of diverse biological information. Nucleic Acids Res. 2009;37(Web Server issue):W317–22.
21. Tabas-Madrid D, Nogales-Cadenas R, Pascual-Montano A. GeneCodis3: A non-redundant and modular enrichment analysis tool for functional genomics. Nucleic Acids Res. 2012;40(Web Server issue):W478–83.
22. Zhang Y, Xie RL, Croce CM, Stein JL, Lian JB, van Wijnen AJ, Stein GS. A program of microRNAs controls osteogenic lineage progression by targeting transcription factor Runx2. Proc Natl Acad Sci USA 2011;108(24):9863–8.
23. Yu X, Cohen DM, Chen CS. miR-125b Is an adhesion-regulated microRNA that protects mesenchymal stem cells from anoikis. Stem Cells 2012;30(5):956–64.
24. Mizuno Y, Yagi K, Tokuzawa Y, Kanesaki-Yatsuka Y, Suda T, Katagiri T, Fukuda T, Maruyama M, Okuda A, Amemiya T, Kondoh Y, Tashiro H, Okazaki Y. miR-125b inhibits osteoblastic differentiation by down-regulation of cell proliferation. Biochem Biophys Res Commun. 2008;368(2):267–72.
25. Kikuchi-Taura A, Taguchi A, Kanda T, Inoue T, Kasahara Y, Hirose H, Sato I, Matsuyama T, Nakagomi T, Yamahara K, Stern D, Ogawa H, Soma T. Human umbilical cord provides a significant source of unexpanded mesenchymal stromal cells. Cytotherapy 2012;14(4):441–50.
26. Zhong XY, Zhang B, Asadollahi R, Low SH, Holzgreve W. Umbilical cord blood stem cells: what to expect. Ann NY Acad Sci. 2010;1205:17–22.
27. Zhang X, Hirai M, Cantero S, Ciubotariu R, Dobrila L, Hirsh A, Igura K, Satoh H, Yokomi I, Nishimura T, Yamaguchi S, Rubinstein P, Takahashi TA. Isolation and characterization of mesenchymal stem cells from human umbilical cord blood: Reevaluation of critical factors for successful isolation and high ability to proliferate and differentiate to chondrocytes as compared to mesenchymal stem cells from bone marrow and adipose tissue. J Cell Biochem. 2011;112(4):1206–18.
28. Attar A, Langeroudi AG, Vassaghi A, Ahrari I, Maharlooei MK, Monabati A. Role of CD271 enrichment in the isolation of mesenchymal stromal cells from umbilical cord blood. Cell Biology Int. 2013;37(9):1010–5.
29. Zhang Q, Jiang Y, Toutounchian JJ, Soderland C, Yates CR, Steinle JJ. Insulin-like growth factor binding protein-3 inhibits monocyte adhesion to retinal endothelial cells in high glucose conditions. Mol Vis. 2013;19:796–803.
30. Zhang H, Issekutz AC. Down-modulation of monocyte transendothelial migration and endothelial adhesion molecule expression by fibroblast growth factor: Reversal by the anti-angiogenic agent SU6668. Am J Pathol. 2002;160(6): 2219–30.
31. Dominici M, Le Blanc K, Mueller I, Slaper-Cortenbach I, Marini F, Krause D, Deans R, Keating A, Prockop D, Horwitz E. Minimal criteria for defining multipotent mesenchymal stromal cells. The International Society for Cellular Therapy position statement. Cytotherapy 2006;8(4):315–7.
32. Crisan M, Yap S, Casteilla L, Chen CW, Corselli M, Park TS, Andriolo G, Sun B, Zheng B, Zhang L, Norotte C, Teng PN, Traas J, Schugar R, Deasy BM, Badylak S, Buhring HJ, Giacobino JP, Lazzari L, Huard J, Péault B. A perivascular origin for mesenchymal stem cells in multiple human organs. Cell Stem Cell 2008;3(3):301–13.
33. Murray IR, West CC, Hardy WR, James AW, Park TS, Nguyen A, Tawonsawatruk T, Lazzari L, Soo C, Peault B. Natural history of mesenchymal stem cells, from vessel walls to culture vessels. Cell Mol Life Sci. 2014;71(8):1353–74.

Biomaterials 75 (2016) 135–147

Contents lists available at ScienceDirect

Biomaterials

journal homepage: www.elsevier.com/locate/biomaterials

A new three dimensional biomimetic hydrogel to deliver factors secreted by human mesenchymal stem cells in spinal cord injury

Ilaria Caron [a, 1], Filippo Rossi [b, 1], Simonetta Papa [a], Rossella Aloe [a], Marika Sculco [a], Emanuele Mauri [b], Alessandro Sacchetti [b], Eugenio Erba [c], Nicolò Panini [c], Valentina Parazzi [d], Mario Barilani [d], Gianluigi Forloni [a], Giuseppe Perale [e], Lorenza Lazzari [d], Pietro Veglianese [a, *]

[a] Dipartimento di Neuroscienze, IRCCS Istituto di Ricerche Farmacologiche "Mario Negri", via La Masa 19, 20156 Milan, Italy
[b] Dipartimento di Chimica, Materiali e Ingegneria Chimica "Giulio Natta", Politecnico di Milano, via Mancinelli 7, 20131 Milan, Italy
[c] Dipartimento di Oncologia, IRCCS Istituto di Ricerche Farmacologiche "Mario Negri", via La Masa 19, 20156 Milan, Italy
[d] Unit of Cell Therapy and Cryobiology, Fondazione IRCCS Ca' Granda Ospedale Maggiore Policlinico, via Francesco Sforza 35, 20122 Milan, Italy
[e] Department of Innovative Technologies, University of Applied Sciences and Arts of Southern Switzerland, SUPSI, via Cantonale, CH-6928 Manno, Switzerland

ARTICLE INFO

Article history:
Received 11 August 2015
Received in revised form
8 October 2015
Accepted 9 October 2015
Available online 22 October 2015

Keywords:
Spinal cord injury
Hydrogels
Human mesenchymal stem cells
Extracellular matrix
Inflammation
Macrophages

ABSTRACT

Stem cell therapy with human mesenchymal stem cells (hMSCs) represents a promising strategy in spinal cord injury (SCI). However, both systemic and parenchymal hMSCs administrations show significant drawbacks as a limited number and viability of stem cells in situ. Biomaterials able to encapsulate and sustain hMSCs represent a viable approach to overcome these limitations potentially improving the stem cell therapy. In this study, we evaluate a new agarose/carbomer based hydrogel which combines different strategies to optimize hMSCs viability, density and delivery of paracrine factors. Specifically, we evaluate a new loading procedure on a lyophilized scaffold (soaked up effect) that reduces mechanical stress in encapsulating hMSCs into the hydrogel. In addition, we combine arginine–glycine–aspartic acid (RGD) tripeptide and 3D extracellular matrix deposition to increase the capacity to attach and maintain healthy hMSCs within the hydrogel over time. Furthermore, the fluidic diffusion from the hydrogel toward the injury site is improved by using a cling film that oriented efficaciously the delivery of paracrine factors *in vivo*. Finally, we demonstrate that an improved combination as here proposed of hMSCs and biomimetic hydrogel is able to immunomodulate significantly the pro-inflammatory environment in a SCI mouse model, increasing M2 macrophagic population and promoting a pro-regenerative environment in situ.

1. Introduction

Many treatments (neuroprotective and/or neuroregenerative) have been proposed to counteract the neuropathological evolution of spinal cord injury (SCI) [1–5]. Among these, stem cell therapy represents a promising strategy [6–8] and accumulating data show that human mesenchymal stem cells (hMSCs) could be a real therapeutic approach in tissue repair after SCI [9–11]. Indeed, coherently with a multi-faceted SCI neuropathology, hMSCs are potentially able to counteract many harmful events and to sustain regeneration through several processes [10]. Different therapeutic effects have been proposed for hMSCs, but it is now well known that a paracrine effect [12], instead of a potential differentiation or transdifferentiation into neuronal or glial cells [13,14], is the most promising approach to exploit the therapeutic efficacy of the hMSCs [12,15,16]. In fact, hMSCs can act therapeutically by releasing exogenous trophic factors [17,18] and/or by modulating, through several factors, the immune system response [19–21]. However, different limitations are still to be overcome in using hMSCs as therapeutic opportunity in SCI. Specifically, cell therapy delivered systemically (intravenous injections) could lead to a limited efficacy due to the unfeasibility of the cells to cross the blood brain barrier

* Corresponding author.
E-mail address: pietro.veglianese@marionegri.it (P. Veglianese).
[1] These authors contributed equally to this work.

http://dx.doi.org/10.1016/j.biomaterials.2015.10.024
0142-9612/

(BBB) and reach the injured site where they could be more useful [22–24]. Furthermore, a cellular systemic administration may give rise to potential side effects (pulmonary embolus) [25] that should not be underestimated. On the other side, an intrathecal injection could cause the loss of many cells in the intrathecal space or in the cerebrospinal fluid [24,26] or could stress and damage cells through mechanical forces [27], thwarting the effort to treat directly the injured site. Another proposed approach is a direct injection in the parenchyma, however, this could lead to a limited viability of stem cells due to both ischemia [28,29] and adverse environment in the injured site that follow SCI [29,30]. In order to overcome these drawbacks, new delivery strategies have been proposed by using original biomaterials [30–32]. Particularly, hydrogels offer the possibility to load and sustain both *in vitro* and *in vivo* hMSCs creating an optimal niche close to the injured site, but preserving them from the hostile tissue [30,33]. A variety of hydrogels (natural or synthetic) has been proposed as scaffolds able to allocate different stem cells [32,34–36]. Nevertheless, these scaffolds have been evaluated only for their own capacity to maintain the cell viability for a short time *in vitro* [37,38] and very few attempts have been proposed for an *in vivo* treatment [39,40]. However, an optimized scaffold able to act as a reservoir of neuroprotective factors secreted by hMSCs has not been developed and investigated yet. There are some concerns in using these scaffolds as potential reservoir *in vivo*. One relevant limit in the maintenance of stem cells allocated in a scaffold is the loss of adhesion due to the scaffold structural properties that do not represent appropriately a biological niche. In particular, a specific cell death (anoikis) occurred when hMSCs are not able to adhere to a biologic supportive niche such as an appropriate extracellular matrix (ECM) [6,41]. ECM has been demonstrated to be a crucial element to sustain hMSCs adhesion, trophic support and survival [42–44], maintaining and preserving also their stemness [45]. So far, only a few studies have been performed to mimic a sustainable ECM for hMSCs in 3D scaffolds. But just one single molecule at time (e.g. fibrin, laminin, collagen, fibronectin or arginine–glycine–aspartic acid (RGD) peptide) has been proposed and characterized [35,46–48]. However, these approaches could not be able to favor appropriately hMSCs adhesion to the scaffold since they do not mimic native ECM that is a combination of several proteins, cytokines and growth factors [49]. Thus, an alternative supporting strategy able to improve the adhesion and viability of the stem cells into the hydrogel is needed. In this study, we propose a new biomaterial coated with 3D ECM, with the aim to create a more optimized niche able to better sustain hMSCs viability and healthy.

2. Materials and methods

2.1. Hydrogels synthesis

Hydrogels were prepared by batch reaction in a phosphate buffered saline solution (PBS, Sigma–Aldrich) at about 80 °C in which a polymeric solution was achieved by stirring polymers: carbomer 974p (branched polyacrylic acid, MW = 1 MDa, Fagron), agarose (MW = 300 kDa, Invitrogen) and polyethylene glycol (PEG, MW = 2000 Da, Sigma–Aldrich). The composition is: 9 mL PBS, 50 mg carbomer 974p, 300 mg PEG and 50 mg agarose [50]. The reaction pH was indeed kept neutral with NaOH 1 N. The effective gelation and reticulation were achieved by means of electromagnetic stimulation (500 W power irradiated) for 15 s per 5 mL of polymeric solution. The mixing reactor was kept closed to avoid any eventual loss of solvent vapors, and the gelation was then achieved in a 48 multiwell cell culture plate (0.25 mL each with the cylinder diameter of 1.1 cm) in which the gelling solution was poured during cooling.

2.2. RGD hydrogel synthesis

RGD functionalized hydrogels (HG RGD) were prepared as presented in previous work [51]. Briefly, the peptide was synthesized manually using the stepwise solid phase Fmoc method and then functionalized with azide group (RGD-azide). Polyacrylic acid (PAA, MW = 130 kDa) with propargyl group was synthesized and dialyzed (PAA-propargyl). RGD-azide (25 mg) was suspended in THF (5 mL) and PAA-propargyl (78 mg) was dissolved in distilled water (10 mL). Two solutions were blended together and added copper iodide (2.2 mg, 0.0116 mmol) and sodium ascorbate (2.2 mg, 0.0111 mmol). The reaction mixture was allowed to stir for 24 h at 60 °C. Subsequently, it was cooled at 25 °C and dialyzed against acid solution consisting of distilled water (2000 mL), sodium chloride (11.2 g) and HCl 37% w/w to reach pH = 5; dialysis occurred for three days, with daily replacement of dialysis solution. Finally, the mixture was frozen at −20 °C and then lyophilized and stored for further use. PAA functionalized is blended in PBS at room temperature, until complete dissolution together with branched PAA (carbomer 974p). PEG is subsequently added and the system kept stirred for 45 min; then the mixing is left to settle. The composition is: 9 mL PBS, 40 mg carbomer 974p, 10 mg PAA-RGD, 300 mg PEG, 50 mg agarose. NaOH 1 N is then added to adjust pH to 7.4 and then, after the addition of agarose powder which is not soluble at room temperature, the system is subjected to electromagnetic stimulation (500 W irradiated power), heating up to 70–80 °C to induce condensation reactions, through interconnections of hydroxyl groups. PAA carboxyl groups constitute crosslinking sites to be reacted with hydroxyl groups from agarose and PEG, forming ester bonds and altogether giving rise to the three dimensional matrix. Mixing reactor was kept closed to avoid any eventual loss of solvent vapors and the gelation was then achieved in a 48 multiwell cell culture plate (0.25 mL each and with the cylinder diameter of 1.1 cm) where the gelling solution was poured during cooling. In order to obtain lyophilized scaffolds, hydrogels were frozen on dry ice for 5 min, transferred at −80 °C over night and then dried in the following conditions: 1 mbar and −45 °C. The lyophilized gels were sterilized for at least 3 h by UV illumination before cells seeding. Obtained freeze-dried hydrogels resemble a sponge and for this reason here after they are indicated as sponge-like hydrogels.

2.3. Cord blood human mesenchymal stem cells culture

Umbilical cord blood was collected from normal deliveries, after written informed consent, in a multiple system bag (Macho-pharma) containing 29 mL of citrate phosphate dextrose as anticoagulant. Briefly, whole blood was centrifuged at 1900 rpm for 15 min, the plasma subsequently discarded and the buffy coat with a portion of red blood cells collected was immunodepleted of CD3+, CD14+, CD38+, CD19+, glycophorin A and CD66b+ using a commercial kit RosetteSep® (StemCell Technologies), according to manufacturer's instructions. In summary, the sample was incubated with 50 μL/mL RosetteSep MSC enrichment cocktail for 20 min at room temperature to isolate MSC precursors.

The buffy coat was then diluted 1:2 with phosphate buffered saline (PBS; Gibco), ethylenediaminetetraacetic acid (EDTA; Sigma–Aldrich) and human serum albumin (HAS; Kedrion), and separated under standard density gradient conditions (Ficoll Paque Plus 1.077 ± 0.001 g/L; GE Healthcare). After, mononuclear cells were then plated at 1×10^6 cells/cm^2 in standard medium: alphaMEM-GlutaMAX (Invitrogen) supplemented with 20% fetal bovine serum (FBS, Life Technologies).

Cultures were maintained at 37 °C in a humidified atmosphere containing 5% CO_2. After 48 h, non-adherent cells were removed and fresh medium was added. At 80% confluence, the cells were

harvested using 25% TrypLE Select 1× (Gibco) and subcultured at a concentration of 4 × 10^3 cells/cm^2 until passage 3 [52]. From passage 3, when the cell population was homogenous with no hematopoietic contamination, human mesenchymal stem cells (hMSCs) were used for *in vitro* and *in vivo* experiments. hMSCs populations derived from ten umbilical cord blood unit, already established and fully characterized for optimal growth properties and defined as long living (LL)-CBMSCs [52], were used for this study. hMSCs identity definition is presented as supplementary information (Fig. S1). All experiments have been conducted according to the principles expressed in the declaration of Helsinki.

2.4. Classic loading

hMSCs were harvested and suspended at a density of 5 × 10^6 cells/mL in growth medium supplemented with 2× FBS. Hydrogels were prepared as described above by mixing polymer powders in PBS. The hydrogel was heated at 80 °C to start gelation. When hydrogel solution temperature fell below 40 °C, a 1:1 solution of cells and hydrogel was prepared (20 μL cells and 20 μL hydrogel). Cells and hydrogel were mixed together and the final solution was pipetted into polystyrene cylinders (5 mm diameter) and let it polymerize for 30 min in incubator at 37 °C. After polymerization, growth medium was added to polymerized hydrogels containing cells. Each hydrogel contained approximately 100,000 cells.

2.5. Sponge-like loading

hMSCs were harvested and suspended at a density of 1.25 × 10^6 cells/mL in growth medium. 80 μL of cells were added directly onto the sponge-like hydrogel (40 μL for each side). Hydrogels were let to swell for 30 min in incubator at 37 °C and then 1 mL of growth medium was added. Each hydrogel contained approximately 100,000 cells.

2.6. ECM quantification

After 1, 7, 14 and 21 days after hMSCs seeding on sponge-like HG RGD, the ECM deposition was quantified by Sirius Red staining. Sirius Red is a method for collagen staining and it allows the evaluation of the ECM deposition overtime [53,54]. In particular, hydrogels were decellularized with an ammonium hydroxide buffer containing Triton X-100, in order to remove cells but preserving ECM deposition, as reported by Prewitz et al. [55] Briefly, hydrogels were immersed in a warm solution containing 0.5% of Triton X-100 and 20 mM of ammonium hydroxide in PBS in fast agitation for 10 min. After 3 washes in PBS, the ECM was stained by picro Sirius Red solution composed of 1% of Sirius Red (Direct Red 80, Sigma–Aldrich) in a saturated aqueous solution of picric acid (Sigma–Aldrich) that was added to the hydrogels and maintained for 30 min at room temperature. Then the excess of staining was eliminated by 3 washes with acidified water (0.5% of acetic acid in distilled water). To quantify the ECM staining, the Sirius Red dye was extracted from the hydrogel through a solution of 0.05 M NaOH and methanol [1:1], in which hydrogels were immersed for 1 h. The obtained solution was evaluated by a spectrophotometer (Infinite M200, TECAN) at an absorbance of 540 nm.

2.7. Extracellular matrix (ECM) deposition

hMSCs were let to grow for 14 days on sponge-like HG RGD. Then all the liquids around hydrogel were removed and the hydrogels were frozen on dry ice for 5 min and then transferred at −80 °C overnight. The lyophilization procedure was conducted as reported above.

2.8. Cellular density and viability analyses in vitro

hMSC density and survival were determined by analyzing confocal images of live cells stained with calcein AM (1:1000, Invitrogen). Calcein AM is a non-fluorescent cell-permeant dye that is converted to a green-fluorescent calcein after acetoxymethyl ester hydrolysis by intracellular esterases. It was added to the well containing hydrogels for 30 min at 37 °C. Then the medium was removed and substituted with fresh growth medium. hMSCs within the scaffold were stained with Calcein AM and acquired by confocal microscope (Olympus Fv1000) equipped with Laser 488. Three optical sections of the hydrogels spaced of 80 μm were acquired at 10× magnification. The number of calcein AM positive cells was measured using a “surface detection” tool of Imaris software (Bitplane). The number of cells was evaluated as cellular density (cells/mm^2).

2.9. Scanning Electron Microscopy (SEM)

SEM analysis was performed in sponge-like HG RGD and HG RGD + ECM after 1 day from hMSCs seeding. Each hydrogel was fixed overnight in a buffer containing 1.5% of glutaraldehyde in 0.1 M of sodium cacodylate. Then hydrogels were dehydrated in an increasing scale of alcohols and frozen at −80 °C overnight. Before SEM analysis hydrogels were dried and gold coated and then analyzed at 10 kV with Evo 50 EP Instrumentation (Zeiss).

2.10. Cellular differentiation assays

hMSC differentiation after encapsulation in HG RGD + ECM was assessed by Real Time PCR. The gene expression for the three main mesodermal lineage differentiation (osteogenic, chondrogenic and adipogenic) was performed. Sponge-like HG RGD + ECM containing hMSCs cultured for 21 days in growth medium were analyzed. As positive control, hMSCs cultured in HG RGD for 21 days and treated with differentiation media were analyzed. In particular, to promote adipogenesis, osteogenesis and chondrogenesis, commercial media (Lonza S.p.A.) were used, and the manufacturer's protocols were followed or slightly modified [52]. For information about differentiation media full composition please refer to www.lonza.com. Data are expressed as fold change compared to steady-state undifferentiated hMSCs (negative control). Hydrogels were homogenized and RNA was extracted using RNeasy mini kit (Qiagen), according to manufacturer's instructions. Briefly, hydrogels containing cells were suspended in QIAzol Lysis Reagent and homogenized with a tissue grinder. Chloroform was added to the homogenate and a phase extraction performed. 0.3 mL of the aqueous phase were added to 450 μL of ethanol and loaded onto an RNeasy column. The column was washed and RNA eluted in 50 μL of RNAse free water. RNA was quantified by a spectrophotometer (Infinite M200, TECAN) at 260 nm for all samples, frozen at −20 °C and stored until use.

Reverse transcription was carried out using iScriptTM cDNA Synthesis Kit (Bio-Rad Laboratories Ltd). Real time PCR was performed on a CFX96 Real Time System using Sso FastEva Green Super mix (Bio-Rad), according to the manufacturer's instructions. The expression of the following genes was evaluated: alkaline phosphatase (ALP), runt-related transcription factor 2 (RUNX2) and osterix are genes involved in various stages of osteogenic differentiation [56]; aggrecan (ACAN) and type 10 collagen alpha 1 (COLLX) are genes correlated to the late phase of chondrogenic differentiation [57]; adipsin and fatty acid binding-protein 4 (FABP4) are genes actively expressed during the late phase of adipogenic differentiation [58]. Ribosomal protein large P0 (RPLP0) gene expression was used as control [59]. Specific primers used are listed below:

- adipsin (Fw: GACACCATCGACCACGA; Rev: CACGTCGCAGAGA GTTC);
- FABP4 (Fw: AAAGAGAAAACGAGAGGATGA; Rev: AACGTCCCTTG GCTTATG);
- RUNX2 (Fw: AAGGCTGCAAGCAGTATTTACAA; Rev: CTCGGATCCC AAAAGAAGTTTTGCT);
- osterix (Fw: CCTGCTTGAGGAGGAAGTTCA; Rev: AGAGTTGTTGA GTCCCGCAG);
- ALP (Fw: TACAAGGTGGTGGGCGGTGAACGA; Rev: TGGCGCAGGG GCACAGCAGAC);
- ACAN (Fw: TCGCCAGGTGTGTGGGACTGA; Rev: ACTCAGCGAGT TGTCATGGTCTGA);
- COLLX (Fw: ACTCCCAGCACGCAGAATCCA; Rev: TGGGCCTTTTAT GCCTGTGGGC);
- RPLP0 (Fw: TGTGGGCTCCAAGCAGATGCA; Rev: GCAGCAGTTTC TCCAGAGCTGGG).

2.11. Surgery

Procedures involving animals and their care were conducted in accordance with institutional guidelines at the IRCCS — Institute for Pharmacological Research "Mario Negri" in compliance with national (Decreto Legge nr.116/92, Gazzetta Ufficiale, supplement 40, February 18, 1992; Circolare nr. 8, Gazzetta Ufficiale, July 14, 1994) and international laws and policies (EEC Council Directive 86/609, OJL 358, 1, Dec. 12, 1987; Guide for the Care and Use of Laboratory Animals, US National Research Council, 8th edition, 2011).

Adult C57BL/6J female mice (23–30 g) were anesthetized by intraperitoneal injection of ketamine hydrochloride (IMALGENE, 100 mg/kg) and medetomidine hydrochloride (DOMITOR, 1 mg/kg). Before surgery, animals received an antibiotic and analgesic subcutaneous treatment with Ampicillin (50 mg/kg) and Buprenorfin (0.15 mg/kg), respectively. The back of the animals was shaved at the dorsal level and a cutaneous incision was made to expose the backbone. Animals were placed on a Cunningam Spinal Cord Adaptor (Stoelting) mounted on a stereotaxic frame. A laminectomy at the T12 level was done to uncover the lumbar spinal cord. A moderate compression of the spinal cord was obtained using an aneurysm clip (30 g compressive force for 60 s) as described previously [50].

2.12. Cellular staining for in vivo tracking

Before the seeding in the scaffold, hMSCs were stained with the marker of cellular viability 5-6-Carboxyfluorescein diacetate N-succinimidyl ester (CFDA-SE, Sigma–Aldrich), a cell-permeant fluorescent based tracer for long-term viable cell labeling. In particular, suspended cells were incubated for 30 min at 37 °C with pre-warmed CFDA-SE solution in PBS (final concentration 5 μM). Then, 5 times the original staining volume of medium was added in order to remove any free dye remaining in the solution. Cells were then incubated for 5 min at 37 °C. Finally, cells were centrifuged at 300 g for 10 min, resuspended in pre-warmed complete culture medium and deposited in sponge-like HG RGD + ECM.

2.13. In vivo positioning of hMSC in HG RGD + ECM

hMSCs were encapsulated for 1 day in sponge-like HG RGD + ECM. Then, hMSCs loaded HG RGD + ECM (a total of 25,000 cells/animal) was positioned in correspondence to the injury level. The hMSC loaded hydrogel was secured by applying a cling film on the top, sealed at the edges with a tissue adhesive (3M Vetbond). Dorsal muscles were then juxtaposed using absorbable sutures and the skin was sutured. After the surgery, the animals were kept on a warm pad for 30 min and then placed in separated cages with facilitated access to food and water for recovery.

As controls for subsequent analyses, other groups of animals were taken into consideration: animals treated with hMSCs directly injected in the parenchyma, animals treated with conditioned medium (CM) directly injected in the parenchyma, animals treated with HG RGD + ECM loaded only with CM. hMSCs and CM were injected as follows: hMSCs were suspended at a concentration of 50,000 cells/μL and, using a 30G needle associated to the stereotaxic, they were injected (0.5 μL/site) very close to the epicenter of the lesion (rostral edge) with a flow rate of 0.25 μL/min. The needle was positioned at the midline, then it was deepened into the parenchyma to 0.6 mm below the pia mater. For the other groups, CM was obtained after 1 day culture of hMSCs in culture plates. Using the same protocol adopted for hMSCs seeding, CM was loaded into the HG RGD + ECM. Briefly, 80 μL of CM were added directly onto the sponge-like hydrogel (40 μL for each side). Then, hydrogels were let to swell for 30 min in incubator at 37 °C.

2.14. hMSCs in vivo tracking

In vivo tracking of viable hMSCs stained with CFDA-SE was obtained using a stereomicroscope (Olympus SZX10). Animals with the backbone and the hydrogel exposed were evaluated by a stereomicroscope and a series of images of the entire hydrogel were acquired at 1.6×. Hydrogels acquisitions were made the same day of the positioning (day 0) and at 3 or 9 days after the positioning. CFDA-SE positive cells were counted using the "spots detection" tool of Imaris software (Bitplane). The number of stem cells detected in each hydrogel at day 0 was considered as 100% of survival. The number of cells detected in the same hydrogels at 3 or 9 days was then reported as a percentage of survival in respect to the same hydrogel at day 0.

2.15. In vivo positioning of Hoechst hydrogels

After the spinal cord compression, sponge-like HG RGD was loaded with 20 μL of 0.7 mg/mL Hoechst 33258 pentahydrate (bisbenzimide) (Life technologies) and positioned at the injury level. The animals were then divided in 2 groups, one with only the positioning of Hoechst-loaded hydrogels onto the injury site, the other where Hoechst-loaded hydrogel was secured by applying a cling film on the top, sealed at the edges with a tissue adhesive (3M Vetbond). Dorsal muscles were then juxtaposed and the skin was sutured. After the surgery, the animals were kept on a warm pad for 30 min and then placed in separated cages with facilitated access to food and water for recovery.

2.16. Spinal cord transcardiac perfusion

For histological evaluations, after 9 days from the Hoechst hydrogels positioning, mice were deeply anesthetized with ketamine hydrochloride (IMALGENE, 100 mg/kg) and medetomidine hydrochloride (DOMITOR, 1 mg/kg) and transcardially perfused with 40 mL of sodium phosphate buffered (PBS) 0.1 M, pH 7.4, followed by 50 mL of 4% paraformaldehyde solution in PBS. Spinal cords were then removed, postfixed overnight in the same fixative and then transferred to 30% sucrose in PBS at 4 °C overnight for cryopreservation and stored at 4 °C until use. The spinal cord was embedded in OCT compound, frozen by immersion in N pentane at 45 °C for 3 min and then stored at 80 °C. Frozen tissues were sectioned at 50 μm on a cryostat at −20 °C. Starting from the rostral edge (about 6 mm rostral to the epicenter), one section every 10 was mounted on slides for a total of 24 sections (about 12 mm sectioned) and coverslipped with a 50% glycerol solution in PBS before to proceed with acquisition at 10× magnification by confocal

microscopy (Olympus Fv1000, Laser 405).

2.17. Hoechst distribution analysis

The quantification of the Hoechst distribution and penetration into tissue was performed using the free software ImageJ, making a threshold based on signal intensity. The thresholded area was then quantified and showed as total Hoechst delivery area evaluated in the tissue. Furthermore, an evaluation of the Hoechst signal in each slice sampled (each 10 sections) in a spinal cord region of 12 mm was performed. Four animals per group were analyzed.

2.18. Flow cytometry

After 9 days of treatment by hMSCs loaded HD RGD + ECM, animals were decapitated and spinal cords were rapidly flushed out by the column. The region around the epicenter of the lesion was put on a cell strainer (40 μm nylon mesh) and a cell suspension was obtained by pressing with the plunger of a 10 mL syringe. Then the cell strainer was washed with 5 mL of GKN solution pH 7.4 (8.00 g/L NaCl, 0.40 g/L KCl, 0.93 g/L NaH_2PO_4, 1.42 g/L Na_2HPO_4, 2.00 g/L D-glucose, 0.02% BSA). For each sample, 1.5 mL of the cell suspension obtained was centrifuged at 2000 rpm for 5 min and pellet cells were resuspended in 500 μL of FACS blocking (1% BSA, 5% FBS in PBS). After 20 min of incubation in FACS blocking at 4 °C, primary antibodies CD11b-APC780 (ebioscience [1:100]) and CD45-PE (BDbioscience [1:100]) were added and incubated for 20 min at 4 °C in the dark. Then, 1 mL of PBS was added and samples were centrifuged at 2000 rpm for 5 min. Pellet cells were resuspended in 1 mL of FACS blocking before proceeding to FACS analysis. A specific isotype antibody staining was performed as negative control. Immunophenotyping analyses were performed on at least 1,500,000 cells for each sample by using MoFlo Astrios instruments (Beckman Coulter) equipped with 488, 546 and 640 nm lasers. Fluorescence pulses were detected using a band pass filter 671/20 for CD45, 795/70 for CD11b. Results were analyzed using Kaluza software (Beckman Coulter). Data are expressed as percentage of positive cells per gated event.

2.19. RNA analysis

After 9 days of treatment by hMSCs loaded HD RGD + ECM, animals were decapitated and spinal cords were rapidly flushed out by the column. The region around the epicenter of the lesion was rapidly frozen on dry ice and stored at −80 °C until use. Total RNA was obtained from tissues using RNeasy Mini Kit (Qiagen), as already reported above. Samples of total RNA were treated with DNAse (Applied Biosystems) and reverse-transcribed with random hexamer primers using Multi-Scribe Reverse Transcriptase (TaqMan Reverse transcription reagents; Applied Biosystems). Real-time RT-PCR was performed according to the manufacturer's instructions using 2 ng of cDNA, 200 nmol of each primer and SYBR Green master mix (Applied Biosystems) in a total volume of 20 μL. Levels of PCR product were measured using SYBR Green fluorescence collected during Real-Time RT-PCR on an Applied Biosystems 7300 system. The expression of the following genes was analyzed:

- YM1 (Fw: TCTGGTGAAGGAAATGCGTAAA; Rev: GCAGCCTTGGA ATGTCTTTCTC);
- Arginase I (Fw: CATGGGCAACCTGTGTCCTT; Rev: TCCTGGTACAT CTGGGAACTTTC);
- IL-1β (Fw: AGTTGACGGACCCCAAAAGA; Rev: GGACAGCCCAG GTCAAAGG);
- TNFα (Fw: AGACCCTCACACTCAGATCATCTTC; Rev: TTGCTACGAC GTGGGCTACA);
- β-Actin (Fw: CGCGAGCACAGCTTCTTT; Rev: GCAGCGATATCGT CATCCAT).

β-Actin was used as reference gene and relative gene expression levels were determined according to the manufacturer's ΔΔCt method (Applied Biosystems). Data are expressed as fold change from untreated injured mice spinal cord samples.

2.20. Statistical analyses

Statistical analyses were performed by Prism software (Graphpad). Statistical tests applied were Mann–Whitney test, one-way ANOVA or two-way ANOVA followed by Bonferroni's post hoc test, as reported in figure legends. Data are presented as mean ± SEM.

3. Results

3.1. Extracellular matrix improves hMSCs adhesion and survival in biomimetic hydrogels

In order to optimize and evaluate the hMSCs adhesion and viability several hydrogel compositions and different loading protocols were developed and tested. Specifically, we synthesized and functionalized the following scaffolds: carbomer/agarose/polyethylene glycol (PEG) based hydrogel incorporating RGD adhesive peptide (HG RGD) or HG RGD with a 3D ECM deposition (HG RGD + ECM) (Fig. 1 A). Furthermore, different loading protocols have been tested: hMSCs were mixed with the hydrogel during its polymerization (hereafter termed classic loading, Fig. 1 B a) or fluidically loaded into lyophilized HG, the latter acting like a sponge able to soak up cells together with the medium solution (hereafter termed sponge-like loading, Fig. 1 B b). Cell survival, adhesion and density within the scaffolds were evaluated by labeling live cells with Calcein AM over time and expressed as number of positive cells per mm^2. To evaluate the different loading protocols proposed we used a HD RGD scaffold demonstrating a significant increase of hMSCs survival at both 14 and 21 days after a sponge-like loading compared to the classic loading (Fig. S2 A, B). Moreover, a partial spindle shape morphology was detected only in the sponge-like HG RGD, but not in the classic loading HG RGD (Fig. S2 A, B), suggesting that a reduced stress and a better adhesion were obtained when hMSCs were loaded by fluidic diffusion into the hydrogel. In order to further increase cell density and adhesion in the scaffold, we developed a HG RGD containing a 3D deposition of ECM potentially able to provide more anchorage for hMSCs and a better supporting environment. We first seeded hMSCs into HG RGD and we measured the ECM deposited over time. A progressive ECM deposition was observed from 1 up to 14 days, where ECM deposition reaches a “plateau” (Fig. S3). Thus, for a second hMSCs seeding, we decided to deposit ECM up to 14 days and then we lyophilized the HG RGD + ECM to allow a new encapsulation of hMSCs by a sponge-like loading (see the Materials and methods section and Fig. 1 A and B). Noteworthy, analyzing hMSCs within HG RGD + ECM, we found a markedly increased cell adhesion to the biomimetic substrate. Indeed, already at the first day after seeding, HG RGD + ECM provided an anchorage for hMSCs. The almost totality of hMSCs showed a healthy spindle shape morphology 1 day after the encapsulation with a significantly higher long lasting cell density (3 fold higher) compared to HG RGD (Fig. 2 a).

3.2. SEM analysis shows a high hMSC density with a spindle shape morphology in HG RGD + ECM

In order to further characterize hMSC adhesion, morphology and density within both HG RGD and HG RGD + ECM, we

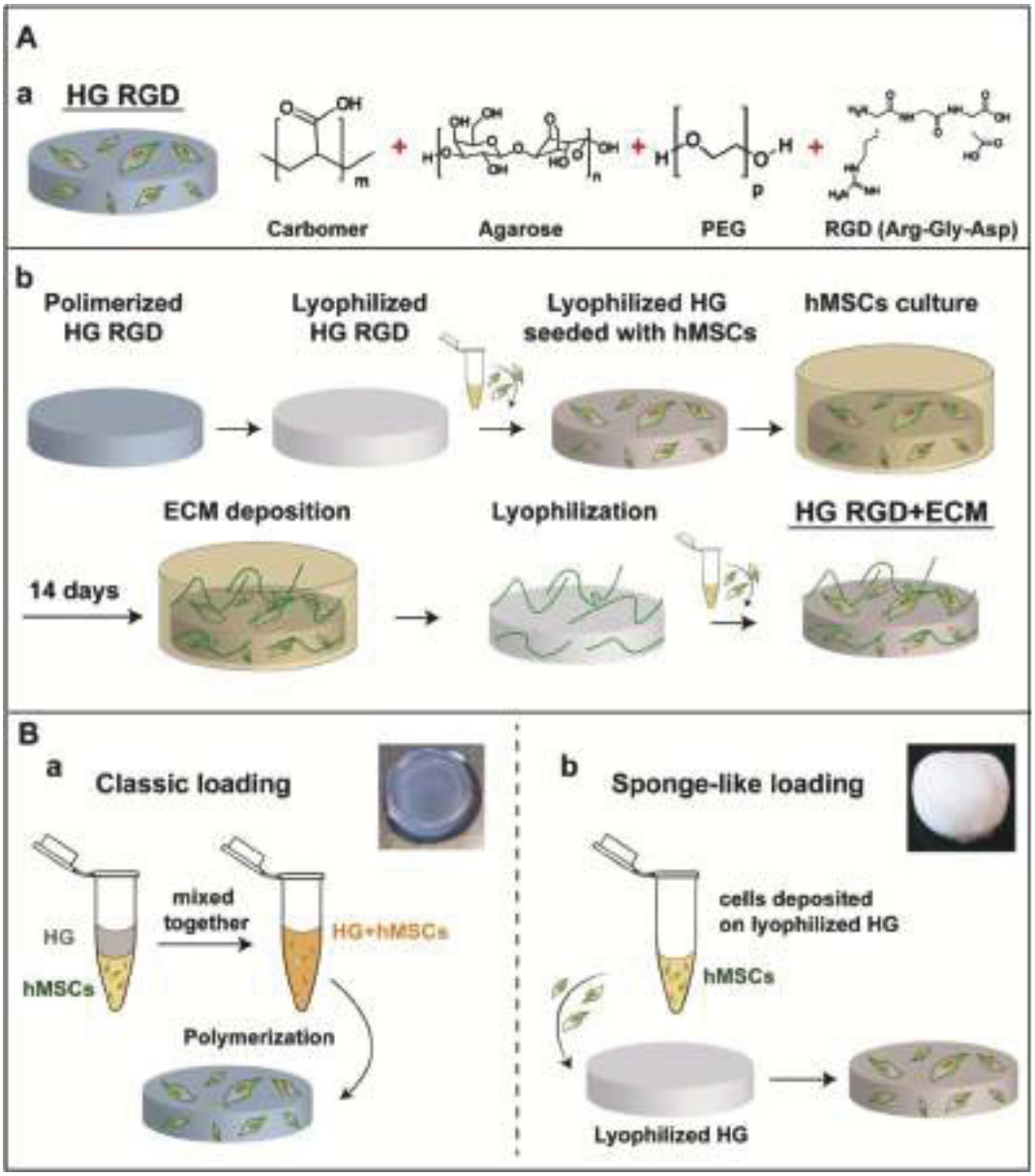

Fig. 1. Schematic representation of different hydrogel compositions and loading protocols tested. (A) Hydrogel compositions tested were: RGD (arginine–glycine–aspartic acid) adhesive peptide incorporated into HG (HG RGD, a) or HG RGD with a 3D-ECM deposition (HG RGD + ECM, b). The latter was obtained by different steps such as represented in panel b. (B) Cartoons represent the different loading protocols tested: a classic loading way in which hMSCs were mixed with HG RGD during its polymerization (a, inset) or sponge like loading in which hMSCs were loaded with a soaked up effect into lyophilized HG RGD (b, inset).

performed Scanning Electron Microscopy (SEM). SEM evaluation showed an irregular surface among the network mesh, varying from rough, in HG RGD, to smooth, in HG RGD + ECM, the latter revealing the ECM deposition (Fig. 3). Furthermore, we observed more clusterized and spindle shape hMSCs attached to the HG RGD + ECM biomimetic scaffold compared to HG RGD, confirming a healthy state and a higher cell adhesion within HG RGD + ECM (Fig. 3).

3.3. HG RGD + ECM preserves hMSC stemness

In order to demonstrate that HG-RGD + ECM did not spontaneously induce any typical MSC differentiation thus preserving the hMSC stemness for a long time, even when encapsulated, we compared the gene expression profile of hMSCs encapsulated in HG-RGD + ECM with the same hMSCs but differentiated towards osteocytes, chondrocytes and adipocytes (Fig. 4 D). Genes evaluated were alkaline phosphatase (ALP), Runt-related transcription factor 2 (RUNX2) and Osterix for osteocytes, Aggrecan (ACAN) and collagen type X (COLLX) for chondrocytes, whereas Adipsin and Fatty acid binding-protein 4 (FABP4) for adipocytes. The analysis was conducted on hMSCs encapsulated within HG RGD + ECM for 21 days and subsequently isolated for PCR analysis. As positive control we used hMSCs loaded within HG RGD and treated with differentiating media up to 21 days. We observed a significantly higher gene expression in positive controls compared to untreated hMSCs loaded in HG-RGD + ECM for all genes tested (Fig. 4 A, 4 B and 4 C) demonstrating that HG-RGD + ECM per se was not able to stimulate any classical mesodermal differentiation preserving stemness for a long time.

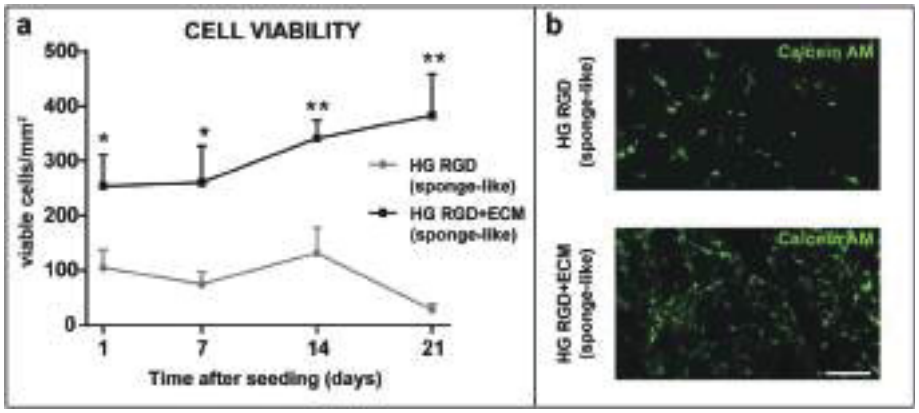

Fig. 2. HG RGD + ECM shows a high hMSC viability with a spindle-shape morphology *in vitro*. (a) Graph representing viability of hMSCs loaded in sponge-like HG RGD or sponge-like HG RGD + ECM scaffolds. Cell viability was evaluated over time by labeling live cells with Calcein AM. Already at the first day after seeding, HG RGD + ECM displays a significantly higher viability and density of hMSCs compared to HG RGD. This high cellular density is preserved over time. In the graph the cell density within the hydrogels is reported as number of calcein AM positive cells per mm^2. Statistical analysis: Mann Whitney test for each time point. Mean ± SEM is reported. (*) $p < 0.05$. (**) $p < 0.01$. $n = 8$ per group. (b) Representative images showing hMSCs stained with Calcein AM in sponge-like HG RGD and sponge-like HG RGD + ECM scaffolds. Already at the first day after seeding here represented, the almost totality of hMSCs within HG RGD + ECM shows a healthy spindle shape morphology. Differently, only a very few hMSCs in HG RGD show a partial adhesion to the scaffold and a spindle shape morphology. Scale bar represents 200 μm.

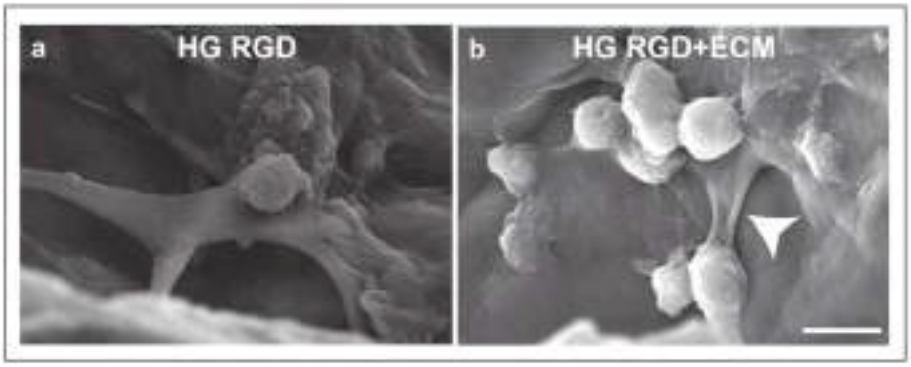

Fig. 3. Morphological analysis of HG scaffolds by SEM. Representative SEM images of both sponge-like HG RGD (a) and sponge-like HG RGD + ECM (b) scaffolds. The ECM deposition is represented by irregular surface among the networks mesh in HG RGD + ECM (arrowhead). A higher cellular density and a higher cell attachment to the substrate can be observed in HG RGD + ECM. Scale bar represents 10 μm. 3000×.

3.4. hMSCs loaded within HG RGD + ECM preserve viability up to 9 days in vivo

Since HG RGD + ECM showed an optimized viability, a higher cellular adhesion and a preserved stemness of hMSCs after a sponge-like loading *in vitro*, we decided to evaluate the behavior of hMCSs loaded in HG RGD + ECM also *in vivo*. To do that, after the implantation in the injured site, we performed a longitudinal study by means of intravital microscopy. Cell survival was evaluated over time by labeling live stem cells with CFDA-SE (a vital fluorescent staining) (Fig. 5 A and B a). Cell density within the hydrogel was evaluated by counting the number of CFDA-SE positive cells that we expressed as percentage, considering 100% of survival immediately after the implantation. Analyzing intravital microscopy at 3 days following positioning, the number of hMSCs in the HG RGD + ECM decreased to about 40% of the initial number, that became 15% at 9 days after the positioning (Fig. 5 B b).

3.5. Oriented delivery optimizes the fluidic release of factors from HG RGD + ECM in vivo

In order to demonstrate that a fluidic diffusion occurs from the hydrogel after implantation in the injury site *in vivo*, we evaluated the release profile of a fluorescent solution (Hoechst 33258) delivered by HG RGD + ECM. After 9 days from the HG RGD + ECM positioning in the lesion site, Hoechst 33258 fluorescence showed an evident intense signal mostly distributed in the epicenter of the injured site, whereas only few sections were stained outside the epicenter of the lesion (Fig. 6 a). This was confirmed by examining quantitatively the distribution of Hoechst 33258 staining in a portion of the spinal cord encompassing 12 mm around the epicenter of the injury (Fig. 6 a, d). In order to increase the fluidic diffusion from the hydrogel toward the injury site, we applied and tested an impermeable cling film that, sealing the hydrogel to the spinal cord, optimizes the fluidic diffusion toward the injury site (Fig. 6 b). Analyzing the Hoechst 33258 staining in spinal cord tissue after an oriented delivery (Fig. 6 b), we found a dramatic increase of fluorescent staining in both the epicenter and in regions outside the lesion, compared to unsealed hydrogel (Fig. 6 a). This was confirmed by evaluating quantitatively the distribution of the Hoechst 33258 staining in the spinal cord segments around the traumatized spinal cord (Fig. 6 c, d). These analyses demonstrated that a more oriented diffusion from the hydrogel, obtained by using a cling film, can potentially optimize a paracrine release of trophic factors toward the injured site, potentially increasing the therapeutic effect.

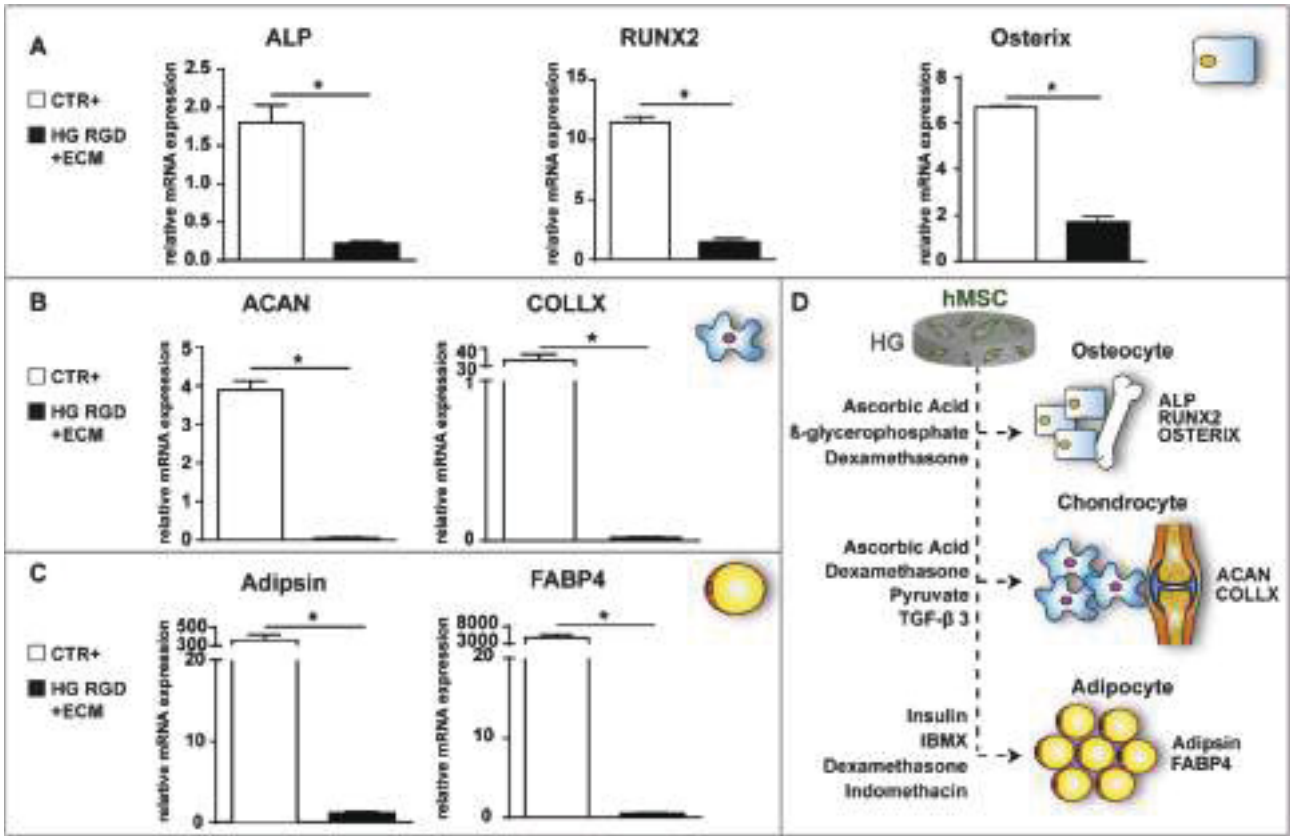

Fig. 4. mRNA analysis of hMSCs encapsulated within biomimetic scaffold. (A, B, C) Graphs representing the expression of specific genes related to three differentiation lineages: alkaline phosphatase (ALP), runt-related transcription factor 2 (RUNX2) and osterix for osteogenic differentiation; aggrecan (ACAN) and collagen type X (COLLX) for chondrogenic differentiation and adipsin and fatty acid binding-protein 4 (FABP4) for adipogenic differentiation. hMSCs encapsulated whithin HG RGD + ECM for 21 days are compared to the positive control represented by hMSCs loaded in HG RGD and treated with specific differentiating media for 21 days. Data are expressed as fold change compared to steady-state undifferentiated hMSCs (negative control). Statistical analysis: Mann Whitney test. Mean ± SEM is reported. (*) $p < 0.05$. $n = 3$ per group. (D) A representative cartoon of the three lineage commitments of hMSCs (osteocytes, chondrocytes and adipocytes) with respective principal pro-differentiating stimuli: ascorbic acid, β-glycerophosphate and dexamethasone to induce osteogenic differentiation; ascorbic acid, dexamethasone, pyruvate and TGF-β 3 to induce chondrogenic differentiation; insulin, 3-isobutyl-1-methylxanthine (IBMX), dexamethasone and indomethacin to induce adipogenic differentiation.

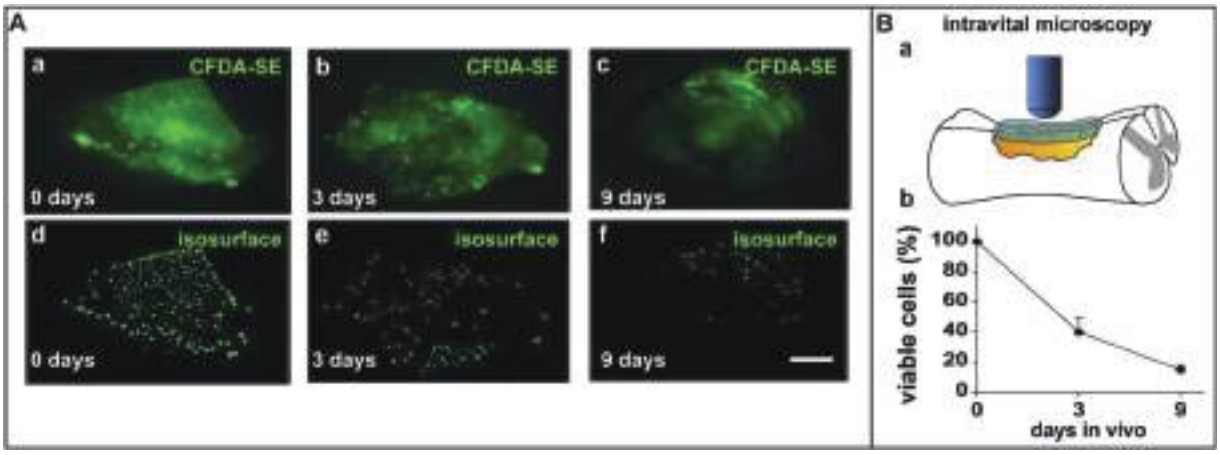

Fig. 5. hMSCs viability within HG RGD + ECM is revealed up to 9 days *in vivo*. (A) (a–c) Representative images of intravital acquisition of CFDA-SE positive hMSCs within HG RGD + ECM positioned in the injury site *in vivo*. Analysis has been performed immediately after the positioning (day 0, a and d) and at 3 (b and e) or 9 days (c and f) after the positioning. (d–f) The isosurfaces represent CFDA-SE positive cells considered for quantification of respective hydrogels. Scale bar represents 0.2 mm. (B) (a) Cartoon represents intravital acquisition of CFDA-SE positive hMSCs within HG RGD + ECM in the injury site. (b) Quantitative evaluation of viable hMSCs within HG RGD + ECM over time. Mean ± SEM is reported. $n = 8$.

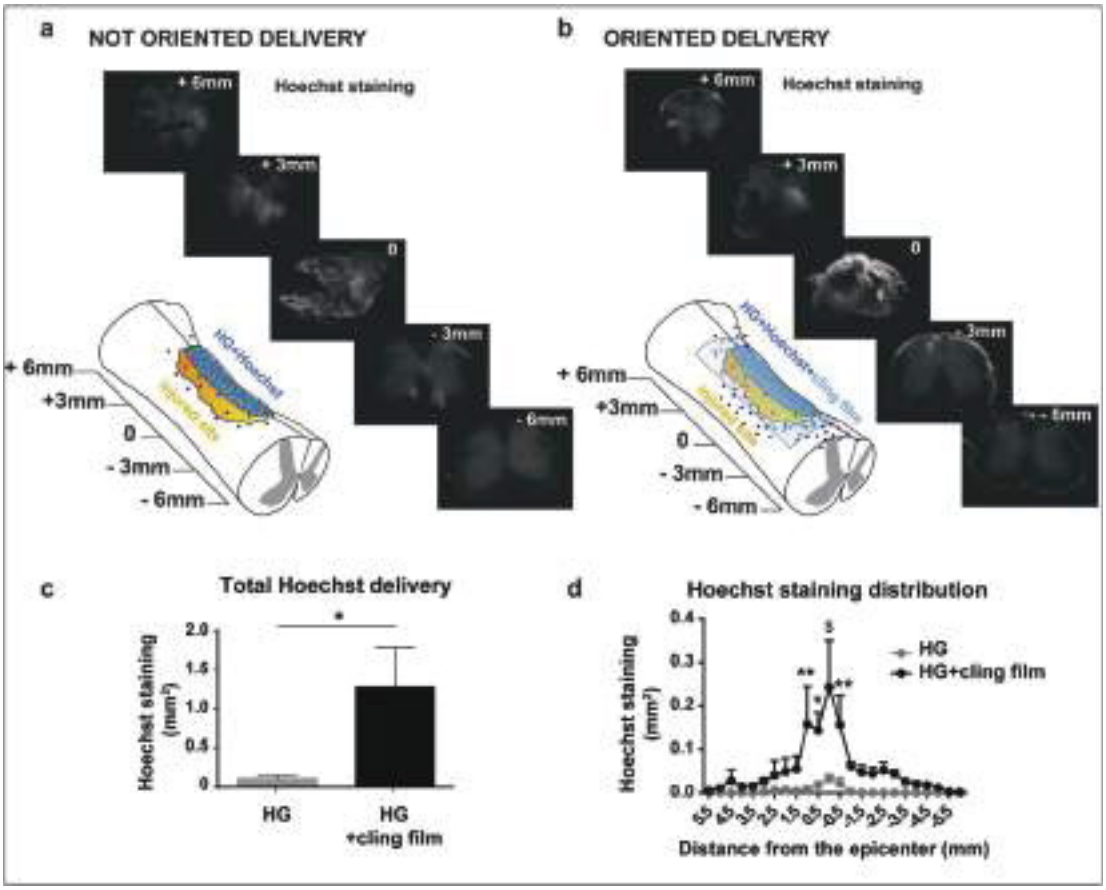

Fig. 6. Hoechst delivery from HG RGD + ECM *in vivo*. Release profile study of a fluorescent solution (Hoechst 33258) delivered by HG RGD + ECM in the injured site of the spinal cord. In a and b, representative images of Hoechst staining are shown in a portion of the spinal cord encompassing 12 mm around the epicenter of the injury. Cartoons show HG RGD + ECM positioning in both not oriented (a) and oriented delivery (b). Spinal cord after an oriented delivery shows a higher Hoechst staining as both total signal (c) and distribution around the epicenter (d) compared to unsealed hydrogel. Statistical analysis: Mann Whitney test for total Hoechst delivery (c), Two-way ANOVA followed by Bonferroni's post hoc test for Hoechst staining distribution (d). Mean ± SEM is reported. (*) $p < 0.05$, (**) $p < 0.01$, ($) $p < 0.0001$. n = 4 per group.

3.6. *hMSCs loaded in HG RGD + ECM modulate inflammatory response in vivo*

We assessed by FACS analysis whether hMSCs loaded in HG RGD + ECM sealed with cling film and implanted in the injured site were able to modulate, through a paracrine effect, resident microglia and recruited macrophages in the traumatized site, one therapeutic effect proposed in literature [60]. To distinguish between the two cell populations we performed, according to the literature [61–63], a double labeling with both CD11b and CD45 antibodies, identifying microglia by a $CD11b^{pos}/CD45^{low}$ signal and recruited macrophages by a $CD11b^{pos}/CD45^{high}$ signal (see Fig. S4 for gating). The amount of CD11b/CD45 positive labeled cells was evaluated in the injury epicenter. In response to SCI, resident microglia and recruited macrophages increased very early, even at 1 day post injury (DPI), reaching a peak of microglia activation and recruited macrophages migration in the damaged site at 7–9 DPI (data not shown). Mice treated with hMSCs loaded in HG RGD + ECM and analyzed at 9 DPI showed a significantly increased amount of recruited macrophages in the injured site (hMSCs, Fig. 7 A, b) compared to untreated mice (injury, Fig. 7 A, a), as demonstrated by dot plots (Fig. 7 A) and by quantitative analysis of microglia/macrophages ratio (Fig. 7 B). No changes were detected comparing FACS analysis of untreated injured mice (INJ) to injured mice treated with conditioned medium loaded within HG RGD + ECM (HG RGD + ECM + CM) or conditioned medium or hMSCs injected into the parenchyma (CM injected and hMSCs injected, respectively) (Fig. S5, A). These data demonstrated that only hMSCs loaded within HG RGD + ECM recruit more macrophages in the injured site via a paracrine effect. Furthermore, to investigate whether the proposed treatment was able to modulate M1 and/or M2 phenotypes in the injured site we performed a gene expression analysis to detect both M1 (IL-1β and TNFα) or M2 (Arg-I and YM1) phenotypes [60]. Analyzing both IL-1β and TNFα mRNA in the epicenter of the lesion in hMSCs loaded HG RGD + ECM + cling film treated mice at 9 DPI (Fig. 7C; a, b), only TNFα mRNA was detected significantly increased in treated injured mice (fold change of about 1.5) compared to the untreated injured mice (Fig. 7C; a). However, evaluating M2 mRNA markers in hMSCs loaded HG RGD + ECM + cling film treated mice, we demonstrated a significant increase of Arginase I M2-related transcript (Fig. 7C; d), but not of YM1 (Fig. 7C; c), compared to untreated injured mice. Noteworthy, Arginase I showed a mean fold change of about 10 compared to the untreated injured mice (Fig. 7C; d). No changes were detected by mRNA analysis comparing untreated injured mice (injury) to injured mice treated with either conditioned medium (CM injected) or hMSCs (hMSCs injected) injected in the parenchyma (Fig. S5, B). However, the analysis of IL-1β expression revealed higher levels of transcription in mice treated with conditioned medium loaded in HG RGD + ECM (HG RGD + ECM + CM, Fig. S4 B, b) compared to untreated mice (fold change of about 2.5), suggesting a partial effect of HG RGD + ECM scaffold in eliciting a polarization toward a pro-inflammatory M1 phenotype. Nevertheless, the treatment of mice with hMSCs loaded HG RGD + ECM

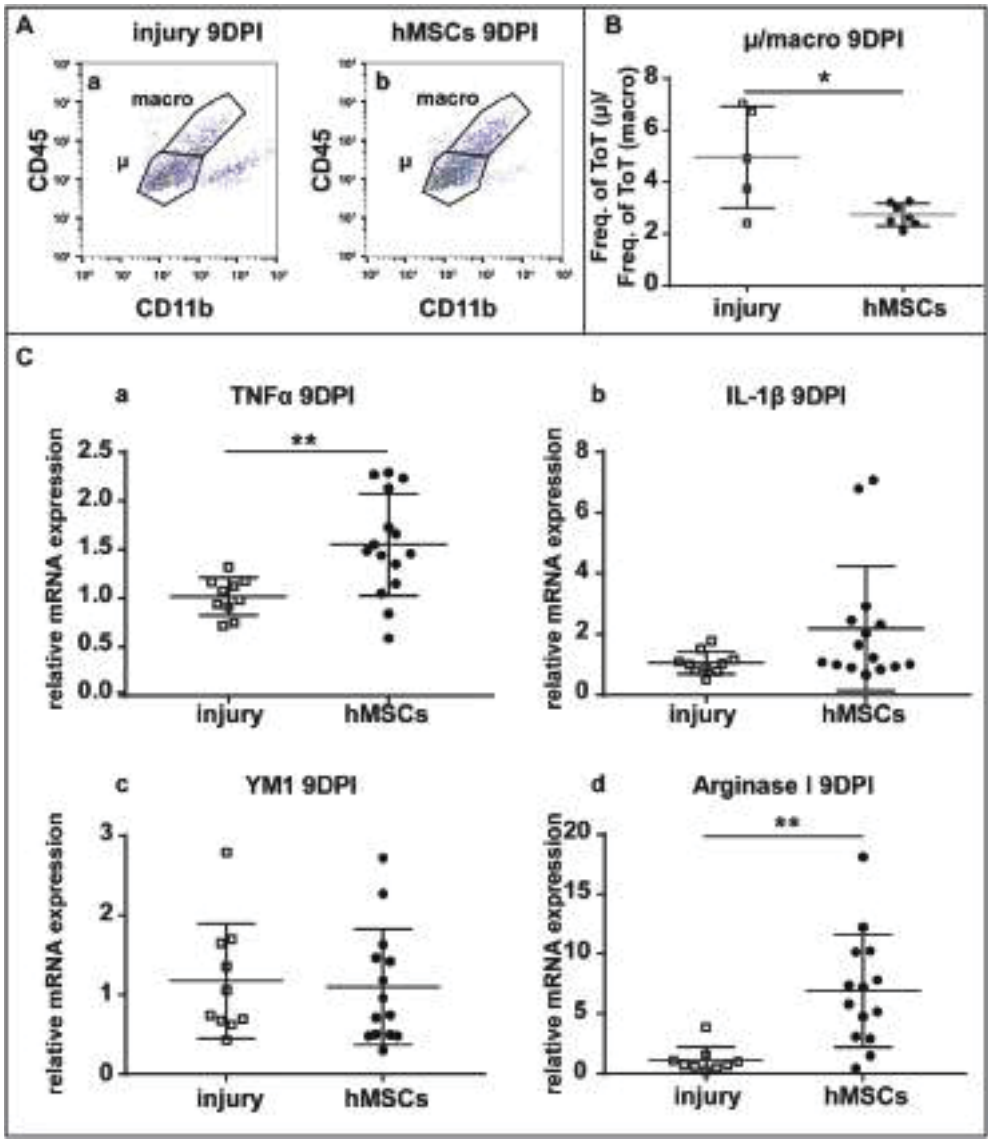

Fig. 7. hMSCs loaded in HG RGD + ECM modulate inflammatory response increasing M2 macrophages *in vivo*. (A) Representative FACS dot plots of microglial cells ($CD11b^{pos}/CD45^{low}$) and macrophages ($CD11b^{pos}/CD45^{high}$) present in SCI epicenter of untreated injured (injury, a) or hMSCs loaded within HG RGD + ECM treated injured mice (hMSCs, b) evaluated at 9 DPI (days post injury). An increased macrophages recruitment in hMSCs treated mice was found (b) compared to untreated mice (a). (B) Quantification of the ratio between microglia ($CD11b^{pos}/CD45^{low}$) and recruited macrophages ($CD11b^{pos}/CD45^{high}$) evaluated in untreated injured (injury) or hMSCs loaded within HG RGD + ECM treated injured mice (hMSCs) at 9 DPI. Graph shows a lower microglia/macrophages ratio in hMSCs group, demonstrating an increase of macrophages recruitment. Mean ± SEM is reported. Statistical analysis: Mann Whitney test. (*) $p < 0.05$. n = 5–7 mice per group. (C) Quantitative evaluation of mRNA expression of both M1 (TNFα, a and IL-1β, b) and M2 (YM1, c and Arginase I, d) markers of microglia/macrophages polarization in untreated injured (injury) or hMSCs loaded HG RGD + ECM treated injured mice (hMSCs) at 9 DPI. A significant increase of TNFα (about 1.5 folds) and Arginase I (about 10 folds) can be observed in mice treated with hMSCs compared to untreated injured mice, suggesting a skew toward an M2 pro-regenerative environment in hMSCs group. Mean ± SEM is reported. Statistical analysis: Mann Whitney test. (**) $p < 0.01$. n = 10–14 mice per group.

was able to revert the increased IL-1β expression, suggesting a further anti-inflammatory paracrine effect of hMSCs *in vivo* (Fig. 7C; b).

4. Discussion

Engineered scaffolds are considered a promising approach to create an optimal environment able to sustain a long lasting cell viability of stem cells in situ with the ability to help the tissue in terms of neuroprotection and neuroregeneration. These scaffolds offer the opportunity to deliver cells appropriately into the injured site optimizing the therapeutic effect of the treatment proposed. However, different limits have been revealed when these hMSCs have been encapsulated into biomaterials hampering their viability and a long lasting effect of the treatment. This was mostly due to the lack of an optimal combination of hMSCs, scaffold design and supporting environment that has limited the capability to support appropriate cell viability *in vitro* and *in vivo* [49]. It is well known that stem cell viability, phenotype and stemness are modulated by the interaction with the complex physicochemical composition of the natural niche mostly composed of ECM [43,55,64,65]. Therefore, the ECM could be considered a building block in sustaining hMSCs within biomaterial for maintaining a high viability and a high cellular density over time. In line with this idea, we here demonstrate and confirm that an optimal combination of an original hydrogel with a pre-constituted ECM deposited by hMSCs, together with an efficient stem cell loading (sponge-like effect), is an effective strategy to increase the viability and the cellular

density within an hydrogel for at least 21 days after seeding. In particular, in this study we establish that a lyophilized gel could be loaded through a soaked up effect preserving a higher cell viability compared to hMSCs loaded during the solution/gel transition. Reduced cell viability detected after a conventional loading procedure is likely due to the mechanical stress to which the cells are exposed [66], that is dramatically reduced loading hMSCs by a sponge-like effect. Furthermore, we demonstrate that RGD motif together with the pre-deposited 3D ECM has increased strongly the density of these cells within the hydrogel already at the first day after seeding. Furthermore, the 3D RGD ECM scaffold as here proposed significantly improves hMSCs maintenance showing a very high cell density up to 21 days *in vitro*. This time of survival is quite striking compared to other scaffolds proposed in literature where cells viability was observed only up to 7–14 days [48,67,68]. Furthermore, we demonstrate that a 3D ECM optimizes a healthy environment by converting hMSCs from a round shape to a spindle-like morphology, representing healthy cells indistinguishable from cells grown within a culture well. Differently, other groups reported a lower stem cells survival with a round shape morphology of hMSCs in the scaffold [48,67,68], suggesting that a spindle shape morphology is indicative of a cellular wellness that can contribute to the long term survival. We demonstrate also a preserved stemness of hMSCs during the time of analysis, confirming that a potential pleiotropic effect is maintained in this condition for a multitherapeutic approach in SCI. Altogether, these data confirm that a 3D ECM is a relevant support for the maintenance of hMSCs in this scaffold. So far, only few attempts have been made to mimic the physiological ECM directly within a biomaterial with the aim to optimize hMSCs viability [46–48,55,68–72]. Several studies used reconstituted monotypic ECM preparations in two dimensions to examine cell-matrix interactions and survival of the cells [55,71,72]. However, this represents a platform that does not constitute an optimal 3D native configuration, but only a 2D interactive structure [55,71,72]. It is well known that cell is affected by the physical environment in which it is grown. Indeed, in living tissue, cells reside in 3D microenvironments and establish many interactions with the surrounding matrix [73–75]. Moreover, cells in 3D culture exhibit different gene expression compared to cells in 2D [73] and provide different cell polarization, such as demonstrated in literature [73] and in our study. Indeed, a 3D framework provides more contact for cell adhesion, which is necessary for protein–protein ligation and cell-matrix signaling [73–75]. In addition, the architecture and conformation of the niche determines the mechanical properties of the ECM which in turn control cell adhesion, proliferation and differentiation [76]. For this reason, our 3D approach represents an optimal condition for cell culture where ECM is widely distributed in a 3D scaffold permitting a more appropriate environment for cell–cell interaction and polarization, and creates a more permissive environment similar to natural niche in which hMSCs can survive properly. Our approach is different also from previous studies whose attempts were to functionalize the scaffold with one single ECM peptide, as laminin, fibrin or RGD peptide [46–48,68,69], or to use a powdered ECM from porcine urinary bladder [70]. Indeed, ECM is composed of proteins, proteoglycans and factors able to establish a dynamic interaction with stem cells. Simultaneously, stem cells remodel actively the ECM in relation to their definite needs. Thus, only a few bioactive peptide sequences incorporated in synthetic hydrogels could represent only a partial support, but not an optimized environment to sustain hMSCs [46–48,68,69]. Therefore, to the best of our knowledge, this is the first study presenting a 3D natural ECM deposition able to increase adherence and viability of loaded hMSCs. *In vivo* experiments further demonstrate that a HG-RGD + ECM loaded with a fluorescent compound (Hoechst 33258) is efficiently implanted in the spinal cord and is able to release efficiently this molecule showing a sustainable delivery from the scaffold toward the injured site. To improve this delivery, we propose the use of an impermeable cling film that dramatically increases an oriented delivery toward the damaged site. Thus, we expect that, once implanted, hMSCs loaded HG-RGD + ECM + cling film will be able to release a higher concentration of factors in the injured spinal cord without any obstruction to their paracrine effect. This is confirmed by FACS and mRNA analyses demonstrating that a paracrine effect sustained by viable hMSCs loaded within HG RGD + ECM in just a few days is able to increase and/or convert efficaciously M2 macrophages (immunomodulation) in the injured site, promoting a pro-regenerative environment that represents a relevant outcome in treating SCI [26,50,77,78]. Noteworthy, injecting the same number of hMSCs directly in the parenchyma, a lack of efficacy is found in terms of macrophages recruitment or M1/M2 polarization. So far, the direct injection of hMSCs has been frequently proposed as preclinical SCI treatment, sometimes demonstrating a protective effect on histological or behavioral outcomes [13,79,80]. However, although a direct injection of stem cells may represent an attractive approach as clinical protocol, it shows deep concerns because very often stem cells leave the zone of injection, as they are not confined by any support. On the other hand, if injected stem cells remain in situ, they could be exposed to a hostile environment due to the tissue degeneration. Thus, a biomimetic scaffold, as proposed in this study, able to maintain MSCs viable, undifferentiated and confined within a 3D structure out of the degenerative environment is a forefront application. Moreover, the original scaffold material here proposed maximizes hMSCs paracrine protective effects, offering the possibility to reduce dramatically the cellular efficacious dose. Indeed, a consistent higher number of hMSCs is required when a direct injection is performed in situ to overcome mechanical forces that could damage stem cells passing from the needle [27] and concomitantly to preserve a sufficient number of them to counteract an inflamed and adverse environment present in the injured site [29,30].

In conclusion, we propose a new sustainable stem cell therapy by using HG RGD + ECM derived from the combination of different promising strategies such as: 1) a new loading procedure on a lyophilized scaffold (soaked up effect) that reduces mechanical stress and preserves hMSC viability when encapsulated into the hydrogel, 2) a RGD motif that increases the capacity to entrap hMSCs within the hydrogel after the seeding, 3) a 3D ECM deposition able to maintain over time healthy hMSCs with an high viability and density and 4) an oriented delivery of paracrine factors for treating efficaciously the injured site. We believe that the optimized scaffold as here proposed results to be a promising and innovative approach that may represent a breakthrough in using stem cells therapy supported by biomaterial with potential beneficial impact on SCI.

Acknowledgments

Authors' research is supported by Ministry of Health (GR-2010-2312573).

Appendix A. Supplementary data

Supplementary data related to this article can be found at http://dx.doi.org/10.1016/j.biomaterials.2015.10.024.

References

[1] G. Onose, A. Anghelescu, D.F. Muresanu, L. Padure, M.A. Haras, C.O. Chendreanu, et al., A review of published reports on neuroprotection in

spinal cord injury, Spinal Cord 47 (2009) 716–726.
[2] G.W. Hawryluk, J. Rowland, B.K. Kwon, M.G. Fehlings, Protection and repair of the injured spinal cord: a review of completed, ongoing, and planned clinical trials for acute spinal cord injury, Neurosurg. Focus 25 (2008) E14.
[3] B.K. Kwon, E. Okon, J. Hillyer, C. Mann, D. Baptiste, L.C. Weaver, et al., A systematic review of non-invasive pharmacologic neuroprotective treatments for acute spinal cord injury, J. Neurotrauma 28 (2011) 1545–1588.
[4] B.K. Kwon, E.B. Okon, W. Plunet, D. Baptiste, K. Fouad, J. Hillyer, et al., A systematic review of directly applied biologic therapies for acute spinal cord injury, J. Neurotrauma 28 (2011) 1589–1610.
[5] N.A. Silva, N. Sousa, R.L. Reis, A.J. Salgado, From basics to clinical: a comprehensive review on spinal cord injury, Prog. Neurobiol. 114 (2014) 25–57.
[6] S. Lee, E. Choi, M.J. Cha, K.C. Hwang, Cell adhesion and long-term survival of transplanted mesenchymal stem cells: a prerequisite for cell therapy, Oxid. Med. Cell. Longev. 2015 (2015) 632902.
[7] S. Thuret, L.D. Moon, F.H. Gage, Therapeutic interventions after spinal cord injury, Nat. Rev. Neurosci. 7 (2006) 628–643.
[8] R. Adami, G. Scesa, D. Bottai, Stem cell transplantation in neurological diseases: improving effectiveness in animal models, Front. Cell Dev. Biol. 2 (2014) 17.
[9] M.F. Azari, L. Mathias, E. Ozturk, D.S. Cram, R.L. Boyd, S. Petratos, Mesenchymal stem cells for treatment of CNS injury, Curr. Neuropharmacol. 8 (2010) 316–323.
[10] S. Forostyak, P. Jendelova, E. Sykova, The role of mesenchymal stromal cells in spinal cord injury, regenerative medicine and possible clinical applications, Biochimie 95 (2013) 2257–2270.
[11] R. Vawda, M.G. Fehlings, Mesenchymal cells in the treatment of spinal cord injury: current & future perspectives, Curr. Stem Cell Res. Ther. 8 (2013) 25–38.
[12] X. Liang, Y. Ding, Y. Zhang, H.F. Tse, Q. Lian, Paracrine mechanisms of mesenchymal stem cell-based therapy: current status and perspectives, Cell Transplant. 23 (2014) 1045–1059.
[13] V.R. Dasari, D.G. Spomar, C.S. Gondi, C.A. Sloffer, K.L. Saving, M. Gujrati, et al., Axonal remyelination by cord blood stem cells after spinal cord injury, J. Neurotrauma 24 (2007) 391–410.
[14] S. Wislet-Gendebien, F. Wautier, P. Leprince, B. Rogister, Astrocytic and neuronal fate of mesenchymal stem cells expressing nestin, Brain Res. Bull. 68 (2005) 95–102.
[15] A.I. Caplan, D. Correa, The MSC: an injury drugstore, Cell Stem Cell 9 (2011) 11–15.
[16] S.A. Hardy, D.J. Maltman, S.A. Przyborski, Mesenchymal stem cells as mediators of neural differentiation, Curr. Stem Cell Res. Ther. 3 (2008) 43–52.
[17] J.R. Lavoie, M. Rosu-Myles, Uncovering the secretes of mesenchymal stem cells, Biochimie 95 (2013) 2212–2221.
[18] G. Paul, S.V. Anisimov, The secretome of mesenchymal stem cells: potential implications for neuroregeneration, Biochimie 95 (2013) 2246–2256.
[19] J.D. Glenn, K.A. Whartenby, Mesenchymal stem cells: emerging mechanisms of immunomodulation and therapy, World J. Stem Cells 6 (2014) 526–539.
[20] K. Le Blanc, D. Mougiakakos, Multipotent mesenchymal stromal cells and the innate immune system, Nat. Rev. Immunol. 12 (2012) 383–396.
[21] A. Uccelli, V. Pistoia, L. Moretta, Mesenchymal stem cells: a new strategy for immunosuppression? Trends Immunol. 28 (2007) 219–226.
[22] M.T. Harting, F. Jimenez, H. Xue, U.M. Fischer, J. Baumgartner, P.K. Dash, et al., Intravenous mesenchymal stem cell therapy for traumatic brain injury, J. Neurosurg. 110 (2009) 1189–1197.
[23] U.M. Fischer, M.T. Harting, F. Jimenez, W.O. Monzon-Posadas, H. Xue, S.I. Savitz, et al., Pulmonary passage is a major obstacle for intravenous stem cell delivery: the pulmonary first-pass effect, Stem Cells Dev. 18 (2009) 683–692.
[24] M.B. Potts, M.T. Silvestrini, D.A. Lim, Devices for cell transplantation into the central nervous system: design considerations and emerging technologies, Surg. Neurol. Int. 4 (2013) S22–S30.
[25] J.W. Jung, M. Kwon, J.C. Choi, J.W. Shin, I.W. Park, B.W. Choi, et al., Familial occurrence of pulmonary embolism after intravenous, adipose tissue-derived stem cell therapy, Yonsei Med. J. 54 (2013) 1293–1296.
[26] F. Rossi, G. Perale, S. Papa, G. Forloni, P. Veglianese, Current options for drug delivery to the spinal cord, Expert Opin. Drug Deliv. 10 (2013) 385–396.
[27] B.A. Aguado, W. Mulyasasmita, J. Su, K.J. Lampe, S.C. Heilshorn, Improving viability of stem cells during syringe needle flow through the design of hydrogel cell carriers, Tissue Eng. Part A 18 (2012) 806–815.
[28] F. Cao, A.H. Sadrzadeh Rafie, O.J. Abilez, H. Wang, J.T. Blundo, B. Pruitt, et al., In vivo imaging and evaluation of different biomatrices for improvement of stem cell survival, J. Tissue Eng. Regen. Med. 1 (2007) 465–468.
[29] T.E. Robey, M.K. Saiget, H. Reinecke, C.E. Murry, Systems approaches to preventing transplanted cell death in cardiac repair, J. Mol. Cell. Cardiol. 45 (2008) 567–581.
[30] M.J. Cooke, aK. Vulicb, M.S. Shoichet, Design of biomaterials to enhance stem cell survival when transplanted into the damaged central nervous system, Soft Matter 6 (2010) 4988–4998.
[31] B. Shrestha, K. Coykendall, Y. Li, A. Moon, P. Priyadarshani, L. Yao, Repair of injured spinal cord using biomaterial scaffolds and stem cells, Stem Cell Res. Ther. 5 (2014) 91.
[32] J. Thiele, Y. Ma, S.M. Bruekers, S. Ma, W.T. Huck, 25th anniversary article: designer hydrogels for cell cultures: a materials selection guide, Adv. Mater. 26 (2014) 125–147.
[33] G. Perale, F. Rossi, E. Sundstrom, S. Bacchiega, M. Masi, G. Forloni, et al., Hydrogels in spinal cord injury repair strategies, ACS Chem. Neurosci. 2 (2011) 336–345.
[34] D. Albani, A. Gloria, C. Giordano, S. Rodilossi, T. Russo, U. D'Amora, et al., Hydrogel-based nanocomposites and mesenchymal stem cells: a promising synergistic strategy for neurodegenerative disorders therapy, Sci. World J. 2013 (2013) 270260.
[35] A. Moshaverinia, C. Chen, X. Xu, S. Ansari, H.H. Zadeh, S.R. Schricker, et al., Regulation of the stem cell-host immune system interplay using hydrogel coencapsulation system with an anti-inflammatory drug, Adv. Funct. Mater. 25 (2015) 2296–2307.
[36] O. Jeon, E. Alsberg, Regulation of stem cell fate in a three-dimensional micropatterned dual-crosslinked hydrogel system, Adv. Funct. Mater. 23 (2013) 4765–4775.
[37] S. Ribeiro-Samy, N.A. Silva, V.M. Correlo, J.S. Fraga, L. Pinto, A. Teixeira-Castro, et al., Development and characterization of a PHB-HV-based 3D scaffold for a tissue engineering and cell-therapy combinatorial approach for spinal cord injury regeneration, Macromol. Biosci. 13 (2013) 1576–1592.
[38] J. Wang, J. Zhang, X. Zhang, H. Zhou, A protein-based hydrogel for in vitro expansion of mesenchymal stem cells, PLoS One 8 (2013) e75727.
[39] X. Zeng, Y.S. Zeng, Y.H. Ma, L.Y. Lu, B.L. Du, W. Zhang, et al., Bone marrow mesenchymal stem cells in a three-dimensional gelatin sponge scaffold attenuate inflammation, promote angiogenesis, and reduce cavity formation in experimental spinal cord injury, Cell Transplant. 20 (2011) 1881–1899.
[40] A.J. Mothe, R.Y. Tam, T. Zahir, C.H. Tator, M.S. Shoichet, Repair of the injured spinal cord by transplantation of neural stem cells in a hyaluronan-based hydrogel, Biomaterials 34 (2013) 3775–3783.
[41] I. Zvibel, F. Smets, H. Soriano, Anoikis: roadblock to cell transplantation? Cell Transplant. 11 (2002) 621–630.
[42] X.D. Chen, Extracellular matrix provides an optimal niche for the maintenance and propagation of mesenchymal stem cells, Birth Defects Res. Part C 90 (2010) 45–54.
[43] F. Guilak, D.M. Cohen, B.T. Estes, J.M. Gimble, W. Liedtke, C.S. Chen, Control of stem cell fate by physical interactions with the extracellular matrix, Cell Stem Cell 5 (2009) 17–26.
[44] L. Coulombel, M.H. Vuillet, C. Leroy, G. Tchernia, Lineage- and stage-specific adhesion of human hematopoietic progenitor cells to extracellular matrices from marrow fibroblasts, Blood 71 (1988) 329–334.
[45] T. Matsubara, S. Tsutsumi, H. Pan, H. Hiraoka, R. Oda, M. Nishimura, et al., A new technique to expand human mesenchymal stem cells using basement membrane extracellular matrix, Biochem. Biophys. Res. Commun. 313 (2004) 503–508.
[46] A. Hejcl, J. Sedy, M. Kapcalova, D.A. Toro, T. Amemori, P. Lesny, et al., HPMA-RGD hydrogels seeded with mesenchymal stem cells improve functional outcome in chronic spinal cord injury, Stem Cells Dev. 19 (2010) 1535–1546.
[47] J. Park, E. Lim, S. Back, H. Na, Y. Park, K. Sun, Nerve regeneration following spinal cord injury using matrix metalloproteinase-sensitive, hyaluronic acid-based biomimetic hydrogel scaffold containing brain-derived neurotrophic factor, J. Biomed. Mater. Res. A 93 (2010) 1091–1099.
[48] S.B. Anderson, C.C. Lin, D.V. Kuntzler, K.S. Anseth, The performance of human mesenchymal stem cells encapsulated in cell-degradable polymer-peptide hydrogels, Biomaterials 32 (2011) 3564–3574.
[49] F.Z. Volpato, T. Führmann, C. Migliaresi, D.W. Hutmacher, P.D. Dalton, Using extracellular matrix for regenerative medicine in the spinal cord, Biomaterials 34 (2013) 4945–4955.
[50] G. Perale, F. Rossi, M. Santoro, M. Peviani, S. Papa, D. Llupi, et al., Multiple drug delivery hydrogel system for spinal cord injury repair strategies, J. Control. Release 159 (2012) 271–280.
[51] A. Sacchetti, E. Mauri, M. Sani, M. Masi, F. Rossi, Microwave-assisted synthesis and click chemistry as simple and efficient strategy for RGD functionalized hydrogels, Tetrahedron Lett. 55 (2014) 6817–6820.
[52] M. Barilani, C. Lavazza, M. Vigano, T. Montemurro, V. Boldrin, V. Parazzi, et al., Dissection of the cord blood stromal component reveals predictive parameters for culture outcome, Stem Cells Dev. 24 (2015) 104–114.
[53] L.C. Junquiera, L.C. Junqueira, R.R. Brentani, A simple and sensitive method for the quantitative estimation of collagen, Anal. Biochem. 94 (1979) 96–99.
[54] A. Lopez-De Leon, M. Rojkind, A simple micromethod for collagen and total protein determination in formalin-fixed paraffin-embedded sections, J. Histochem. Cytochem. 33 (1985) 737–743.
[55] M.C. Prewitz, F.P. Seib, M. von Bonin, J. Friedrichs, A. Stissel, C. Niehage, et al., Tightly anchored tissue-mimetic matrices as instructive stem cell microenvironments, Nat. Methods 10 (2013) 788–794.
[56] T.M. Liu, E.H. Lee, Transcriptional regulatory cascades in Runx2-dependent bone development, Tissue Eng. Part B Rev. 19 (2013) 254–263.
[57] F. Barry, R.E. Boynton, B. Liu, J.M. Murphy, Chondrogenic differentiation of mesenchymal stem cells from bone marrow: differentiation-dependent gene expression of matrix components, Exp. Cell Res. 268 (2001) 189–200.
[58] M. Kamata, Y. Okitsu, T. Fujiwara, M. Kanehira, S. Nakajima, T. Takahashi, et al., GATA2 regulates differentiation of bone marrow-derived mesenchymal stem cells, Haematologica 99 (2014) 1686–1696.
[59] E. Ragni, M. Vigano, P. Rebulla, R. Giordano, L. Lazzari, What is beyond a qRT-PCR study on mesenchymal stem cell differentiation properties: how to choose the most reliable housekeeping genes, J. Cell. Mol. Med. 17 (2013) 168–180.
[60] E.R. Zanier, F. Pischiutta, L. Riganti, F. Marchesi, E. Turola, S. Fumagalli, et al.,

Bone marrow mesenchymal stromal cells drive protective M2 microglia polarization after brain trauma, Neurotherapeutics 11 (2014) 679–695.
[61] A.L. Ford, A.L. Goodsall, W.F. Hickey, J.D. Sedgwick, Normal adult ramified microglia separated from other central nervous system macrophages by flow cytometric sorting. Phenotypic differences defined and direct ex vivo antigen presentation to myelin basic protein-reactive CD4+ T cells compared, J. Immunol. 154 (1995) 4309–4321.
[62] A. Capotondo, R. Milazzo, L.S. Politi, A. Quattrini, A. Palini, T. Plati, et al., Brain conditioning is instrumental for successful microglia reconstitution following hematopoietic stem cell transplantation, Proc. Natl. Acad. Sci. U. S. A. 109 (2012) 15018–15023.
[63] D.P. Stirling, V.W. Yong, Dynamics of the inflammatory response after murine spinal cord injury revealed by flow cytometry, J. Neurosci. Res. 86 (2008) 1944–1958.
[64] G. Pennesi, S. Scaglione, P. Giannoni, R. Quarto, Regulatory influence of scaffolds on cell behavior: how cells decode biomaterials, Curr. Pharm. Biotechnol. 12 (2011) 151–159.
[65] S.F. Badylak, D.O. Freytes, T.W. Gilbert, Extracellular matrix as a biological scaffold material: structure and function, Acta Biomater. 5 (2009) 1–13.
[66] D.M. Cohen, C.S. Chen, Mechanical control of stem cell differentiation, StemBook, Cambridge (MA), 2008.
[67] H.K. Cheung, T.T. Han, D.M. Marecak, J.F. Watkins, B.G. Amsden, L.E. Flynn, Composite hydrogel scaffolds incorporating decellularized adipose tissue for soft tissue engineering with adipose-derived stem cells, Biomaterials 35 (2014) 1914–1923.
[68] F.R. Maia, K.B. Fonseca, G. Rodrigues, P.L. Granja, C.C. Barrias, Matrix-driven formation of mesenchymal stem cell-extracellular matrix microtissues on soft alginate hydrogels, Acta Biomater. 10 (2014) 3197–3208.
[69] K. Marycz, D. Szarek, J. Grzesiak, K. Wrzeszcz, Influence of modified alginate hydrogels on mesenchymal stem cells and olfactory bulb-derived glial cells cultures, Bio-Med Mater. Eng. 24 (2014) 1625–1637.
[70] L. Penolazzi, G. Lisignoli, E. Lambertini, E. Torreggiani, C. Manferdini, A. Lolli, et al., Transcription factor decoy against NFATc1 in human primary osteoblasts, Int. J. Mol. Med. 28 (2011) 199–206.
[71] M.J. Cooke, T. Zahir, S.R. Phillips, D.S. Shah, D. Athey, J.H. Lakey, et al., Neural differentiation regulated by biomimetic surfaces presenting motifs of extracellular matrix proteins, J. Biomed. Mater. Res. A 93 (2010) 824–832.
[72] X.D. Chen, V. Dusevich, J.Q. Feng, S.C. Manolagas, R.L. Jilka, Extracellular matrix made by bone marrow cells facilitates expansion of marrow-derived mesenchymal progenitor cells and prevents their differentiation into osteoblasts, J. Bone Min. Res. 22 (2007) 1943–1956.
[73] F. Pampaloni, E.G. Reynaud, E.H. Stelzer, The third dimension bridges the gap between cell culture and live tissue, Nat. Rev. Mol. Cell Biol. 8 (2007) 839–845.
[74] G.D. Prestwich, Simplifying the extracellular matrix for 3-D cell culture and tissue engineering: a pragmatic approach, J. Cell. Biochem. 101 (2007) 1370–1383.
[75] J. Lee, M.J. Cuddihy, N.A. Kotov, Three-dimensional cell culture matrices: state of the art, Tissue Eng. Part B Rev. 14 (2008) 61–86.
[76] L.G. Griffith, M.A. Swartz, Capturing complex 3D tissue physiology in vitro, Nat. Rev. Mol. Cell Biol. 7 (2006) 211–224.
[77] I. Caron, S. Papa, F. Rossi, G. Forloni, P. Veglianese, Nanovector-mediated drug delivery for spinal cord injury treatment, Wiley Interdiscip. Rev. Nanomed. Nanobiotechnol. 6 (2014) 506–515.
[78] S. Papa, F. Rossi, R. Ferrari, A. Mariani, M. De Paola, I. Caron, et al., Selective nanovector mediated treatment of activated proinflammatory microglia/macrophages in spinal cord injury, ACS Nano 7 (2013) 9881–9895.
[79] C. Mannoji, M. Koda, K. Kamiya, M. Dezawa, M. Hashimoto, T. Furuya, et al., Transplantation of human bone marrow stromal cell-derived neuroregenerative cells promotes functional recovery after spinal cord injury in mice, Acta Neurobiol. Exp. 74 (2014) 479–488.
[80] H. Nakajima, K. Uchida, A.R. Guerrero, S. Watanabe, D. Sugita, N. Takeura, et al., Transplantation of mesenchymal stem cells promotes an alternative pathway of macrophage activation and functional recovery after spinal cord injury, J. Neurotrauma 29 (2012) 1614–1625.

Supporting Information

Title: A New Three Dimensional Biomimetic Hydrogel to Deliver Factors Secreted by Human Mesenchymal Stem Cells in Spinal Cord Injury

Ilaria Caron[1,^], Filippo Rossi[2,^], Simonetta Papa[1], Rossella Aloe[1], Marika Sculco[1], Emanuele Mauri[2], Alessandro Sacchetti[2], Eugenio Erba[3], Nicolò Panini[3], Valentina Parazzi[4], Mario Barilani [4], Gianluigi Forloni[1], Giuseppe Perale[5], Lorenza Lazzari[4], Pietro Veglianese[1,]*

1 Dipartimento di Neuroscienze, IRCCS Istituto di Ricerche Farmacologiche "Mario Negri", via La Masa 19, 20156 Milan, Italy,

2.Dipartimento di Chimica, Materiali e Ingegneria Chimica "Giulio Natta", Politecnico di Milano, via Mancinelli 7, 20131 Milan, Italy,

3 Dipartimento di Oncologia, IRCCS Istituto di Ricerche Farmacologiche "Mario Negri", via La Masa 19, 20156 Milan, Italy,

4 Unit of Cell Therapy and Cryobiology, Fondazione IRCCS Ca' Granda Ospedale Maggiore Policlinico, via Francesco Sforza 35, 20122, Milan, Italy

5 Department of Innovative Technologies, University of Applied Sciences and Arts of Southern Switzerland, SUPSI, via Cantonale, CH-6928 Manno, Switzerland

^These authors contributed equally to this work

***Corresponding author: pietro.veglianese@marionegri.it**

A

Surface markers	%
CD90	99.0 ± 0.5
CD105	97.7 ± 0.8
CD73	98.8 ± 0.7
CD34	negative
CD45	negative

B

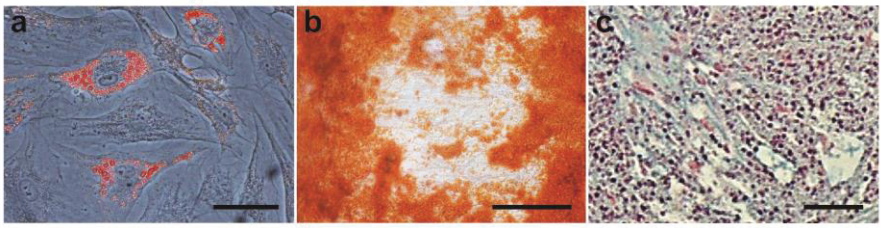

Figure S1: hMSCs identity definition. *(A) Representative immunoprofile of hMSCs. (B) Staining data assessing MSC identity: (a) Oil Red O-positive adipocytes, scale bar represents 50 µm; (b) Alizarin Red S-positive osteocytes, scale bar represents 100 µm; (c) Alcian blue-positive chondrocytes. Scale bar represents 100 µm.*

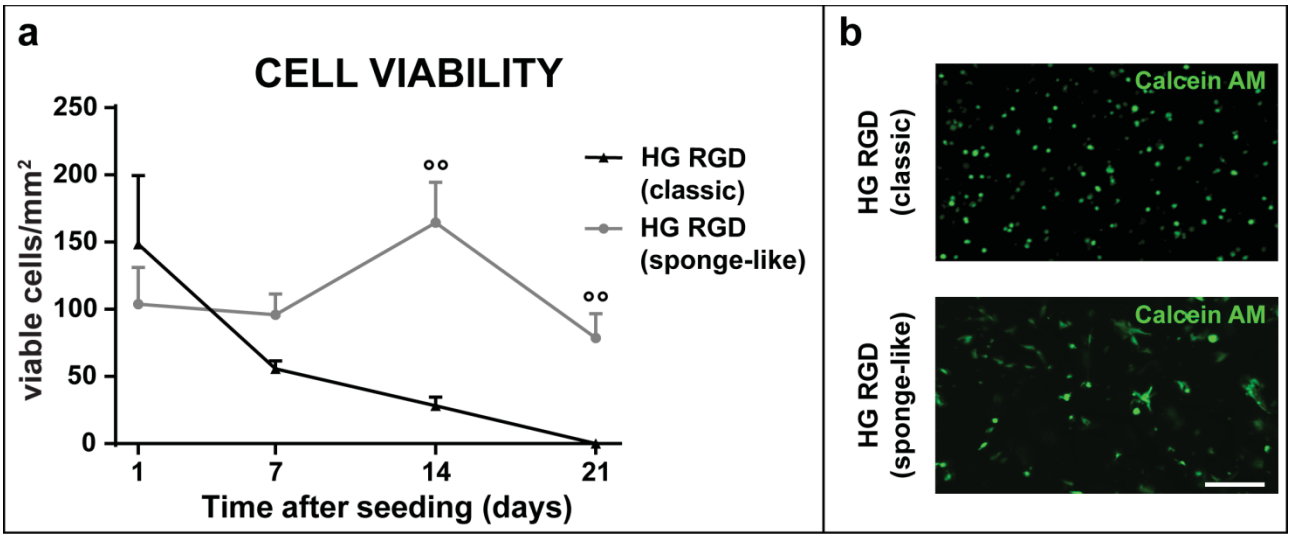

Figure. S2 hMSCs viability in vitro. *(a) Graph representing hMSC viability after a classic or sponge-like loading within HG RGD scaffolds. Cell viability was evaluated over time by labeling live cells with Calcein AM. In the graph the cell density within the hydrogels is reported, as the number of calcein AM positive cells per mm^2. hMSCs after a classic loading display a viability that decreases dramatically already at 7 days post seeding and no viable cells could be observed 21 days after seeding. Contrarily, hMSCs after a sponge-like loading preserve a viability that results to be significant at both 14 and 21 days after seeding compared to classic loading. Statistical analysis: One way Anova for each time point. Mean±SEM is reported. (°°) $p<0.01$ $n=8$ per group. (b) Representative images show hMSCs stained with Calcein AM within HG RGD scaffolds after a classic or sponge-like loading. Some hMSCs with spindle shape morphology are detected in the sponge-like HG RGD, but not in the HG RGD after a classic loading. Scale bar represents 200 µm.*

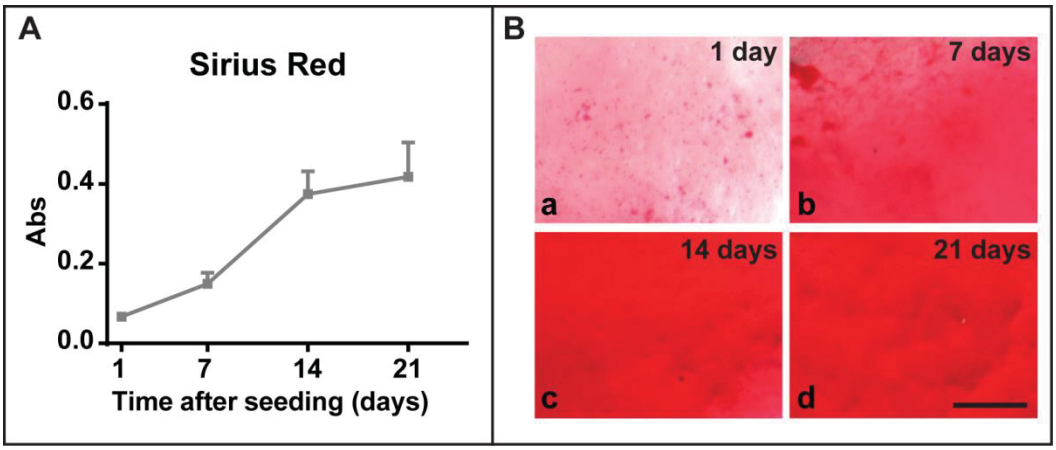

Figure. S3 Quantification of extracellular matrix (ECM) deposition. *(a) Graph representing Sirius Red quantification of ECM deposited by hMSCs seeded in sponge-like HG RGD scaffold. An increase of ECM deposition could be observed from 1 up to 14 days, where ECM deposition reaches a "plateau". (b) Images representing Sirius Red staining of HG RGD scaffold after 1 (a), 7 (b), 14 (c) and 21 (d) days after hMSCs seeding. Scale bar represents 500µm.*

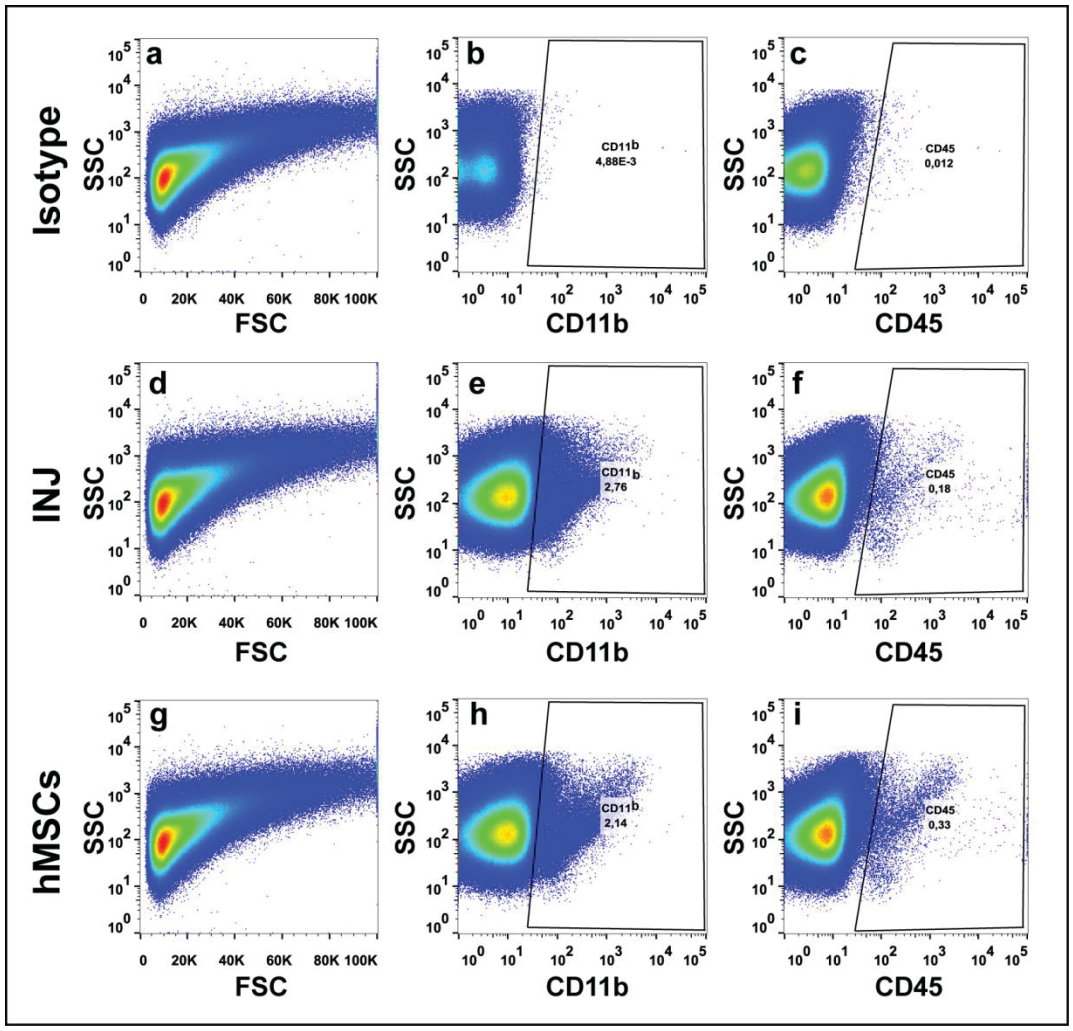

Figure. S4 Gating strategy in FACS analysis for CD11b and CD45 staining. *Representative gating strategy for CD11b (b, e, h) and CD45 (c, f, i) staining in injury (d-f) and hMSCs loaded in HG RGD+ECM (g-i) treated mice evaluated at 9 DPI. Gating performed on the isotype (a-c).*

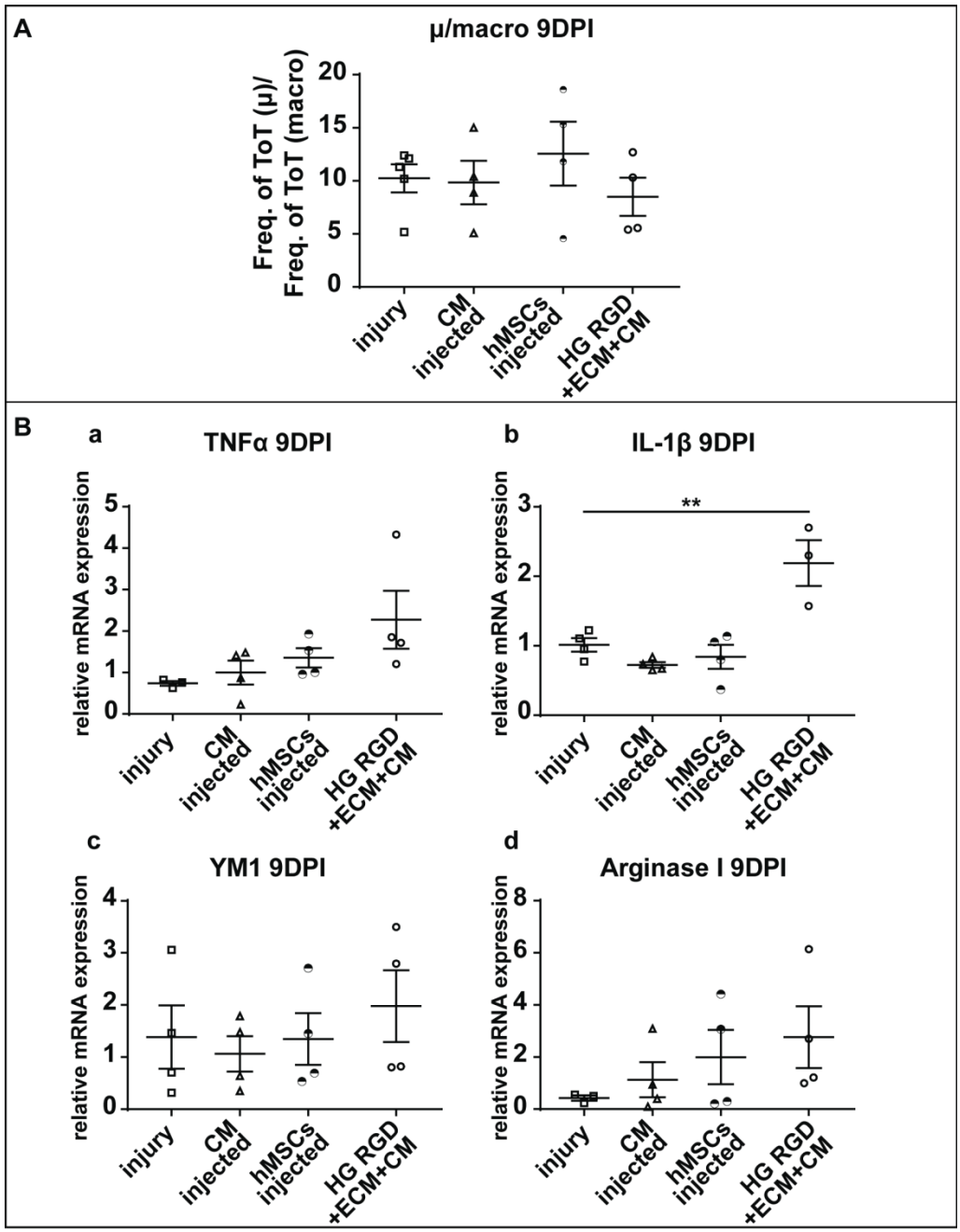

Figure. S5 FACS and mRNA analysis. . *(A) Quantification of the ratio between microglia (CD11b^{pos}/CD45^{low}) and recruited macrophages (CD11b^{pos}/CD45^{high}) evaluated in untreated injured mice (injury), injured mice treated with conditioned medium (CM injected) or hMSCs injected in the parenchyma (hMSCs injected) and injured mice treated with conditioned medium loaded in HG RGD+ECM (HG RGD+ECM+CM) at 9 DPI. No differences are detected among groups analyzed. Mean±SEM is reported. Statistical analysis: One-way ANOVA. n= 5-4 mice per group. (B)*

Quantitative evaluation of mRNA expression of M1 (TNFα, a and IL-1β, b) and M2 (YM1, c and Arginase I, d) markers for microglia/macrophages. No differences are detected among untreated injured mice (injury) and injured mice treated with conditioned medium (CM injected) or hMSCs injected in the parenchyma (hMSCs injected). However, mice treated with conditioned medium loaded within HG RGD+ECM (HG RGD+ECM+CM) show a significant higher IL-1β expression compared to untreated injured mice, suggesting an effect of HG RGD+ECM scaffold in eliciting a pro-inflammatory response. Mean±SEM is reported. Statistical analysis: One-way ANOVA followed by Bonferroni's post hoc test comparing groups to the injury condition. (**) $p<0.01$. n= 5-4 mice per group.

European Journal of Cell Biology 95 (2016) 228–238

Contents lists available at ScienceDirect

European Journal of Cell Biology

journal homepage: www.elsevier.com/locate/ejcb

Research paper

Angiogenic and anti-inflammatory properties of mesenchymal stem cells from cord blood: soluble factors and extracellular vesicles for cell regeneration

Tiziana Montemurro[a,1], Mariele Viganò[a,1], Enrico Ragni[a], Mario Barilani[a], Valentina Parazzi[a], Valentina Boldrin[a], Cristiana Lavazza[a], Elisa Montelatici[a], Federica Banfi[a], Eleonora Lauri[b], Silvia Giovanelli[c], Marco Baccarin[d], Silvana Guerneri[d], Rosaria Giordano[a], Lorenza Lazzari[a,*]

[a] Unit of Cell Therapy and Cryobiology, Fondazione IRCCS Ca' Granda Ospedale Maggiore Policlinico, Milano, Italy
[b] Anatomia Patologica, Ospedale Sacco, Università degli Studi di Milano, Milano, Italy
[c] Milano Cord Blood Bank, Fondazione IRCCS Ca' Granda Ospedale Maggiore Policlinico, Milano, Italy
[d] Laboratorio Citogenetica e Genetica molecolare, Fondazione IRCCS Ca' Granda Ospedale Maggiore Policlinico, Milano, Italy

ARTICLE INFO

Article history:
Received 9 September 2015
Received in revised form 25 February 2016
Accepted 6 April 2016

Keywords:
Cord blood
Human mesenchymal stem cells
miRNA
Angiogenesis
Growth factors
Extracellular vesicles

ABSTRACT

In a recent work, our group showed the existence of two distinct mesenchymal stem cell (MSC) subsets within human umbilical cord blood. One less proliferative and short-living (SL-CBMSC), the other with higher growth rate and long-living (LL-CBMSC), and therefore better suited for regenerative medicine applications. We examined whether LL-CBMSC possess peculiar paracrine properties able to affect angiogenesis or inflammatory processes. It was shown for the first time that pro-angiogenic, proliferation—stimulating and tissue repairing factors were released at high level not only as soluble cytokines, but also as mRNA precursors embedded in membrane vesicles. The combination of this primary (proteic factors interacting with surface receptors) and delayed (mRNA transferred and translated *via* vesicle fusion and cargo release) interaction in endothelial target cells resulted in strong blood vessel induction with the development of capillary-like structures. In addition, LL-CBMSC dynamically modulated their release of pro-angiogenic and anti-inflammatory factors in an *in vitro* model of damage. In conclusion, LL-CBMSC synthesize and secrete multiple factors that may be attuned in response to the status of the target cell, a crucial requisite when paracrine mechanisms are needed at onset of tissue regeneration.

1. Introduction

A great interest has recently arisen in the field of mesenchymal stem cells (MSC) because of their high potential for multi-lineage differentiation and proliferation, characteristics that make these cells useful for clinical applications in tissue engineering, regenerative medicine, cell and gene therapy (Phinney and Prockop, 2007; Murphy et al., 2013; Das et al., 2013). Elective tissues for MSC isolation are bone marrow (BMMSC) and adipose tissue (ADMSC), although their use has disadvantages, including the necessity of invasive harvest from patients or donors. Therefore, alternate sources of MSC have been intensively sought and umbilical cord blood resulted to be an interesting candidate because it is usually discarded at the time of birth after a painless and non-invasive collection process (Bieback et al., 2004; Erices et al., 2000; Gang et al., 2004; Lee et al., 2004). Umbilical cord blood-derived MSC (CBMSC) rapidly gained importance in the regenerative medicine field since, due to their low immunogenicity, they do not elicit the proliferative response of allogeneic lymphocytes (Le Blanc et al., 2003).

In the last few years researchers affiliated with cord blood bank networks provided more and more details in order to improve CBMSC isolation efficiency and identity definition (characteristic and potentialities), essential prerequisites for supporting new clinical concepts in cellular therapy (Kögler et al., 2004; Zhang et al., 2011). In a previous work we clearly showed the existence of at

* Corresponding author at: Unit of Cell Therapy and Cryobiology, Fondazione IRCCS Ca' Granda Ospedale Maggiore Policlinico, Via F. Sforza 35, 20122 Milano, Italy.
E-mail address: lorenza.lazzari@policlinico.mi.it (L. Lazzari).
[1] These authors equally contributed to the work.

http://dx.doi.org/10.1016/j.ejcb.2016.04.003
0171-9335/

least two distinct MSC subsets within the umbilical cord blood: one mainly short-living and less proliferative (SL-CBMSCs), the other long-living, with higher growth rate, and, very importantly, with significantly longer telomere (LL-CBMSCs) (Barilani et al., 2015). Notably, LL-CBMSC retained a higher clonogenic potential together with a high osteogenic commitment, both parameters commonly used to define effective MSC populations.

In this work, we characterized this multipotent LL-CBMSC (hereafter named for simplicity CBMSC) population with respect to several factors related to their practical utility as therapeutic MSC. These include proliferation kinetics, extensive immunophenotypization, gene expression and differentiation capabilities, cytokine secretion, paracrine properties and angiogenesis potential. In this frame, for the first time the presence of mRNA coding for pro-angiogenic and anti-inflammatory factors was investigated in the fraction of secreted extracellular vesicles. These data are therefore intended to be a milestone when working with MSC isolated from umbilical cord blood and intended for clinical applications.

2. Materials and methods

2.1. Isolation of MSC from cord blood (CBMSC)

Human umbilical cord blood (CB, n = 264 samples) was collected from full-term newborns after written informed consent of the mother. After vaginal or cesarean delivery of the baby, the umbilical cord was clamped and disinfected; CB was recovered from umbilical cord veins into sterile collection bag containing 29 mL of citrate-phosphate dextrose (CPD) as anticoagulant (MacoPharma, France). CBMSC isolation was performed as described in Barilani et al., 2015. Complete culture medium consisting of aMEM (Life Technologies, Carlsbad, CA, USA) supplemented with 20% FBS (Life Technologies) was changed every 3 days. At 80% confluence, the cells were harvested using 25% TrypLE Select 1X (Gibco) and were washed with PBS (Gibco) and subcultured at a concentration of 4×10^3 cells/cm^2 till reaching a plateau in the growth curve.

2.2. Cumulative population doublings

Population doubling was calculated for each CBMSC lineage using the following equation: population doubling (PD) = log10(N)/log10(2); where N is the number of cells harvested at the end of the culture/the number of seeded cells. To calculate the expansion potential of cells, cumulative population doublings (CPD) was calculated by recording the cell counts and the cellular dilution factor at each passage (P). Cell counting was performed using Trypan Blue (Fluka, Buchs, Switzerland) to discriminate dead cells.

2.3. Clonogenic potential

The clonogenic potential of CBMSC (n = 7) was tested by fibroblastic-colony-forming unit (CFU-F) assay. For optimal counting of colonies, 200 cells were seeded in duplicate in complete medium 100-mm dishes (Corning) from culture at P2, P4, P6 and P8. The medium was changed weekly and after two weeks the cells were washed with PBS (Life Technologies), fixed with methanol (Sigma-Aldrich), and stained with carbolic gentian violet solution (Ral diagnostics, Cedex, France). After 2 washing steps with milliQ-grade water, colonies with diameter bigger than 1–2 mm were counted.

2.4. Flow cytometric analysis

CBMSC were extensively characterized by flow cytometry at p3 and p5 (n = 7). Cells were washed in PBS for 20 min at RT and incubated in the dark with the following mouse anti-human antibodies: CD3–APC (Beckman Coulter – BC, Brea, CA, USA), CD13–PE (BC), CD14–PE (BC), CD34–APC (Becton Dickinson—BD, San Jose, CA, USA), CD40–FITC (BD), CD44–APC (Miltenyi Biotec, Bergisch Gladbach, Germany), CD45–PC7 (BC), CD56–APC (BC), CD90–FITC (BD), CD73–APC (Miltenyi Biotec), CD105–PE (BC), CD133–PE (Miltenyi Biotec), CD146–PC5 (BC), alpha-SMA–FITC (Sigma-Aldrich), HLA-ABC–FITC (BC), HLA-DR–PE (BC), NG2–PE (BC), NGFR–PE(BD), PDGFR-beta–PE (BD), VE-Cadherin–FITC (Bender Medsystem, Vienna, Austria). The isotype-matched immunoglobulins IgG1–FITC (BC), IgG1–PE (BC), IgG1–PC7 (BC) and IgG1–APC (BC) were used as negative controls under the same conditions. After staining, the cells were washed once with PBS. At least 10,000 events were acquired with a Cytomics FC500 flow cytometer (BC) and data were analyzed using the CXP analysis software.

2.5. Immunofluorescence

CBMSC at p3 were first fixed with cold methanol/acetone (1:1) for 2 min. When necessary, cells were permeabilized with 0.1% Triton X-100 (10 min), then washed in PBS. Non-specific binding sites were blocked with PBS containing 2% bovine serum albumin (Sigma-Aldrich) for 20 min at RT. Cells were incubated with directly conjugated anti-human antibodies against: CD34–FITC (DAKO, Glostrup, Denmark, 1:50), CD144–FITC (Bender MedSystems, 1:25), CD146–PE (ByoCytex, Marseille, France, 1:20), alpha-SMA–FITC (Sigma-Aldrich, 1:100), PDGFR-beta–PE (BD, 1:20), for 1 h at RT. Purified mouse anti-human antibodies were against: CD133 (Miltenyi Biotec, 1:50), Nanog (AbCam, Cambridge, UK, 1:200), Oct-4 AB (Millipore, Billerica, MA, USA, 1:50), SSEA-4 (Chemicon, Temecula, CA, USA, 1:25), Signal Transducers and Activators of Transcription (STAT) 3 (AbCam, 1:10), STAT5 (AbCam, 1:50), STAT6 (AbCam, 1:10) and von Willebrand factor (vWF; DAKO, 1:40). After staining with primary purified antibodies, cells were first incubated with Fluorescence Enhancement Probe (Biocare Medical Inc, Concord, CA, USA) for 30 min at RT and then with DyLight 488 or 549 detection component (Biocare Medical Inc 1:100) for 30 min at RT. Nuclear counterstaining with DAPI (Roche Diagnostic Corporation, Indianapolis, IN, USA) was performed for 15 min at RT. An isotype-matched negative control was performed for each immunostaining. All slides were mounted with DakoCytomation Fluorescent Mounting Medium (DAKO) and the cells were analyzed using a video confocal microscope (ViCo-Eclipse 80i, Nikon, Tokyo, Japan) equipped with Plan Fluor 40x1.30 DIC H/N2 and Plan Apo VC 60x/1.40 DIC N2 oil objectives (Nikon). Photographs were acquired with a CCD cooled interline-transfer FireWire camera (Nikon) and processed using Media Cybernetics Image Pro Plus (Media Cybernetics Inc., Rockville, MD, USA).

Negative controls were performed using a species-specific labelled secondary antibody for indirect immunofluorescence while isotype-matched controls were used for direct staining.

2.6. RNA and microRNA isolation, qRT-PCR analysis

Total RNA including small RNAs as microRNA (miRNA) was isolated with miRNeasy Mini Kit (Qiagen, Hilden, Germany) following manufacturer's instructions from 0.5×10^6 CBMSC (n = 5 at p4) or 1×10^{10} purified extracellular vesicles (EV) (n = 3 at p4). RNA purity was determined by measuring A260/A280 ratio in a Nanodrop spectrophotometer. RNA integrity was assessed using electrophoretic techniques.

For miRNA detection, miR-302b and miR-335 levels, normalized against housekeeping miR-191 and miR-214 (Bargaje et al., 2010), were assayed by qRT-PCR using the miScript II RT Kit for cDNA synthesis (Qiagen) and miScript SYBR Green PCR Kit (Qiagen) as per manufacturer's instructions. Briefly, RNA was first polyadenylated

and then reverse-transcribed to generate first-strand cDNA that was prepared for qRT-PCR with miRNA-specific forward primers (miScript Primer Assay, Qiagen) and a universal qRT-PCR primer included in the miScript SYBR Green PCR mix, and SYBR Green reference dye. All reactions were run in triplicate in a BioRad CFX96 Real-Time PCR Detection System instrument.

For qRT-PCR assays on mRNA, first strand cDNA synthesis and PCR analysis were performed as described in Ragni et al., 2013a using the CFX96™ Real- Time PCR detection system (Biorad, Richmond, CA, USA).

For cell differentiation analyses, differences in expression of Osterix (*OSX*), Osteopontin (*OPN*), Collagen type II alpha 1 (*COL2A1*), Collagen type X alpha 1 (*COL10A1*), Peroxisome proliferator-activated receptor gamma (*PPARG*), Glucose transporter type 4 (*GLUT4*), *ADIPSIN* genes were evaluated by comparing differentiated CBMSC with non-differentiated control CBMSC. TATA-binding protein (*TBP*) and Tyrosine 3-monooxygenase/tryptophan 5-monooxygenase activation protein, zeta polypeptide (*YWHAZ*) were used as reference genes, according to our previous work about stability of different reference genes in MSC (Ragni et al., 2013a).

For mRNA embedded in secreted EV, expression of connective tissue growth factor (*CTGF*), fibroblast growth factor (*FGF*), interleukin-6 (*IL-6*), transforming growth factor beta 1 (*TGFB1*), vascular endothelial growth factor (*VEGF*) and hepatocyte growth factor (*HGF*) was evaluated.

For all genes, primers will be provided upon request.

2.7. qRT-PCR array expression profiling

Mesenchymal-related gene expression profiling was performed with Human Mesenchymal Stem Cells RT^2 Profiler PCR Array System (http://www.sabiosciences.com/rt_pcr_product/HTML/PAHS-082D.html, Qiagen) following manufacturer's instructions and relative expression of each mRNA was determined using the software RT^2 Profiler PCR Array Data Analysis (http://pcrdataanalysis.sabiosciences.com/pcr/arrayanalysis.php). All reactions were run in a BioRad CFX96 Real-Time PCR Detection System instrument (Bio-Rad Laboratories). Results were interpreted with GeneCodis (National Center of Biotechnology—CNB-CSIC, Universidad Complutense de Madrid), a web-based tool for the biologic interpretation of high-throughput experiments.

2.8. Cell lineage differentiation

CBMSC (n = 5 at p4) were differentiated into adipogenic, osteogenic and chondrogenic cell lineages, as previously described (Ragni et al., 2013a). Completion of the differentiation processes were confirmed by qRT-PCR assaying the differentiation-specific mRNA levels in induced and non-induced cultures.

2.9. Hematopoietic support assay

CD34+ hematopoietic progenitors were immunoselected (CD34 Microbead Kit, Miltenyi Biotec) from full term CB units (CB CD34+ cells, n = 3) and were seeded at 5.0×10^3 cells/cm^2 in triplicate on confluent layers of irradiated (10 Gy) CBMSC (n = 3 at p4). As a positive control, MS5 BM stromal cells, which allow the proliferation of very primitive human progenitor cells and allow having reproducible and standardized culture conditions (Issaad et al., 1993), were used. Hematopoietic and mesenchymal cells were co-cultured for 5 weeks in a classical extended long-term culture-initiating cell (LTC-IC) assay in a complete medium (MyeloCult H5100, Stem Cell Technologies) containing freshly prepared hydrocortisone (final concentration 10^{-6} M), but no cytokines. Half of the medium was collected, immediately stored at −80 °C and replaced once a week, and cultures were observed daily for the presence of cobblestone areas (CA). After 5 weeks, 2500 cells were seeded in methylcellulose (H4435, StemCell Technologies) and CFU-granulocyte, erythroid, macrophage, megakaryocyte (GEMM), CFU- granulocyte-macrophage (GM) and high-proliferative-potential colony precursors (HPPC) were scored after 14-day incubation (37 °C, 5% CO_2) (Corselli et al., 2013). In addition, cells in the supernatants and adherent fractions were characterized by flow cytometry for the expression of the following hematopoietic cell markers: CD34, CD38, CD133 and CD45.

2.10. ELISA

The release of stem cell factor (SCF) was measured using a single proteome assay (Human Quantikine ELISA kit, R&D Systems, Minneapolis, MN, USA) in the supernatants of hematopoietic support cultures at different time points (1 to 5 weeks). The collected supernatants were thawed and centrifuged to remove the particulate. The assay was performed following the manufacturer's instructions. The optical density of each sample was determined, until half an hour, using a microplate reader set to 450 nm with wavelength correction set to 570 nm (Genios Plus, TECAN, Salzburg, Austria). Data were analyzed using Magellan Software (TECAN) and expressed as mean concentration (pg/mL) of the secreted factor.

A multiplex sandwich ELISA was performed to quantify some human angiogenesis factors released by CBMSC (n = 5 at p3), such as heparin-binding epidermal growth factor (HB-EGF, lower detection limit: 1.8 pg/mL), hepatocyte growth factor (HGF, lower detection limit: 3.1 pg/mL), fibroblast growth factor (FGF, lower detection limit: 2.0 pg/mL) and vascular endothelial growth factor (VEGF, lower detection limit: 4.9 pg/mL). These evaluations were performed on steady-state MSC supernatants and on supernatants collected from the cell damage assay at different time points (24, 48, 72, 192 h after injury). In addition, on the supernatants collected from the cell damage assay some inflammatory factors tested were tested such as interleukin-10 (IL10, lower detection limit: 0.2 pg/mL), interleukin-12 (IL12 p70, lower detection limit: 0.4 pg/mL), interferon gamma (IFNg, 0.2 pg/mL), tumor necrosis factor (TNFalpha, lower detection limit: 1.6 pg/mL). Briefly, each well of the microplate was pre-spotted with target protein-specific antibodies and 50 μL of standards, and samples were added to the plate for one hour at RT with shaking (200 rpm). After washing away unbound proteins, 50 μL of biotinylated antibodies were added to the plate (30 min, RT, with shaking). Excess of biotinylated antibodies was washed away, and 50 μL of Streptavidin-Horseradish Peroxidase (SA-HRP) was added to the plate (30 min, RT, with shaking). In order to identify the signal, we used SuperSignal ELISA femto chemiluminescent substrate (Pierce, Rockford, IL, USA); the luminescent signal was recorded within 10 min using a cooled CCD camera and amount of each target protein was analyzed using Microsoft Excel 2003 (Microsoft Corporation) as recommended by the manufacturers. Complete medium was also tested as a blank and the value obtained was subtracted from values recorded in cell-conditioned media.

2.11. Response to cell damage

Co-culture assay was set up using a confluent proximal tubular cell line (HK2; ATCC, CRL-2190) cultured with aMEM-GlutaMax™ supplemented with 5% FBS. The damage was induced in HK2 cells by adding 8 μM cisplatin for 6 h (Morigi et al., 2010). After that, cisplatin was removed and, in some wells, CBMSC were added to the culture at a concentration of 5.0×10^4 cells/well. Media were collected from cisplatin-damaged HK-2 cells alone, from CBMSC alone and from co-cultures at 24, 72, 192 h after injury. Angiogenic

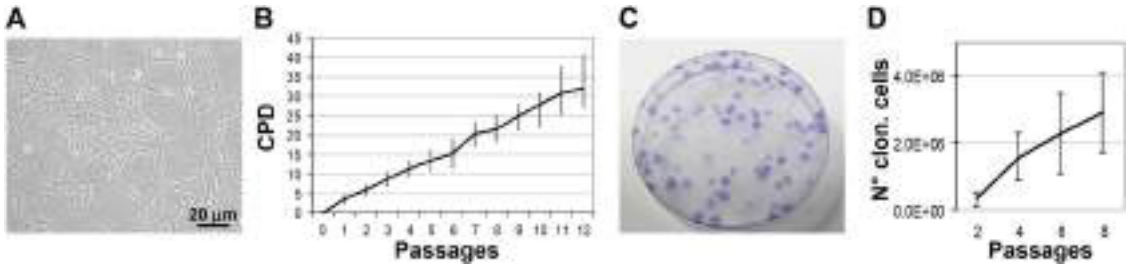

Fig. 1. Morphology, CPD and clonogenic potential of CBMSC. (A) A representative image displaying morphology of CBMSC at passage 3. (B) Growth kinetics of different CBMSC batches expressed as CPD (mean ± SD). (C) A representative CFU-F picture. (D) Absolute number of clonogenic cells during culture.

and inflammatory factors released in the media were quantified by a multiplexed sandwich ELISA, as described above.

2.12. Tube formation assay

Seventy-two hours after addition of complete medium, CBMSC-conditioned media (CM) were harvested from 80% confluent CBMSC cultures (n = 3 at p4) and they were stored at −20 °C until used for the angiogenic assay. The angiogenic potential of CBMSC was investigated using the AngioKit assay (TCS CellWorks Ltd., Buckingham, UK) according to the manufacturer's instructions. In this assay, the CBMSC-CM were tested on co-cultures of human endothelial cells with human interstitial cells at the earliest stages of tubule formation in a 24 well plate format. The angiogenic stimulator VEGF (5 ng/mL) and the well-known inhibitor suramin (10 µg/mL) were included as positive and negative controls, respectively. Complete medium was also used as negative control. Media were changed every 72 h; after 11 days, cells were fixed, stained with blood vessel markers such as CD31 and vWF antibodies and then revealed with diaminobenzidine (DAB) staining. Vascular tubular structures were visualized by an optical microscope. All experiments were performed in triplicate.

2.13. EV preparation

CBMSC (n = 3 at p4) were grown to 80% confluence and then fresh medium without FBS was added. After 24 h, conditioned culture medium was collected and serially centrifuged to remove floating cells and cellular debris (400*g* for 10 min, 600*g* for 10 min and 3000*g* for 15 min) and ultracentrifuged at 100,000*g* for 1 h at 4 °C. The pellet was suspended in PBS or dissolved in lysis buffer for RNA extraction.

2.14. Measurement of particle number and size distribution by nanoparticle tracking analysis (NTA)

NTA was carried out using the Nanosight system (NanoSight, Wiltshire, UK) on EV suspended in PBS. NTA related the rate of brownian motion to particle size. Vesicles were visualized by light scattering using a conventional optical microscope aligned perpendicularly to the beam axis. After a video was taken, the NTA software tracked between frames the Brownian motion of individual vesicles and calculated total concentration and their size through application of the Stokes-Einstein equation.

2.15. Statistical analysis

Results were analyzed by unpaired Student's *t*-test and the statistical significances were accepted for p-values ≤ 0.05.

3. Results and discussion

3.1. Isolation, culture and growth of human CBMSC

After the processing of umbilical cord blood samples, the mononucleated cell fraction was seeded. The appearance of the first fibroblastic adherent cells occurred a median of 16 days after seeding, with a minimum of 4 days to a maximum of 64. These isolated adherent cells presented diamond-like morphological features, with a homogeneous spindle-shaped morphology (Fig. 1A). In order not to cause stress or early senescence to the "newly born" cells, the first trypsinization was set a median of 22 days after seeding, accordingly with our previous data showing consistent and non-senescent phenotype until high passages (10-13) for long-living CBMSC isolated following this protocol (Barilani et al., 2015). To examine the proliferation capacity of the CBMSC *in vitro*, the cumulative population doubling (CPD) was measured (Fig. 1B). Notably, CBMSC reached very high CPD values (between 28 and 42). These data are similar to those previously published for foetal MSC (Guillot et al., 2007; Sung et al., 2010), where CPD values (30-40) resulted to be consistently higher than for adult MSC as BMMSC (CPD between 20 and 25).

Finally, another major breakthrough for MSC definition is that seeding cell suspensions at clonal density results in the establishment of discrete colonies initiated by single cells (the colony-forming unit fibroblastic, CFU-Fs; Friedenstein et al., 1970) and their number and concentration was reported to positively correlate with effective clinical outcomes (Hernigou et al., 2005). Fig. 1C and 1D clearly show that in CBMSC the total number of clonogenic cells continues to rise along time up to passages 6-8 that, for clinical purposes using adult MSC, are generally avoided (6% of reported clinical trials for BMMSC; Ikebe and Suzuki, 2014). All these data confirm both CBMSC "young" features and their intriguing potentialities for prolonged expansion leading to higher cell amount, often a bottleneck for clinical preparations.

3.2. Immunophenotype profiling

MSC: immunophenotyping by flow cytometry is a routinely used approach to characterize purity and homogeneity of clinical preparations (Nery et al., 2013). Stem cell community established that a minimal phenotypic pattern for the identification of MSC requires them to be immunopositive for CD73, CD90, and CD105 expression, while being negative for CD34, CD45, and HLA-DR (Dominici et al., 2006). Furthermore, in the last years many other markers have been associated with stemness although caveats need to be taken into consideration when designing or interpreting MSC immunophenotype panels (Lv et al., 2014; Lin et al., 2013). To have a comprehensive CBMSC characterization, the expression of many verified and postulated MSC cell-surface antigens was evaluated by flow cytometry on cultured cell lines at p3 and p5. As shown in Fig. 2, CBMSC expressed CD13, CD44, CD73, CD90, CD105, HLA

A

Surface Antigen	Mean ± SD (%)	
	CBMSC p3	CBMSC p5
alphaSMA+	84.4 (± 3.8)	97.2 (± 2.0) **
CD3+	0.1 (± 0.1)	0 (± 0)
CD13+	99.5 (± 0.4)	98.3 (± 0.6)
CD14+	0.1 (± 0.1)	0.1 (± 0.1)
CD34+	0.1 (± 0.1)	0 (± 0)
CD40+	0 (± 0)	0.1 (± 0.1)
CD44+	95.0 (± 3.0)	97.3 (± 1.3)
CD45+	0.1 (± 0.1)	0 (± 0)
CD56+	0.1 (± 0.1)	0.2 (± 0.1)
CD73+	98.8 (± 1.0)	97.5 (± 1.7)
CD90+	98.6 (± 0.4)	94.4 (± 3.6)
CD105+	98.0 (± 1.7)	97.7 (± 1.5)
CD133+	0.1 (± 0.1)	0.1 (± 0.1)
CD146+	90.0 (± 7.5)	95.4 (± 5.4)
HLA ABC+	98.0 (± 2.8)	98.8 (± 1.0)
HLA DR+	0.1 (± 0.1)	0.1 (± 0.1)
NG2+	90.3 (± 0.6)	91.8 (± 6.0)
NGFR/CD271+	4.3 (± 1.8)	2.3 (± 2.7)
PDGFRb+	98.1 (± 1.3)	96.5 (± 2.3)
VE-Cadherin+	0.2 (± 0.1)	0.8 (± 0.6)
alphaSMA+/CD146+	85.0 (± 2.5)	93.2 (± 5.7)
alphaSMA+/NG2+	80.0 (± 0.5)	90.8 (± 2.3) **
CD44+/PDGFRb+	93.1 (± 2.3)	94.0 (± 3.9)
CD73+/CD90+	97.8 (± 1.8)	91.2 (± 2.5)
CD90+/CD105+	97.1 (± 1.5)	92.6 (± 2.9)
CD146+/NG2+	88.1 (± 3.6)	90.1 (± 6.2)

B

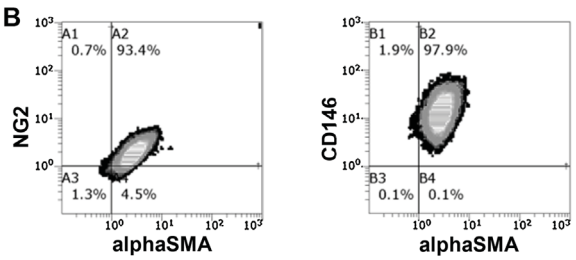

Fig. 2. Flow cytometry analysis of expanded CBMSC. (A) Percentages of cells positive for markers assayed both in single and double staining (mean and standard deviation of 7 replicates) are reported and statistical analysis was performed between passage 3 and 5. ** for p-value ≤ 0.01 (B) representative dot plot panel showing co-expression of CBMSC at p5 for perivascular/pericyte-like markers such as alphaSMA and NG2 and alphaSMA and CD146.

ABC, NGFR and PDGFR-beta. CBMSC were negative for HLA DR, CD3, CD14, CD34, CD40, CD45, CD56, CD133 and VE-Cadherin. These cells also expressed CD146, alpha-SMA and NG2 (Fig. 2A and B), which altogether characterize a multipotent adult stem cell population consistent with a perivascular/pericyte-like phenotype and origin (Crisan et al., 2009). No relevant differences were observed between the two passages and by different batches, except for alpha-SMA (p-value ≤ 0.01) and alpha-SMA/NG2 positive cells (p-value ≤ 0.01) that increased at passage 5. Altogether, these data confirm that CBMSC possess all the stemness markers commonly used to define effective MSC populations and that extensive culturing does not affect their immunophenotype, again suggesting high cell stability during expansion.

3.3. Immunofluorescence

To reinforce flow cytometry data, some crucial stemness markers were visualized by immunofluorescence techniques. Fig. 3A confirms high CBMSC positivity for CD146 and alpha-SMA that, by flow cytometry, resulted to be present in 95% and 97% of analyzed cells at passage 5, respectively. CD146 showed a surface localization, more abundant in the area of cell body, confirming data previously presented in BMMSC (Tormin et al., 2011), whereas alpha-SMA distributed in typical intracellular fibers-resembling structures along the cell longitudinal axis and becoming more tightly associated in the cellular protrusions. Fig. 3B confirms both alpha-SMA localization and high positivity for PDGFRB (96% at passage 5 by flow cytometry), that distributes throughout the cell surface as observed in endothelial progenitor cells (Wang et al., 2012).

Few reports have shown that umbilical cord blood-derived progenitors can express pluripotent/multi-lineage markers, as Oct3/4, Sox2, Nanog and SSEA4 (Habich et al., 2006; Peters et al., 2010; van de Ven et al., 2007). Fig. 3C shows high positivity for the transcription factor Oct4 which is distributed in a punctuate pattern both in the nucleus and in the perinuclear area of the cytoplasm, accordingly with its phosphorylation-dependent nucleocytoplasmic redistribution and its trafficking through nuclear pores (Yang et al., 2014). This localization pattern may be of functional relevance since it was recently demonstrated that transient retention of Oct4 in the nucleus was sufficient to maintain an undifferentiated state in embryonic stem cells (Oka et al., 2013). Fig. 3D shows positivity for cell surface SSEA4 that is seen in the cytoplasm and on the cell surface, both in punctuate patterns and in fibers-resembling aggregates, as shown in periodontal ligament-derived MSC (Trubiani et al., 2010). Finally, we also analyzed the expression of members of the STAT family, which are required for embryonic stem cell maintenance and self-renewal (Bausek, 2013). Notably, CBMSC were positive for STAT-5, -6 and most importantly STAT-3, a key transcriptional determinant for the maintenance of an undifferentiated phenotype in embryonic stem cell and directly regulating the expression of pluripotency-related genes Oct4 and Nanog (Raz et al., 1999; Chih-I et al., 2012) (Fig. 3E–G). Taken altogether, these results suggest that CBMSC, often considerate as foetal MSC, are primitive cells, somewhere between embryonic stem cells and mature adult stem cells.

3.4. Molecular profiling

Among molecular factors discriminating between various stem cell types, microRNA (miRNA) were recently identified (Huang and Lin, 2012). miRNA are non-coding RNAs able to regulate gene expression at a post-transcriptional level, with each miRNA being able to target a number of different mRNA species and to establish complex networks of interactions to coordinate cellular responses. Also, miRNAs are involved in stem cell self-renewal and differentiation by targeting components that determine stem cell fate (Yu et al., 2012). Therefore, to characterize at molecular level the stemness properties of CBMSC, the expression of "stemness" miR-302b and miR-335 (Tomé et al., 2011; Lee et al., 2008) was assessed. Such analysis was performed in comparison with standard and validated BMMSC populations routinely used in our laboratory and using miR-191/miR-214 as housekeepers (Bargaje et al., 2010), since their stability and thus suitability to be used as miRNA reference between CBMSC and BMMSC was confirmed in a recent publication of our group (Ragni et al., 2013b). Notably, both markers were significantly (p-value ≤ 0.05) more expressed in CBMSC than in bone marrow MSC, with miR-302b being 17 times upregulated (Fig. 4A). These data are a further confirmation for CBMSC primitive identity since miR-302b was shown to play an important role in maintaining pluripotency in embryonic stem cells and in maintaining cell self-renewal (Lee et al., 2008).

Further, specific gene expression signatures were also demonstrated to be correlated with stemness properties of mesenchymal stem cells (Wang et al., 2011; Jansen et al., 2010). Thus, we profiled the expression of key genes involved in maintaining pluripotency and self-renewal status and encompassing several functions

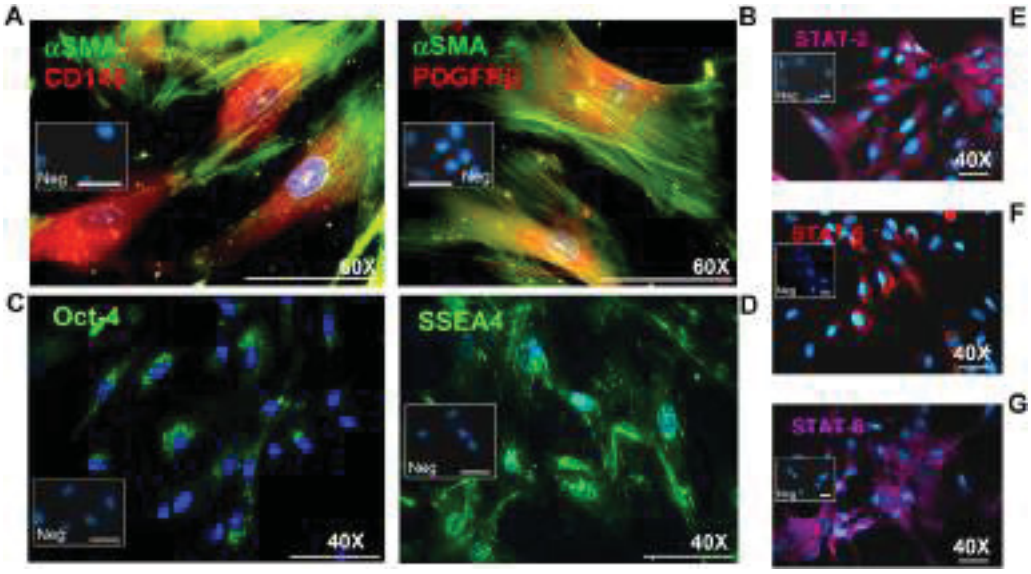

Fig. 3. Immunofluorescence analysis. Cultured CBMSC were positive for perivascular markers (A and B) and for embryonic markers such as Oct-4 AB and SSEA-4 (C and D). CBMSC were positive also for STAT-3 (E), STAT-5 (F) and STAT-6 (G). Magnification 40–60× as reported in figure. Scale bars 20 μm. Negative controls with a species-specific labelled secondary antibody for indirect immunofluorescence and isotype-matched controls for direct staining are shown in small boxes.

(stemness markers, MSC-specific markers, MSC-differentiation markers and MSC-associated genes) in three independent CBMSC isolates (see Supplementary Table 1 in the online version at DOI: 10.1016/j.ejcb.2016.04.003). Notably, all three CBMSC showed a consistent similarity in the expression of tested genes (R value > 0.9 for each couple of datasets) that allowed extracting a panel of 55 genes to be submitted to hierarchical clustering analysis (Fig. 4B). This defined a panel of 22 candidates consistently expressed at homogeneously high levels (*VIM*, *COL1A1*, *ITGB1*, *RHOA*, *ANXA5A*, *CTA2*, *ALCAM*, *CD44*, *MMP2*, *ITGAV*, *TGFB1*, *SMURF2*, *VEGFA*, *JAG1*, *KITLG*, *ENG*, *GTF3A*, *IL6*, *NT5E*, *ANPEP*, *FGF2* and *THY1*). On these identified genes, the GeneCodis program was run to find statistically enriched biological processes with respect to the entries of the whole human genome (Carmona-Saez et al., 2007; Nogales-Cadenas et al., 2009; Tabas-Madrid et al., 2012). Interestingly, the most significant biological processes were angiogenesis (pValue 6.6e-10), positive regulation of cell proliferation (2.0e-09) and cell adhesion (4.0e-08). Consistently, looking for enriched molecular functions, GeneCodis identified growth factor activity (6.7e-10), protein binding (4.3e-06) and cytokine activity (3.4e-06). Finally, five genes, *ANXA5* (coding for a calcium-dependent phospholipid binding protein expressed in perycites with the capacity to differentiate into multiple mesenchymal lineages; Brachvogel et al., 2005), *COL1A1* (Collagen, type I, alpha 1 expressed in bone marrow MSC with high osteogenic potential; Kulterer et al., 2007), *ITGB1* (Integrin, beta 1 surface antigen specifically marking MSC populations; Salem and Thiemermann, 2010), *RHOA* (small GTPase with an essential role in the migration of MSC *via* reorganization

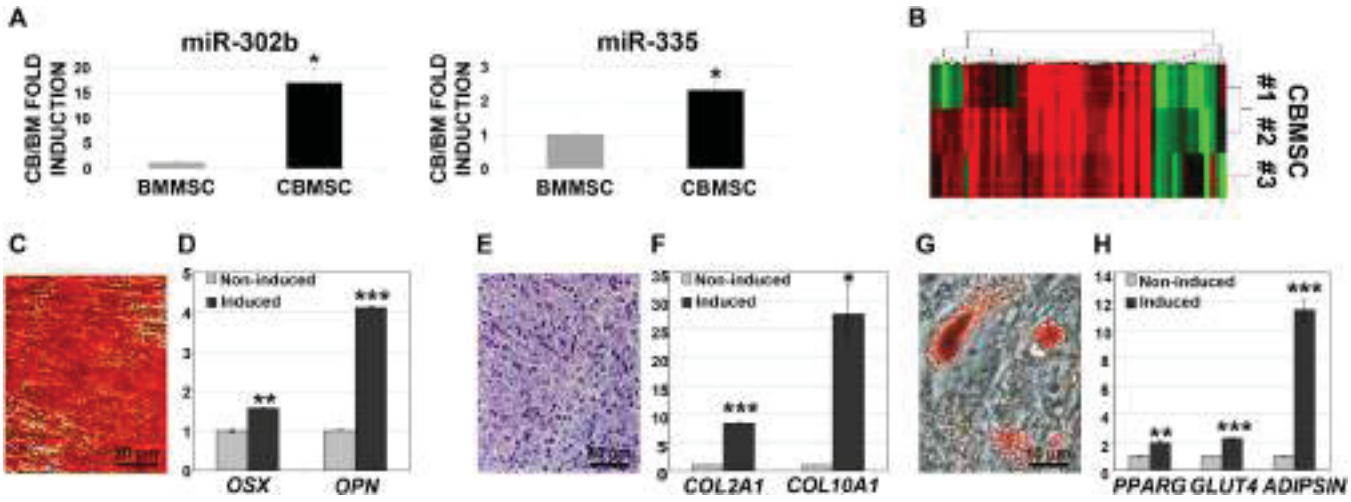

Fig. 4. Molecular profile and cell differentiation of CBMSC. (A) qRT-PCR analysis of mi*R*-302b and mi*R*-335 in CBMSC vs BMMSC with normalized BMMSC values set as 1. Error bars represent SEM. * for p-value ≤ 0.05. (B) Hierarchical clustering of mesenchymal stem cell-associated genes of three independent CBMSC isolates at passage 5, obtained with Cluster 3.0 software following default settings. (C and D) The osteogenic induction was verified by alizarin red staining, which marks calcium-rich minerals deposits and by quantification of osteo-related genes, Osterix (*OSX*), and Osteopontin (*OPN*); ** for p-value ≤ 0.01, *** for p-value ≤ 0.001. (E and F) Chondrogenesis was proved by alcian blue staining of the chondrocyte-specific glucosaminoglycan and by expression of Collagen type II and type X, alpha 1 (*COL2A1*, *COL10A1*) in induced cells respect to control cells; * for p-value ≤ 0.05, *** for p-value ≤ 0.001. (G and H) Lipid droplets in the adipogenic-differentiated CBMSC stained positive for Oil red O. For this differentiation Peroxisome proliferator-activated receptor gamma (*PPARG*), Glucose transporter type 4 (*GLUT4*) and *ADIPSIN* genes were evaluated; ** for p-value ≤ 0.01, *** for p-value ≤ 0.001.

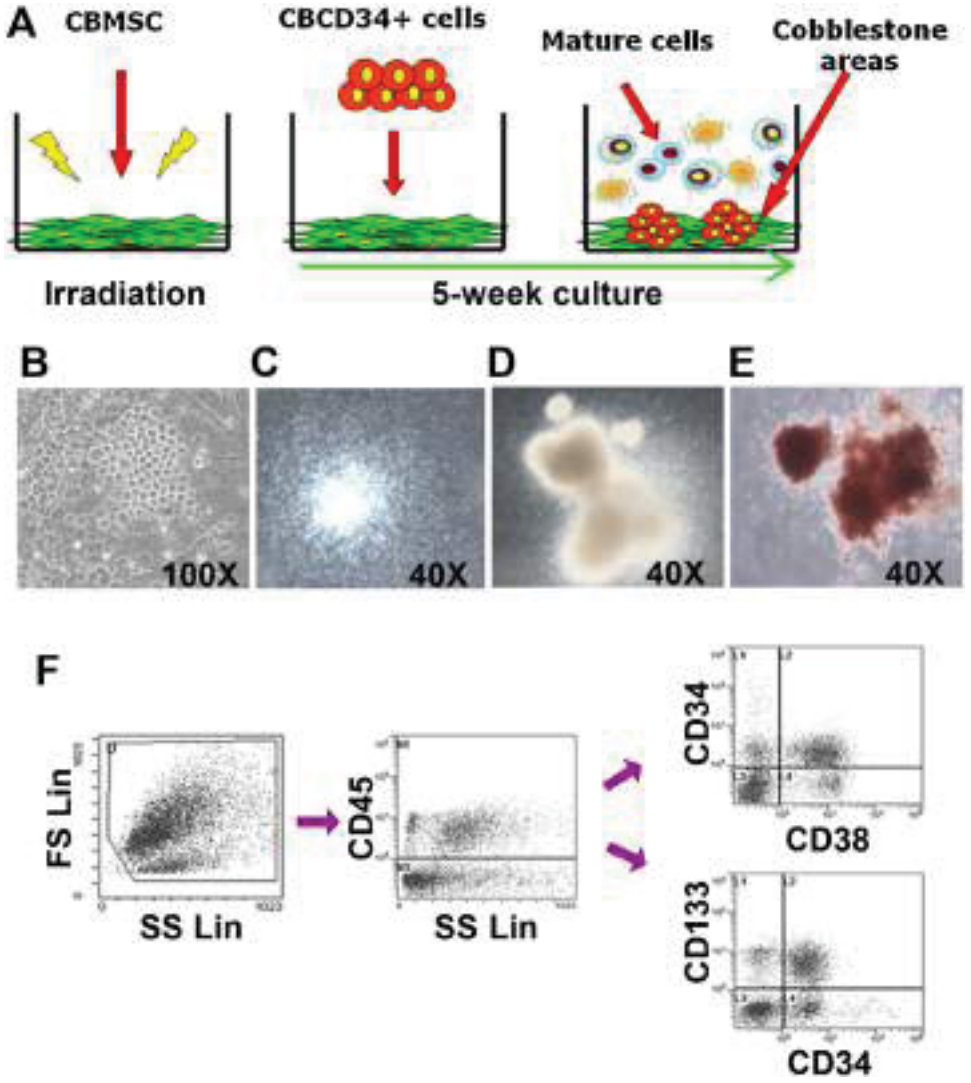

Fig. 5. Hematopoietic support. (A) HSC CD34+ from CB units were co-cultured with CBMSC, according to the scheme pictured. (B) Phase-contrast microscopic view of adherent cells showed the dark round cells forming a cobblestone area underneath the fibroblastic cell layer. (C–E) HSC CD34+ cells were grown on CBMSC for 5 weeks, harvested, and allowed to form colonies in semisolid media for 14 days before scoring colony phenotypes (C: HPPC, D: CFU-GM, E: CFU-GEMM). Magnification B: 100×; C–E: 40×. (F) Cells harvested at the end of LTC-IC assay were analyzed by flow cytometry for the detection of hematopoietic markers CD34, CD38 and CD133 within the CD45+ cell compartment.

of the cytoskeleton; Raheja et al., 2011) and *VIM* (Vimentin, a type III intermediate filament protein that is expressed in mesenchymal cells; Madeira et al., 2012), were always the most expressed in each CBMSC, thus defining a subset of five highly reliable and abundant MSC markers to unequivocally define umbilical cord blood-derived mesenchymal stem cells.

3.5. Cell lineage differentiation

As a whole with a unique molecular signature, a distinguishing feature of MSC is their great capacity for self-renewal while maintaining their multipotency. MSC are capable of differentiating to mesengenic osteocytic, chondrocytic, and adipocytic lineages when stimulated under appropriate conditions (Augello and De Bari, 2010). We studied this potency in CBMSC by exposure to appropriate inductive media *in vitro*.

In osteogenic conditions, CBMSC acquired extended area of mineralization, as evidenced by staining with the calcium-specific dye Alizarin red (Fig. 4C). Induced cells consistently showed elevated levels of the late stage marker associated with osteogenesis *OPN* (4-fold increase) (Fig. 4D). Both aspects confirm the ability of CBMSC to complete *in vitro* the osteogenic process.

CBMSC cultured in chondrogenic conditions demonstrated the presence of intracellular matrix mucopolysaccharides, that are cartilage-specific proteoglycans, as evidenced by Alcian Blue staining (Fig. 4E). Effective chondrogenesis was further corroborated by analyzing the mRNA level increase of type II collagen (*COL2A1*, 8-fold increse) and type X collagen (*COL10A1*, 27-fold increase), both being routinely used as marker of late-stage chondrocyte hypertrophy (associated with endochondral ossification) (Fig. 4F). Again, such data indicate the full potential to differentiate *in vitro* into mature chondrocytes.

Under adipogenic induction, few CBMSC generated sporadic lipid vacuoles with very small intracellular lipid droplets stainable by the triglyceride-specific dye Oil Red O (Fig. 4G). Poor adipogenic potential detected by microscopic analysis was consistent with the qRT-PCR results observed for late adipogenesis markers *PPARG* (2-fold increase), *GLUT4* (2-fold increase) and *ADIPSIN* (11-fold increase) (Fig. 4H) that, in ADMSC and BMMSC, after adipogenic process were demonstrated to display much higher increase ratios (eg, *ADIPSIN* increase of 110-fold for ADMSC and

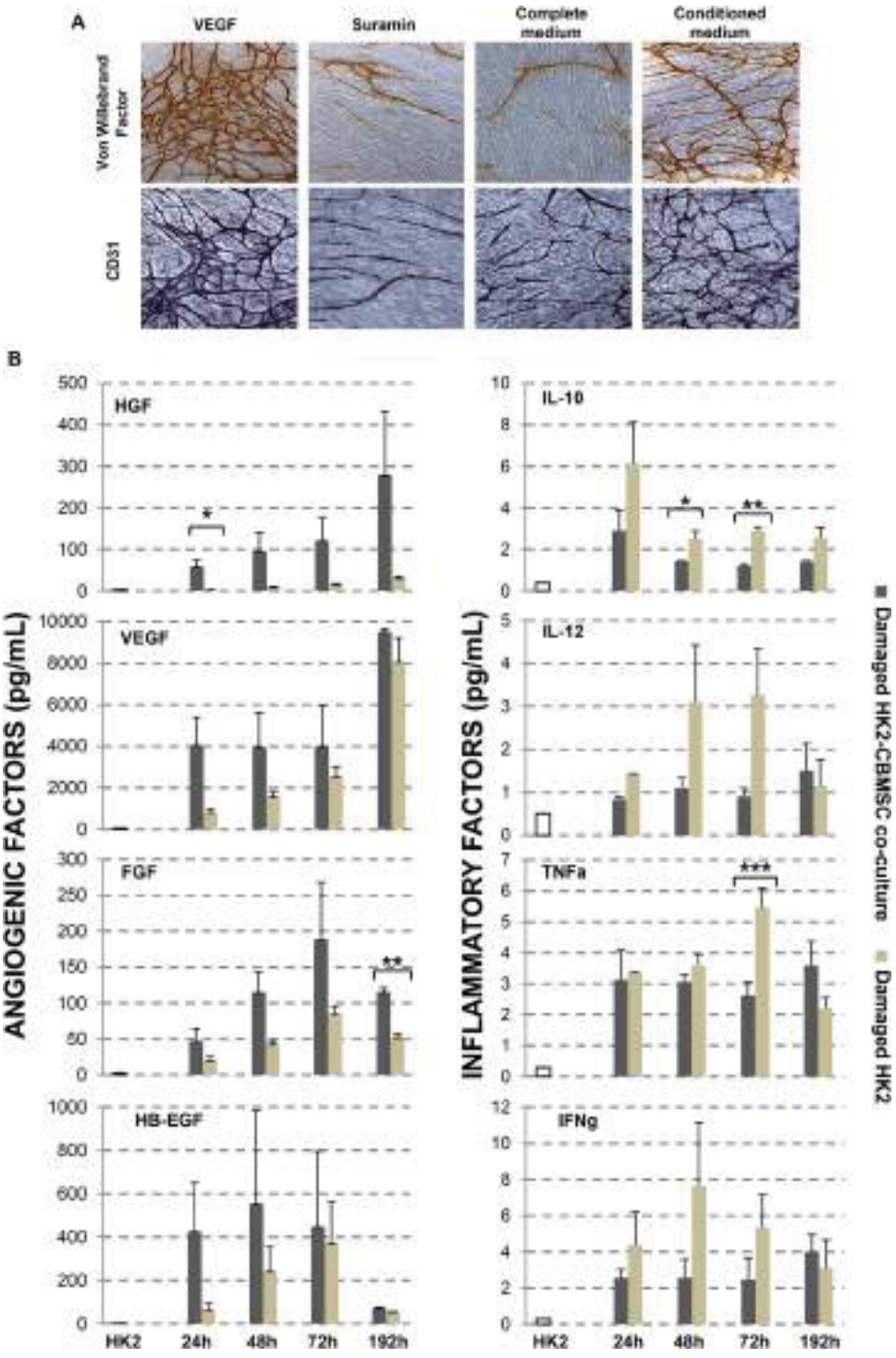

Fig. 6. Angiogenic potential of CBMSC and secretory profile in response to cell damage. (A) Tube formation and the presence of capillary-like networks were induced by CBMSC conditioned media, as highlighted by staining endothelial cells with antibodies against von Willebrand factor and CD31. VEGF was used as positive control; suramin and complete medium were used as negative control. (B) To explore the angiogenic and anti-inflammatory potential, CBMSC were co-cultured for 24–48–72–192 h in an *in vitro* system of damage repair (cisplatin-damaged HK2 cells). Black bars: co-culture of HK2 cell line after cisplatin damage together with CBMSC; grey bars: HK2 cell line after cisplatin damage. HK2 cell line without damage was used as steady-state: white bars. * for p-value ≤ 0.05, ** for p-value ≤ 0.01, *** for p-value ≤ 0.001.

60-fold for BMMSC, as shown in a recent publication of our group, Ragni et al., 2013a). Intriguingly, low efficiency of the adipogenic *in vitro* differentiation remains one of the major limitations also for embryonic stem cells (Dani et al., 1997; Schaedlich et al., 2010; Chen et al., 2007), being this another trait connecting CBMSC with primitive stem cell populations.

3.6. Hematopoietic support ability

Together with their multilineage potential, one of the first features that unequivocally characterized MSC populations isolated from the bone marrow stroma was their ability to provide microenvironmental support for hematopoietic stem cells (HSC) (Morrison and Scadden, 2014). Thus, in order to deeply define CBMSC

identity in the frame of stem cell-related potentialities, we explored umbilical cord blood-derived cells ability to sustain *ex vivo* HSC expansion.

By co-culturing CBMSC with umbilical cord blood CD34+ HSC, according to the scheme presented in Fig. 5A, we observed a robust ability to support hematopoietic cell proliferation, also if compared to standardized MS5 murine bone marrow stromal cell line used as a feeder. Notably, already after 10 days, the appearance of typical colonies of adherent haematopoietic cells named cobblestone areas (tightly knit group of phase-dark, angular cells in the stroma) was observed (Fig. 5B), confirming that CBMSC could support and expand HSC. During all the long-term culture-initiating cell assay (LTC-IC), the cobblestone areas were strongly maintained. Then, after 5 weeks, these primary stroma-supported cultures were scored for replatable colony-forming cells (CFC) that are released into the culture supernatant and assayed in semisolid culture systems (Bock, 1997). Very large hematopoietic colonies were detected as shown in Fig. 6C–E with a strong presence of high proliferative potential cells (Fig. 5C) together with colony forming (CFU) such as granulocyte/macrophage CFU (Fig. 5D) and granulocyte/erythroid/macrophage/megakaryocyte CFU (Fig. 5E). In addition, at the end of the LTC-IC, the immunophenotype of the cells after trypsinization was analyzed by flow cytometry and confirmed the presence of primitive hematopoietic cells expressing CD34, CD133 and CD38 within the CD45+ cell compartment (Fig. 5F).

Finally, if compared to MS5, CBMSC secreted high levels (83.7 + 22.1 pg/mL *versus* undetectable levels) of SCF, an essential hematopoietic cytokine that interacts, with other cytokines, to preserve the viability of hematopoietic stem and progenitor cells (Hassan and Zander, 1996). Altogether, these results demonstrated that CBMSC may provide a useful source of stromal support for CD34+ HSC expansion and suggest the use of these cells in place of commonly used BMMSC to positively impact *ex vivo* expansion and preservation of the 'stemness' potential of HSC.

3.7. Secretory profile

As clearly shown by the effective hematopoietic support ability, MSC may influence surrounding cells or reconstruct a coordinating function, in particular *via* the secretion of factors like cytokines and chemokines (Schinköthe et al., 2008). Molecular data suggested that CBMSC may be strongly involved in angiogenesis and promotion of cell proliferation. Thus, cytokines involved in these processes were evaluated in the growth medium. At steady state CBMSC spontaneously released 13.5 pg/mL (range 8.7–16.7) HB-EGF (angiogenesis and wound healing), 22.4 pg/mL (range 16.3–39.1) HGF (angiogenesis and tissue regeneration), 10.6 pg/mL (range 7.1–13.5) FGF (angiogenesis and wound healing) and 471.3 (range 369.3–590.0) pg/mL VEGF (vasculogenesis and angiogenesis), as assessed by quantitative multiplex ELISA measurement of angiogenic factors.

In addition to their role as biomarkers, released extracellular vesicles (EV) have been very recently included among the players contributing to MSC regenerative potential (Teng et al., 2015; Zhang et al., 2015; Anderson et al., 2016) although, to date, a molecular definition of their cargo is missing. In this frame, we deeply investigated the ability of CBMSC to secrete EV and further characterized their nucleic acids content for mRNA promoting angiogenesis and cell proliferation. CBMSC spontaneously secreted 4500 EV/cell/day (range 3200–5300). CBMSC-EV showed a mean size of 250 nm (range 50–450 nm), suggesting absence or negligible contamination of apoptotic bodies that usually fall into the size range of 1–5 μm. qRT-PCR analysis demonstrated the presence of several transcripts related to angiogenic and proliferative functions. The most abundantly detected were *CTGF* (inductor of vascular endothelial angiogenesis), *FGF* and *IL-6* (inductor of VEGF expression) mRNAs. We also clearly observed *TGFB1* (angiogenesis) and *VEGF* transcripts. Finally, *HGF* mRNA was amplified, although at low amount.

Altogether, these data confirm that CBMSC secrete crucial proangiogenic, proliferation-stimulating and tissue repair factors, either as soluble cytokines (fast and transitory response) or as membrane vesicles embedded precursors (delayed and durable support through translated mRNA), that may sequentially contribute to cell recovery and regeneration.

3.8. Tube formation assay

The angiogenic potential of CBMSC was investigated by assessing the effect of conditioned medium (CM), containing both secreted factors and EV, on endothelial cell culture. CBMSC-CM was able to significantly induce blood vessel response with the development of capillary-like structures resulting positive for the endothelial markers von Willebrand Factor (glycoprotein present in the subendothelial matrix of the vessel wall) and CD31 (glycoprotein present in endothelial cells) (Fig. 6A). Also, CM augmented the number of blood vessels crossing the delimited area and increased the formation of new blood vessels as observed with recombinant VEGF, used as positive control; conversely, the unconditioned medium did not display any pro-angiogenic activity, analogously to suramin (an anti-trypanosomal agent with an antiangiogenic action). These results suggest that CBMSC could be particularly attractive for their pro-angiogenic properties, especially in those processes requiring new blood vessel formation.

3.9. Response to cell damage

During wound healing, angiogenic capillary sprouts invade the fibrin/fibronectin-rich wound clot and within a few days organize into a microvascular network throughout the granulation tissue (Tonnesen et al., 2000). The chemotherapeutic agent cisplatin is known to promote acute kidney injury with vasoconstriction, detachment of tubular cells, luminal tubular obstruction and trans-tubular back-leakage of the glomerular filtrate (Ozkok and Edelstein, 2014). Among other factors, renal function healing is associated with an adequate blood supply and, in animal models, MSC supplementation promoted the recovery of damaged blood vessels, thereby contributing to the maintenance of blood perfusion and to the stabilisation of the vasculature (Kucic et al., 2008; Tögel et al., 2009). Therefore, to confirm CBMSC secretome angiogenic support, a standardized *in vitro* model of renal damage caused by cisplatin was performed (Morigi et al., 2010). In the co-culture wells with damaged renal HK-2 cells, angiogenic factors were strongly released in a much higher quantity if compared to the steady state levels (Fig. 6B). In particular, the production of HGF significantly increased compared to cisplatin-damaged HK-2 cells alone at different time points (p value ≤ 0.05 at 24 h). Consistently, the other assayed angiogenic factors showed an increased trend, even if not statistically significant, in the first 48–72 h in the presence of the damage. These results strongly suggest that CBMSC are responding dynamically in the wound bed niche promoting angiogenesis observed in animal models.

Finally, the secretion of immunomodulatory molecules in our renal damage model was assayed (Fig. 6B). A significant reduction of inflammatory factors such as TNFalpha, IL10, IL1beta and INFgamma was observed at all the major time points when CBMSC were co-cultured in the presence of the damage. These results confirm the plasticity of mesenchymal stem cells in immunomodulation and reinforce the idea of CBMSC as potent cellular products

for therapeutic applications when paracrine mechanisms are needed as it happens during tissue regeneration.

4. Conclusions

Whereas a plethora of different tissue origins for the isolation of mesenchymal stem cells have been described, human umbilical cord blood presents a large number of advantages being devoid from any ethical controversy with non-invasive harvesting procedures. Isolated CBMSC possess all the features of the most commonly used adult MSC with striking and specific features such as their increased proliferative and pro-angiogenic capacities. Intriguingly, this ability may be due to a two-step mechanism involving in a first instance fast-acting secreted soluble factors and subsequently EV-delivered nucleic acids for a durable response. Therefore, data herein presented support CBMSC as a very promising stem cell population for all clinical applications relying on tissue regeneration most of all when new blood vessel formation together with immunomodulation and paracrine support are critical component of wound healing process.

Conflict of interest

Authors declare no conflicts of interest.

Acknowledgements

This study was partially supported by grants from Fondazione Il Sangue, Fondazione NovusSanguis, from Regione Lombardia (PB 0098), from Ministero della Salute Italiano ("Young Researchers" grants: R.F.G.R. 2010-2318448, R.F.G.R. 2010-2312573) and the 6FP EU Project – THERCORD, the 7FP EU Project – CASCADE and REBORNE (Grant Agreement Number 241879). The authors thank Francesca Chelli, Gabriella Spaltro, Gabriella Andriolo and Viviana Lo Cicero for their strong CBMSC commitment. And all the Milano Cord Blood Bank group for their support.

References

Anderson, J.D., Johansson, H.J., Graham, C.S., Vesterlund, M., Pham, M.T., Bramlett, C.S., Montgomery, E.N., Mellema, M.S., Bardini, R.L., Contreras, Z., Hoon, M., Bauer, G., Fink, K.D., Fury, B., Hendrix, K.J., Chedin, F., El-Andaloussi, S., Hwang, B., Mulligan, M.S., Lehtiö, J., Nolta, J.A., 2016. Comprehensive proteomic analysis of mesenchymal stem cell exosomes reveals modulation of angiogenesis via NFkB signaling. Stem Cells (January), 19.

Augello, A., De Bari, C., 2010. The regulation of differentiation in mesenchymal stem cells. Hum. Gene Ther. 21, 1226–1238.

Bargaje, R., Hariharan, M., Scaria, V., Pillai, B., 2010. Consensus miRNA expression profiles derived from interplatform normalization of microarray data. RNA 16, 16–25.

Barilani, M., Lavazza, C., Viganò, M., Montemurro, T., Boldrin, V., Parazzi, V., Montelatici, E., Crosti, M.C., Moro, M., Giordano, R., Lazzari, L., 2015. Dissection of the cord blood stromal component reveals predictive parameters for culture outcome. Stem Cells Dev. 1, 104–114.

Bausek, N., 2013. JAK-STAT signaling in stem cells and their niches in *Drosophila*. JAKSTAT 2, e25686.

Bieback, K., Kern, S., Klüter, H., Eichler, H., 2004. Critical parameters for the isolation of mesenchymal stem cells from umbilical cord blood. Stem Cells 22, 625–634.

Bock, T.A., 1997. Assay systems for hematopoietic stem and progenitor cells. Stem Cells 1, 185–195.

Brachvogel, B., Moch, H., Pausch, F., Schlötzer-Schrehardt, U., Hofmann, C., Hallmann, R., von der Mark, K., Winkler, T., Pöschl, E., 2005. Perivascular cells expressing annexin A5 define a novel mesenchymal stem cell-like population with the capacity to differentiate into multiple mesenchymal lineages. Development 132, 2657–2668.

Carmona-Saez, P., Chagoyen, M., Tirado, F., Carazo, J.M., Pascual-Montano, A., 2007. GENECODIS: a web-based tool for finding significant concurrent annotations in gene lists. Genome Biol. 8, R3.

Chen, T.L., Shen, W.J., Qiu, X.W., Li, T., Hoffman, A.R., Kraemer, F.B., 2007. Generation of novel adipocyte monolayer cultures from embryonic stem cells. Stem Cells Dev. 16, 371–380.

Corselli, M., Chin, C.J., Parekh, C., Sahaghian, A., Wang, W., Ge, S., Evseenko, D., Wang, X., Montelatici, E., Lazzari, L., Crooks, G.M., Péault, B., 2013. Perivascular support of human hematopoietic stem/progenitor cells. Blood 121, 2891–2901.

Crisan, M., Chen, C.W., Corselli, M., Andriolo, G., Lazzari, L., Péault, B., 2009. Perivascular multipotent progenitor cells in human organs. Ann. N. Y. Acad. Sci. 1176, 118–123.

Dani, C., Smith, A.G., Dessolin, S., Leroy, P., Staccini, L., Villageois, P., Darimont, C., Ailhaud, C., 1997. Differentiation of embryonic stem cells into adipocytes in vitro. J. Cell Sci. 110, 1279–1285.

Das, M., Sundell, I.B., Koka, P.S., 2013. Adult mesenchymal stem cells and their potency in the cell-based therapy. J. Stem Cells 8, 1–16.

Dominici, M., Le Blanc, K., Mueller, I., Slaper-Cortenbach, I., Marini, F., Krause, D., Deans, R., Keating, A., Prockop, D.J., Horwitz, E., 2006. Minimal criteria for defining multipotent mesenchymal stromal cells: The International Society for Cellular Therapy position statement. Cytotherapy 8, 315–317.

Erices, A., Conget, P., Minguell, J.J., 2000. Mesenchymal progenitor cells in human umbilical cord blood. Br. J. Haematol. 109, 235–242.

Friedenstein, A.J., Chailakhjan, R.K., Lalykina, K.S., 1970. The development of fibroblast colonies in monolayer cultures of guinea-pig bone marrow and spleen cells. Cell Tissue Kinet. 3, 393–403.

Gang, E.J., Hong, S.H., Jeong, J.A., Hwang, S.H., Kim, S.W., Yang, I.H., Ahn, C., Han, H., Kim, H., 2004. In vitro mesengenic potential of human umbilical cord blood-derived mesenchymal stem cells. Biochem. Biophys. Res. Commun. 13, 102–118.

Guillot, P.V., Gotherstrom, C., Chan, J., Kurata, H., Fisk, N.M., 2007. Human first-trimester fetal MSC express pluripotency markers and grow faster and have longer telomeres than adult. MSC Stem Cells 25, 646–654.

Habich, A., Jurga, M., Markiewicz, I., Lukomska, B., Bany-Laszewicz, U., Domanska-Janik, K., 2006. Early appearance of stem/progenitor cells with neural-like characteristics in human cord blood mononuclear fraction cultured in vitro. Exp. Hematol. 34, 914–925.

Hassan, H.T., Zander, A., 1996. Stem cell factor as a survival and growth factor in human normal and malignant hematopoiesis. Acta Haematol. 95, 257–262.

Hernigou, P., Poignard, A., Beaujean, F., Rouard, H., 2005. Percutaneous autologous bone-marrow grafting for nonunions: influence of the number and concentration of progenitor cells. J. Bone Joint Surg. Am. 87, 1430–1437.

Huang, X.A., Lin, H., 2012. The miRNA regulation of stem cells. Wiley Interdiscip. Rev. Membr. Transp. Signal. 1, 83–95.

Ikebe, C., Suzuki, K., 2014. Mesenchymal stem cells for regenerative therapy: optimization of cell preparation protocols. Biomed. Res. Int., 95151.

Issaad, C., Croisille, L., Katz, A., Vainchenker, W., Coulombel, L., 1993. A murine stromal cell line allows the proliferation of very primitive human CD34+/CD38- progenitor cells in long-term cultures and semisolid assays. Blood 81, 2916–2924.

Jansen, B.J., Gilissen, C., Roelofs, H., Schaap-Oziemlak, A., Veltman, J.A., Raymakers, R.A., Jansen, J.H., Kögler, G., Figdor, C.G., Torensma, R., Adema, G.J., 2010. Functional differences between mesenchymal stem cell populations are reflected by their transcriptome. Stem Cells Dev. 19, 481–490.

Kögler, G., Sensken, S., Airey Trapp, T., Müschen, M., Feldhahn, N., Liedtke, S., Sorg, R.V., Fischer, J., Rosenbaum, C., Greschat, S., Knipper, A., Bender, J., Degistirici, O., Gao, J., Caplan, A.I., Colletti, E.J., Almeida-Porada, G., Müller, H.W., Zanjani, E., Wernet, P., 2004. A new human somatic stem cell from placental cord blood with intrinsic pluripotent differentiation potential. J. Exp. Med. 200, 123–135.

Kucic, T., Copland, I.B., Cuerquis, J., Coutu, D.L., Chalifour, L.E., Gagnon, R.F., Galipeau, J., 2008. Mesenchymal stromal cells genetically engineered to overexpress IGF-I enhance cell-based gene therapy of renal failure-induced anemia. Am. J. Physiol. Renal Physiol. 295, F488–496.

Kulterer, B., Friedl, G., Jandrositz, A., Sanchez-Cabo, F., Prokesch, A., Paar, C., Scheideler, M., Windhager, R., Preisegger, K.H., Trajanoski, Z., 2007. Gene expression profiling of human mesenchymal stem cells derived from bone marrow during expansion and osteoblast differentiation. BMC Genomics 8, 70.

Le Blanc, K., Tammik, C., Rosendahl, K., Zetterberg, E., Ringdén, O., 2003. HLA expression and immunologic properties of differentiated and undifferentiated mesenchymal stem cells. Exp. Hematol. 31, 890–896.

Lee, M.W., Choi, J., Yang, M.S., Moon, Y.J., Park, J.S., Kim, H.C., Kim, Y.J., 2004. Mesenchymal stem cells from cryopreserved human umbilical cord blood. Biochem. Biophys. Res. Commun. 320, 273–278.

Lee, N.S., Kim, J.S., Cho, W.J., Lee, M.R., Steiner, R., Gompers, A., Ling, D., Zhang, J., Strom, P., Behlke, M., Moon, S.H., Salvaterra, P.M., Jove, R., Kim, K.S., 2008. miR-302b maintains stemness of human embryonal carcinoma cells by post-transcriptional regulation of Cyclin D2 expression. Biochem. Biophys. Res. Commun. 377, 434–440.

Lin, C.S., Xin, Z.C., Dai, J., Lue, T.F., 2013. Commonly used mesenchymal stem cell markers and tracking labels: limitations and challenges. Histol. Histopathol. 28, 1109–1116.

Lv, F.J., Tuan, R.S., Cheung, K.M., Leung, V.Y., 2014. Concise review: the surface markers and identity of human mesenchymal stem cells. Stem Cells 32, 1408–1419.

Madeira, A., da Silva, C.L., dos Santos, F., Camafeita, E., Cabral, J.M., Sá-Correia, I., 2012. Human mesenchymal stem cell expression program upon extended ex-vivo cultivation, as revealed by 2-DE-based quantitative proteomics. PLoS One 7, e43523.

Morigi, M., Rota, C., Montemurro, T., Montelatici, E., Lo Cicero, V., Imberti, B., Abbate, M., Zoja, C., Cassis, P., Longaretti, L., Rebulla, P., Introna, M., Capelli, C., Benigni, A., Remuzzi, G., Lazzari, L., 2010. Life-sparing effect of human cord blood-mesenchymal stem cells in experimental acute kidney injury. Stem Cells 28, 513–522.

Morrison, S.J., Scadden, D.T., 2014. The bone marrow niche for haematopoietic stem cells. Nature 505, 327–334.

Murphy, M.B., Moncivais, K., Caplan, A.I., 2013. Mesenchymal stem cells: environmentally responsive therapeutics for regenerative medicine. Exp. Mol. Med. 45, e54.
Nery, A.A., Nascimento, I.C., Glaser, T., Bassaneze, V., Krieger, J.E., Ulrich, H., 2013. Human mesenchymal stem cells: from immunophenotyping by flow cytometry to clinical applications. Cytometry A 83, 48–61.
Nogales-Cadenas, R., Carmona-Saez, P., Vazquez, M., Vicente, C., Yang, X., Tirado, F., Carazo, J.M., Pascual-Montano, A., 2009. GeneCodis: interpreting gene lists through enrichment analysis and integration of diverse biological information. Nucleic Acids Res. 37, W317–W322.
Oka, M., Moriyama, T., Asally, M., Kawakami, K., Yoneda, Y., 2013. Differential role for transcription factor Oct4 nucleocytoplasmic dynamics in somatic cell reprogramming and selfrenewal of embryonic stem cells. J. Biol. Chem. 288, 15085–15097.
Ozkok, A., Edelstein, L.C., 2014. Pathophysiology of cisplatin-induced acute kidney injury. Biomed. Res. Int., 967826.
Peters, R., Wolf, M.J., van den Broek, M., Nuvolone, M., Dannenmann, S., Stieger, B., Rapold, R., Konrad, D., Rubin, A., Bertino, J.R., 2010. Efficient generation of multipotent mesenchymal stem cells from umbilical cord blood in stroma-free liquid culture. PLoS One 5, e15689.
Phinney, D.G., Prockop, D.J., 2007. Concise review: mesenchymal stem/multipotent stromal cells: the state of transdifferentiation and modes of tissue repair—current views. Stem Cells 25, 2896–2902.
Ragni, E., Viganò, M., Rebulla, P., Giordano, R., Lazzari, L., 2013a. What is beyond a qRT-PCR study on mesenchymal stem cell differentiation properties: how to choose the most reliable housekeeping genes. J. Cell. Mol. Med. 17, 168–180.
Ragni, E., Montemurro, T., Montelatici, E., Lavazza, C., Viganò, M., Rebulla, P., Giordano, R., Lazzari, L., 2013b. Differential microRNA signature of human mesenchymal stem cells from different sources reveals an environmental-niche memory for bone marrow stem cells. Exp. Cell Res. 319, 1562–1574.
Raheja, L.F., Genetos, D.C., Wong, A., Yellowley, C.E., 2011. Hypoxic regulation of mesenchymal stem cell migration: the role of RhoA and HIF-1α. Cell Biol. Int. 35, 981–989.
Raz, R., Lee, C.K., Cannizzaro, L.A., d'Eustachio, P., Levy, D.E., 1999. Essential role of STAT3 for embryonic stem cell pluripotency. Proc. Natl. Acad. Sci. U. S. A. 96, 2846–2851.
Salem, H.K., Thiemermann, C., 2010. Mesenchymal stromal cells: current understanding and clinical status. Stem Cells 28, 585–596.
Schaedlich, K., Knelangen, J.M., Navarrete Santos, A., Fischer, B., Navarrete Santos, A., 2010. A simple method to sort ESC-derived adipocytes. Cytometry A 77, 990–995.
Schinköthe, T., Bloch, W., Schmidt, A., 2008. In vitro secreting profile of human mesenchymal stem cells. Stem Cells Dev. 17, 199–206.
Sung, H.J., Hong, S.C., Yoo, J.H., Oh, J.H., Shin, H.J., Choi, I.Y., Ahn, K.H., Kim, S.H., Park, Y., Kim, B.S., 2010. Stemness evaluation of mesenchymal stem cells from placentas according to developmental stage: comparison to those from adult bone marrow. J. Korean Med. Sci. 25, 1418–1426.
Tögel, F., Zhang, P., Hu, Z., Westenfelder, C., 2009. VEGF is a mediator of the renoprotective effects of multipotent marrow stromal cells in acute kidney injury. J. Cell. Mol. Med. 13, 2109–2114.
Tabas-Madrid, D., Nogales-Cadenas, R., Pascual-Montano, A., 2012. GeneCodis3: a non-redundant and modular enrichment analysis tool for functional genomics. Nucleic Acids Res. 40, W478–W483.
Teng, X., Chen, L., Chen, W., Yang, J., Yang, Z., Shen, Z., 2015. Mesenchymal stem cell-derived exosomes improve the microenvironment of infarcted myocardium contributing to angiogenesis and anti-inflammation. Cell. Physiol. Biochem. 37, 2415–2424.
Tomé, M., López-Romero, P., Albo, C., Sepúlveda, J.C., Fernández-Gutiérrez, B., Dopazo, A., Bernad, A., González, M.A., 2011. miR-335 orchestrates cell proliferation: migration and differentiation in human mesenchymal stem cells. Cell Death Differ. 18, 985–995.
Tonnesen, G.M., Feng, X., Clark, R.A.F., 2000. Angiogenesis in wound healing. J. Invest. Dermatol. Symp. Proc. 5, 40–46.
Tormin, A., Li, O., Brune, J.C., Walsh, S., Schütz, B., Ehinger, M., Ditzel, N., Kassem, M., Scheding, S., 2011. CD146 expression on primary nonhematopoietic bone marrow stem cells is correlated with in situ localization. Blood 117, 5067–5077.
Trubiani, O., Zalzal, S.F., Paganelli, R., Marchisio, M., Giancola, R., Pizzicannella, J., Bühring, H.J., Piattelli, M., Caputi, S., Nanci, A., 2010. Expression profile of the embryonic markers nanog, OCT-4, SSEA-1, SSEA-4 and frizzled-9 receptor in human periodontal ligament mesenchymal stem cells. J. Cell. Physiol. 225, 123–131.
van de Ven, C., Collins, D., Bradley, M.B., Morris, E., Cairo, M.S., 2007. The potential of umbilical cord bloodmultipotent stem cells for nonhematopoietic tissue and cell regeneration. Exp. Hematol. 35, 1753–1765.
Wang, T.H., Lee, Y.S., Hwang, S.M., 2011. Transcriptome analysis of common gene expression in human mesenchymal stem cells derived from four different origins. Methods Mol. Biol. 698, 405–417.
Wang, H., Yin, Y., Li, W., Zhao, X., Yu, Y., Zhu, J., Qin, Z., Wang, Q., Wang, K., Lu, W., Liu, J., Huang, L., 2012. Over-expression of PDGFR-b promotes PDGF-induced proliferation, migration, and angiogenesis of EPCs through PI3 K/Akt signaling pathway. PLoS One 7, e30503.
Yang, J., Cai, N., Yi, F., Liu, G.H., Qu, J., Izpisua Belmonte, J.C., 2014. Gating pluripotency via nuclear pores. Trends Mol. Med. 20, 1–7.
Yu, Z., Li, Y., Fan, H., Liu, Z., Pestell, R.G., 2012. miRNAs regulate stem cell self-renewal and differentiation. Front. Genet. 3, 191.
Zhang, X., Hirai, M., Cantero, S., Ciubotariu, R., Dobrila, L., Hirsh, A., Igura, K., Satoh, H., Yokomi, I., Nishimura, T., Yamaguchi, S., Yoshimura, K., Rubinstein, P., Takahashi, T.A., 2011. Isolation and characterization of mesenchymal stem cells from human umbilical cord blood: reevaluation of critical factors for successful isolation and high ability to proliferate and differentiate to chondrocytes as compared to mesenchymal stem cells from bone marrow and adipose tissue. J. Cell. Biochem. 112, 1206–1218.
Zhang, Y., Chopp, M., Meng, Y., Katakowski, M., Xin, H., Mahmood, A., Xiong, Y., 2015. Effect of exosomes derived from multipluripotent mesenchymal stromal cells on functional recovery and neurovascular plasticity in rats after traumatic brain injury. J. Neurosurg. 122, 856–867.

Supplementary Table 1

	CBMSC 1	**CBMSC 2**	**CBMSC 3**
ABCB1	34.36	39.39	36.64
ALCAM	25.67	24.24	25.85
ANPEP	29.67	26.42	26.53
ANXA5	22.78	23.47	24.67
BDNF	27.81	28.05	29.25
BGLAP	32.36	31.33	32.10
BMP2	40.00	36.46	39.12
BMP4	40.00	40.00	40.00
BMP6	37.10	35.02	35.21
BMP7	40.00	40.00	40.00
CASP3	28.69	27.84	28.85
CD44	26.01	24.39	25.62
COL1A1	23.31	19.63	19.85
CSF2	37.28	37.13	37.47
CSF3	36.76	37.94	40.00
CTNNB1	31.43	27.84	27.78
EGF	28.37	31.23	35.93
ENG	28.40	25.76	26.54
ERBB2	35.56	32.14	31.02
FGF10	39.54	38.82	40.00
FGF2	25.65	26.49	27.31
FUT1	40.00	39.78	39.69
FUT4	40.00	37.53	35.15
FZD9	40.00	38.52	37.62
GDF15	33.71	34.18	27.09
GDF5	33.67	29.19	27.26
GDF6	36.66	32.76	30.76
GDF7	40.00	40.00	38.41
GTF3A	24.07	25.86	28.07
HAT1	23.88	27.85	29.02
HDAC1	28.87	27.21	27.84

HGF	40.00	35.76	30.60
HNF1A	40.00	38.02	40.00
ICAM1	32.22	29.66	28.50
IFNG	40.00	39.06	40.00
IGF1	40.00	39.83	40.00
IL10	40.00	39.91	39.96
IL1B	34.62	29.20	28.38
IL6	24.20	26.17	28.83
INS	38.85	40.00	40.00
ITGA6	29.27	28.87	28.92
ITGAV	26.85	24.95	25.78
ITGAX	38.21	40.00	40.00
ITGB1	22.87	21.90	22.56
JAG1	31.31	25.63	27.19
KDR	34.40	32.33	34.85
KITLG	26.63	25.71	28.16
LIF	30.33	27.89	28.73
MCAM	28.92	27.13	27.96
MMP2	26.36	24.46	25.26
NES	31.17	31.07	34.09
NGFR	39.76	39.51	40.00
NOTCH1	36.91	33.51	33.70
NT5E	26.49	26.19	27.12
NUDT6	28.69	29.58	27.19
PDGFRB	35.62	29.23	27.70
PIGS	30.74	27.98	27.71
POU5F1	38.05	34.58	34.68
PPARG	34.03	33.08	31.95
PROM1	36.74	40.00	40.00
PTK2	29.85	27.94	28.66
PTPRC	40.00	40.00	40.00
RHOA	21.70	22.63	24.78
RUNX2	32.55	27.86	30.88

SLC17A5	30.46	29.39	29.63
SMAD4	29.49	27.53	29.02
SMURF1	32.17	29.16	29.82
SMURF2	24.99	25.22	26.94
SOX2	40.00	40.00	40.00
SOX9	31.97	31.43	31.70
TBX5	40.00	39.31	40.00
TERT	39.33	38.99	40.00
TGFB1	28.57	24.99	25.51
TGFB3	34.21	31.81	30.41
THY1	29.14	26.89	25.94
TNF	40.00	39.56	40.00
VCAM1	29.17	29.64	30.51
VEGFA	25.61	25.25	26.56
VIM	19.75	19.36	21.71
VWF	38.13	38.28	37.26
WNT3A	38.02	37.85	40.00
ZFP42	40.00	40.00	34.63

II. Unpublished data

a. NG2, CD56 and IGF1 as multipotent mesenchymal stromal cell markers reminiscent of adult or perinatal tissue harvest

Barilani M[1,2], Ragni E[1], Banfi F[1], Sironi S[1], Cherubini A[1], Guillaumin S[1], Lazzari L[1]

[1]Unit of Cell Therapy and Cryobiology, Fondazione IRCCS Ca' Granda, Ospedale Maggiore Policlinico, Milano, Italy
[2]Department of Industrial Engineering, University of Padoa, Padova, Italy

Introduction

Over the past 15 years, multipotent mesenchymal stromal cell (MSC) research has grown exponentially and a plethora of additional MSC sources have been unraveled [1], suggesting that they can be present virtually in any vascularized tissue of the body [2, 3].

Nowadays, MSCs can be divided mainly into adult and perinatal stem cells, depending on their tissue source. Adult MSCs include those deriving from bone marrow [4] and adipose tissue [5], whereas perinatal MSCs are isolated from amniotic fluid [6], cord blood [7-9], umbilical cord perivascular compartment [10] and Wharton's jelly [11, 12].

In 2006, Dominici et al. [13] provided milestone guidelines with a minimal set of standard criteria to define the specific characteristics of MSCs. The properties that define MSC populations were classified into three categories: physical properties, defined by their ability to adhere to plastic culture surfaces; immunophenotypic properties, corresponding to the expression of specific surface antigens (CD105-, CD73- and CD90-positive, and CD45-, CD34-, CD14- or CD11b-, CD79a- or CD19- and HLA-DR-negative cells); functional properties, defined as the potential to differentiate into osteoblasts, adipocytes and chondrocytes *in vitro*.

These criteria have been extremely helpful to initially provide common accepted parameters in the MSC field. Nonetheless, we think it is now mandatory to shed new light on MSC features, with a focus on adult and perinatal MSCs, compared to human foreskin fibroblasts (HSFs).

With the present study we will be able to answer very relevant questions: are there alternative determinants able to discriminate tissue-specific MSCs? Can we clearly distinguish MSCs from adult and perinatal sources? Summarizing: are all MSCs the same?

Materials and methods

Cell isolation, growth and MSC characterization

Each stem cell type was isolated from independent healthy donors (n=3), after informed consent was obtained. The isolation protocols were already described by Ragni et al. [14, 15] for ADMSCs and BMMSCs, Barilani et al. [8, 9] for CBMSCs, Bossolasco et al. [16] for AFCs, Montemurro et al. [17] for PVCs, Batsali et al. [10] for WJMSCs, Gioventù et al. [18] for DPMSCs, Normand et al. [19] for HSFs. All cells were cultured in αMEM (Thermo Fisher Scientific, Waltham, MA, USA) supplemented with 20% FBS (Thermo Fisher Scientific). AFCs were cultured in a medium specific for amniocytes (Amniomed; Euroclone, Pero, Italy). Stem cell identity of isolated MSCs was assessed by immunophenotype profiling, which confirmed high expression of typical MSC surface markers, such as CD90, CD73, CD44, and CD105, and negativity for the hematopoietic markers CD34, CD133 and CD45. Characterization of each MSC type was performed by adipogenic, osteogenic and chondrogenic differentiation protocols and subsequent histochemical staining, as previously described in Barilani et al. (2016) (data not shown).

All the following analyses (flow cytometry, PCR-array, Real Time qRT-PCR, ELISA) were performed at passage 3-5 for each cell population, with a medium change 24 hours before cell harvesting or collection of conditioned media.

RNA isolation

RNA was isolated using RNeasy Plus Mini-kit (Qiagen, Hilden, Germany), following manufacturer's instructions. RNA purity was determined by measuring absorbance A260/A280 in a Nanodrop spectrophotometer (ND-1000; Thermo Fisher Scientific, Waltham, MA, USA). RNA integrity was assessed using electrophoretic techniques.

qRT-PCR array expression profiling

mRNA expression profiling was performed with Mesenchymal Stem Cell RT2 Profiler PCR Array System (Qiagen), following manufacturer's instructions. Relative expression of each mRNA was determined with the Ct method using the software RT2 Profiler PCR Array Data Analysis (Qiagen) and the housekeeping genes of the array.

cDNA synthesis and quantitative RT-PCR assays

cDNAs were synthesized from 800 ng of total RNA in 20 µL reactions, using the iScript cDNA synthesis kit (Bio-Rad Laboratories, Hercules, CA, USA), according to the manufacturer's instructions. Specific primers for BMP7, CD56, CD146, CD271, EGF, FUT1, IGF1, NG2, PDGFR and TBX5 were designed in-house, selecting only the primers spanning an exon-exon junction and producing a PCR amplificate with length between 70 and 150 base pairs. Real Time qRT-PCR was carried out using SsoFast EvaGreen Supermix (Bio-Rad) in a BioRad CFX96 Real-Time PCR Detection System instrument (Bio-Rad), using standard PCR conditions. All experiments were perfomed in triplicates and values exceeding standard deviation >10% were discarded; each assay included a blank. To confirm product specificity, a melting curve analysis was performed after each amplification. Relative gene expression was normalized to ACTB, B2M, GAPDH, and RPLP0 gene expression using the ΔΔCt method. For statistical analysis and expression data generation, the Bio-Rad CFX Manager software was used. Primer sequences will be provided upon request.

Flow cytometry

100,000 cells were harvested for each cell population. The cells were centrifuged at 350 xg for 7 minutes, after which the supernatant was discarded. The resuspended cell pellet was then incubated with fluorochrome-conjugated antibodies in a total volume of 200 µL of PBS for 20 minutes in the dark at RT. The following antibodies (BD, Franklin Lakes, NJ, USA) were used: CD271-PE, PDGFR-β-PE, CD56-PC5, CD146-PC7, SSEA4-FITC, NG2-PE, CD34-PerCP-C5.5. Unstained samples were prepared to assess autofluorescence. A total of 10,000 events were acquired using a BD FACSCanto II cytometer (BD) and analyzed by the BD FACSDiva version 7 analysis software (BD). The use of the

application setting option for the cytometer parameter adjustment guaranteed consistent and unbiased analysis of samples within different experiments.

ELISA

Supernatants of MSCs and HSFs were collected at passage 3-5 after centrifugation at 350 xg for 10 minutes and stored at -20°C. Human MCP-1 and IGF1 proteins were quantified in with the human MCP-1 ELISA Kit (Thermo Scientific, Rockford, IL, USA) and human IGF1 ELISA Kit (Elabscience, WuHan, China), according to manufacturer's instructions. The optical density (OD value) was detected with a plate reader (GENios Plus; TECAN, Männedorf, Switzerland) with a 450 nm filter set. The data were analyzed with Magellan software (TECAN).

Statistical analysis

All statistical analysis were performed with Prism version 6.0 (GraphPad, La Jolla, CA, USA), if not indicated otherwise. Single linkage clustering was performed with R software (https://www.r-project.org).

Principal component analysis was performed with Multibase software (www.numericaldynamics.com).

Results: qRT-PCR array

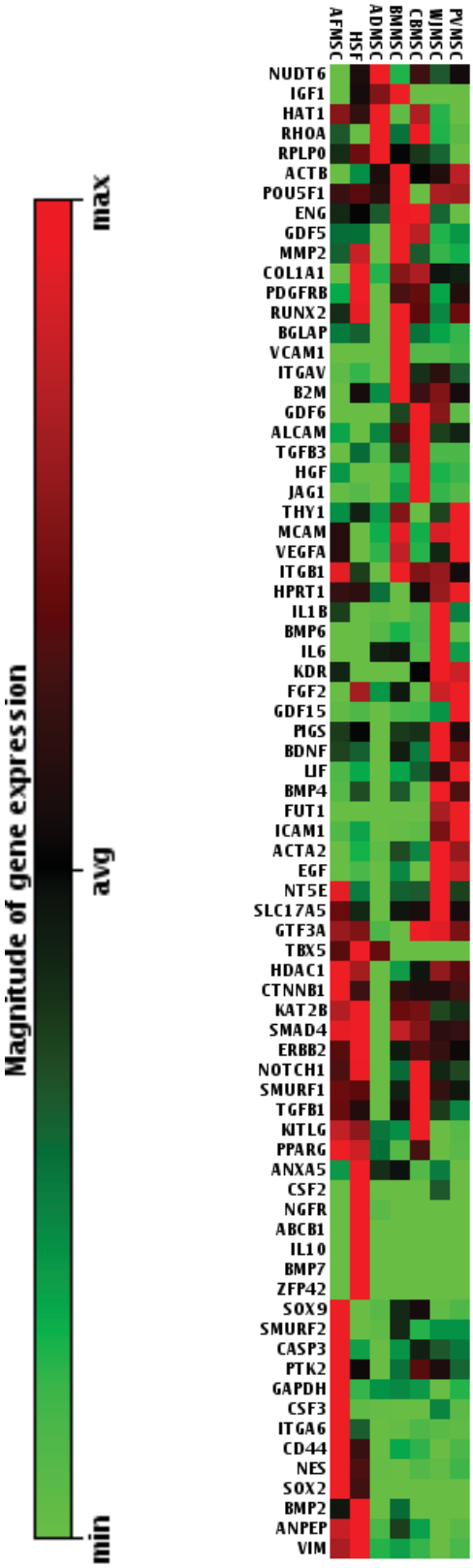

Complete qRT-PCR array. Fold change (Magnitude of gene expression) between multipotent mesenchymal stromal cells (MSCs) from different sources is represented. Min, minimum; avg, average; max, maximum; AF, amniotic fluid; HSF, human skin fibroblasts; AD, adipose tissue; BM, bone marrow; CB, cord blood; WJ, Wharton's jelly; PV, perivascular compartment.

Bibliography

1. Hass, R., et al., *Different populations and sources of human mesenchymal stem cells (MSC): A comparison of adult and neonatal tissue-derived MSC.* Cell Commun Signal, 2011. **9**: p. 12.
2. Crisan, M., et al., *A perivascular origin for mesenchymal stem cells in multiple human organs.* Cell Stem Cell, 2008. **3**(3): p. 301-13.
3. Corselli, M., et al., *Perivascular ancestors of adult multipotent stem cells.* Arterioscler Thromb Vasc Biol, 2010. **30**(6): p. 1104-9.
4. Pontikoglou, C., et al., *Bone marrow mesenchymal stem cells: biological properties and their role in hematopoiesis and hematopoietic stem cell transplantation.* Stem Cell Rev, 2011. **7**(3): p. 569-89.
5. Bunnell, B.A., et al., *Adipose-derived stem cells: isolation, expansion and differentiation.* Methods, 2008. **45**(2): p. 115-20.
6. Steigman, S.A. and D.O. Fauza, *Isolation of mesenchymal stem cells from amniotic fluid and placenta.* Curr Protoc Stem Cell Biol, 2007. **Chapter 1**: p. Unit 1E.2.
7. Bieback, K. and H. Kluter, *Mesenchymal stromal cells from umbilical cord blood.* Curr Stem Cell Res Ther, 2007. **2**(4): p. 310-23.
8. Barilani, M., et al., *A Chemically Defined Medium-Based Strategy to Efficiently Generate Clinically Relevant Cord Blood Mesenchymal Stromal Colonies.* Cell Transplant, 2016. **25**(8): p. 1501-14.
9. Barilani, M., et al., *Dissection of the cord blood stromal component reveals predictive parameters for culture outcome.* Stem Cells Dev, 2015. **24**(1): p. 104-14.
10. McElreavey, K.D., et al., *Isolation, culture and characterisation of fibroblast-like cells derived from the Wharton's jelly portion of human umbilical cord.* Biochem Soc Trans, 1991. **19**(1): p. 29s.
11. Batsali, A.K., et al., *Mesenchymal stem cells derived from Wharton's Jelly of the umbilical cord: biological properties and emerging clinical applications.* Curr Stem Cell Res Ther, 2013. **8**(2): p. 144-55.
12. Wang, H.S., et al., *Mesenchymal stem cells in the Wharton's jelly of the human umbilical cord.* Stem Cells, 2004. **22**(7): p. 1330-7.

13. Dominici, M., et al., *Minimal criteria for defining multipotent mesenchymal stromal cells. The International Society for Cellular Therapy position statement.* Cytotherapy, 2006. **8**(4): p. 315-7.
14. Ragni, E., et al., *Differential microRNA signature of human mesenchymal stem cells from different sources reveals an "environmental-niche memory" for bone marrow stem cells.* Exp Cell Res, 2013. **319**(10): p. 1562-74.
15. Ragni, E., et al., *Adipogenic potential in human mesenchymal stem cells strictly depends on adult or foetal tissue harvest.* Int J Biochem Cell Biol, 2013. **45**(11): p. 2456-66.
16. Bossolasco, P., et al., *Molecular and phenotypic characterization of human amniotic fluid cells and their differentiation potential.* Cell Res, 2006. **16**(4): p. 329-36.
17. Montemurro, T., et al., *Differentiation and migration properties of human foetal umbilical cord perivascular cells: potential for lung repair.* J Cell Mol Med, 2011. **15**(4): p. 796-808.
18. Gioventu, S., et al., *A novel method for banking dental pulp stem cells.* Transfus Apher Sci, 2012. **47**(2): p. 199-206.
19. Normand, J. and M.A. Karasek, *A method for the isolation and serial propagation of keratinocytes, endothelial cells, and fibroblasts from a single punch biopsy of human skin.* In Vitro Cell Dev Biol Anim, 1995. **31**(6): p. 447-55.

II. Unpublished data

b. EXTRACELLULAR VESICLE-SHUTTLED mRNA IN MESENCHYMAL STEM CELL COMMUNICATION

Enrico Ragni[1], Federica Banfi[1], Mario Barilani[1,2], Alessandro Cherubini[1], Valentina Parazzi[1], Paola Larghi[3,4], Vincenza Dolo[5], Valentina Bollati[6], Lorenza Lazzari[1]*

[1]Cell Factory, Unit of Cell Therapy and Cryobiology, Fondazione IRCCS Ca' Granda Ospedale Maggiore Policlinico, Milan, Italy
[2]Department of Industrial Engineering, University of Padova, Padova, Italy
[3]Autoimmunity Program, Istituto Nazionale di Genetica Molecolare "Romeo Ed Enrica Invernizzi", Milan, Italy
[4]Department of Pathophysiology and Transplantation, University of Milan, Milan, Italy
[5]Department of Life, Health and Environmental Sciences, University of L'Aquila, L'Aquila, Italy
[6]EPIGET - Epidemiology, Epigenetics and Toxicology Lab, Department of Clinical Sciences and Community Health, University of Milano, Milan, Italy; Epidemiology Unit, Fondazione IRCCS Ca' Granda Ospedale Maggiore Policlinico, Milan, Italy

Author contribution:
E.R.: conception and design, collection and assembly of data, data analysis and interpretation, manuscript writing, final approval of manuscript; F.B.: conception and design, collection and assembly of data, data analysis and interpretation, final approval of manuscript; M.B., V.P., A.C., P.L., V.D., V.B.: collection and assembly of data, final approval of manuscript; L.L.: conception and design, final approval of manuscript.

* Corresponding author: Lorenza Lazzari, PhD, Cell Factory, Unit of Cell Therapy and Cryobiology, Fondazione IRCCS Ca' Granda Ospedale Maggiore Policlinico, Via F. Sforza 35, 20122 Milan, Italy, Tel: +390255034053, Fax: +390255032796, lorenza.lazzari@policlinico.mi.it

Acknowledgements:
This study has been in part supported by “Ricerca Corrente Fondazione IRCCS Ca’ Granda Ospedale Maggiore Policlinico Milano” 2015 and the Italian program of liberal donation for research “5 per mille” 2015 (both to L.L.).

Disclosure of potential conflicts of interest:
The authors indicate no potential conflicts of interest.

Keywords:
Mesenchymal Stem Cells; Extracellular Vesicles; mRNA; 3’UTR; IL-10.

ABSTRACT

Mesenchymal stem cells (MSC) are multipotent cells able to differentiate into several cell types, hence providing cell reservoirs for therapeutic applications. The absence of detectable MSC homing at injury sites suggests that paracrine functions could, at least in part, be mediated by extracellular vesicles (EVs); EVs are newly identified players that are studied mainly as predictive or diagnostic biomarkers. Together with their clinical interests, EVs have recently come to the fore for their role in cell-to-cell communication. In this context, we investigated gene-based communication mechanisms in EVs generated by bone marrow and umbilical cord blood MSC (BMMSC and CBMSC, respectively). Both MSC types released vesicles with similar physical properties, although CBMSC were able to secrete EVs with faster kinetics. A pattern of preferentially incorporated EV transcripts was detected with respect to random internalization from the cytosol, after a validated normalization procedure was established. In the paradigm where EVs act as bioeffectors educating target cells, we demonstrated that kidney tubular cells lacking *IL-10* expression and exposed to BMMSC-EVs and CBMSC-EVs acquired the *IL-10* transcript, which was efficiently translated into the corresponding protein. These findings suggest that horizontal mRNA transfer through EVs is a new mechanism in the MSC restoring ability observed *in vivo* that is here further demonstrated in an *in vitro* rescue model after acute cisplatin injury of tubular cells.

INTRODUCTION

MSC are multipotent, non-hematopoietic adult stem cells, which can be isolated from almost all tissues and possess *in vitro* multilineage differentiation into mesodermic, endodermic and ectodermic lineages (Ullah et al., 2015, Crisan et al, 2011). During the last 10 years, these multipotent cells have generated considerable interest owing to their immunomodulatory activity and ability to escape the allogeneic immune response (Stoltz et al., 2015). Such unique properties make MSC an invaluable cell type for the repair of tissue/organ damage, attracting attention as a potential solution for tissue repair and wound healing (Gao et al., 2016). Multiple mechanisms identifying how MSC mediate their regenerative and immunomodulatory effects have been proposed, although, to date, several ambiguities and inconsistencies persist (Najar et al., 2016).

The initially proposed differentiation-based rationale for MSC use has become increasingly untenable. MSC engraftment and subsequent differentiation into appropriate cell types were rare, with <1% of the administered cells surviving for more than one week (Ferrand et al., 2011; Spees et al., 2003; Vassilopoulos et al., 2003). Therefore, the predominantly short-lived paracrine effects of MSC became evident (Ringdén et al., 2006; Lee et al., 2009; Parekkadan and Milwid, 2010). The paracrine effects of MSC were shown to include the release of both soluble factors, and extracellular vesicles (EVs) as parallel mechanisms for cell-to-cell communication (Yáñez-Mó et al., 2015).

EVs are composed of at least two distinct subtypes: exosomes (40–100 nm in diameter) formed within the endosomal network and microvesicles (100–1000 nm) produced by outward budding of the plasma membrane. Cargo components and loading mechanisms are still a matter of debate, although it has become clear that specific subsets of lipid, protein, and nucleic factors may distinguish both EVs sub-populations and EVs secreted from different cell types (Yáñez-Mó et al., 2015). The emerging role for EVs as a shuttle of bioactive molecules, either as mediators to educate the surrounding environment or as screening markers in early-stage diagnosis, is being investigated, particularly by cancer researchers.

In the stem cell field, a limited, albeit increasing, number of recent reports have demonstrated beneficial EVs effects in *in vitro* and animal models of kidney, liver,

and lung injury and wound healing (reviewed in Rani et al., 2015), together with a low propensity to trigger innate and adaptive immune responses (Yu et al., 2014). Because EVs appear to recapitulate the therapeutic effects of stem cell transplantation, the prevailing hypothesis is that MSC-EVs may exert their effects by transferring biologically active molecules such as proteins, lipids and various classes of nucleic acids including transcripts encoding therapeutic mediators. Therefore, the goal of our work was to characterize MSC-EV mRNAs and demonstrate a clear proof-of-concept for the efficient transfer of EV mRNAs to target cells and their subsequent translation in those cells as a novel mechanism of cellular communication.

MATERIALS AND METHODS

Cell isolation and growth

MSC from bone marrow aspirate and umbilical cord blood were obtained from healthy donors after informed consent. MSC isolation was performed as described in Ragni et al., 2016. MSC were propagated in alpha MEM supplemented with 20% FBS (Life Technologies, CA, USA). Stem cell identity of isolated BMMSC and CBMSC was confirmed by immunophenotype profile: cells were negative for the pan-hematopoietic marker CD45 and positive for the MSC cell-surface antigens CD73, CD90, and CD105, officially recommended for their concurrent use to define unambiguously a MSC type (Dominici et al., 2006). MSC were able to differentiate *in vitro* into adipocytes, osteocytes and chondrocytes following what reported in Ragni et al., 2013 (data not shown). All subsequent studies were carried out in technical triplicate on two independent cell lines named #1 and #2. Experiments were performed at passage 5. Human proximal tubular cells HKC8 were cultured in DMEM/F12 media supplemented with 10% FBS.

EVs preparation

MSC were grown to 80% confluence and then fresh medium without FBS was added. After 4-8-24 hours, conditioned culture medium was collected and serially centrifuged to remove floating cells and cellular debris (400 xg for 10 minutes and 5,000 xg for 15 minutes for three times) before being ultracentrifuged at 100,000 xg for 1 hour at 4°C with a fixed angle rotor (Fiberlite F37L-8x100) (Thermo Fisher Scientific, San Francisco, CA, USA). The pellet was suspended in PBS, dissolved in lysis buffer for RNA extraction or RIPA buffer for protein analysis.

Scanning Electron Microscopy

MSC grown on a glass coverslip were first fixed in 2% glutaraldehyde (Electron Microscopy Sciences, Hatfield, PA, USA) in PBS and then dehydrated through a graded series of ethanol solutions. Samples were critical-point dried and sputter coated with a SCD040 Balzer Sputterer (Balzers Union, Liechtenstein). A SEM

Philips 505 scanning electron microscope (Philips, Eindhoven, Netherlands) was used to examine the samples, using an accelerating voltage of 20 kV.

Transmission Electron Microscopy

According to proper dilutions, the EVs suspended in PBS were adsorbed to 300 mesh carbon-coated copper grids (Electron Microscopy Sciences, Hatfield, PA, USA) for 5 minutes in a humidified chamber at room temperature. Vesicles on grids were then fixed in 2% glutaraldehyde in PBS for 10 minutes and then briefly rinsed in milli-Q water. Grids with adhered vesicles were examined with a Philips CM 100 transmission electron microscope TEM at 80kV, after negative staining with 2% phosphotungstic acid, brought to pH 7.0 with NaOH. Images were captured by a Kodak digital camera.

Measurement of particle number and size distribution by nanoparticle tracking analysis (NTA)

NTA was carried out using the Nanosight system (NanoSight, Wiltshire, UK) on EVs suspended in PBS that were further diluted 50-fold for analysis. NTA related the rate of Brownian motion to particle size. Vesicles were visualized by light scattering using a conventional optical microscope aligned perpendicularly to the beam axis. After a video was taken, NTA software tracked between frames the Brownian motion of individual vesicles and calculated total concentration and their size through application of Stokes-Einstein equation.

PKH26-labeled EVs transfer

EVs suspended in Diluent C were mixed with PKH26 (Sigma-Aldrich, St. Louis, MO, USA) and incubated for twenty minutes at RT in the dark. Labeling reaction was stopped by adding an equal volume of 1% BSA. EVs were ultracentrifuged at 100,000 xg for 1 hour, washed with PBS, ultracentrifuged again at 100,000 xg for 1 hour and finally suspended in PBS. Labeled vesicles were incubated with HKC8 cultured in a 20,000/1 (EVs/cell) ratio. PBS that received the same treatment as above was used as a control. Cells were observed after 24 hours under a Leica SP5 confocal microscope (Leica Microsystems, Wetzlar, Germany)

or by flow cytometry with a FACSCanto II instrument (Becton Dickinson, San Diego, CA, USA) by measuring the fluorescence of PKH26 detected at 567 nm.

Determination of the number of EVs incorporated by kidney tubular cells

PKH26-labeled EVs were administrated to HKC8 cells with a 20,000/1 EVs/cell ratio. After 24 hours, cells were washed, detached and suspended in PBS to a concentration of 1,000,000 cell/mL. 0.1 mL was analyzed by ELISA in a 96-well plate with a 530 nm filter for PKH26 excitation and a 570 nm filter for PKH26 emission. Cells treated with unlabeled EVs were used as negative CTRL and to subtract fluorescence background. In a separate well, $2.5exp^{9}$ PKH26-labeled vesicles suspended in 0.1 mL PBS were also scored for fluorescence. Signal intensity of EVs-treated cells after background subtraction was compared to labeled EVs fluorescence to determine the number of incorporated EVs.

qRT-PCR analysis

RNA was isolated using RNeasy Micro kit (Qiagen, Hilden, Germany). Quantitative PCR was carried out using SsoFast EvaGreen Supermix (Bio-Rad Laboratories, CA, USA). Gene specific primers (Neuroprotection: *NGF, BDNF, GDNF, NTF3, CDNF, CNTF, MANF;* Proliferation: *FGF2, FGF7, ANGPT1, ANGPT2, CTGF, HGF, VEGF;* Immunomodulation: *IL-4, IL-6, IL-10, IL1RN, TGF-β1, TNFα;* Stemness: *ALCAM, BMP2, BMP7, KDR, PDGFRB, THY1, BGLAP, COL1A1, ICAM1;* Housekeeping: *GAPDH*) were used. Triplicates of all reactions were analyzed. All replicates should be within 0.5 Ct of each other for further processing. To confirm product specificity, a melting curve analysis and an agarose gel electrophoresis for the less abundant transcripts were performed after each amplification. Relative gene expression was normalized in EVs using a combined method relying on *GAPDH*, mean Ct value and cDNA input (see Results). For MSC and to compare MSC and EVs, *GAPDH* was used. For statistical analysis and expression data generation, the Bio-Rad CFX Manager software was used. Primer sequences will be provided upon request.

RT-PCR analysis of 3'UTR and full length IL-10

RNA was isolated as previously described. cDNA was prepared using SuperScript IV VILO (Thermo Fisher Scientific) following manufacturer's instructions. RT-PCR was carried out using GoTaq Green Master Mix (Promega, Madison, WI, USA). To design 3'UTR specific primers, online tool http://utrdb.ba.itb.cnr.it/search was first used to identify 3'UTR sequences of *IL-6*, *MANF*, *BGLAP* and *IL-4* transcripts. Then, Forward and Reverse primers were designed in the first or last 50 bp of the 3'UTR sequences, respectively. Expected RT-PCR amplificates were: *IL-6* 392 bp out of 429 bp, *MANF* 296 bp out of 308 bp, *BGLAP* 157 bp out of 158 bp, *IL-4* 79 bp out of 89 bp. For full length *IL-10* transcript, Forward and Reverse primers were designed in the first 50 bp of the 5'UTR or last 50 bp of 3'UTR of *IL-10* mRNA sequence deposited in NCBI Nucleotide database (NM_000572.2, http://www.ncbi.nlm.nih.gov/nucleotide). Expected amplicon was 1589 bp out of 1629 bp. Primer sequences will be provided upon request.

Pathway analysis

After 3' UTR identification, miRNA binding sites within 3'UTR regions of EVs-accumulated mRNA were identified using miRANDA algorithm (http://www.microrna.org/microrna/home.do), with a mirSVR scores < -1.0 to exclude weak hits. Verified mRNA targets of selected miRNAs were identified using miRWalk database (http://www.umm.uni-heidelberg.de/apps/zmf/mirwalk/index.html) (Dweep et al., 2011). Final target lists were then uploaded to GeneCodis tool (http://genecodis.cnb.csic.es/) to find statistically enriched biological processes with respect to the entries of the whole human genome.

Flow cytometry

To detect CFSE positive EVs, vesicles were first 1:50 diluted in PBS and then incubated for 30 minutes at RT with 5 µL of CFSE cell-permeable precursor carboxyfluorescein diacetate succinimidyl ester (CFDA-SE). Unlabeled samples were incubated with 5 µl PBS. Finally, stained and unstained EVs were analyzed on a FACSCanto II (BD).

To detect viable cells after 24 hours FBS depletion, MSC were detached with trypsin, washed with PBS and, after suspension, 1/20 volume 7-AAD (7-Aminoactinomycin D) was added 10 minute incubation at RT. Labeled cells were immediately analyzed on a FACSCanto II (BD). At least 30,000 events were acquired.

Immunostaining

Immunofluorescence experiments were performed on HKC8 cells grown on fibronectin-coated coverslips using standard procedures. Briefly, 24 hours after cell seeding, EVs were delivered into two consecutive administrations (EVs/cell ratio 20,000/1), with a gap of 24 hours between them. 40 hours after first EVs administration, cell secretion was blocked by administration of Brefeldin A (final concentration 10 µg/mL); after 8 hours, Brefeldin A was removed and cells fixed in 4% PFA. Cell permeabilization was performed with 1% saponin for 15 minutes at RT, then a blocking solution of 3% BSA was added for 30 min at RT and finally the primary antibody was added in blocking solution at a final concentration of 5 µg/mL (mouse anti-human IL-10, Santa Cruz Biotechnology, Santa Cruz, CA, USA) and incubated overnight at 4 ˚C. Goat anti-mouse PE-conjugated antibody was used as secondary antibody, incubating cells for 1 hour at RT. Cell nuclei were stained with DAPI. Images were acquired using a Leica TCS SP5 confocal microscope with HCX PL APO 63x/1.25 objective (Leica). No primary antibody stained and no EVs incubated cells were used to set up experimental conditions and antibody dilutions.

Western Blot

Purified EVs or HKC8 collected 72 hours after EVs administration and 8 hours after Brefeldin A block were suspended in RIPA buffer supplemented with protease and phosphatase inhibitors and denatured in Laemmli Sample Buffer (Bio-Rad Laboratories) at 60 °C for 15 minutes. 10 µg of EVs proteins or 50 µg of cell extracts were separated by SDS-PAGE, transferred onto nitrocellulose membranes and incubated 1 hour at RT with blocking solution (5% BSA in TBS, 0.1% Tween-20) (Sigma-Aldrich). Membranes were incubated overnight at 4 °C with the following primary antibodies: i) mouse anti-human IL-10 (Santa Cruz

Biotechnology cat. n° sc-8438, 1:200 dilution in 5% BSA in PBS, 0.1% Tween-20), ii) mouse anti-human CD81 (BD cat. n° 551112, 1:200 dilution in 5% BSA in PBS, 0.1% Tween-20), iii) mouse anti-human CD63 (Santa Cruz Biotechnology cat. n° sc-5275, 1:100 in 5% BSA in PBS, 0.1% Tween-20), iv) mouse anti-human CD90 (Abcam cat. n° ab133350, 1:100 in 5% BSA in PBS, 0.1% Tween-20), v) mouse anti-human CD105 (Dako cat. n° M3527, 1:200 in 5% BSA in PBS, 0.1% Tween-20), vi) mouse anti-GAPDH (Millipore cat. n° CS204254, 1:10000 in 5% BSA in PBS, 0.1% Tween-20). Proteins of interest were detected with HRP-conjugated sheep anti-mouse IgG antibody (1:3000, Bio-Rad Laboratories) and visualized with the Amersham ECL Western Blotting Analysis System (GE Healthcare, UK).

MTT assay

1.25exp^4 HKC8 cells were seeded into 96-well plates and, after 24 hours, treated for 6 hours with 10 μM cisplatin. After drug removal, cells were washed twice and 100 μL phenol red-free medium added and this time point was set as 0. At time 0, 24 and 48 hours 20,000 EVs/cell were added. At time 0, 24, 48 and 72 hours MTT assay was performed. Briefly, 25 μL of a 3 mg/mL Thiazolyl Blue Tetrazolium Bromide (Sigma-Aldrich) were added to each well and the colorimetric reaction was allowed to proceed for 4 hours at 37°C. Then, 25 μL of 40% SDS were added and the plate incubated overnight at 37°C in the dark. The next day, viable cells with MTT dye uptake were determined by measuring the optical density at 570 nm after background subtraction scored at 650 nm. Values shown are the mean of at least six measurements.

Statistical Analysis

Comparison of variances for the expression of distinct genes was used to analyze the significance of differences using one-way analysis of variance (ANOVA) (GraphPad Prism Software version 6, San Diego, CA, USA). A p-value < 0.05 was considered statistically significant.

RESULTS

Characterization of MSC-derived EVs

Electron microscopy on MSC showed structures resembling EVs protruding from the cell surface (Fig. 1A). Interestingly, EV secretion was located in the peripheral protrusions and concentrated at the edges of the plasma membrane for both MSC types. Then, we followed the capacity of the different MSC to secrete EVs by nanoparticle tracking analysis (NTA) at 4 h, 8 h, and 24 h after FBS removal (to remove vesicles present in serum). In all MSC, the number of secreted vesicles increased as a function of time with a significant gain at 24 h ($p < 0.05$, N = 5; Fig. 1B). Because no cell toxicity was observed in FBS starved BMMSC and CBMSC (≤ 10% 7AAD+ cells observed at 0, 4, 8, and 24 h time points), we chose the 24 h FBS starvation time point for EVs harvesting.

Using NTA we determined that the EVs of CBMSC and BMMSC ranged in size from 40–50 nm to 600–700 nm, indicating the presence of both exosomes and microvesicles. The mean values for the size of CBMSC-EVs and BMMSC-EVs laid between 230 nm and 275 nm and did not differ significantly ($p > 0.05$, N = 10; Fig. 1C). Interestingly, the observed particle size suggests the absence of apoptotic bodies, which usually fall into the size range of 1–5 μm. We then used NTA quantification to determine the number of EVs secreted per MSC line as function of the number of seeded cells (Fig. 1C). Notably, the CBMSC samples secreted 1.5–2 times more vesicles than BMMSC ($p < 0.05$, N = 10). The CBMSC #2 sample produced the most EVs/cell within a 24 h period (5,000 secreted EVs/cell; Fig. 1C). Similar results were obtained after monitoring vesicles released by other independent BMMSC (N = 4) and CBMSC (N = 4) cell lines (CB/BM EVs ratio of 1.6, $p < 0.01$, N = 12), suggesting no major variability between donors.

To confirm the integrity of analyzed EVs, carboxyfluorescein diacetate succinimidyl ester (CFDA-SE) staining was performed directly on EV-containing supernatants. Flow cytometry analysis showed that > 90% of the particles were positive for staining, indicating that vesicles are intact and contain cytoplasmic esterase reacting with CFDA-SE (Fig. 1D). Purification by ultracentrifugation at 100,000 × *g* yielded a similar percentage of positive EVs, confirming that the

centrifugation step of the isolation protocol does not damage EVs (data not shown). Western blot analysis of BMMSC- and CBMSC-EVs confirmed the expression of both exosome (CD63 and CD81) and MSC (CD90 and CD105) specific markers (Fig. 1E). Finally, transmission electron microscopy images showed an expected morphology consistent with pure extracellular vesicle preparations (Fig. 1F).

Molecular analysis of MSC-EVs

It has been reported previously that MSC-EVs contain mRNAs (Deregibus et al, 2007; Valadi et al., 2007; Bolstad et al., 2003; Bruno et al., 2009; Ragni et al., 2016). While these studies identified some of the encapsulated transcripts, they did not assess their relative expression levels or the ratios between different EV isolates. As detailed in the Materials and Methods, 30 mRNAs characteristic of mesenchymal cells (functions involved in neuroprotection, control of proliferation, and immunomodulation; see Materials and Methods for more details) were quantified in parallel by qRT-PCR. We were able to amplify (C_t < 40) 18 transcripts from the EVs of BMMSC #1 and CBMSC #1, and 19 transcripts from the EVs of BMMSC #2 and CBMSC #2. To confirm the specificity of the assay, melting curve tests and agarose gel electrophoresis of amplified DNA were performed comparing EVs and cell extracts (*ALCAM*, *NGF*, *TGFB1* and *VEGFA*) (Fig. 2A). Interestingly, 11 candidates were always undetectable (*GDNF*, *NTF3*, *CDNF*, *ANGPT1*, *ANGPT2*, *IL-1RN*, *TNF*, *BMP2*, *PDGFRB*, *BMP7* and *ICAM1*). *HGF* gave positive amplification from EVs from samples BMMSC #2 and CBMSC #2 (both with C_t values > 35). *FGF7*, *COL1A1*, *CNTF*, *CTGF* and *IL-6* transcripts had the highest expression levels in the MSC-EVs (Supplementary Table 1).

To obtain reliable EV molecular signatures, we had to decide on a method for normalization. To date, no universal reference mRNA has been identified to compare transcript levels in EVs isolated from independent cell lines. Recently, *GAPDH* mRNA has been proposed as a housekeeping transcript for MSC-EVs (Zhu et al., 2014). To increase reliability of our analysis, we decided to combine three different and independent normalization approaches. First, we measured *GAPDH* mRNA levels in parallel with the target transcripts. Second, we employed a global mean normalization procedure based on the positively

amplified mRNAs. This method has a higher accuracy than the multiple reference gene normalization method when no reliable data about housekeepers are available; however, this method is restricted by the number of detected transcripts (Vandesompele et al., 2002; D'haene et al., 2012). Finally, we also normalized expression to EV volumes, calculated as EV number × EV mean size, assuming that identical EV volumes contain comparable nucleic acid levels. Each normalization procedure generated expression ratios used to calculate a ΔC_t value with respect to BMMSC #1-EVs. Notably, the values obtained from the independent methods were similar and therefore averaged for a final normalization value to analyze the qRT-PCR data of the four MSC-EVs under analysis (BMMSC #1-EVs: 1.00; BMMSC #2-EVs: 1.06 ± 0.25; CBMSC #1-EVs: 0.87 ± 0.17; CBMSC #2-EVs: 2.10 ± 0.26).

To exclude potential erroneous mRNA expression detection due to low cDNA input or technical issues, we performed random individual qRT-PCRs on a few selected genes (*IL-6*, *FGF7*, and *TGFB1*) to increase the amount of available template. Notably, results were consistent with those obtained in the initial screening (within 2-fold modulation) (Fig. 2B). Finally, to confirm that the target mRNAs are present within the vesicles and not just bound to the external membrane surface, isolated EVs were treated with proteinase K and RNAse A. No decrease in the amount of *CTGF* and *FGF7* transcripts was observed, confirming that isolated EVs are intact with mRNA engulfed in the lumen (Fig. 2C).

MSC-EV mRNA cargo comparison

The four EV molecular signatures were then compared in order to identify mRNAs that vary significantly in expression between EVs from BMMSC and CBMSC (fold change > 2 with $p < 0.05$). After normalization, no major differences were observed, with few exceptions. CBMSC-EV *IL-4* expression was > 2-fold higher, and *THY1* expression was reduced compared to expression levels in BMMSC-EVs (Fig. 3A). Interestingly, *VEGFA* and *HGF* resulted to have opposite trend, with vascular endothelial growth factor significantly more abundant (2- to 4-fold higher) in EVs from BMMSC #1 and CBMSC #1 compared to EVs from BMMSC #2 and CBMSC #2, and hepatic growth factor absent in EVs from

BMMSC #1 and CBMSC #1 while it was readily detectable in EVs from BMMSC #2 and CBMSC #2 (Fig. 3A).

The molecular signatures observed for EV types was also found in the corresponding cell extracts, with a few exceptions (Fig. 3B): *FGF7* expression levels were higher in BMMSC (50–100 fold), whereas *KDR* expression levels were more abundant in CBMSC. Therefore, we observed a strong correlation in specific mRNA levels between donor cells and the EVs derived from them, indicating a consistent transcript distribution within these distinct cellular compartments.

The next step was to assess whether some mRNAs were preferentially loaded into EVs with respect to random incorporation from the cytoplasm. Because of its reliability in the previous EV qRT-PCR experiments, *GAPDH* expression was used as a normalization factor. A > 4-fold enrichment or exclusion was chosen as the threshold for analyses. Seven mRNAs were clearly and consistently accumulated in EVs (Table 1). *IL-4* and *IL-10* showed the highest incorporation ratios followed by *BGLAP*, *CNTF* and *FZD9*. Notably *FGF7* always resulted between the two most detected transcripts despite its low expression in CBMSC cell extracts. In contrast, despite their elevated expression in the cytoplasm, *TGFB1* and *ALCAM* resulted under expressed in all four EVs. Finally, of the mRNAs that were not detected in the qRT-PCR assays in EVs, we could not find candidates with high cellular expression, suggesting that their absence of detection was due mainly to low cytoplasm abundance rather than selective exclusion. Altogether, these results suggest preferential loading of some mRNAs into EVs.

3'UTR analysis of preferentially accumulated mRNAs

A recent report suggested that the presence of a core 3'UTR "CTGCC" region (or variations CTGC, CTCCC, CGCCC, TGCC) within the wider consensus sequence (CCCCTGCCTGGACC) and/or a miR-1289 binding site may enhance targeting of mRNAs into EVs (Bolukbasi et al., 2012). After confirmation of full length 3'UTRs (Fig. 3C) in EVs-embedded transcripts as assessed for randomly selected candidates (*IL-6*, *MANF*, *BGLAP* and *IL-4*), multiple alignment (http://www.ebi.ac.uk/Tools/msa/muscle/) showed the presence of a conserved

“core” region in the *KDR*, *CNTF*, *BGLAP*, and *FZD9*, with *FGF7* transcripts harboring the variation *CTGC*. Notably, the CTGCC region was found four times in the 3’UTR of *COL1A1*, the most abundant mRNA in all of the MSC-EVs. On the contrary, the miR-1289 sequence was not found in any of the 3’UTRs tested.

To further identify other potential elements involved in mRNA enrichment, we searched miRNA binding sites within the 3’UTR regions of accumulated mRNAs using the miRANDA algorithm (http://www.microrna.org/microrna/home.do), using a threshold mirSVR score < -1.0 to exclude weak hits. A total of 73 unique sites were identified: 34 miRNA sequences were identified for *FGF7*, 19 for *IL-10*, 19 for *KDR,* 5 for *CNTF*, 3 for *IL-4*, and 2 for *BGLAP* for a total of 73 unique sites. A deeper analysis showed the absence of conserved miRNA binding patterns, with only 9 miRNA sites shared by two 3’UTR. Finally, Batagov and colleagues proposed specific sequence motifs (ACCAGCCU, CAGUGAGC and UAAUCCCA) that may potentially function as cis-acting elements targeting RNAs to EVs in glioblastoma cells (Batagov et al., 2011). None of the five most enriched EV mRNAs contained these elements. Therefore, preferential mRNA loading into EVs may rely on cell type, still unidentified specific motifs, or selectively engulfed mRNA binding proteins able to discriminate between different transcripts, as suggested by Waris et al., 2014.

Moreover, it was shown recently that multiple sites for regulatory miRNA binding in 3′UTRs may compete with recipient cell RNAs for binding of miRNA or RNA-binding proteins so as to regulate their stability and translation in recipient cells (Batagov et al., 2013). Accordingly, we performed a literature-validated gene target identification for the pool of 73 previously identified miRNA using miRWalk, a database of experimentally validated miRNA-gene interactions (Dweep et al., 2014). The 73 submitted micro-RNAs generated a list of 2,294 potentially regulated targets. Then, we ran these results through the GeneCodis program (http://genecodis.cnb.csic.es/) to find statistically enriched biological processes. We focused our attention on the top five ranked biological processes which were primarily RNA generation and stability GO:0006355 (DNA-dependent regulation of transcription, p-value 8.57801e-48), GO:0010467 (gene expression, 3.79091e-44), GO:0016070 (RNA metabolic process, 2.57193e-39), GO:0016071 (mRNA metabolic process, 9.8859e-35) and GO:0006915 (apoptotic process, 4.91476e-

34) with the majority of apoptosis-related genes being anti-apoptotic (GO:0006916, anti-apoptosis 1.42074e-17). Notably, out of the first 15 categories, 8 were related to various aspects of RNA processing. These results suggest that the inclusion of mRNAs with specific 3'UTR motifs into EVs may have significant effects on the regulation of gene expression in target cells.

mRNA translation in recipient cells

Beside the "miRNA sponge" activity of the 3'UTR, another paradigm of vesicle intercellular communication is that EVs may shuttle functional mRNAs that can be internalized and translated. Therefore, immunomodulatory transcripts embedded in MSC-EVs, together with secreted factors, could be important players for the paracrine properties of mesenchymal stem cells. To test this hypothesis, we used a human-derived renal proximal tubular cell line (HKC-8) as the target cell; in a previous publication we assessed the *in vivo* anti-inflammatory action of BMMSC and CBMSC supernatants in mice with Acute Kidney Injury (AKI) induced by cisplatin treatment (Morigi et al., 2010).

EVs were labeled with the membrane-dye PKH26 without altering membrane integrity (data not shown). After a 24 h co-culture, the labeled EVs were engulfed by 100% of HKC8 cells, as shown by FACS analysis and confocal microscopy (Fig. 4A and 4B). In our experimental settings, both EVs were incorporated into HKC8 cells with a similar efficiency (4,100 ± 1,400 BMMSC-EVs/cell and 4,000 ± 1,500 CBMSC-EVs/cell). The PKH26 signal was preferentially accumulated in the perinuclear area. Intriguingly, incubation of PKH26-stained EVs with parental MSC resulted in dramatically lower incorporation rates than for HKC8 cells (e.g. for BMMSC #1 EVs: Mean Fluorescence Intensity-Ratio, stained *vs* unstained: HKC8 18.1 ± 4.3, BMMSC #1 2.9 ± 0.7, BMMSC #2 2.1 ± 0.8, CBMSC #1 1.9 ± 0.4, and CBMSC #2 2.3 ± 0.3, n = 3). Similar results were obtained with the other combinations of EV and MSC, suggesting a conserved and preferential targeting to non-mesenchymal cells, independently of the MSC type.

As a proof-of-concept of the anti-inflammatory paracrine activity of MSC-EVs, we chose to track the expression of *IL-10,* which is absent in target HKC8 cells and is present in EVs only as mRNA (Fig. 5A) and not as protein (Fig. 5B). Full-length *IL-10* mRNA was demonstrated to be engulfed in EVs through RT-PCR, being

this a prerequisite for efficient translation into a functional protein (Fig. 5C). Then, after EV/HKC8 co-culture, *IL-10* mRNA was identified in HKC8 target cells as confirmation of positive transcript transfer (Fig. 5A). Finally, *de novo* IL-10 protein expression was detected in tubular HKC8 cells that were co-cultured with either of the MSC-EV type by western blot (Fig. 5D) and immunofluorescence analyses (Fig. 5E). The observed perinuclear localization of IL-10 resembling the ER compartment was due to Brefeldin A treatment to block transport from the ER to the Golgi apparatus to increase the amount of detectable protein (Fig. 5E).

Intriguingly, Soranno and colleagues showed *in vivo* that delivery of IL-10 following AKI mitigates the local and systemic pro-inflammatory cascade, reducing fibrosis and eventually cell death (Soranno et al., 2016). Similarly, *in vitro* IL-10 production after EV administration may resemble such a mechanism and promote viability. Therefore, HKC8 cells where treated with 10 □□ cisplatin for 6 hours to mimic acute injury. After drug removal, EVs were added and cell viability was scored by the MTT assay. Although at 24 h no major EV-protective effects were detected, higher viability was observed at 48 h (70% with respect to 60% of cisplatin-treated cells) and even further pronounced at 72 h (80% viability *vs.* 40% viability in cisplatin-treated cells), possibly due to an additional proliferative stimulus (Fig. 5F). These results are in agreement with the kinetics of EVs incorporation and mRNA translation, explaining the delay between EVs supplementation and the appearance of protective effects. Altogether, these results demonstrate that mRNAs incorporated into MSC-EVs are efficiently transferred to target cells and eventually translated, contributing to the well-known paracrine activities of MSC (Fig. 6).

DISCUSSION

A significant body of literature has shown that the molecular constituents of extracellular vesicles, especially proteins and microRNAs (miRNA), hold great promise as novel biomarkers for clinical diagnosis (Liu and Lu, 2015; Fujita et al., 2016). On the contrary, less attention has been devoted to the role of EVs in cell-to-cell communication and fate determination, especially in the stem cell and regenerative medicine fields (Quesenberry et al., 2015; Nawaz et al., 2016). A major inadequacy for studying MSC-EVs is that there is no data comparing their clinical efficacy and production feasibility. The majority of studies used only one MSC type, generating controversy on most favorable MSC (Yu et al., 2014; Rani et al., 2015). A few studies have described efficacy of EVs isolated from different tissues on the same model. For example, bone marrow and Wharton's Jelly MSC were studied for their effects on acute lung injury (ALI) showing similar outcomes (Lee et al., 2012; Zhu et al., 2014). Similarly, BMMSC and umbilical cord-MSC were tested in Liver Injury models (Li et al., 2013; Tan et al., 2014). Furthermore, BMMSC- and CBMSC-EVs were shown to protect against ischemic AKI (Bruno et al., 2009; Kilpinen et al., 2013). Despite that the different protocols and experimental settings do not allow for direct comparisons, the similar efficacies observed between these studies suggested conserved properties of MSC-EVs. Our data show, for the first time, that CBMSC and BMMSC are able to secrete vesicles that are almost identical in their physical properties and cargo content, especially for transcripts involved in immunomodulation and proliferation. The only striking difference was the higher EV/cell ratio displayed by CBMSC. This may be relevant for MSC type selection in future clinical applications where it is often desirable to have the highest production rate to minimize cost, space, and time. Furthermore, the kinetics of CBMSC proliferation are substantially higher than those of either adipose derived- or BM-MSC (Zhang et al., 2011; Barilani et al., 2015). Therefore, due to their higher proliferation and vesicle secretion rates, CBMSC may be the preferred choice for MSC-EV production.

Despite several reports that MSC-EVs have functions similar to those of MSC, very few of these work have tried to link EV efficacy with the identification of the shuttled active components, mainly proteins (Shentu et al., 2016). In the context

of nucleic acid transfer, main attention has been focused on miRNAs (Chen et al., 2010). Very recently, the Camussi group nicely demonstrated the crucial role in miRNA enrichment during EV biogenesis of Alix, an accessory protein of ESCRT, through the interaction with the miRNA binding protein Ago2 (Iavello et al., 2016). Similarly, EV enrichment of other extracellular RNAs, including mRNAs, may depend on their association with specific subsets of RNA-binding proteins. Intriguingly, EVs released from the human liver stem-like cells were shown to contain members of several families of RNA-binding proteins, each specific for a different transcript motif (Waris et al., 2014). Consistent with this hypothesis, Bruno and coworkers suggested that BMMSC-EVs may also engulf a specific subset of mRNAs rather than a random sample of cellular mRNA (Bruno et al., 2009).

In this study, we identified a subgroup of mRNAs that are preferentially loaded into MSC-EVs, thus potentiating their role in intercellular communication. *FGF7*, which is expressed at very low levels in donor CBMSC, was among most enriched transcripts in both types of MSC-EVs, suggesting a pivotal function. Supporting this notion, Zhu and coworkers demonstrated that BMMSC-EVs were therapeutically effective following *E. coli* endotoxin-induced ALI in mice through the expression of EV-transferred *FGF7* mRNA in the injured alveolus (Zhu et al., 2014). Therefore, FGF7 protein expression from MSC-EV mRNA restored lung protein permeability and reduced alveolar inflammation, though through a still unknown mechanism. Similar functions may be postulated for *IL-10* mRNA, which we demonstrated to be highly enriched in EVs and efficiently translated in kidney tubular cells. We have demonstrated previously that MSC supernatant administration in mice with cisplatin-induced AKI ameliorated both renal function and tubular cell injury, and prolonged survival (Morigi et al., 2010). Moreover, MSC-EVs treatment after kidney injury prevents renal fibrosis (Bruno et al., 2009). These effects were intriguingly similar to those observed upon IL-10 administration (Soranno et al., 2016), that in the adult kidney is secreted by mesangial cells (Jin et al., 2013). Thus, due to absence of IL-10 protein in MSC-EVs, *IL-10* mRNA transfer and translation may be a novel mechanism of the complex recovery and anti-inflammatory processes recently proposed for *in vivo* kidney repair by MSC (Morigi and Benigni, 2013). In fact, existence of such new

paradigm in tubular cells has been confirmed by the *in vitro* MSC-EV mediated transfer of *IGF-1R* mRNA that, after translation, potentiates tubular cell sensitivity to locally produced IGF-1 (Tomasoni et al., 2013). Similarly, translated IL-10 may enhance IL-10/IL-10R1R2 anti-inflammatory pathway at tubular cell level, suggesting a potential therapeutic role for *IL-10* mRNA transfer from EVs. Altogether, these data provide a new mechanism to explain how the restricted homing of mesenchymal stem cells at the site of injury may still result in enhanced protective effects via gene-based communication amplified through the enrichment of therapeutic mRNAs in EVs.

In addition to the transfer of therapeutic mRNAs, the enrichment of mRNAs with specific 3′UTR sequences into EVs may also have a role in modulating target cells, as was reported in glioblastoma-EVs (Batagov et al., 2013). One intriguing possibility is that miRNA binding sites in 3′UTRs, may compete with target cell RNAs for binding in order to alter mRNA stability and translation. Our *in silico* analysis showed that the 3'UTR of preferentially enriched mRNAs may interact with at least 73 different miRNAs, potentially affecting the stability and thus translation of more than 2,000 transcripts. Intriguingly, the top biological processes altered by their products were related to RNA transcription and metabolism, gene expression and anti-apoptotic processes. These categories are strictly related, because increase in RNA synthesis and translation have potent inhibitory effects on apoptotic processes (Bushell et al., 2004). Consistently, MSC-EV administration resulted in strong anti-apoptotic and pro-proliferative outcomes in both *in vitro* (Bruno et al., 2009; Bruno et al., 2012; Zhang et al., 2015) and *in vivo* experimental models (Gatti et al., 2011; Tan et al., 2014). Thus, transcripts incorporated into MSC-EVs may regulate target cells to different levels, increasing the array of targets addressed by vesicles and shuttled factors.

CONCLUSION

In summary, we demonstrated that MSC load specific transcripts into secreted EVs independently of their cytosolic abundance, suggesting purposeful transfer to target cells. These transferred molecules may act directly through their protein products or interact with other nucleic acids or nucleic acid-binding proteins. These results shed new light on the knowledge of a complex and still uncharacterized mechanism involving EVs as factors of MSC autocrine and paracrine action.

REFERENCES

Barilani M, Lavazza C, Viganò M et al. Dissection of the cord blood stromal component reveals predictive parameters for culture outcome. Stem Cells Dev 2015;24:104-114.

Batagov AO, Kurochkin IV. Exosomes secreted by human cells transport largely mRNA fragments that are enriched in the 3'-untranslated regions. Biol Direct 2013;8:12.

Batagov AO, Kuznetsov VA, Kurochkin IV. Identification of nucleotide patterns enriched in secreted RNAs as putative cis-acting elements targeting them to exosome nano-vesicles. BMC Genomics 2011;12:S18.

Bolstad BM, Irizarry RA, Astrand M et al. A comparison of normalization methods for high density oligonucleotide array data based on variance and bias. Bioinformatics 2003;19:185–193.

Bolukbasi MF, Mizrak A, Ozdener GB et al. miR-1289 and "Zipcode"-like Sequence Enrich mRNAs in Microvesicles. Mol Ther Nucleic Acids 2012;1:e10.

Bruno S, Grange C, Collino F et al. Microvesicles derived from mesenchymal stem cells enhance survival in a lethal model of acute kidney injury. PLoS One 2012;7:e33115.

Bruno S, Grange C, Deregibus MC et al. Mesenchymal stem cell-derived microvesicles protect against acute tubular injury. J Am Soc Nephrol 2009;20:1053–1067.

Bushell M, Stoneley M, Sarnow P et al. Translation inhibition during the induction of apoptosis: RNA or protein degradation? Biochem Soc Trans 2004;32:606-610.

Carmona-Saez P, Chagoyen M, Tirado F et al. GENECODIS: a web-based tool for finding significant concurrent annotations in gene lists. Genome Biol 2007;8:R3.

Chen TS, Lai RC, Lee MM et al. Mesenchymal stem cell secretes microparticles enriched in pre-microRNAs. Nucleic Acids Res 2010;1:215–224.

Crisan M, Corselli M, Chen CW et al. Multilineage stem cells in the adult: a perivascular legacy? Organogenesis 2011;7:101-114.

Deans RJ, Moseley AB. Mesenchymal stem cells. Exp Hematol 2000;28:875–884.

Deregibus MC, Cantaluppi V, Calogero R et al. Endothelial progenitor cell-derived microvescicles activate an angiogenic program in endothelial cells by a horizontal transfer of mRNA. Blood 2007;110:2440–2448.

D'haene B, Mestdagh P, Hellemans J et al. miRNA expression profiling: from reference genes to global mean normalization. Methods Mol Biol 2012;822:261-272.

Dominici M, Le Blanc K, Mueller I et al. Minimal criteria for defining multipotent mesenchymal stromal cells. The International Society for Cellular Therapy position statement. Cytotherapy 2006;8:315-317.

Dweep H, Gretz N, Felekkis K. A schematic workflow for collecting information about the interaction between copy number variants and microRNAs using existing resources. Methods Mol Biol 2014;1182:307-320.

Ferrand J, Noel D, Lehours P et al. Human bone marrow-derived stem cells acquire epithelial characteristics through fusion with gastrointestinal epithelial cells. PLoS ONE 2011;6:e19569.

Fujita Y, Yoshioka Y, Ochiya T. Extracellular vesicle transfer of cancer pathogenic components. Cancer Sci 2016;107:385-90.

Gao F, Chiu SM, Motan DA et al. Mesenchymal stem cells and immunomodulation: current status and future prospects. Cell Death Dis 2016; 7:e2062.

Gatti S, Bruno S, Deregibus MC et al. Microvesicles derived from human adult mesenchymal stem cells protect against ischaemia-reperfusion-induced acute and chronic kidney injury. Nephrol Dial Transplant 2011;26:1474–1483.

Iavello A, Frech VS, Gai C, Deregibus MC, Quesenberry PJ, Camussi G. Role of Alix in miRNA packaging during extracellular vesicle biogenesis. Int J Mol Med 2016;37:958-966.

Jin Y, Liu R, Xie J et al. Interleukin-10 deficiency aggravates kidney inflammation and fibrosis in the unilateral ureteral obstruction mouse model. Lab Invest 2013;93:801-811.

Kilpinen L, Impola U, Sankkila L et al. Extracellular membrane vesicles from umbilical cord blood-derived MSC protect against ischemic acute kidney injury, a feature that is lost after inflammatory conditioning. J Extracell Vesicles 2013;2.

Lee C, Mitsialis SA, Aslam M et al. Exosomes mediate the cytoprotective action of mesenchymal stromal cells on hypoxia-induced pulmonary hypertension. Circulation 2012;126:2601.

Lee RH, Pulin AA, Seo MJ et al. Intravenous hMSC improve myocardial infarction in mice because cells embolized in lung are activated to secrete the anti-inflammatory protein TSG-6. Cell Stem Cell 2009;5:54–63.

Li T, Yan Y, Wang B et al. Exosomes derived from human umbilical cord mesenchymal stem cells alleviate liver fibrosis. Stem Cells Dev 2013;22:845–854.

Liu Y, Lu Q. Extracellular vesicle microRNAs: biomarker discovery in various diseases based on RT-qPCR. Biomark Med 2015;9:791-805.

Morigi M, Rota C, Montemurro T et al. Life-sparing effect of human cord blood-mesenchymal stem cells in experimental acute kidney injury. Stem Cells 2010; 28(3):513-522.

Morigi M, Benigni A. Mesenchymal stem cells and kidney repair. Nephrol Dial Transplant 2013;28:788-793.

Najar M, Raicevic G, Fayyad-Kazan H et al. Mesenchymal stromal cells and immunomodulation: A gathering of regulatory immune cells. Cytotherapy 2016; 18(2):160-171.

Nawaz M, Fatima F, Vallabhaneni KC et al. Extracellular Vesicles: Evolving Factors in Stem Cell Biology. Stem Cells Int 2016:1073140.

Nogales-Cadenas R, Carmona-Saez P, Vazquez M et al. GeneCodis: interpreting gene lists through enrichment analysis and integration of diverse biological information. Nucleic Acids Res 2009;37:W317-322.

Parekkadan B, Milwid JM. Mesenchymal stem cells as therapeutics. Annu Rev Biomed Eng 2010;12:87–117.

Quesenberry PJ, Aliotta J, Deregibus MC et al. Role of extracellular RNA-carrying vesicles in cell differentiation and reprogramming. Stem Cell Res Ther 2015;6:153.

Ragni E, Lommel M, Moro M et al. Protein O-mannosylation is crucial for human mesencyhmal stem cells fate. Cell Mol Life Sci 2016;73:445-58.

Ragni E, Viganò M, Rebulla P et al. What is beyond a qRT-PCR study on mesenchymal stem cell differentiation properties: how to choose the most reliable housekeeping genes. J Cell Mol Med 2013;17:168-180.

Rani S, Ryan AE, Griffin MD et al. Mesenchymal Stem Cell-derived Extracellular Vesicles: Toward Cell-free Therapeutic Applications Molecular Therapy 2015;5:812–823.

Ringdén O, Uzunel M, Rasmusson I et al. Mesenchymal stem cells for treatment of therapy-resistant graft-versus-host disease. Transplantation 2006;81:1390-1397.

Shentu TP, Wong S, Espinoza C et al. Extracellular vesicles isolated from human mesenchymal stem cells promote resolution of pulmonary fibrosis. The FASEB Journal 2016; 30.

Soranno DE, Rodell CB, Altmann C et al. Delivery of interleukin-10 via injectable hydrogels improves renal outcomes and reduces systemic inflammation following ischemic acute kidney injury in mice. Am J Physiol Renal Physiol 2016;311:F362-72.

Spees JL, Olson SD, Ylostalo J et al. Differentiation, cell fusion, and nuclear fusion during ex vivo repair of epithelium by human adult stem cells from bone marrow stroma. Proc Natl Acad Sci U S A 2003;100:2397–2402.

Stoltz JF, de Isla N, Li YP et al. Stem Cells and Regenerative Medicine: Myth or Reality of the 21th Century. Stem Cells Int 2015; 2015:734731.

Tabas-Madrid D, Nogales-Cadenas R, Pascual-Montano A. GeneCodis3: a non-redundant and modular enrichment analysis tool for functional genomics. Nucleic Acids Res 2012;40:W478-483.

Tan CY Lai RC Wong Wet al. Mesenchymal stem cell-derived exosomes promote hepatic regeneration in drug-induced liver injury models. Stem Cell Res Ther 2014;5:76.

Tomasoni S, Longaretti L, Rota C et al. Transfer of growth factor receptor mRNA via exosomes unravels the regenerative effect of mesenchymal stem cells. Stem Cells Dev 2013;22(5):772-780.

Ullah I, Subbarao RB, Rho GJ. Human mesenchymal stem cells - current trends and future prospective. Biosci Rep 2015;35(2).

Valadi H, Ekström K, Bossios A et al. Exosome-mediated transfer of mRNAs and microRNAs is a novel mechanism of genetic exchange between cells. Nat Cell Biol 2007;9:654–659.

Vandesompele J, De Preter K, Pattyn F et al. Accurate normalization of real-time quantitative RT-PCR data by geometric averaging of multiple internal control genes. Genome Biol 2002;3.

Vassilopoulos G, Wang PR, Russell DW. Transplanted bone marrow regenerates liver by cell fusion. Nature 2003;422:901–904.

Waris S, Wilce MC, Wilce JA. RNA recognition and stress granule formation by TIA proteins. Int J Mol Sci 2014;15:23377-23388.

Yáñez-Mó M, Siljander PR, Andreu Z et al. Biological properties of extracellular vesicles and their physiological functions. J Extracell Vesicles 2015;4:27066.

Yu B, Zhang X, Li X. Exosomes derived from mesenchymal stem cells. Int J Mol Sci 2014;15:4142-4157.

Zhang B, Wang M, Gong A et al. HucMSC-exosome mediated-Wnt4 signaling is required for cutaneous wound healing. Stem Cells 2015;33:2158-2168.

Zhang X, Hirai M, Cantero S et al. Isolation and characterization of mesenchymal stem cells from human umbilical cord blood: reevaluation of critical factors for successful isolation and high ability to proliferate and differentiate to chondrocytes as compared to mesenchymal stem cells from bone marrow and adipose tissue. J Cell Biochem 2011;112:1206-1218.

Zhu YG, Feng XM, Abbott J et al. Human mesenchymal stem cell microvesicles for treatment of Escherichia coli endotoxin-induced acute lung injury in mice. Stem Cells 2014;32:116-125.

LAZZARI L. – FIGURE 1 - TOP

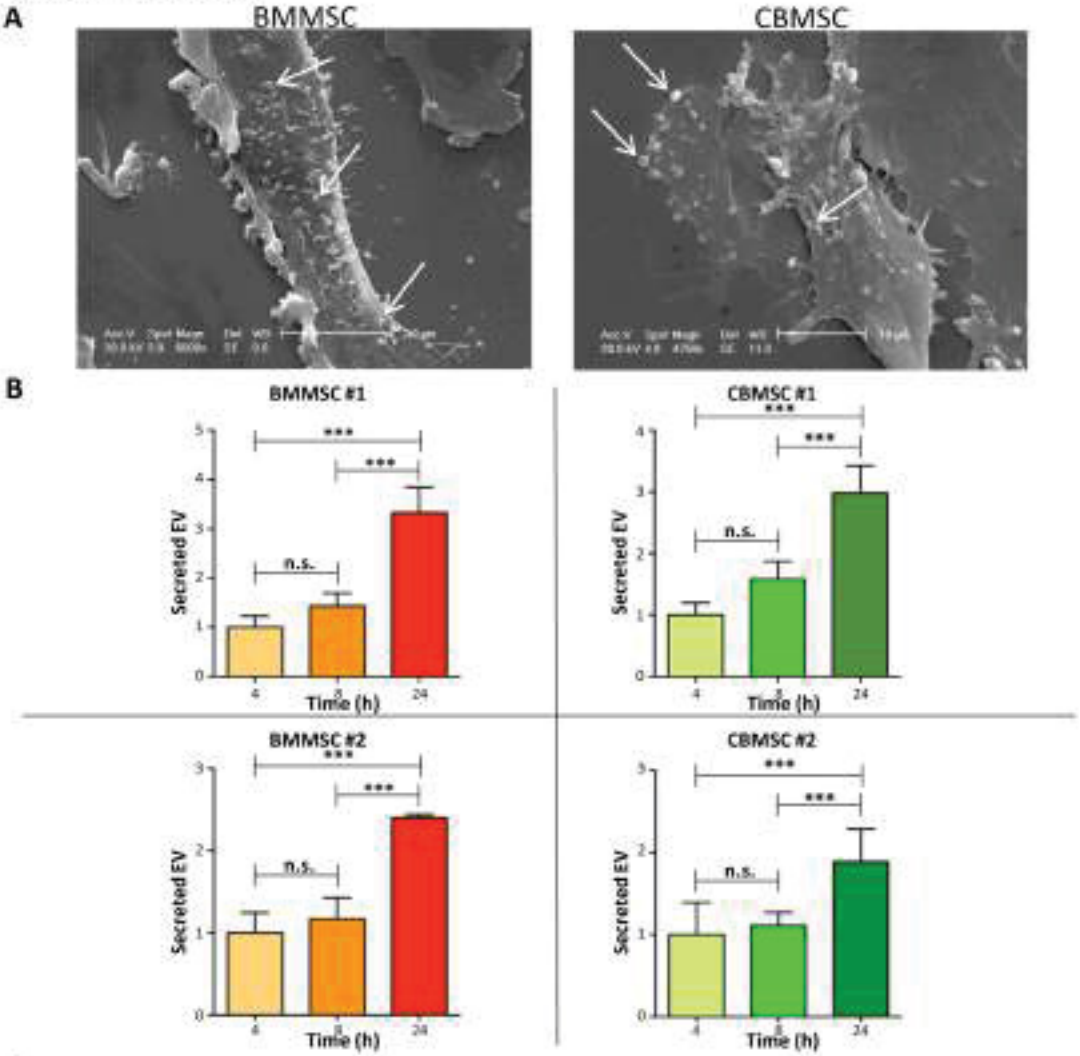

C

	BMMSC #1	BMMSC #2	CBMSC #1	CBMSC #2
SIZE (nm)	258 ± 19	276 ± 41	229 ± 29	269 ± 10
EV / CELL	1880 ± 681	1764 ± 148	3172 ± 14	5303 ± 906

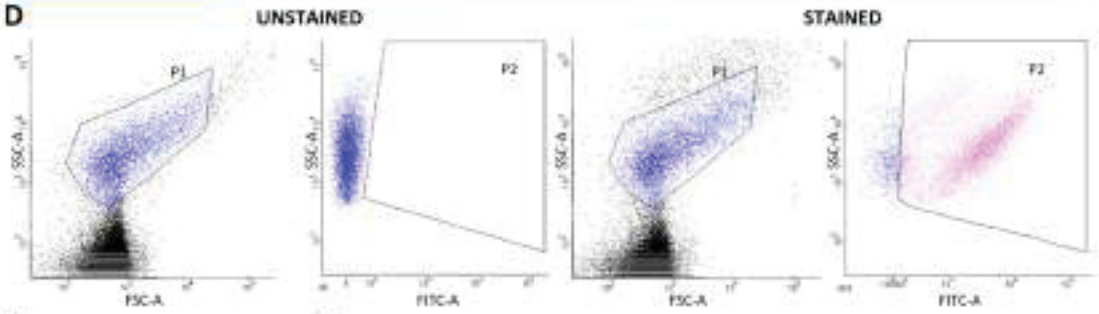

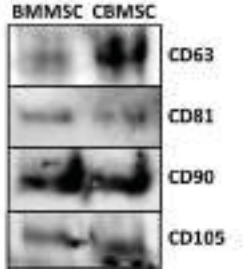

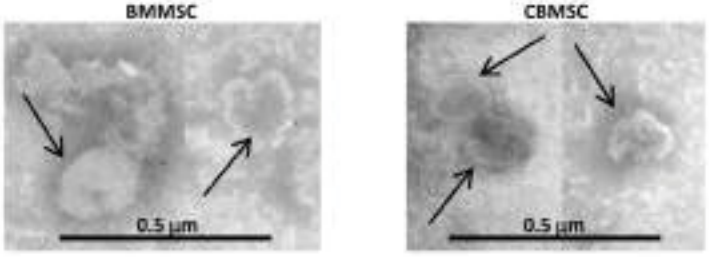

LAZZARI L. – FIGURE 2 - TOP

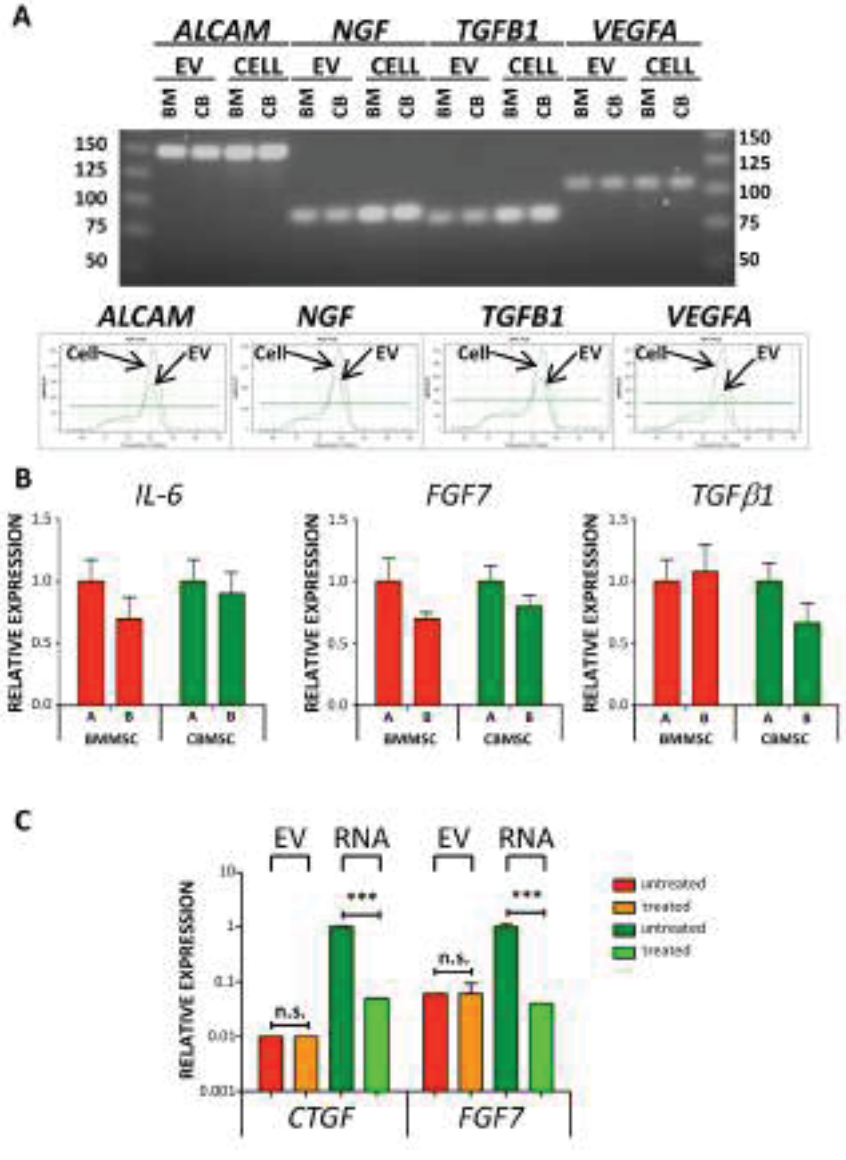

LAZZARI L. – FIGURE 3 - TOP

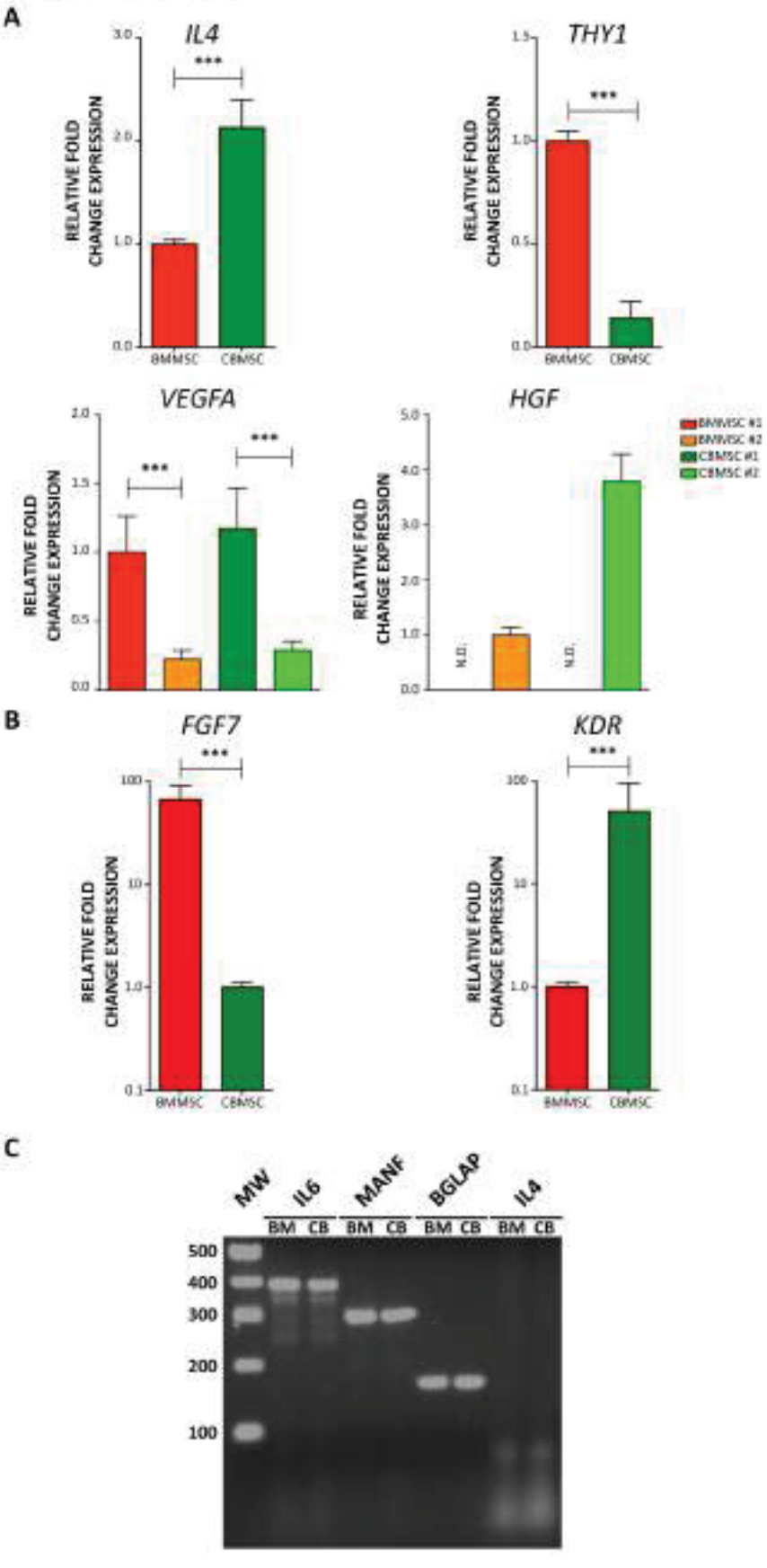

LAZZARI L. – FIGURE 4 - TOP

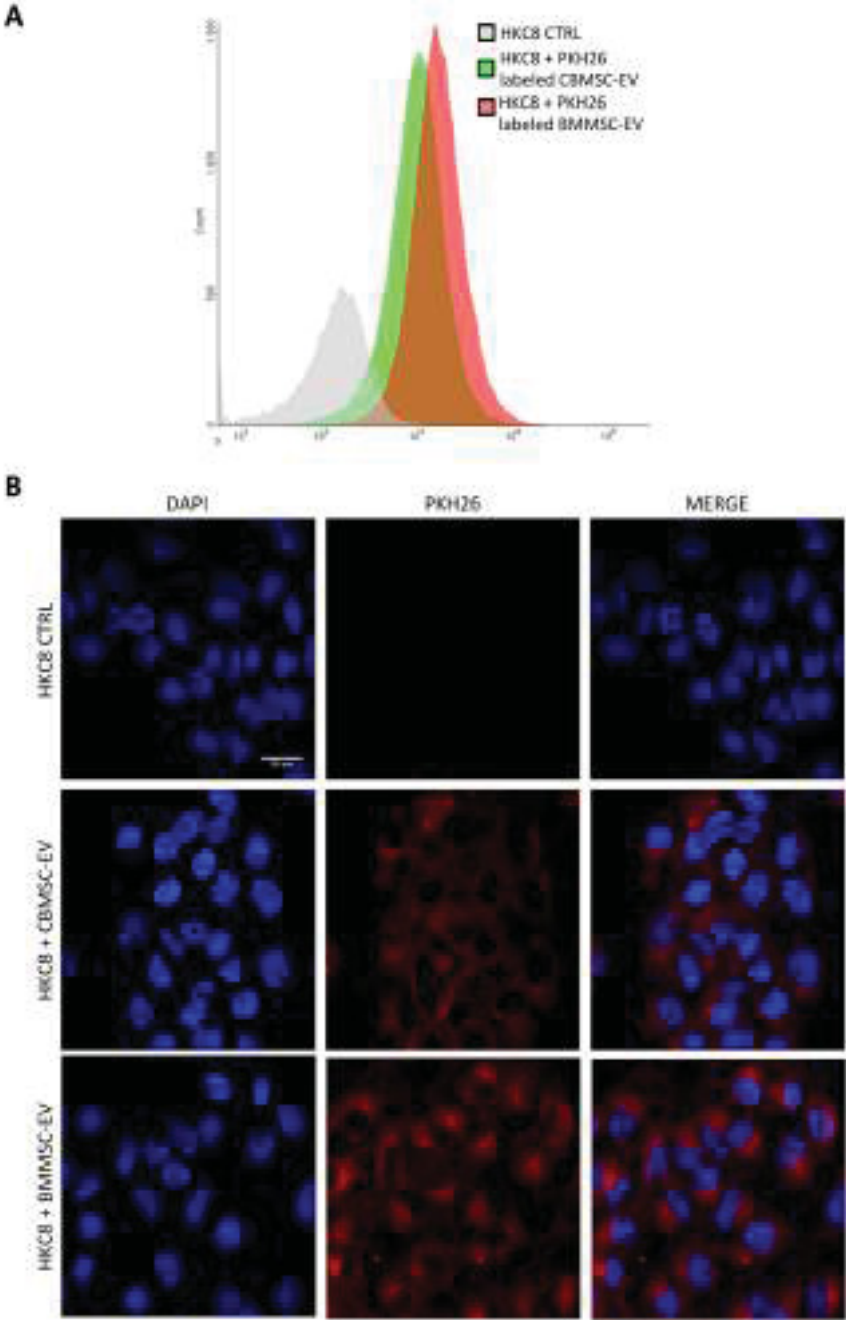

LAZZARI L. – FIGURE 5 - TOP

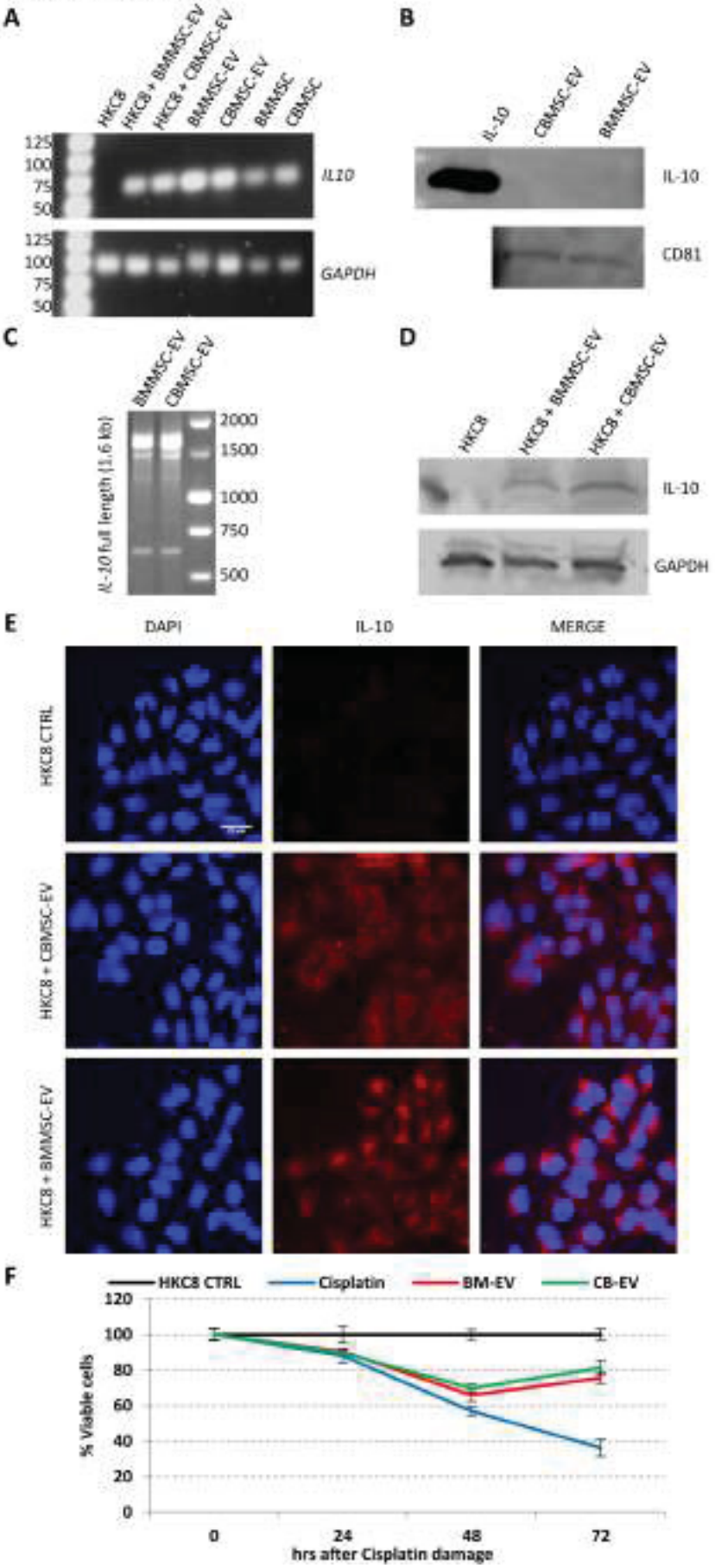

LAZZARI L. – FIGURE 6 - TOP

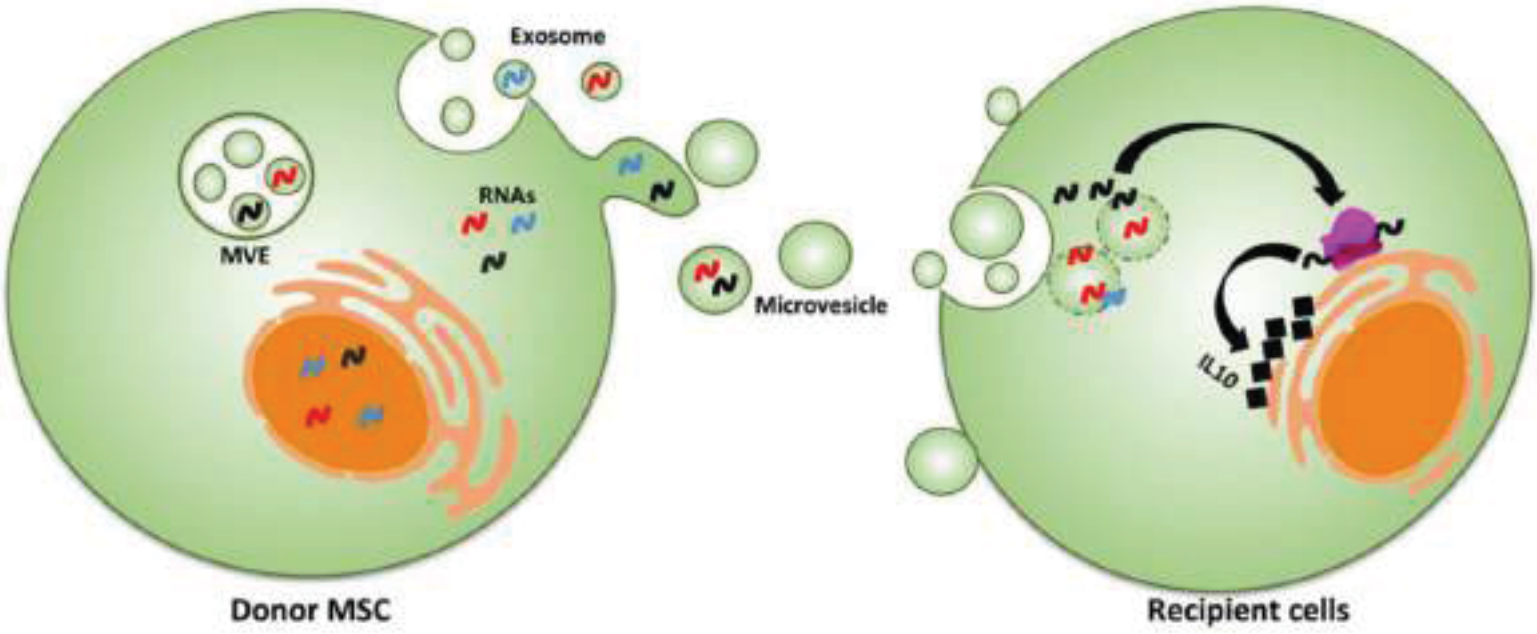

Table 1. Differentially enriched mRNA in MSC-EV.

BMMSC #1		BMMSC #2		CBMSC #1		CBMSC #2	
GENE	**EV/ CELL**	**GENE**	**EV/ CELL**	**GENE**	**EV/ CELL**	**GENE**	**EV/ CELL**
IL-10	6472.02	***IL-10***	3769.09	***IL-4***	9026.81	***IL-10***	11425.74
IL-4	2610.30	***KDR***	3104.19	***IL-10***	6517.03	***IL-4***	10226.32
KDR	1964.57	***IL-4***	792.35	***BGLAP***	955.43	***FGF7***	744.43
BGLAP	352.14	***BGLAP***	162.02	***FGF7***	245.57	***BGLAP***	680.29
CNTF	125.37	***CNTF***	78.25	***CNTF***	123.64	***KDR***	188.71
FZD9	31.12	***FZD9***	64.89	***FZD9***	119.43	***CNTF***	139.10
FGF7	14.93	***FGF7***	5.43	***KDR***	36.25	***FZD9***	64.89
IL-6	8.82	***NGF***	4.17	***BDNF***	4.28	***BDNF***	5.82
NGF	2.99	***BDNF***	1.77	***FGF2***	1.68	***NGF***	4.17
BDNF	2.62	***IL-6***	1.59	***NGF***	1.38	***FGF2***	2.45
FGF2	1.57	***FGF2***	1.19	***MANF***	0.56	***IL-6***	1.16
MANF	0.81	***THY1***	0.44	***VEGFA***	0.41	***THY1***	0.38
THY1	0.42	***MANF***	0.40	***IL-6***	0.24	***MANF***	0.31
VEGFA	0.37	***CTGF***	0.24	***CTGF***	0.12	***COL1A1***	0.13
COL1A1	0.31	***COL1A1***	0.12	***COL1A1***	0.12	***CTGF***	0.08
CTGF	0.26	***ALCAM***	0.07	***TGFB1***	0.08	***VEGFA***	0.07
TGFB1	0.15	***VEGFA***	0.03	***THY1***	0.08	***TGFB1***	0.03

Supplementary Table 1. Normalized qRT-PCR Ct data.

	CELLS				EV			
	BMMSC #1	BMMSC #2	CBMSC #1	CBMSC #2	BMMSC #1	BMMSC #2	CBMSC #1	CBMSC #2
GENE	Ct	Ct	Ct	Ct	Ct	Ct	Ct	Ct
ALCAM	22.5	22.9	22.7	22.8	33.9	34.7	34.7	36.1
BDNF	23.9	24.2	25.4	24.4	30.5	31.4	31.1	29.9
BGLAP	32.9	32.3	34.0	33.9	32.4	32.9	32.1	32.5
CNTF	29.4	29.1	29.4	29.1	30.4	30.8	30.4	30.0
COL1A1	18.4	18.0	18.5	18.5	28.0	29.0	29.6	29.4
CTGF	20.1	20.4	19.6	19.2	30.0	30.4	30.6	30.8
FDZ9	29.8	31.6	31.3	31.3	32.8	33.6	32.4	33.3
FGF2	24.1	24.7	24.6	24.9	31.4	32.4	31.8	31.6
FGF7	24.3	23.3	29.9	29.7	28.4	28.9	29.9	28.1
HGF	27.9	27.9	33.9	25.9	ND	38.0	ND	35.8
IL-10	36.0	35.7	36.7	36.7	31.4	31.8	32.0	31.2
IL-4	35.1	33.9	35.7	36.1	31.7	32.2	30.5	30.8
IL-6	25.2	23.7	20.8	22.8	30.0	31.0	30.9	30.5
KDR	35.2	36.8	28.7	31.8	32.2	33.2	31.5	32.2
MANF	23.4	23.3	22.8	23.1	31.7	32.6	31.6	32.8
NGF	27.5	28.4	26.3	27.1	33.9	34.3	33.8	33.1
TGFB1	22.8	22.9	22.9	22.8	33.5	36.2	34.6	35.8
THY1	22.0	22.6	23.3	24.4	31.2	31.8	34.9	33.7
VEGFA	23.7	22.5	23.4	23.4	33.1	35.8	32.7	35.1

FIGURE LEGENDS

Figure 1. Kinetics and physical properties of MSC-EVs. A) Scanning Electron Microscopy of BMMSC and CBMSC showing EVs shedding from cell protrusions. Arrows point out representative examples of vesicles dismissed from the cell surface. B) EVs secretion kinetics normalized on values at 4 hours set as 1 (n = 5 per cell population, errors as SD). Significant differences between groups are noted as *** (p-value < 0.001). C) EVs mean size obtained from Nanosight analysis (n = 10 per cell population, errors as SD) together with quantification of EVs secreted per seeded cell at 24 hours after medium change (n = 10 per cell population, errors as SD). D) CFSE staining of a representative EVs sample showing high integrity of isolated vesicles. P1 = total EV; P2 = CFSE positive EVs. E) Western Blot analysis of exosome (CD63 and CD81) and MSC (CD90 and CD105) surface markers in purified EVs from BM- and CB-MSC supernatants. F) Transmission electron microscopy performed on isolated vesicles to visualize their ultrastructural morphology. EVs are indicated with black arrows.

Figure 2. Validation of EV-embedded mRNA transcriptional analysis. A) Validation of qRT-PCR specificity for low abundant transcripts *ALCAM* (expected 148 bp), *NGF* (85 bp), *TGFB1* (81 bp) and *VEGFA* (105 bp). Agarose gel electrophoresis and representative melting curve tests for BMMSC cell and EVs amplicons are shown. B) Comparison of *IL-6*, *FGF7* and *TGFB1* abundance in BMMSC and CBMSC EVs between multiple transcripts analysis (A) and individual qRT-PCR (B) (n = 3 per cell population, errors as SEM). Expression in A was set as 1. C) *CTGF* and *FGF7* mRNA detection in MSC-EVs analysis after Proteinase K and RNAse A treatment (treated) (n = 3 per cell population, errors as SEM). Cell RNA was used as control for positive enzymes digestion, as showed by significant (*** p-value < 0.001) reduction in Real-Time PCR amplification. Expression of untreated cell RNA was set as 1.

Figure 3. Molecular differences in MSC and secreted EVs. A) EV-embedded transcripts (*IL-4* and *THY1*) differentially incorporated in CBMSC vs BMMSC (BMMSC set as 1; n=6, errors as SD; *** p-value < 0.001). *VEGFA* and *HGF* showed alternative expression in a cell line dependent fashion (BMMSC #1 set as 1 for *VEGFA* and BMMSC #2 set as 1 for *HGF*, n = 3, errors as SD; *** p-value < 0.001). B) *FGF7* and *KDR* resulted to have significant differential expression in MSC cell extracts (CBMSC set as 1 for *FGF7* and BMMSC set as 1 for *KDR*; n = 6, errors as SD; *** p-value < 0.001). C) Agarose gel electrophoresis analysis of RT-PCR amplification for detection of complete 3'UTR in *IL-6* (expected 392 bp), *MANF* (296 bp), *BGLAP* (157 bp) and *IL-4* (79 bp) EV-embedded transcripts.

Figure 4. PKH26 EVs labeling and HKC8 incorporation. A) FACS analysis of HKC8 cells after 24 hours co-culture with PKH26-EVs or vehicle (negative control). B) Confocal microscopy images of HKC8 after 24 hours co-culture with labeled EVs.

Figure 5. Incorporation and translation of IL-10 mRNA into HKC8 cells. A) Agarose gel electrophoresis analysis of *IL-10* mRNA RT-PCR amplification. *GAPDH* mRNA detection is shown as internal control for positive cDNA synthesis. Lane 1, DNA molecular weights. B) Molecular confirmation of absence of IL-10 protein loading into EVs by Western Blotting analysis. EVs preparations were confirmed for their positivity for the exosomal markers CD81. Purified IL-10 was used as positive control for primary antibody. C) Agarose gel electrophoresis analysis of *IL-10* intact full-length mRNA (expected 1589 bp) embedded in MSC-EVs. Lane 3, DNA molecular weights. D) Western Blot analysis showing absence of IL-10 protein in HKC8 and its appearance after EVs administration. GAPDH was used as positive control for loading. E) Confocal microscopy images of translated IL-10 protein after MSC-EVs administration to tubular cells. All IL-10 panels show HKC8 cells (with or without EVs supplementation) treated with both primary and secondary antibodies. HKC8 CTRL (not treated with MSC-EVs) confirms endogenous IL-10 absence. F) MTT test assaying viable cells after cisplatin treatment (Cisplatin) or after drug injury and vesicles administration every 24 h (BM-EVs and CB-EVs). Both vesicle types are able to increase recovery and reduce acute injury-driven cell death. Values are related to control cells (HKC8 CTRL) that were not damaged and set as 100% viability for each time point.

Figure 6. Model of horizontal transfer of EV-embedded mRNA as part of paracrine and autocrine communication network.

TABLE LEGEND

Table 1. Differentially enriched mRNA in MSC-EVs. The amount ratios for indicated gene transcripts in EVs versus cell extracts (EVs/CELL) are shown. The dashed line separates the seven transcripts that are consistently and preferentially accumulated in EVs for all 4 cell lines used in the study. Values higher than 2 indicate transcripts present in EVs with at least a double amount of what expected from a random internalization from the cytoplasm, whereas values lower than 0.5 indicate messengers excluded in secreted vesicles.

Supplementary Table 1. qRT-PCR Ct data are shown. Presented values are the mean of three independent experiments.

III. Protocols

a. Induced cellular reprogramming

Reprogramming System

CytoTune-iPS 2.0 Reprogramming System vectors (Thermo Fisher Scientific, Waltham, MA, USA) are based on the genome of a non-transmissible form of Sendai virus (SeV) to deliver and to express the genetic factors (*OCT4*, *SOX2*, *KLF4*, *cMYC*) necessary to reprogram somatic cells into human induced pluripotent stem cells (iPSCs). These vectors are non-integrating and they remain in the cytoplasm, meaning they are zero-footprint. The reprogramming factors are expressed by three different vectors: one contains the *KLF4*, *OCT4* and *SOX2* sequences (KOS vector); one contains only *KLF4* sequence (K vector); the last contains only *cMYC* sequence (M vector). An important modification introduced in the SeV genome is that the gene encoding for the F protein, essential for the viral envelope to fuse with cell membranes, is deleted from all reprogramming vectors. Therefore, they are unable to produce infectious particles from infected cells.

Transduction feasibility

CytoTune-EmGFP Reporter Control Transduction (Thermo Fisher Scientific) was used to assess feasibility of long living (LL)-cord blood (CB) multipotent mesenchymal stromal cell (MSC) transduction. This reporter system consists in the same modified SeV vector used to deliver reprogramming factors, but it expresses emerald green fluorescent protein (EmGFP).

Briefly:

1) On day -1, LL-CBMSCs were plated in four wells of a 6-well plate at 15,000 cells/cm^2 in αMEM-GlutaMAX (Thermo Fisher Scientific) 20% fetal bovine serum (FBS, Thermo Fisher Scientific) (LL-CBMSC medium);
2) On day 0, LL-CBMSCs had reached 70–80% confluence, and cell count was performed on one well;

3) Then, the volumes of virus (V) to reach the chosen multiplicity of infection (MOI) were calculated as follows:

$$V(\mu L) = MOI \text{ (cell infection units, CIU/cell) X number of cells/ titer of virus (CIU/mL) X } 10^3 \text{ (}\mu L/mL\text{)}$$

MOI 3, 5 and 7 were tested;

4) A volume of 2 mL of culture medium was warmed for each well to be transduced in a 37 °C water bath;
5) One tube of CytoTune-EmGFP Sendai Fluorescence Reporter was thawed immediately before transduction by an initial immersion in a 37 °C water bath for 10 seconds and subsequent thawing at room temperature. Once thawed, the tube was briefly centrifuged and placed on ice;
6) The calculated volumes of virus were added to the pre-warmed cell culture medium and thoroughly mixed by pipetting;
7) Rapidly, the cell culture medium from LL-CBMSCs was aspirated and the viral solution added;
8) The cells were then incubated overnight at 37 °C, 5% CO_2;
9) On day 2, transduced LL-CBMSCs were visualized on a fluorescence microscope (Nikon Eclipse Ti; Nikon, Tokyo, Japan) using a standard FITC filter set. EmGFP expression was visible in 35% (MOI=3), 50% (MOI=5) and 60% (MOI=7) of total infected cells, measured by standard flow cytometry (FACSCantoII; BD, Franklin Lakes, NJ, USA).

Reprogramming protocol

1) On day -2, LL-CBMSCs were plated into two wells of a 6-well plate in LL-CBMSC medium;
2) On day 0, 70-80% confluent LL-CBMSCs were transduced using the CytoTune-iPS 2.0 Sendai reprogramming vectors at MOI=5 (KOS and M vectors) and MOI=3 (K vector), following the procedure previously described for the CytoTune-EmGFP Sendai Fluorescence Reporter;
3) LL-CBMSCs were then incubated overnight at 37 °C, 5% CO_2;

4) On day 1, the medium was replaced with fresh medium to remove viral particles;
5) On day 2-6, the medium was replaced every other day;
6) On day 7, the transduced cells were detached and seeded on matrigel (BD)-coated culture Petri dishes in LL-CBMSC medium;
7) On day 8, the LL-CBMSC medium was switched to StemMACS iPS-Brew XF medium (Miltenyi Biotec, Bergisch Gladbach, Germany);
8) On day 9-28, the medium was replaced every day and the culture vessels were monitored for the emergence of human (h) iPSC colonies;
9) When hiPSC colonies were ready for transfer, manual mechanical picking using a 150 µm diameter needle mounted on a stripper micropipette was performed. Colony clumps of 20-200 cells were seeded in StemMACS medium onto matrigel-coated culture Petri dishes for expansion;
10) Bright field images of colonies from established hiPSC lines were taken with a Nikon Eclipse Ti microscope (Nikon).

Karyotype

Karyotyping was performed in collaboration with the Laboratory of Cytogenetics and Molecular Genetics, Fondazione IRCCS Ca' Granda, Ospedale Maggiore Policlinico, Milan, Italy. In order to prepare hESCs and hiPSCs for karyotyping, the cells were seeded onto matrigel-coated amniodish (Euroclone, Pero, Italy), following a 1:3 split ratio was performed, so that many little and not too compact colonies were attached to the culture surface by the day after. The colonies were allowed to grow for 48 hours and then they were processed for metaphase analysis. Conventional karyotyping was carried out according to the standard laboratory protocols (Hsu TC, , 1972). All karyotyping was achieved using Q-banding technique. Numerical and structural abnormalities have been analysed at 400 banding level, according to the international system for human cytogenomic nomenclature and the european general guidelines and quality assurance for cytogenetics. Moreover, the analysis included a minimum of 20 cells to exclude clonal rearrangiaments. The capture of metaphase images was

performed by the automated sample analysis system IKAROS (MetaSystems, Altlussheim, Germany).

Stem cell immunophenotype

Colonies of hiPSCs (passage 3) and hESC (passage 43), and LL-CBMSCs (passage 4) were detached by a 5 minute TrypLE select enzyme (Thermo Fisher Scientific) incubation at 37 °C, 5% CO_2, to produce a single cell suspension, which was then collected with PBS (Thermo Fisher Scientific) and centrifuged at 350 xg for 7 minutes at room temperature (RT). The cell pellets were incubated for 20 minutes in the dark at RT with 10 µL of the antibodies or isotype controls specified in table 1, in a total volume of 200 µL of PBS. Then, the cells were washed with PBS to remove the unbound antibodies, centrifuged at 350 xg for 7 minutes, and resuspended in 350 µL of PBS. The immunophenotype was assessed using a FACSCantoII cytometer (BD), acquiring at least 10,000 total events. Flow cytometry data were analyzed using FACSDiva software version 7.0 (BD).

	Fluorochrome			
	FITC	*PE*	*PerCP-Cy5.5*	*APC*
Tube 1	IgG (BD)	IgG (BD)	IgG (BC)	IgG (BD)
Tube 2	CD45 (BC)	CD271 BD)	CD34 (BC)	
Tube 3	HLA-DR BD)			CD90 (MB)
Tube 4	CD31 (BD)	CD105 BC)		CD73 (MB)
Tube 5	HLA-ABC (BD)	CD44 (BD)		

Table 1. Flow cytometry experimental layout. BC, Beckman Coulter, Brea, CA, USA; BD, Becton Dickinson, Franklin Lakes, NJ, USA; MB, Miltenyi Biotec, Bergisch Gladbach, Germany.

III. Protocols

b. Culture and characterization of pluripotent stem cells

Cell culture

Human embryonic stem cells (hESC) and hiPSCs were cultured in StemMACS iPS-Brew XF medium (Miltenyi Biotec (MB), Bergisch Gladbach, Germany) onto matrigel (BD, Franklin Lakes, NJ, USA)-coated culture dishes. The medium was changed every day. At 80% confluence, the colonies were detached by ethylenediaminetetraacetic acid (EDTA; Thermo Fisher Scientific, Waltham, MA, USA) passaging. Briefly, the medium was removed and the cells washed with PBS (Thermo Fisher Scientific). Then, the cells were incubated with 5 mM EDTA for 4 minutes in a 37 °C, 5% CO_2 incubator. EDTA was gently removed and the colonies detached and disgregated in 20-200 cell clumps by pipetting, using StemMACS iPS-Brew medium (MB). The cells were seeded in new matrigel(BD)-coated culture dishes, observing a 1:3-1:8 split ratio, depending on experimental needs. Freezing medium was composed of StemMACS iPS-Brew XF medium (MB) supplemented with 10% DMSO (Bioniche Pharma, Costelloe, Ireland); thawing medium was composed of StemMACS iPS-Brew XF medium (MB) supplemented with 10 μM Rock inhibitor (Stemcell technologies, Vancouver, Canada). The day after passaging and thawing, the medium was not changed.

Alkaline phosphatase activity

Direct alkaline phosphase activity was assessed using the Alkaline Phosphatase (AP) Live Stain kit (Life Technologies, Carlsbad, CA United States). The analysis was performed on hiPSC and hESC colonies (positive control) and on LL-CBMSCs (negative control). All cells were grown on chamber slides (BD, Franklin Lakes, NJ, USA), following the cell culture conditions previously described. The following steps were performed:

- The medium was removed, and the cells were washed with PBS;

- The cells were incubated for 15 minutes at room temperature (RT) with a 4% paraformaldehyde (PFA; Thermo Fisher Scientific) fixative solution (PBS-diluted);
- The fixative solution was removed and the cells were washed with PBS;
- The cells were incubated 30 minutes at RT with 1 µL of AP Live Stain solution in 0.5 mL of DMEM/F-12 (Sigma-Aldrich, Saint Louis, MO, USA);
- The AP Live Stain solution was removed and the cells were washed twice with DMEM/F-12 to reduce background signal.

The detection of fluorescent colonies was performed on an inverted phase-contrast microscope (Nikon Eclipse Ti; Nikon, Tokyo, Japan).

RNA extraction

The RNeasy Plus Mini kit (Qiagen, Hilden, Germany) was used to extract RNA from cell pellets previously frozen at -20 °C. The samples were first lysed and homogenized in RNeasy Plus lysis buffer (Qiagen). Then, the lysate was filtered through a gDNA-eliminator spin column (Qiagen), which allows efficient removal of genomic DNA after a centrifugation at ≥ 8000 xg for 30 seconds. Next, the flow-through was collected and 350 µL of 70% ethanol were added. The samples were then transferred to an RNeasy spin column (Qiagen), and centrifuged for 15 seconds at 800 xg. Then, 700 µL of Buffer RW1 (Qiagen) were added to the RNeasy spin column and centrifuged again for 15 seconds at ≥ 8000 xg to wash the spin column membrane. The flow-through was discarded. Then, 500 µL RPE Buffer (Qiagen) were added to the RNeasy spin column and centrifuged for 15 seconds at ≥ 8000 xg to wash again the spin column membrane. This passage was repeated one more time with a 2 minute centrifugation. RNA was then eluted in 30 µL of distilled water. RNA quantification was performed with a Nanodrop 1000 instrument (ND-1000 Spectrophotometer; Cellbio, Pero, Italy), reading absorbance at 260 nm; purity was assessed by A260/A230 (organic compound contamination) and A260/A280 (protein contamination) ratios. Integrity of GelRed (Biotium, Fremont, CA USA)-stained RNA was assessed by 1% agarose gel electrophoresis at 100 V (1 hour), after staining detection using the GelDoc XR instrument (Bio-Rad, Hercules, CA, USA).

Retrotranscription

Each RNA sample (800 ng) was retrotranscribed with the iScript cDNA synthesis kit (Bio-Rad). Briefly, 4 µL of 5x iScript reaction mix (salts, dNTPs, oligo(dT), examer random primers) and 1 µL of iScript reverse transcriptase were added to 15 µL of RNA in a PCR tube. Then, the tubes were placed in a thermal cycler (DNA Engine Peltier Thermal Cycler PTC-200; Bio-Rad) and the following steps were performed: 25 °C for 5 minutes, 42 °C for 30 minutes, 85 °C for 5 minutes and 4 °C until storage.

Real time quantitative polymerase chain reaction

To assess gene expression, Real Time quantitative reverse transcription-polymerase chain reaction (Real Time qRT-PCR) was performed. A 10 µL PCR reaction mix was prepared with 5 µL of 2x SsoFast EvaGreen Supermix (Bio-Rad), 500 nM of forward and reverse primers and 12 ng of cDNA. Then, the reaction mix for each sample was loaded into a Real Time qRT-PCR 96-well plate, in triplicate. Amplification data were studied using the Bio-Rad CFX Manager software (Bio-Rad); technical replicate values were checked for differences inferior to 0.5 threshold cycles (Ct). The melting curve relative to every reaction was examined to exclude aspecific amplification. In addition, amplification reactions with Ct values higher than 35 were not considered. Finally, gene expression was calculated with the ΔΔCt method, using *GAPDH* as house-keeping gene and normalizing to hESC (positive control). When feasible, the primers were designed to anneal to exon-exon junction regions of the mature transcripts and amplificate exons separated by at least one intron, to decrease the risk of unspecific amplification of genomic DNA. PCR cycling conditions and primer sequences are provided in table 1 and 2.

	Temperature	Time	Cycles
Initial denaturation	98 °C	30 seconds	1
Denaturation	95 °C	5 seconds	46
Annealing and Polymerization	60 °C	20 seconds	
Melting curve	65 °C	5 seconds	1
	95 °C		
Hold	4 °C	> 5 minutes	1

Table 1. PCR thermal profiles.

	Name	Sequences	
House-keeping gene	*GAPDH*	forward primer:	CCCTTCATTGACCTCAACTACATG
		reverse primer:	TGGGATTTCCATTGATGACAAGC
Target genes	*KLF4*	forward primer:	ACGATCGTGGCCCCGGAAAAGGACC
		reverse primer:	TGATTGTAGTGCTTTCTGGCTGGGCTCC
	LIN28A	forward primer:	TTCGGGTTCCAGGGAGAC
		reverse primer:	CGTTTCAACACAGTAAGGTAGG
	cMYC	forward primer:	GCGTCCTGGGAAGGGAGATCCGGAGC
		reverse primer:	TTGAGGGGCATCGTCGCGGGAGGCTG
	NANOG	forward primer:	GAGATGCCTCACACGGAGACTG
		reverse primer:	GGGTTGTTTGCCTTTGGGACTG
	OCT4A	forward primer:	CAGCCTGAGGGCGAAGCAG
		reverse primer:	GCTTTGATGTCCTGGGACTCCTC
	SOX2	forward primer:	GTACTGGCGAACCATTCTTG
		reverse primer:	AAATTACCAACGGTGTCAACCTG

Table 2. Primer sequences.

Immunofluorescence

Immunofluorescence analyses were performed on undifferentiated and differentiated (see in vitro differentiation paragraph) hiPSC and hESC (positive control) colonies; the same procedure was also carried out on LL-CBMSCs (negative control). The cells were grown on chamber slides (BD, as previously described.

The following protocol was used:

- The medium was removed, and the cells were washed with PBS;
- The cells were fixed with a 4% PFA (Thermo Fisher Scientific) solution for 15 minute at RT;
- Then, the cells were permeabilized with 1% saponin (Thermo Fisher Scientific) for 15 minute at RT;

- Next, the cells were incubated with a blocking solution (3% bovine serum albumin (BSA; Sigma-Aldrich), diluted in PBS) for 30 minutes at RT;
- Primary antibodies (Table 3) were added directly to the blocking solution still covering the cells;
- An overnight incubation at 4 °C, or alternatively a 3 hour incubation at RT, followed;
- Then, the solution was removed and the cells were washed with PBS for 3 minutes in gentle agitation at RT. This washing step was repeated 3 times;
- The washing buffer was removed and secondary antibodies (Table 4), diluted in blocking solution, were added;
- The cells were then incubated with the secondary antibody solution for 1 hour at RT;
- The solution was removed and the cells were washed as previously described;
- 2 drops of 4',6-diamidino-2-phenylindole (DAPI; Thermo Fisher Scientific) were added to the last washing step and incubated for 5 minutes at RT.

The samples were imaged using a Nikon Eclipse 80i VideoConfocal microscope (ViCo; Nikon) and analyzed with Image-Pro Plus 6.2 analysis software (Media Cybernetics, Rockville, MD, USA).

	Primary antibody		Host	Dilution
Stemness	anti-OCT4 (Thermo Fisher Scientific)		Rabbit	1:100
	anti-SSEA4 (Thermo Fisher Scientific)		Mouse	
	anti-TRA 1-60 (Thermo Fisher Scientific)		Mouse	
	anti-SOX2 (Thermo Fisher Scientific)		Rat	
Germ layer derivatives	Endoderm	anti-AFP (Thermo Fischer Scientific)	Mouse	1:500
	Neuroectoderm	anti-NCAM (Thermo Fischer Scientific)	Mouse	1:100
	Mesoderm	anti-SMA (Thermo Fischer Scientific)	Mouse	

Table 3. Primary antibodies.

	Secondary antibody		Host	Dilution
Stemness	TRITC-conjugated anti-rabbit (Thermo Fischer Scientific)		Donkey	1:250
	FITC-conjugated anti-mouse (Thermo Fisher Scientific)		Goat	
	TRITC-conjugated anti mouse (Thermo Fisher Scientific)		Goat	
	FITC-conjugated anti-rat (Thermo Fisher Scientific)		Donkey	
Germ layer derivatives	Endoderm	FITC-conjugated anti-mouse (Thermo Fisher Scientific)	Goat	
	Mesoderm			
	Neuroectoderm	TRITC-conjugated anti-mouse (Thermo Fisher Scientific)	Goat	

Table 4. Secondary antibodies.

DNA extraction

Cell pellets were collected from subconfluent LL-CBMSC, hESC H9 or hiPSC cultures and immediately frozen at -80 °C until use. DNA was extracted by the QIAamp DNA Blood Mini Kit (51104; Qiagen, Hilden, Germany). Briefly, 200 µL of buffer AL were added to the sample and mixed by pulse-vortexing for 15 seconds. Then, the samples were incubated at 56 °C for 10 minutes, after which 200 µL of ethanol (96-100%) were added to the sample and mixed again by pulse-vortexing for 15 seconds. The mixture was applied to the QIAamp Mini spin columns and centrifuged at 6000 x g for 1 minute, after which the filtrate was discarded. Then, 500 µL of buffer AW1 were added to the QIAamp Mini spin columns and centrifuged at 6000 x g for 1 minute, after which the filtrate was discarded. The same procedure was repeated for buffer AW2, but at full speed (20,000 xg) for 3 minutes. To elute the filter-bound DNA, 200 µL of buffer AE were added to the QIAamp Mini spin columns, which were incubated at room temperature for 1 minute, before they were centrifuged at 6000 x g for 1 minute. DNA quantification was performed with a Nanodrop 1000 instrument, reading absorbance (A) at 260 nm; purity was assessed by A260/A230 (organic compound contamination) and A260/A280 (protein contamination) ratios; integrity was assessed by agarose gel electrophoresis, as previously described.

Bisulfite conversion

Each sample DNA (500 ng) was treated with the EZ DNA Methylation-Gold Kit (Zymo Research, Orange, CA, USA) to obtain bisulfite conversion. Briefly, 130 µL of the CT conversion reagent were added to 20 µL of DNA in a PCR tube. Then, the tube was placed in a thermal cycler and the following steps were performed: 98 °C for 10 minutes, 64 °C for 2.5 hours and 4 °C for storage. Then, 600 µL of M-binding buffer were added to a Zymo-Spin IC column, which was placed into a collection tube. The sample was loaded into the column and it was mixed by inverting the column several times. Centrifugation at full speed (>10,000 x g) for 30 seconds was performed and the flow-through discarded. Then, 100 µL of M-wash buffer were added to the column and centrifugation at full speed for 30 seconds was performed. Next, 200 µL of M-desulphonation buffer were added to the column, which was let stand at room temperature for 20 minutes. After the incubation, centrifugation at full speed for 30 seconds was performed, followed by two washing steps with 200 µL of M-wash buffer. The column was placed into a 1.5 mL microcentrifuge tube. Finally, bisulfite-treated DNA was eluted in 30 µL of M-elution buffer and stored at -20 °C for later use.

Pyrosequencing

To analyze DNA methylation, a 50 µL PCR reaction was carried out with 25 µL of GoTaq Hot Start Green Master mix (Promega, Madison, WI, USA), 10 µM of forward primer, 10 µM of biotinylated reverse primer and 500 ng of bisulfite-treated DNA. PCR cycling conditions and primer sequences are provided in table 1 and 2, respectively. Biotin-labeled primers were used to purify the final PCR product with sepharose beads: 10 µL of PCR product were bound to 1 µL of Streptavidin Sepharose HP affinity chromatography medium (Amersham Biosciences, Uppsala, Sweden) in presence of 40 µL of binding buffer (Amersham Biosciences), after a 10 minute incubation in agitation. Sepharose beads containing the immobilized PCR product were purified, washed, denatured with 0.2 M NaOH and washed again with the Pyrosequencing Vacuum Prep Tool (Pyrosequencing, Inc., Westborough, MA, USA), according to the manufacturer's instructions. Pyrosequencing primer (0.3 µM) was annealed to the purified single-stranded PCR product in presence of 15 µL of

annealing buffer, during an incubation of 2 minutes at 85 °C, then pyrosequencing was performed in duplicate with the PyroMark MD System (Pyrosequencing, Inc. Westborough, MA, USA). The percentage of methylated cytosines was calculated as the number of methylated cytosines divided by the sum of methylated and unmethylated cytosines, multiplied by 100%.

Temperature	Time	Cycles
95 °C	5 minutes	1
95 °C	30 seconds	45
54 °C for NANOG promoter 59 °C for OCT4 promoter 56 °C for OCT4 proximal enhancer	45 seconds	
72 °C	45 seconds	
72 °C	5 minutes	1
6 °C	For ever	1

Table 1. PCR thermal profiles.

Assay	Sequences
NANOG promoter	Forward TTGTTGTTGGGTTTGTTTTTAGG Reverse BIO-ACCTTAAACCCACCCCTCCTA Sequencing TTTGGTGAGATTGGTAGA
OCT4 promoter	Forward AAGTTTTTGTGGGGGATTTGTAT Reverse BIO-CCACCCACTAACCTTAACCTCTA Sequencing 1 TGAGGTTTTGGAGGG Sequencing 2 GTTATTATTATTAGGTAAATATTTT
OCT4 proximal enhancer	Forward AGTTTTAGGATATTTAGGTTAGGTTTAGAA Reverse BIO-CAACAACCCCCCTCTACAAT Sequencing 1 GGATATTTAGGTTAGGTTTAGAAA Sequencing 2 GTATATTTTTTAATTTGTTAGGTT

Table 2. Primer sequences.

In vitro differentiation

To obtain endoderm and mesoderm cell derivatives, an initial embryoid body (EB) formation step was performed. Briefly, hiPSC and hESC colonies were detached using the previously described non-enzymatic method. Next, cell aggregation was promoted by transferring 150 µL of cell suspension per well into a low-attachment V-bottom 96-well plate. The cells were cultured in KO-DMEM (Sigma-Aldrich) supplemented with 20% KO-Serum Replacement (KO-SR; Life Technologies), 2mM Glutamax (Life Technologies), 50 µM 2-mercaptoethanol (Life Technologies), 10 mL/L penicillin/streptomycin (Sigma-Aldrich) and 1mM non-essential amminoacids (Life Technologies) (KO medium) for 3-4 days to allow EB formation. Then, EBs were transferred into low-attachment 24-well plate and maintained in suspension in KO medium for 2-3 supplementary days. Finally, the EBs were transferred onto 0.1% gelatin (StemCell Technologies, Vancouver, Canada)-coated glass chamber slides (BD). Endodermal differentiation medium was composed of DMEM (Sigma Aldrich), 20% FBS (Life Technologies), 2 mM L-glutamine (Capricorn Scientific; Ebsdorfergrund, Germany), 0.1 mM 2-mercaptoethanol (Life Technologies), 1 mM non-essential aminoacids (Life Technologies) and 10 mL/L penicillin/streptomycin (Sigma-Aldrich). The mesodermal differentiation medium was the same used for endodermal differentiation, supplemented with 100 mM ascorbic acid (Sigma-Aldrich). The EBs were maintained onto the gelatin-coated glass chamber slides for 2-3 weeks. The medium was replaced twice a week.

In order to obtain differentiation to early neuro-epithelial cells, Neurobasal (Life Technologies), 1X N2 (Life Technologies), 1X B27 (Life Technologies), 10 mL/L penicillin/streptomycin (Sigma-Aldrich), 2 mM L-glutamine (Capricorn Scientific) (N2-B27 medium) was used. The following protocol was carried out:

- hESCs and hiPSCs were grown in chamber slides (BD), in the previously described culture conditions;
- At 80% confluence, the medium was removed and KO medium was added to the cells;
- The KO medium was not changed for 5 days;
- At day 5, the medium was carefully aspirated and replaced entirely with 75% KO medium, 25% N2-B27 medium;

- At day 7, the medium was changed to 50% KO medium, 50% N2-B27 medium;
- At day 9, the medium was changed to 25% KO medium, 75% N2-B27 medium;
- At day 12, the medium was carefully aspirated and replaced entirely with 100% N2-B27 medium;
- Between day 12 and day 15, the medium was partially changed once: 1/3 of medium was kept and 2/3 of fresh N2-B27 medium was added;
- When the cells acquired an early neuro-epithelial-like morphology, the medium was removed and the samples were processed for immunofluorescence.

Extracellular vesicle isolation

In order to isolate extracellular vesicles (EVs), different approaches were used for LL-CBMSCs, hESCs and hiPSCs, due to the different cell culture conditions. LL-CBMSCs were grown in 75 cm^2 flasks (BD). At 80%-90% confluence LL-CBMSC culture medium was removed, the cells were washed twice with PBS to remove bovine EVs present in the serum and αMEM (Sigma-Aldrich) without FBS (Life Technologies) was added (starving step). After 24 hours, EV-containing medium was collected and serially centrifuged to remove dead cells (350 xg for 10 minutes) and cellular debris (5,000 xg for 15 minutes). Then, EVs were collected with a 3 hour 100,000 xg ultracentrifugation at 4 °C (F37L 8X100 rotor, Sorvall WX 80+ ultracentrifuge; Thermo Fisher Scientific). Since hESC and hiPSC growth medium did not contain serum, the starving step was not performed. hESCs and hiPSCs were grown in Petri dishes (100 mm) in standard culture medium, until they reached 80% confluence. Then, 24 hour conditioned medium was collected and serially centrifuged, as already described. The supernatant was discarded and the EV pellets resuspended in 150 µL of PBS, for both LL-CBMSCs and pluripotent stem cells. Finally, EVs were stored at -20 °C for subsequent studies.

Nanoparticle tracking analysis

To estimate the number and size of isolated EVs, Nanoparticle Tracking Analysis (NTA) was performed using the NanoSight LM10 instrument (NanoSight, Malvern, UK), which exploits light scattering of a laser beam caused by nanoparticle Brownian movements to count EVs. Immediately after isolation, EVs diluted 1:100 in 500 µL of PBS were analyzed. The EV number was calculated from the mean of n=5 independent counts on the same sample. The culture media were checked for absence of a significant number of nanoparticles.

Flow cytometry protocol for extracellular vesicles

Integrity of EVs was investigated by carboxyfluorescein diacetate succinimidyl ester (CFDA-SE) staining (BD). CFDA-SE is a cell-permeable precursor which can be converted into a fluorescent molecule, carboxyfluorescein succinimidyl ester (CFSE), by cytoplasmic esterases. In addition, the EV immunophenotype was also assessed. To stain EVs, 50 µL of starved LL-CBMSC- or pluripotent stem cell-conditioned medium were collected. Next, EVs were incubated with 5 µL of 100 µM CFDA-SE for 30 minutes in the dark at RT. Alternatively, EVs were incubated with 10 µL of CD63 (BD), CD81 (BD) or isotype (BD) antibodies for 15 minutes at RT. Right after incubation, 300 µL of PBS were added to each sample and EVs were analyzed immediately. In order to visualize EVs on a FACSCantoII standard cytometer (BD), its physical parameters were pushed to their limit of detection. Moreover, forward scatter (FSC) and side scatter (SSC) were set on a logarithmic scale and the FSC threshold was set to a value of 200-350. The data were analyzed with the FACS Diva version 7 analysis software (BD).

Electron microscopy

For Scanning Electron Microscopy (SEM), LL-CBMSCs, hESCs and hiPSCs were cultured on glass coverslips, fixed in 2% glutaraldehyde (Sigma-Aldrich) diluted in PBS, washed twice with PBS and stored at 4 °C. For Transmission Electron Microscopy (TEM), EVs were collected, resuspended in 200 µL PBS and analyzed within 24 hours. SEM and TEM analyses were performed in

collaboration with Università degli Studi dell'Aquila, Dipartimento di Medicina Clinica, Sanità Pubblica, Scienze della Vita e dell'Ambiente.

For SEM analysis, the samples were dehydrated through a graded series of ethanol solutions. Samples were critical-point dried and sputter coated with a SCD040 Balzer Sputterer (Balzers Union, Liechtenstein). A Philips 505 SEM microscope (Philips, Eindhoven, Netherlands) was used to examine the samples, using an accelerating voltage of 20 kV. For TEM analysis, the EVs resuspended in PBS were adsorbed to 300 mesh carbon-coated copper grids (Electron Microscopy Sciences, Hatfield, PA, USA) for 5 minutes in a humidified chamber at RT. EVs on grids were then fixed in 2% glutaraldehyde (Sigma-Aldrich) in PBS for 10 minutes and then briefly rinsed with milliQ water. Grids with adhered EVs were examined with a Philips CM 100 TEM microscope (Philips) at 80kV, after negative staining with 2% phosphotungstic acid (Sigma-Aldrich), brought to pH 7.0 with NaOH. Images were captured by a Kodak digital camera.

miRNA extraction

Isolated extracellular vesicles (EVs) were lysed with 700 µL of QIAzol Lysis Reagent (Qiagen, Hilden, Germany), vortexed and stored at -20 °C until use. To extract miRNA, the miRNeasy Mini Kit (Qiagen) and the RNeasy MinElute Cleanup Kit (Qiagen) were used. Briefly, 140 µL of chloroform were added to the samples, which were shaken vigorously for 15 seconds and let stand for 3 minutes at room temperature (RT). Then, the samples were centrifuged for 15 minutes at 12,000 xg at 8 °C. The resulting upper aqueous phase was transferred to a new collection tube, and 350 µL of 70% ethanol were added. After vortexing, the samples were transferred in RNeasy spin columns, placed in 2 mL collection tubes at RT, and centrifuged for 15 seconds at speed speed at 20 °C. The filters were discarded and 450 µL of 100% ethanol were added to the miRNA-containing flow-through. Next, 700 µL of samples were transferred to RNeasy MinElute spin columns and centrifuged for 15 seconds at speed speed at 20 °C; the flow-through was discarded. This step was repeated for the remaining 700 µL of samples. Then, 500 µL of RPE Buffer were added to the RNeasy MinElute spin columns and centrifuged for 15 seconds at speed speed.

The flow-through was discarded and the columns were placed into new collection tubes. Next, 500 µL of 80% ethanol were added to the columns and centrifuged for 2 minutes at speed speed. The flow-through was discarded and the columns were transferred into new collection tubes. An additional centrifugation at speed speed for 5 minutes was performed with open lids. To elute miRNAs, the columns were transferred into 1.5 mL collection tubes and 20 µL of RNase free-water were added to the filters. The filters were let stand at RT for 5 minutes and then the samples were centrifuged for 1 minute at full speed. RNA quality and quantification were assessed on a 2100 Bioanalyzer instrument (Agilent, Santa Clara, CA, USA). The samples were stored at -80 °C until further use.

miRNA Real Time PCR-array

The miRNome analysis was performed in collaboration with Dipartimento di Scienze Cliniche e di Comunità, University of Milan, Milan, Italy. The complete miRNome was investigated using the Real Time PCR TaqMan OpenArray Human MicroRNA Panel array (Thermo Fisher Scientific, Waltham, MA, USA), covering a total of 754 human miRNAs. The array allowed the simultaneous automated manipulation and analysis of the 3 samples. The experiment was carried out on a QuantStudio 12K Flex Real Time PCR System (Thermo Fisher Scientific). Statistical analysis was performed with R free software version 3.3.1 (https://cran.r-project.org), using VennDiagram package venn.diagram() function and gplots package heatmap.2() function.

Statistical analysis

Online interrogation of miRTarBase experimentally-validated miRNA version 7 database was performed using DIANA miRPath version 3 tool (http://snf-515788.vm.okeanos.grnet.gr/), considering KEGG pathway database. The results were merged by pathways union; 0.05 p-value threshold; 0.8 microT threshold; FDR correction on.

III. Protocols

c. Setting up and analysis of an *ex vivo* organotypic mouse model of brain ischemia

Animals

Experimental procedures involving animals and their care were conducted in conformity with the institutional guidelines at the IRCCS Institute for Pharmacological Research “Mario Negri” in compliance with national (Decreto Legge nr 116/92, Gazzetta Ufficiale, supplement 40, February 18,1992; Circolare nr 8, Gazzetta Ufficiale, July 14, 1994) and international laws and policies (EEC Council Directive 86/609, OJL 358, 1, Dec. 12, 1987; Guide for the Care and Use of Laboratory Animals, U.S. National Research Council (Eighth Edition) 2011). Mice (Harlan Laboratories, Italy) were housed in a specific pathogen-free vivarium (room temperature (RT) 21±1 °C, 12 hour light-dark cycle, free access to food and water). All efforts were made to minimize animal suffering and to reduce the number of animals used.

Mouse brain slice preparation

Organotypic cortical brain slices (named cortical slices from now on) were obtained from prefrontal cortex of C57BL/6 mouse pups (P1-3). Mouse pup brains were removed from the skull under sterile conditions and were immersed into a 3% agar solution. Tissue blocks containing mesencephalic and forebrain levels were dissected out, fixed onto a specimen stage of a vibratome (VT 1000S; Leica Biosystems, Nussloch, Germany) with Super Attack glue, and placed in ice-cold (4 °C) artificial cerebral spinal fluid (ACSF) solution (NaCl=87 mM, $NaHCO_3$=25 mM, NaH_2PO_4=1.25 mM, $MgCl_2$=7 mM, $CaCl_2$=0.5 mM, KCl=2.5 mM, D-glucose=25 mM, sucrose=75 mM, Penicillin=50 U/ml, Streptomicin=50 µg/ml, equilibrated with 95% O_2 and 5% CO_2, pH=7.4). Prefrontal cortex coronal sections of 200 µm thickness were cut. Cortical slices were transferred into Petri dishes filled with ice-cold ACSF. Only intact cortical

slices were placed on membranes of tissue culture inserts (0.4 µm pore size Millicell Culture insert; Merk Millipore, Darmstadt, Germany) with two slices per insert and placed in 6-well plate wells, each filled with 1 mL of culture medium (MEM-Glutamax 25%, basal medium eagle 25% (Life Technologies, Carlsband, CA, USA), horse serum 25% (Euroclone, Pero, Italy), glucose 0.6%, penicillin 100 U/mL, streptomicin 100 µg/mL (Euroclone); pH=7.2). All the cultures were maintained at 37° C in 5% CO_2. After two days, the incubation medium was changed with neurobasal medium (Life Technologies) supplemented with B27 (1:50) (Life Technologies), L-glutamine (1:100) (Life Technologies), penicillin (100 U/mL), streptomycin (100 µg/mL) (Euroclone) (NB/B27 medium) and replaced there after every two days.

Ischemic insult

After one week in culture, cortical slices were subjected to oxygen and glucose deprivation (OGD), an *in vitro* model of brain ischemia. The culture medium was removed, cortical slices were washed twice with PBS (Euroclone) and transferred into a temperature-controlled (37±1 °C) hypoxic chamber (Invivo$_2$ 400; Baker Ruskinn, Bridgend, UK) at [O_2]=0.1%, [CO_2]=5%, [N_2]=95%. Once in the hypoxic chamber, the PBS was replaced with deoxygenated glucose-free medium. After a 2 hour OGD insult, cortical slices were transferred to a normoxic incubator and the medium was replaced with NB/B27 medium. Control cortical slices, not exposed to ischemic injury, were maintained in normoxic incubator with NB/B27 medium. The rescue experiment was conducted according to the experimental plan depicted in figure 5.1.

Propidium iodide incorporation

To evaluate cell death 48 hours after injury, the inserts with cortical slices were moved to new plates and fresh NB/B27 medium containing 2 µM of propidium iodide (PI; Sigma-Aldrich, Saint Louis, MI, USA) was added. After a 30 minute incubation, images were captured at X4 magnification, using the TRITC filter of an Olympus IX71 microscope (Olympus, Tokyo, Japan). Images were then analyzed with Fiji software (University of Wisconsin-Madison, WI, USA) for quantification of PI-positive cells.

Extracellular vesicle labeling

Extracellular vesicles (EVs) resuspended in Diluent C (Sigma-Aldrich) were mixed with PKH26 (Sigma-Aldrich) and incubated for 20 minutes at RT in the dark. The reaction was stopped by adding an equal volume of 1% BSA (Sigma-Aldrich). EVs were then ultracentrifuged at 100,000 xg for 1 hour and resuspended in PBS (Euroclone). PBS (Euroclone) that received the same treatment as above was used as negative control. Cortical slices which received labeled EVs and PBS were observed after 24 hours. Images were captured at X4 magnification, using the TRITC filter of an Olympus IX71 microscope (Olympus, Tokyo, Japan).

Gene expression

Forty-eight hours after injury, cortical slices were collected and total RNA was extracted by miRNeasy mini kit (Qiagen, Hilden, Germany). The samples were treated with DNase (Life Technologies) and reverse-transcribed with random hexamer primers using Multi-Scribe Reverse Transcriptase (Life Technologies). Real time reverse transcription quantitative PCR was performed and relative gene expression determined by the $\Delta\Delta C_t$ method; *β-Act*, *Rpl27* and *B2m* were used as house-keeping genes. Data are expressed as $\log_2$ of the fold difference compared to the control group. Genes and primer sequences are reported in Table 1; the primer pairs were designed not to amplify human sequences.

Gene	Forward Primer	Reverse Primer
β-act	CGCGAGCACAGCTTCTTT	GCAGCGATATCGTCATCCAT
Rpl27	TCATGAAACCCGGGAAAGT	GAGGTGCCATCGTCAATGT
B2m	CTGACCGGCCTGTATGCTAT	TATGTTCGGCTTCCCATTCT
Map2	TCAGCTGACAGAGAAACAGCA	TTGTGTTGGGCTTCCTTCTC
Cd31	GTCGTCCATGTCCCGAGAA	GCACAGGACTCTCGCAATCC
Gfap	GAAACCGCATCACCATTCC	TCGGATGGAGGTTGGAGA
Cd11b	GAGCAGCACTGAGATCCTGTTTAA	ATACGACTCCTGCCCTGGAA
Bdnf	AGGCACTGGAACTCGCAATG	AAGGGCCCGAACATACGATT
Vegf	CATTCCTGGCCCTGAGTCAA TCGC	TGGTTGGAACCGGCATCTTT
Bcl2	GTGCCTGTGGTCATGGATCTG	CCTGTGCCACTTGCTCTTTAG

Bax	GAGAGGCAGCGGCAGTGAT	TGCTCGATCCTGGATGAAACC
Mki67	GATAACGCCACCGAGGACAA	ATGGATGCTCTCTTCGCAGG
Pcna	ACCTTTGAAGATTGCTCCTGAGA	ACTTGGTGACAGAAAAGACCTC

Table 1. List of primers used for real-time reverse transcription polymerase chain reaction.

Evaluation of metabolic and oxidative stress

To investigate levels of metabolites and parameters of oxidative stress in cortical slice conditioned medium, colorimetric or fluorescence reaction-based assays were used for ATP (Abcam, Cambridge, UK), adenosine (Biovision, Milpitas, CA, USA), glutamate (Fitzgerald Industries International, North Acton, MA, USA), malondialdehyde (Fitzgerald Industries International), superoxide dismutase (Biovision) and glutathione (Fitzgerald Industries International).

Multiplex quantification of inflammatory factors

The Cytokine 1 mouse Cyraplex assay (Aushon BioSystems, Billerica, MA, USA) was used to detect inflammatory cytokines present in cortical slice conditioned medium. The assay allowed the simultaneous quantification of murine TNFα, INFγ, IL1β, IL2, IL6, IL10, IL12p70 and IL17. The cell culture supernatants were centrifuged at 350 xg for 10 minutes to remove dead cells, and then they were stored at -80 °C. The samples were thawed completely and mixed by gently vortexing, before performing the assay. Also, unconditioned NB/B27 medium was used as blank. All the samples were used undiluted and diluted 1:10 in Sample Diluent (Aushon BioSystems) Lyophilized analyte standards were reconstituted in Sample Diluent (Aushon BioSystems) and standard curves were prepared by serial dilution, following manufacturer's instructions. Briefly, the MicroClime Lid (Aushon BioSystems) was filled with distilled water and stored until use. The assay plate was washed four times with 300 µL of wash buffer (Aushon BioSystems), then it was dried by firmly patting on absorbent paper. Next, 50 µL of standards or sample were pipetted into each well. The plate was covered with the MicroClime Lid (Aushon BioSystems) and then it was incubated for 3 hours at RT on a plate shaker set at 60 rpm. Another wash step was performed as previously described. Next, 50 µL of Biotinylated Antibody Reagent (Aushon BioSystems) were added to each well.

The plate was covered with the MicroClime Lid (Aushon BioSystems) and then it was incubated for 30 minutes at RT on a plate shaker set at 60 rpm. A final washing step was performed as previously described. The wells were then filled with Block/Stabilizing Solution (Aushon BioSystems) and incubated for 30 minutes at RT. Next, the solution in excess was removed, avoiding to dry completely the wells. The final steps for imaging and analysis were performed at the laboratories of “Tema Ricerca”, located in Castenago, Bologna, Italy. The detection of chemiluminescence was performed on the Cyrascan instrument (Aushon BioSystems) and analyzed by the Cyrasoft software (Aushon BioSystems).

Statistical analysis

All statistical analyses were performed using Prism software (GraphPad, La Jolla, CA, USA). Online interrogation of miRTarBase experimentally-validated miRNA version 7 database was performed using DIANA miRPath version 3 tool (http://snf-515788.vm.okeanos.grnet.gr/), considering KEGG pathway database. The results were merged by pathways union; 0.05 p-value threshold; 0.8 microT threshold; FDR correction on.

This appendix is partially a modified excerpt of a recent paper by the collaborators for the *ex vivo* experiments (Pischiutta F *et al.*, Critical care medicine, 2016).